Uli Micksch

The Chilean subduction zone at 38.2° S: New geophysical images derived from seismic reflection data of project TIPTEQ

Implications for the subduction channel and the seismogenic coupling zone

Scientific Technical Report STR08/14

Uli Micksch

The Chilean subduction zone at 38.2° S: New geophysical images derived from seismic reflection data of project TIPTEQ

Implications for the subduction channel and the seismogenic coupling zone

Scientific Technical Report STR08/14

The Chilean subduction zone at 38.2° S:
New geophysical images derived from seismic reflection data of project TIPTEQ
- Implications for the subduction channel and the seismogenic coupling zone -
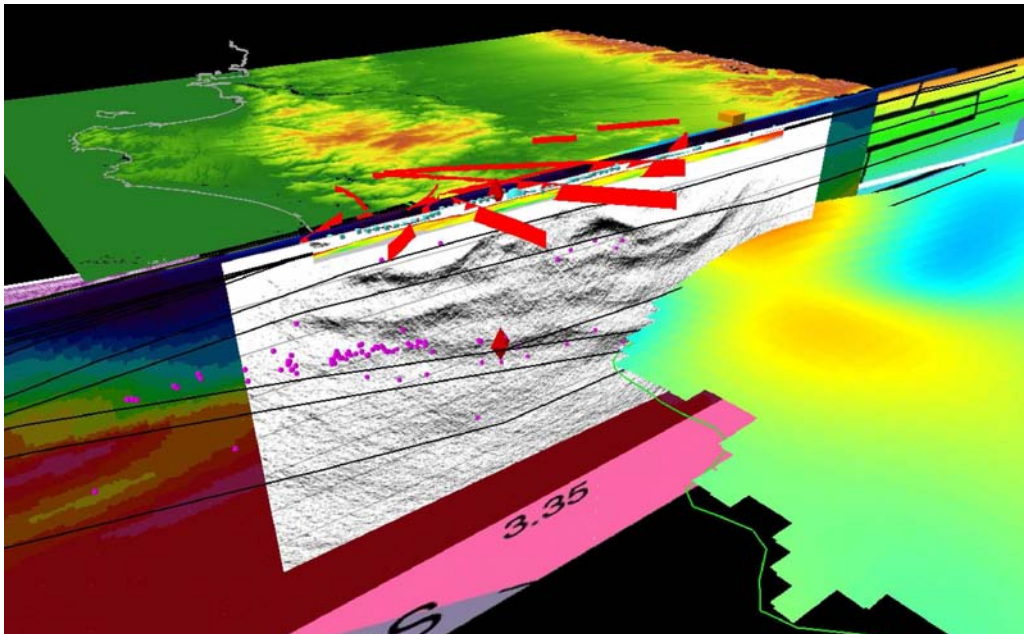

Dipl.-Geophys. Uli Micksch

1. Gutachter: Prof. Dr. O. Oncken
GeoForschungsZentrum Potsdam, Freie Universität Berlin

2. Gutachter: Prof. Dr. C. M. Krawczyk
GGA-Institut Hannover, Technische Universität Berlin

Mitglieder der Kommission:
Prof. Dr. O. Oncken, GeoForschungsZentrum Potsdam, Freie Universität Berlin
Prof. Dr. C. M. Krawczyk, GGA-Institut Hannover, Technische Universität Berlin
Prof. Dr. R. Kind, GeoForschungsZentrum Potsdam, Freie Universität Berlin
Prof. Dr. M. R. Handy, Freie Universität Berlin
Dr. P. Wigger, Freie Universität Berlin

Datum der Disputation: 15.09.2008

Eidesstattliche Erklärung

Hiermit versichere ich, dass die vorliegende Dissertation ohne unzulässige Hilfe Dritter und ohne Benutzung anderer als der angegebenen Literatur angefertigt wurde. Die Stellen der Arbeit, die anderen Werken wörtlich oder inhaltlich entnommen sind, wurden durch entsprechende Angaben der Quellen kenntlich gemacht.

Diese Arbeit hat in gleicher oder ähnlicher Form noch keiner Prüfungsbehörde vorgelegen.

Uli Micksch, Potsdam, Juni 2008

FEBRUARY 20, 1835, Valdivia

A bad earthquake at once destroys our oldest associations: the earth, the very emblem of solidity, has moved beneath our feet like a thin crust over a fluid; – one second of time has created in the mind a strange idea of insecurity, which hours of reflection would not have produced. In the forest, as a breeze moved the trees, I felt only the earth tremble, but saw no other effect. Captain Fitz Roy and some officers were at the town during the shock, and there the scene was more striking; for although the houses, from being built of wood, did not fall, they were violently shaken, and the boards creaked and rattled together. The people rushed out of doors in the greatest alarm. It is these accompaniments that create that perfect horror of earthquakes, experienced by all who have thus seen, as well as felt, their effects. Within the forest it was a deeply interesting, but by no means an awe-exciting phenomenon.

Charles Darwin, A Naturalist's Voyage Round the World - The Voyage Of The Beagle
(Excerpt taken from 'Project Gutenberg', http://www.gutenberg.org/etext/3704)

Nothing in life is to be feared. It is only to be understood.
Marie Curie

Nothing shocks me. I'm a scientist.
Harrison Ford as Indiana Jones

An experiment is a question which science poses to nature,
and a measurement is the recording of nature's answer.
Max Planck

Indes sie forschten, röntgten, filmten, funkten,
entstand von selbst die köstlichste Erfindung:
der Umweg als die kürzeste Verbindung zwischen zwei Punkten.
Erich Kästner

This thesis is dedicated to my family

Abstract

The joint project TIPTEQ (from The Incoming Plate to mega-Thrust EarthQake processes) refers to an integrated approach in order to investigate the processes active in the seismogenic coupling zone at the southern Central Chilean margin and to validate their importance for both the initiation of mega-thrust earthquakes and the evolution of the forearc. The lateral variability of these processes and related parameters is investigated along five marine corridors offshore the south Chilean continental margin. The northernmost marine transect is continued onshore with a reflection seismic survey at 38.2° S which crosses the hypocenter of the largest ever recorded earthquake, the 1960 Great Chilean earthquake (Mw = 9.5). The processing and structural interpretation of this high-resolution seismic data set is one major task of this thesis. Furthermore, a first-break tomography was conducted to construct a near-surface velocity model. Several tests to validate the tomographic images were conducted and the limitations of the data set and method were explored in detail. The reflection seismic transect lies in the center of an extensive geophysical program comprising magnetotelluric surveys and a large seismological network. An integrative interpretation with the results of the other geophysical groups of TIPTEQ concludes the thesis. The depth section of the TIPTEQ NVR data set shows the subducting Nasca plate below the segmented forearc and a highly reflective overriding South American plate down to a depth of 60 km. High reflectivity directly above the plate interface suggested to be associated with the existence of a subduction channel with a varying thickness of 2 - 5 km down to a depth of at least 38 km. It might continue towards depth. Local seismicity possibly defines the upper bound of the subduction channel. The continental Moho is not clearly imaged. However, one possible location is at 38 - 40 km depth given by the 1960 earthquake hypocenter. The Moho may be continued eastwards to a depth of 35 km where a prominent structure is imaged. This reflector coincides with the modeled Moho interface from a 3–D density model along the Chilean margin. The reflectivity east and above of the 1960 hypocenter area may exhibit alternative eastward continuations of the continental Moho. The position and extent of the continental mantle wedge changes accordingly. Major forearc features such as the crustal Lanalhue Fault Zone and a strong west-dipping reflector perpendicular to the plate interface can be observed. The reflectivity of the oceanic crust increases in depths below 35 km. This increase might be caused by fluid release due to the porosity collapse in basalt. The integrative interpretation links this observation with a zone of high Vp/Vs ratio calculated from the seismological velocity model. Combining all available data sets of seismological, magnetotelluric and gravimetrical findings results in a complex image of the southern Chilean subduction zone, which this thesis addresses to decode.

Zusammenfassung

Das Verbundprojekt TIPTEQ (from The Incoming Plate to mega-Thrust EarthQake processes) untersucht aktive Prozesse in der seismogenen Koppelzone am südchilenischen konvergenten Plattenrand, um ihren Einfluss auf die Entstehung von mega-thrust Erdbeben sowie die Evolution des forearcs abzuschätzen. Die laterale Variabilität dieser Prozesse und die mit ihnen verknüpften Parameter werden entlang von fünf marinen Korridoren untersucht. Landwärts schließt sich dem nördlichsten Korridor ein reflexionsseismisches Profil bei 38.2° S an. Dieses Profil quert das Hypozentrum des größten je gemessenen Erdbebens, das Chile Beben von 1960 (Mw = 9.5). Ein Hauptschwerpunkt der vorliegenden Doktorarbeit ist das Prozessieren und die anschließende strukturelle Interpretation dieses hoch aufgelösten reflexionsseismischen Datensatzes von TIPTEQ. Weiterhin wurde eine Ersteinsatz-Tomographie durchgeführt, um ein oberflächennahes Geschwindigkeitsmodell des Untergrundes zu erstellen. Die verschiedenen geophysikalischen Messungen innerhalb von TIPTEQ decken ein Gebiet ab, in dessen Mitte das reflexionsseismische Profil liegt, so dass eine integrative Interpretation der Ergebnisse möglich ist, worauf im dritten Teil der Doktorarbeit der Schwerpunkt liegt. Die Tiefensektion des Steilwinkeldatensatzes zeigt die subduzierende Nazca Platte bis in eine Tiefe von 60 km. Hohe Reflektivität über der Plattengrenze kann einem möglichen Subduktionskanal zugewiesen werden. Dieser variiert in der Mächtigkeit zwischen 2-5 km und kann mindestens in eine Tiefe von 38 km verfolgt werden. Die lokale Seismizität bestimmt möglicherweise die obere Begrenzung des Kanals. Die kontinentale Moho ist strukturell im seismischen Bild nicht aufgelöst. Das Hypozentrum des Erdbebens von 1960 markiert ein mögliches Aufeinandertreffen der kontinentalen Moho und der subduzierenden Plattengrenze in 38 bis 40 km Tiefe. In Richtung Osten verringert sich die Tiefenposition der interpretierten kontinentalen Moho auf ca. 35 km. Von da aus kann sie mit einem Reflektor in Verbindung gebracht werden, der im gleichen Tiefenintervall verläuft, wie es gravimetrische Modellierungen entlang des Profils für den Tiefenverlauf der Moho suggerieren. Alternative Tiefen der Moho können anhand der beobachteten Reflektionsmuster nicht ausgeschlossen werden, wodurch sich auch die Geometrie des Mantelkeils entsprechend ändern würde. Markante Strukturen des forearcs wie die Lanalhue Störungszone werden in der Seismik abgebildet. Am östlichen Ende des Profils ist ein mysteriöser Reflektor zu erkennen, der zwischen 65 und 40 km Tiefe senkrecht zum Platteninterface liegt. Die Reflektivität in der ozeanischen Kruste nimmt unterhalb einer Tiefe von 35 km rapide zu. Dies könnte mit der Dehydration der ozeanischen Kruste zusammenhängen, die durch den Kollaps des im Basalt vorhandenen Porenraums ausgelöst wird. Die integrierte Interpretation verknüpft diese Information mit einer Zone von erhöhtem Vp/Vs Verhältnis, das

sich aus einem Geschwindigkeitsmodell der Seismologie Gruppe innerhalb TIPTEQs ergibt. Diese Korrelationen von allen Resultaten der anderen TIPTEQ Arbeitsgruppen lassen ein sehr komplexes Bild der Subduktionszone entstehen, dessen Entschlüsselung in dieser Arbeit nachgegangen wird.

Contents

Contents

Contents

List of Figures

List of Tables

List of abbreviations

°	Degrees
'	Minutes
AC	Alternating Current
AGC	Automatic Gain Control
ANCORP	ANdean COntinental Research Program to image an active subduction
ASCII	American Standard Code for Information Interchange
asl	Above Sea Level
AWK	AWK, programming language, initials of developers
b	Byte
C	Celsius
c	Speed of light, speed of air
CDP	Common Depth Point
cf.	ConFer
CGM	Computer Graphics Metafile
Ch	CHannel
CINCA	Crustal Investigation off- and onshore Nazca/Central Andes
CPU	Central Processing Unit
D	Dimension, 2–D, 3–D
d	Day
DC	Direct Current
DEM	Digital Elevation Modell
DMO	Dip MoveOut
E	ESP
E	East
e.g	Exempli Gratia, for example
EDL	Earth Data Logger
elev	Elevation
ES	Eastern Series
ESP	Expanding Spread Profilling
f	Frequency
f-k	Frequency-wavenumber (k)
FAST	3-D First Arrival Seismic Tomography programs

List of abbreviations

FFID	....	Field File IDentification number
FU	....	Free University of Berlin
G	....	Giga, 10^9
GFZ	....	GeoForschungsZentrum Potsdam, the German Research Centre for Geosciences (A Helmholz center)
GMT	....	Generic Mapping Tools
GPS	....	Global Positioning System
h	....	Hour
HD	....	Hard-Disk
Hz	....	Hertz
ID	....	IDentification number
IRIS	....	Incorporated Research Institutions for Seismology
ISSA	....	Integrated Seismological experiment in the Southern Andes
JPG	....	Joint Photographic Experts Group
KPSDM	....	Kirchhoff PreSack Depth Migration
lat	....	Latitude
LINUX	....	computer operating system
LMO	....	Linear MoveOut
long	....	Longitude
42	....	The answer to life, the universe, and everything
LVZ	....	Low Velocity Zone
M	....	Mega, 10^6
m	....	Meter
m	....	Million
m	....	Minutes
m	....	Month
min	....	MINute
Moho	....	Mohorovičić discontinuity
ms	....	MilliSecond, 10^{-3}
MT	....	MagnetoTellurics
Mw	....	Moment magnitude scale
N	....	North
n	....	NVR
NAN	....	Not A Number
NASA	....	National Aeronautics and Space Administration
nloc	....	Nearest LOCation
NMO	....	Normal MoveOut
no.	....	Number of ...
nts	....	Not To Scale
NVR	....	Near Vertical incidence Reflection
OBS	....	Ocean Bottom Seismometer
OPF	....	Ordered Parameter File

P	<u>P</u>ressure
P-wave	<u>P</u>ressure wave
PC	<u>P</u>ersonal <u>C</u>omputer
PDAS	Teledyne-Geotech PDAS-100 data logger
pers. comm.	Personal communication
PhD	<u>D</u>octor of <u>P</u>hilosophy
PNG	<u>P</u>ortable <u>N</u>etwork <u>G</u>raphics
PS	<u>P</u>ost<u>S</u>cript
r	<u>R</u>adius
RAM	<u>R</u>andom <u>A</u>ccess <u>M</u>emory
RMS	<u>R</u>oot <u>M</u>ean <u>S</u>quare
RV	<u>R</u>esearch <u>V</u>essel
S	<u>S</u>outh
s	<u>S</u>H
s	<u>S</u>econd
S-wave	<u>S</u>hear wave
SEG-Y	The <u>S</u>ociety of <u>E</u>xploration <u>G</u>eophysicists, standardized seismic data format
SEGMI	<u>S</u>ervicios <u>G</u>eofisicos en <u>M</u>ineria e <u>I</u>ngenieria LTDA.
SERNAGEOMIN	<u>SER</u>vicio <u>NA</u>cional de <u>GEO</u>logía y <u>MIN</u>nería, Santiago de Chile
SH	<u>S</u>hear wave, polarized <u>H</u>orizontally
SNR	<u>S</u>ignal to <u>N</u>oise <u>R</u>atio
SP	<u>S</u>hot<u>P</u>oint
SPOC	<u>S</u>ubduction <u>P</u>rocesses <u>O</u>ff <u>C</u>hile
SRF	<u>S</u>u<u>RF</u>ace
SRTM	<u>S</u>huttle <u>R</u>adar <u>T</u>opography <u>M</u>ission
T	<u>T</u>emperature
t	<u>T</u>ime
TIPTEQ	From <u>T</u>he <u>I</u>ncoming <u>P</u>late to mega-<u>T</u>hrust <u>E</u>arth<u>Q</u>ake processes
TR	<u>T</u>Race
TWT	<u>T</u>wo <u>W</u>ay <u>T</u>ravel-time
UNIX	computer operating system
v	<u>V</u>elocity
VE	<u>V</u>ertical <u>E</u>xaggeration
Vp	<u>V</u>elocity of <u>P</u>ressure wave
vs.	versus
W	<u>W</u>est
WS	<u>W</u>estern <u>S</u>eries
x	distance in 'x' direction; horizontal east-west axis direction
y	<u>Y</u>ear
y	distance in 'y' direction; horizontal north-south axis direction
z	distance in 'z' direction; vertical axis direction

1. Introduction

1.1. Overview

The Andes are a spectacular mountain range that extends along the whole western South American continent over 7500 km in length. It reaches a maximum width of 800 km and elevations up to 6962 m (Aconcagua). The convergent plate margin between the South American continental upper plate and the subducting oceanic plates, e.g. the Nazca and Antarctic plates, forms the Andes as we see them today. Subduction was active at least the past $\approx$ 305 m.y. (Willner et al., 2004). The 'Andean' type of subduction started $\approx$ 200 m.y. ago (Mpodozis and Ramos, 1989), when a geochemical change from crust-dominated to more mantle-dominated magmas occurred (Glodny et al., 2007). Current convergence rates are 6.6 cm/y with an azimuth of 078° calculated from modeling GPS data (Angermann et al., 1999; Kendrick et al., 2003). Different research groups such as the Collaborative Research Center (SFB 267) "Deformation processes in the Andes"[1] (Oncken et al., 2007) or the Cornell Andes Project[2] focused on different key areas for the last decades and provided a huge database in all fields of geosciences from the offshore Nazca plate to the Subandean mountain ranges in the east. These studies revealed a highly diverse configuration of the subduction zone along the margin with respect to e.g. subduction mode and in particular the presence of a subduction channel, flat slab segmentation, or structural development. The underlying geodynamic processes are suggested to be dependent on climate, convergence rates, structure of the oceanic lower plate, or slab geometry. But the main suspects which are responsible for the shape and evolution of the orogeny are still under debate.

The joint project TIPTEQ (from The Incoming Plate to mega-Thrust EarthQake processes) refers to an integrated approach in order to investigate the processes active in the seismogenic coupling zone at the southern Central Chilean margin and to validate their importance for both the initiation of mega-thrust earthquakes and the evolution of the forearc (cf. Krawczyk et al. (2002) for references). The lateral variability of these processes and related parameters and structures is investigated along five marine corridors offshore the south Chilean continental margin. This enables to study different ages and therefore thermal regimes of the incoming plate and to asses the lateral variability of the trench sediments. The northernmost marine transect is continued onshore with a reflection seismic survey. This seismic profile is the focus of the thesis presented here. The transect at 38.2° S crosses the hypocenter of the 1960

---

[1]SFB 267: `http://www.fu-berlin.de/sfb/sfb267/index.html`
[2]Cornell Andes Project: `http://www.geo.cornell.edu/geology/cap/`

Chilean earthquake (Mw = 9.5), the largest ever recorded earthquake (Kanamori, 1977). The reflection seismic profile lies also in the center of the extensive landward geophysical program of TIPTEQ, including seismology or magnetotelluric studies. Substantial knowledge was gained in the survey area over the last years with geophysical programs like SPOC (Krawczyk and the SPOC Team, 2003) or ISSA-2000 (Lüth et al., 2003; Bohm, 2004), but until now, high resolution reflection seismic images lack at this part of the margin.

The rupture plane of the 1960 Chilean earthquake started at 38.2° S and extends ≈ 900 km in length towards the Chile Triple Junction. The earthquake induced tsunamis which caused severe devastation along the Chilean coast and caused deaths even as far away as in Japan. Remarkable changes in land levels were observed along the whole rupture plane. Coseismic elevation changes of +0.1 and -2.5 m were observed, submerging large areas in the vicinity of Valdivia (Barrientos and Ward, 1990). A cyclicity of such mega-thrust events is observed in the available historic record and the seismic energy is released repeatedly along individual segments (cf. Melnick et al. (2006) and references therein). Volcanic eruptions that occur after those large earthquakes are another natural hazard in southern Chile (Barrientos, 1994). During the 'Beagle' Expedition (1831 - 1836) Charles Darwin experienced a large earthquake in the study area. He documented consequences such as coseismic uplift or reported on erupting volcanoes temporally delayed to the earthquake event (Darwin, 1839). A collection of papers addressing the resultant tsunami and onshore effects of the 1960 Chile earthquake is found in a special issue of the Bulletin of the Seismological Society of America (Various, 1963).

This thesis focusses on the reflection seismic part of the TIPTEQ experiment and comprises the poststack processing and structural interpretation of the vertical component of the near-vertical-incident reflection seismic data set. The resultant depth section is discussed in terms of tectonic processes in the forarc, subduction channel, Moho depth and serpentinisation processes. The migrated depth section is also compared in detail with results of other geophysical groups within TIPTEQ to conclude with an integrative interpretation. In addition, a first-break tomography was conducted with the available seismic data set and the limitations of this method were investigated in detail.

Chapter 1 introduces the thesis and gives an brief overview of the used geological maps and geophysical data of former experiments in the working area.

Chapter 2 provides all necessary information on the active source seismic experiment and related geometry information needed in the subsequent chapters.

Chapter 3 and 4 deal with the extensive preprocessing and processing of the reflection seismic data, followed by the presentation of the stacked time section and the migrated depth sections in chapter 5.

Chapter 6 - 8 concentrate on the first-break tomography. The preparation of the data, the procedure and model setup are shown first. The first tomographic images and the efforts to validate them are presented afterwards. Unstable inversion results and low ray coverage lead

to a revised, limited input for the tomographic inversion, resulting in the final tomographic velocity model of chapter 8.

Migration tests to assess the deviations due to different subsurface velocity models were conducted and are presented in chapter 9.

The interpretation and discussion of the depth section in a geodynamic context is given in chapter 10 which also includes a detailed integrated comparison and discussion with results of other geophysical groups of TIPTEQ.

Chapter 11 summarizes the major results from this thesis and gives a short prospect.

The extensive appendix contains tables, detailed information on conducted validation tests or the MATLAB scripts to merge velocity models.
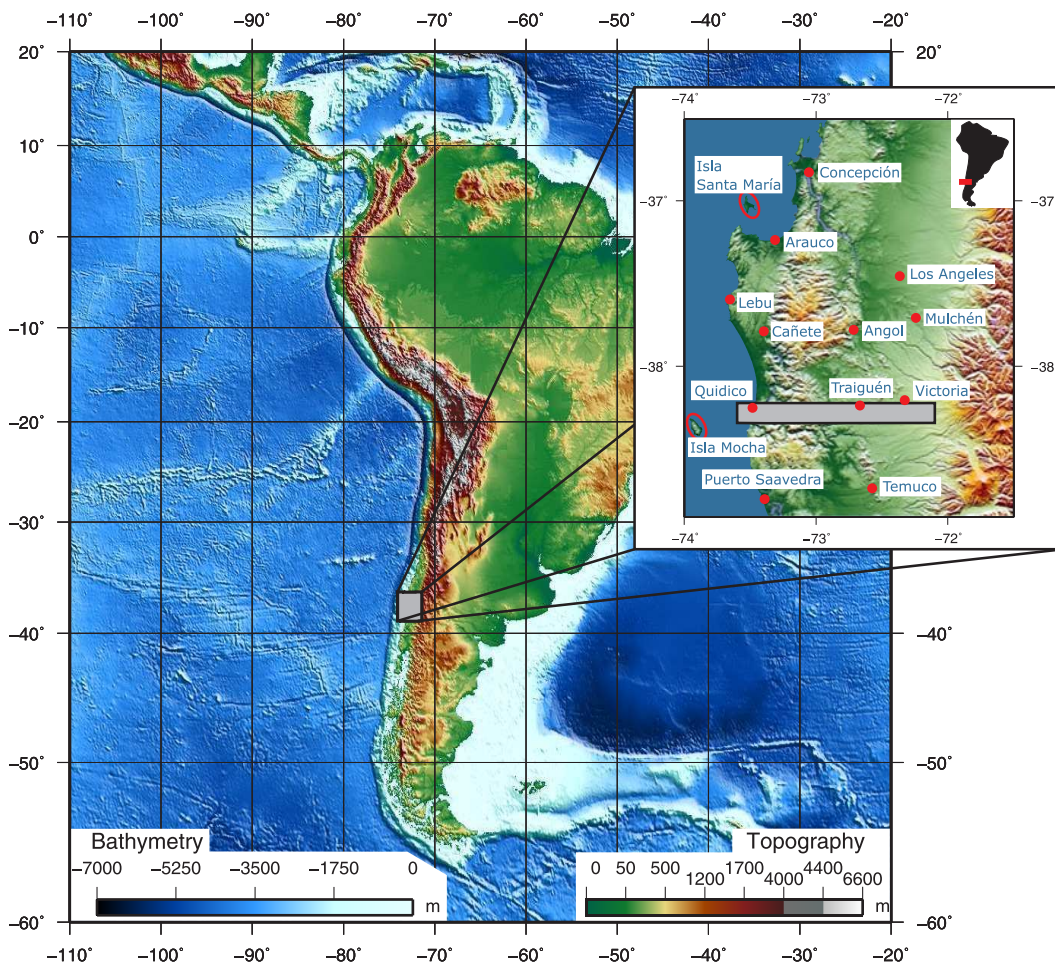
Figure 1.1.: Topographic and bathymetric map of South America, the inset shows the Arauco area with local cities and villages. The grey rectangle encompasses the TIPTEQ active source reflection seismic profile. A detailed map of the survey geometry is shown in figure 2.5.

1.2. Used geological maps and geophysical data

The recent book title 'The Andes - Active Subduction Orogeny' (Oncken et al., 2007) contains several papers which deal with the TIPTEQ working area. Two key papers are by Glodny et al. (2007) addressing the geological evolution of the margin between 36° - 42° S and by Krawczyk et al. (2007) summarizing the results of the SPOC-2001 and ISSA-2000 geophysical experiments.

The geological setting, deformation rates and fault kinematics of the coastal forearc since the Neogene are documented in a PhD thesis by Melnick (2007).

A recent PhD thesis by Bachmann (2008), compares an ancient subduction zone in the Alps with the ongoing subduction in southern central Chile. The author gives a detailed review on concepts of plate interfaces - like the 'subduction channel' - and decodes the anatomy and processes active along such a channel with extensive field work data.
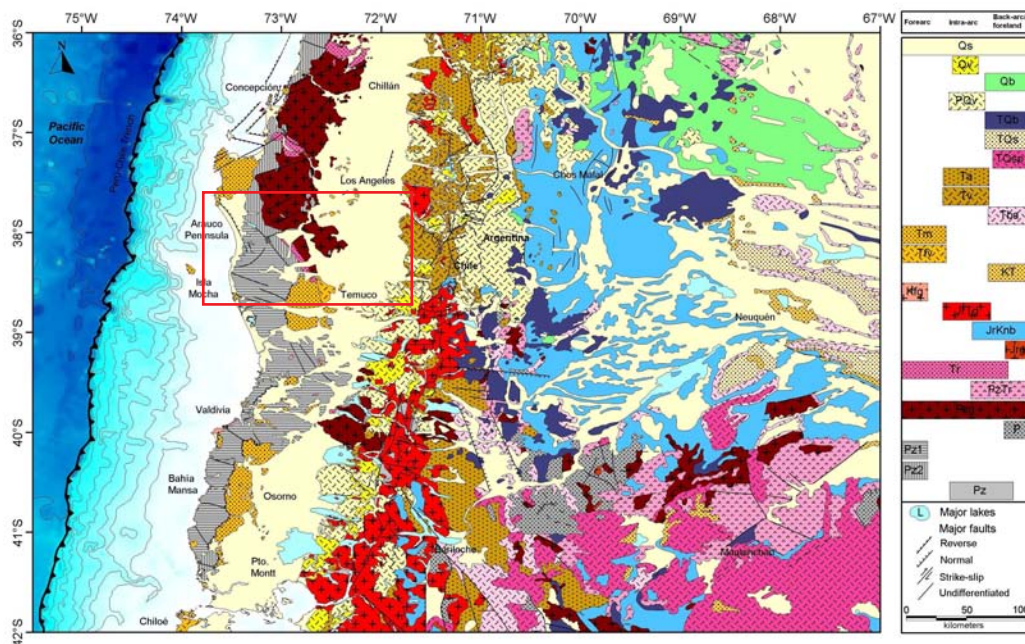
Figure 1.2.: Geological map compilation of the south central Andes, the TIPTEQ working area is marked by a red box. This map was used for the interpretation of the first-break tomography. Figure taken from Melnick and Echtler (2007).
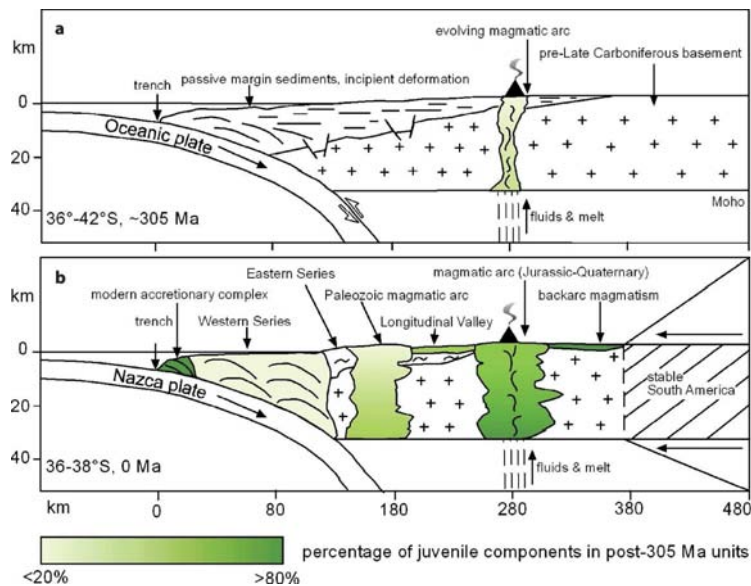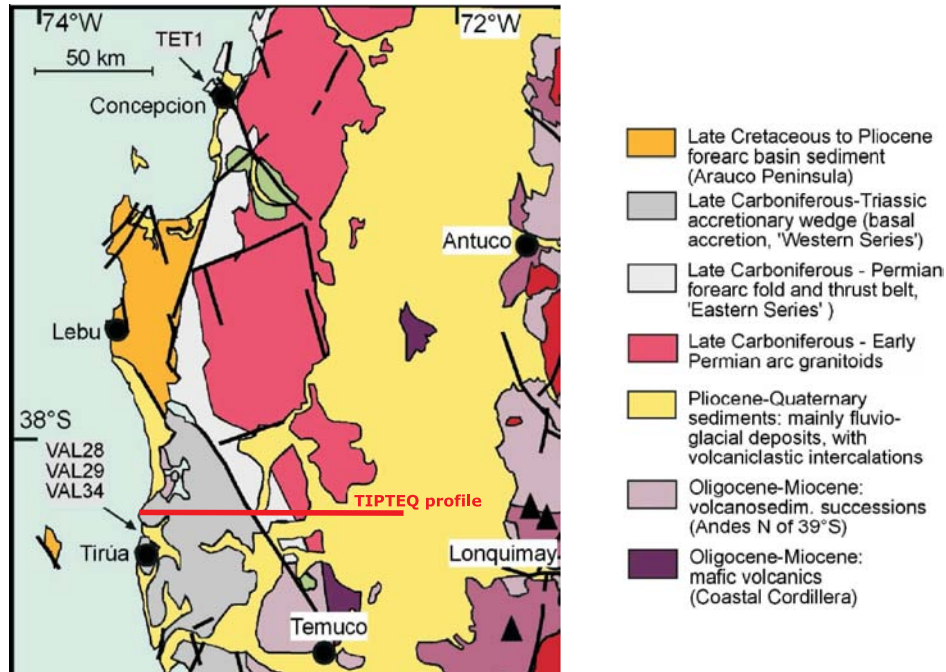
Figure 1.3.: Upper panel: Geological map compilation of the south central Andes after SERNAGEOMIN (2003). Lower panel: Schematic model of margin geometries showing the distribution of juvenile additions within the continental crust. a) Situation immediately after the initiation of subduction with incipient arc magmatism and progressively deforming, former, passive-margin sequences. b) Today's architecture north of 38° S. Displacement of both, the Palaeozoic arc and stable South America, towards the trench signifies margin truncation by 100 km in the early Permian. Figures taken from Glodny et al. (2007).
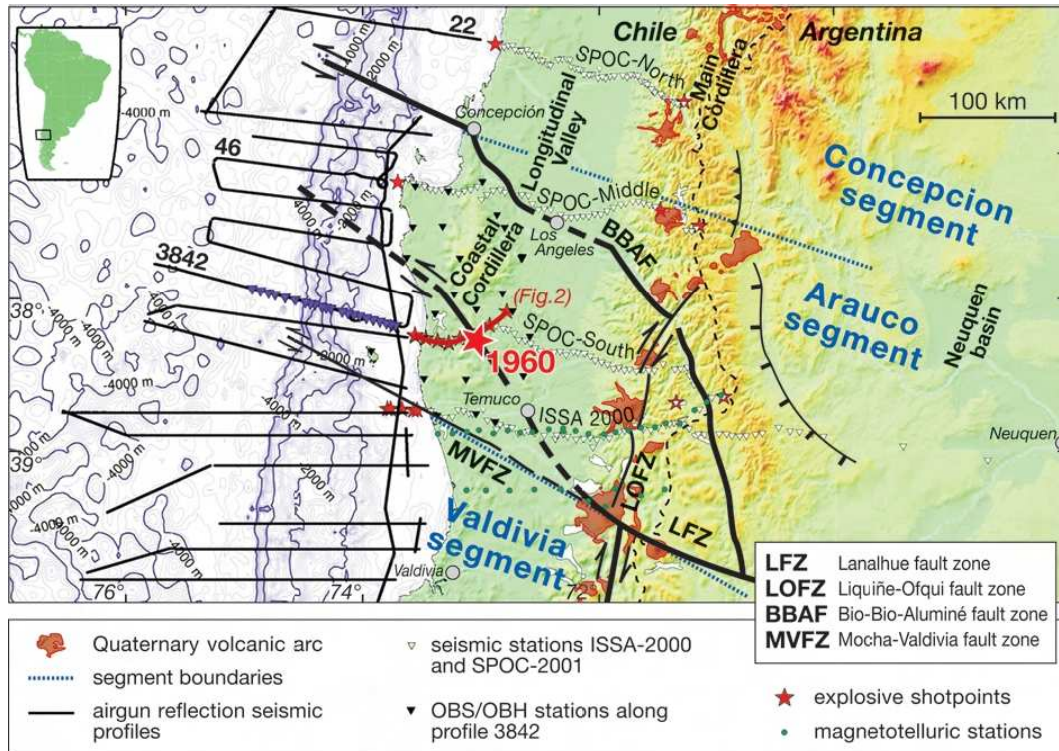
Figure 1.4.: Map of existing geophysical transects between 36° - 40° S (Krawczyk et al., 2007). The TIPTEQ seismic line crosses the red star (marking the 1960 earthquake hypocenter) in an EW direction and coincides partly with the SPOC-NVR CDP line shown in red. The margin can be divided into seismic segments in NS direction, where historic subduction earthquakes repeatedly initiated (Melnick et al., 2006). From the West to the East, the margin is divided into trench-parallel elements like the Coastal Cordillera, Longitudinal Valley and the Main Cordillera. The main tectonic elements and fault zones are (Melnick and Echtler, 2007): LFZ: Lanalhue fault zone; LOFZ: Liquiñe-Ofqui fault zone; BBAF: Bio-Bio-Aluminé fault zone; MVFZ: Mocha-Valdivia fault zone; red areas: Quaternary volcanic arc; blue dotted lines mark segment boundaries; black lines: airgun reflection seismic profiles; yellow and black triangles: seismic stations deployed along refraction and reflection seismic profiles during the ISSA-2000 and SPOC-2001 projects; blue triangles: OBS/OBH stations that recorded airgun shots along profile 3842; red stars: explosive shotpoints; green dots: magnetotelluric stations.
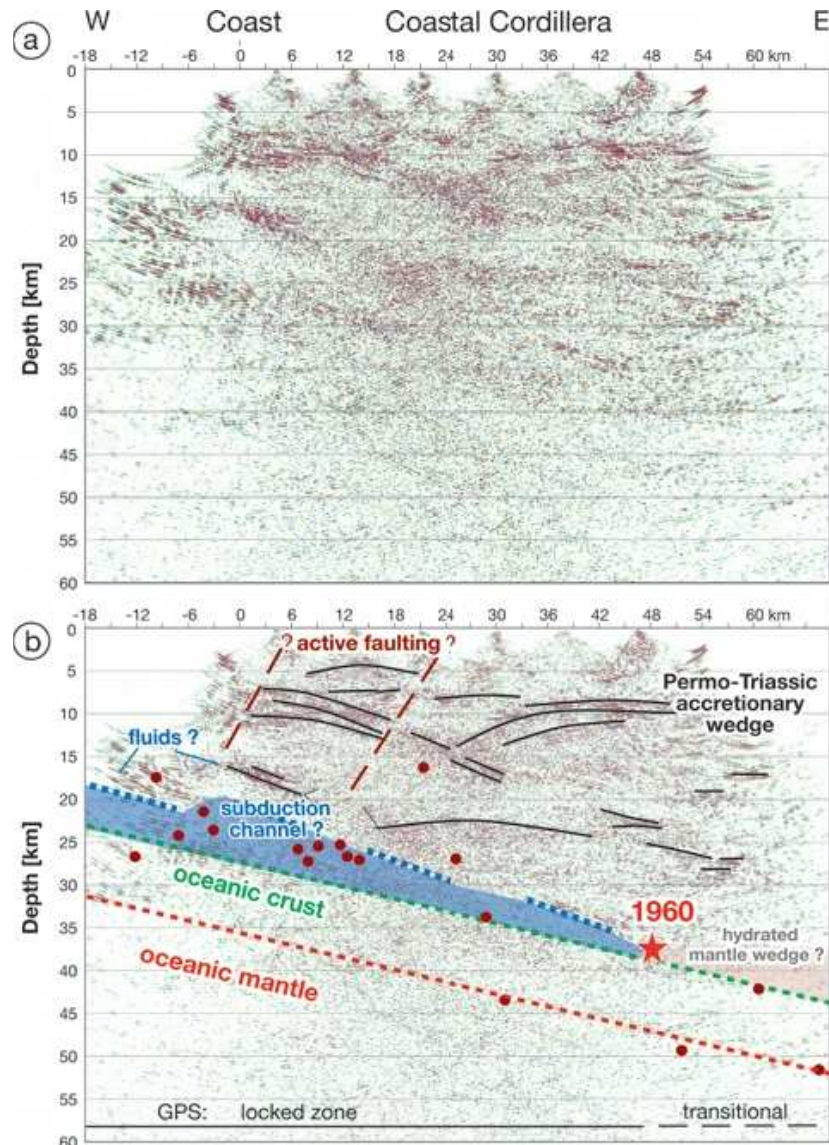
Figure 1.5.: a) SPOC near-vertical incidence reflection seismic profile after depth migration. The line covers the westernmost 70 km of the onshore part of the SPOC–South refraction profile. b) In the interpreted section, the subducting plate is projected into the section from the SPOC wide-angle model. Immediately above, a possible subduction channel that transports material from W to E below the overriding plate and the presumed hypocenter of the 1960 Chile earthquake are marked. The upwardly convex reflective structures are interpreted to represent the Permo-Triassic accretionary wedge. Seismicity is sparse within a 25 km-wide clip area. Figure taken from Krawczyk et al. (2007).
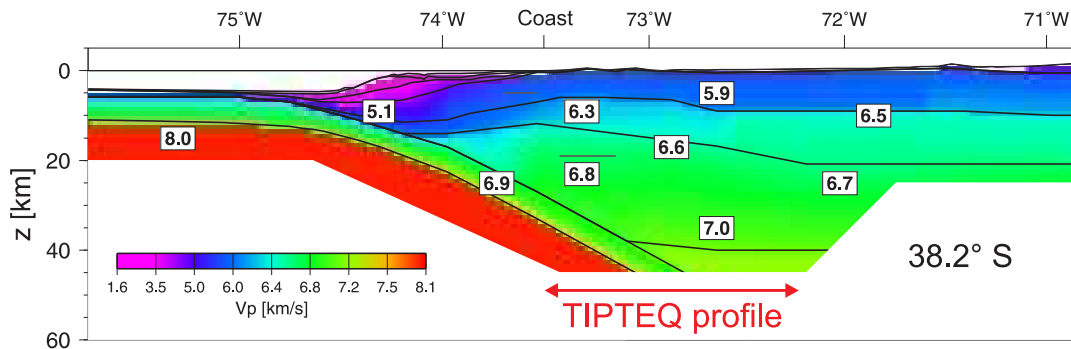
Figure 1.6.: SPOC–South wide-angle P-wave model, figure modified after Krawczyk and the SPOC Team (2003) and Lüth et al. (2003). The model resolves the geometry of the downgoing plate and the velocity structure at 38.2° S. The oceanic Moho is well constrained in the data, the thickness of the oceanic crust was inferred from a marine seismic line at the coast. The SPOC–South data contain no reflected or refracted phases of the continental Moho. The continental Moho is drawn where velocities over 7.2 km/s are reached in the velocity model. This is based on upper mantle velocities found along the ISSA-2000 transect one degree south of the onshore TIPTEQ/SPOC profile (Lüth et al., 2003). The SPOC–South velocity model served as reference velocity model for the stacking and migration of the TIPTEQ NVR data set.

2. The seismic experiment

The active source seismology experiment of TIPTEQ was conducted between 13. - 31. January 2005. The work commenced with the setup of the first headquarter in Traiguen several days before the shooting where the equipment was checked and prepared. The available time was used to train the field crews consisting of multinational teams of German and Chilean scientists and students. The receiver points for the first receiver deployment were also pegged out with wooden stakes. Their coordinates were calculated prior to the experiment with data from the pre-site survey.

The local roads were mapped with GPS during the pre-site survey. The most ideal east-west trending roads were selected as profile line from Victoria in the east to Quidico at the Pacific Ocean. A so called CDP line was calculated with linear regression (Wikipedia, 2008a) using the GPS data of the selected roads. This straight line represents the ideal profile line. A deployment of the seismic stations directly on this line is not possible because of the vegetation, topography and land usage. So, a crooked line geometry must be used. Each 100 m along the CDP line a perpendicular line was calculated and the intersection of that line with the mapped roads pinpoints the exact receiver location. The receiver line meanders north and south of the CDP line to keep the crossline offset minimal, which is here below 3 km (cf. figure 6.2 in the appendix). This approach results in 955 receiver stations, each 100 m apart, the first station is located in the Central Valley east of Traiguen. 180 stations (= 18 km) were deployed at once to form the active spread, which was designed to move 4.5 km (45 stations) in a daily roll-along towards the ocean. All seismic stations were equipped with buried, three-component geophones. The shotpoint locations were distributed in the same manner approximately 1.5 km apart, the exact position was finally determined by the local conditions around the shotpoint in terms of feasibility, safety or property of land. Three shotpoints off the line in the east complete the seismic line to obtain subsurface information in the Central Valley east of the last receiver.

Three types of shot setups form different experiment components. The core experiment component is the near-vertical incident reflection seismic profile (NVR) consisting of 4 shots within each active spread (see figure 2.2). Two are fired from each end of the spread, the other two are executed within the spread in 6 km distance, respectively. 76 shots are fired in that way, including the three shots off the line in the east. The highest fold achieved with this setup is 8-fold. The z-component data resulting from this setup is used for the migrations shown in this thesis.

9

The second experiment component is called SH, which aims to generate horizontally polarized shear waves. The method of 'Camouflet' shooting (Dohr, 1985) was tested in a crustal regime as a pilot study. The idea behind this method is to create a cavern with one central shot in the subsurface. Two additional shots perpendicular to the profile line create shear waves through conversions of pressure waves to shear waves on the created cavern surface. The result is a tippled P wave energy for those three shots, whereas if the two shots with crossline offsets are subtracted from each other, the P wave energy is cancelled out, but the antithetic polarized SH waves are summed up, and therefore amplified (see figure 2.1). Only 13 additional shots are needed (see figure 2.2), because the used roll-along tech-

Figure 2.1.: Scheme of the Camouflet shooting method (Dohr, 1985) which uses a 3 hole setup (figure by M. Stiller, GFZ, pers. comm.).

nique allows to use some shotpoints several times. These shots are basically repeated NVR shots and are included in the tomographic inversions presented in this thesis. More information on the results of the pilot study can be found in a PhD thesis by Groß (2008) where a coherency analysis of the SH shots showed a good repeatability and waveform semblance of the seismic traces up to 60 s two way travel-time. The expected increased generation of SH waves was not observed, perhaps due to the lack of conversions at the created cavern of the first shot. The third experiment component consists of an expanding spread profile (ESP). When the active spread moves along the profile, 15 additional shots are fired at certain offsets to the spread (see figure 2.3). This setup focuses at the downdip end of the seismogenic coupling zone where the hypocenter of the 1960 mega-thrust earthquake is assumed. This results in a short ten-fold section in the central part of the profile. The ESP shot data were tested to be included in the tomographic inversions, because it was hoped that the greater offsets result in a deeper coverage of the subsurface. More information on results from the ESP experiment component can also be found in Groß (2008).

The first shot (FFID1) was executed at shotpoint 97 at the 13th of January 2005. The shot times were measured with two methods. A geophone was placed close to the borehole, and the first-break time of the explosion on the recorded trace gives the shot time. The second, main method used to determine the shot time for the TIPTEQ shots, is to measure the time of the electrical pulse created by the trigger box via induction in the ignition lead. Three milliseconds were added to that shot time to account for the time which is needed for the blasting cord to 'burn' before igniting the blasting agent. 104 shots were planned to be fired for all three experiment components in total, two misfires occurred at shotpoints 9 and 12. Table A.1 in the appendix gives a detailed list of all shot related information like coordinates and shot times. The deployed receiver stations consisted of an 'earth data logger' recording
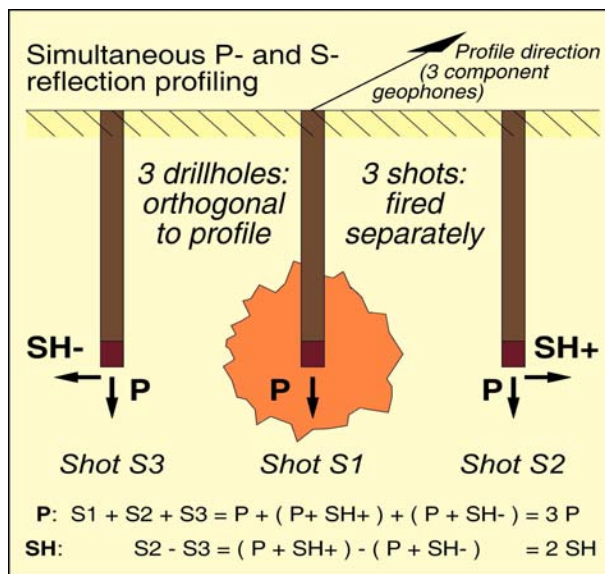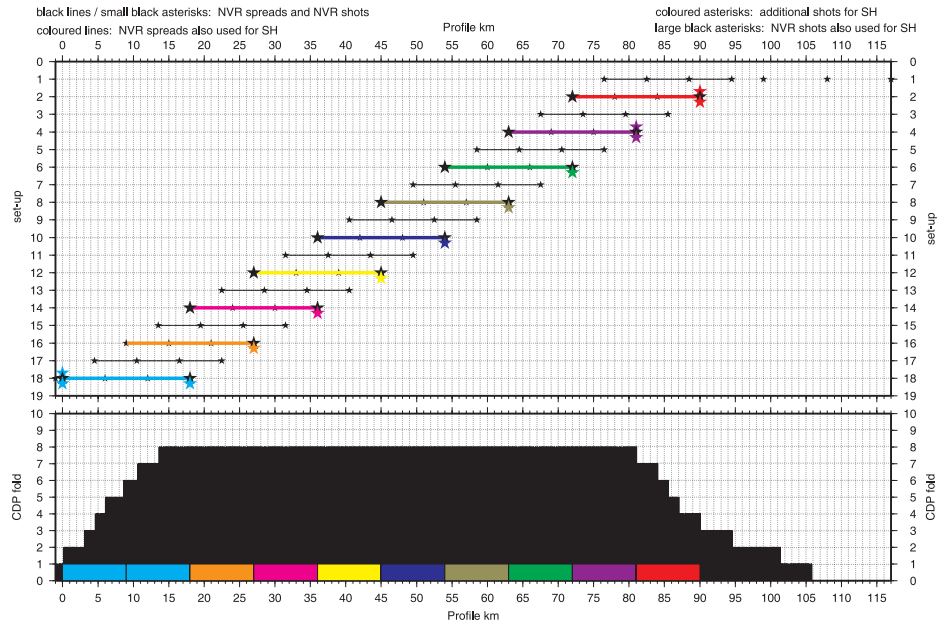
Figure 2.2.: The NVR (black) and SH (colored) shot and receiver configuration is plotted along profile kilometer for each spread set-up. The first active receiver spread starts at ≈ 95 km. The lower part of the figure shows the corresponding CDP fold (figure by M. Stiller, GFZ, pers. comm.).
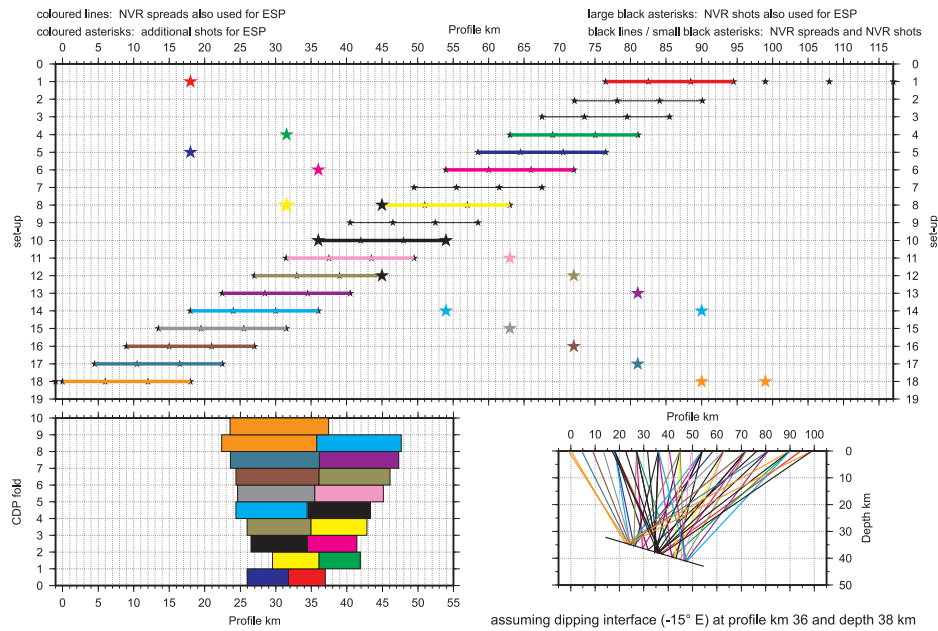
Figure 2.3.: ESP (colored) and NVR (black) shot and receiver configuration for each set-up day. Additional shots at certain offsets to the active spread focus on the plate interface at a depth of 38 km. The lower part of the figure shows the resulting CDP fold and ray-paths of the ESP shots (figure by M. Stiller, GFZ, pers. comm.).

unit (EDL) which was powered by rechargeable batteries. A GPS antenna provided the exact time, a 3-component geophone with a eigenfrequency of 4.5 Hz was used to convert the seismic waves into electric currents. Each geophone was buried $\approx$ 20 - 40 cm deep in a drilled hole and was oriented using a compass. A list containing all station coordinates is provided in the appendix in table A.2. The daily routine of the experiment started with the shooting early in the morning to limit the noise in the data produced by traffic. The 45 stations were moved next by the field teams. One group tended to the pegging of the receiver stations for the following spreads, whereas two other groups drilled the geophone holes on these marked positions after the redeployment of the seismic stations. Approximately 20 persons were needed in the field, including the manned headquarter. Figure 2.4 shows pictures of two seismic stations, and the used shooting equipment. All boreholes were drilled and loaded by a local contractor, the shooting was carried out by persons with the required qualifications in the TIPTEQ field crew. Table 2.1 summarizes all important acquisition and field parameters. Figure 2.5 shows a detailed map of the profile where all items described above can be found. The shots are color-coded for each experiment component and labeled after their shotpoint number. FFID (chronological field file ID) is ambiguous to identify unique shot locations, since some were used several times (cf. table A.1 to match FFID and shotpoint numbers). Figure 2.6 shows a shot gather recording of shotpoint 56. The data is almost raw data, just a bandpass filter and scaling operators were applied to visualize the subsurface reflections in all crustal layers.

Figure 2.4.: Receiver stations and shooting equipment. Panel a shows the buried and oriented 3-component geophone and the EDL recording unit in a weatherproof box. The picturesque last receiver station 955 at the Pacific Ocean is shown in b. Panel c shows two similar boxes to record the exact shot times, e.g., with pliers around the ignition lead, not yet connected to the trigger box (d). Image courtesy of C. Krawcyzk.

General information	
recording period	2005, Jan. 13-30
area	southern central Chile,
	$\sim 38.2°$ S, 73.5-72° W
profile length	105 km along CDP line
total data amount	3 components, 1.5 GB each
Recording	
recording system	portable field recorders,
	EarthDataLogger PR6-24
	(GPS-clock, 6-40 GB HDs)
sampling rate	5 ms
recording format	MiniSEED, continuous
extracted event time	102 s
Receivers	
number of channels	180
geophone type	3-component geophone,
	Sensor P-6/B, 4.5 Hz
geophones/station	1 (buried)
geophone spacing	100 m (projected on CDP line)
spread length	18.0 km
daily roll-along	4.5 km (east to west)
number of stations	955
Sources	
source type	explosive shots in boreholes
explosive charge/shot	
NVR, SH	75 kg (1 hole, 20 m deep)
east off the line	100/150/200 kg (1/2/2
	holes; 25/20/25 m deep)
ESP	150-300 kg (2 holes,
	20-30m deep)
shot spacing	
NVR/SH/ESP	1.5/9.0/9.0 km
number of shots	
NVR/SH/ESP	73/13/15
east off the line	3 (all during first set-up)
Subsurface coverage	
NVR/SH/ESP	8/1/10-fold (nominal)

Table 2.1.: Acquisition and field parameters of the controlled-source seismology experiment of the TIPTEQ project (Groß, Micksch, and TIPTEQ Research Group, 2008).
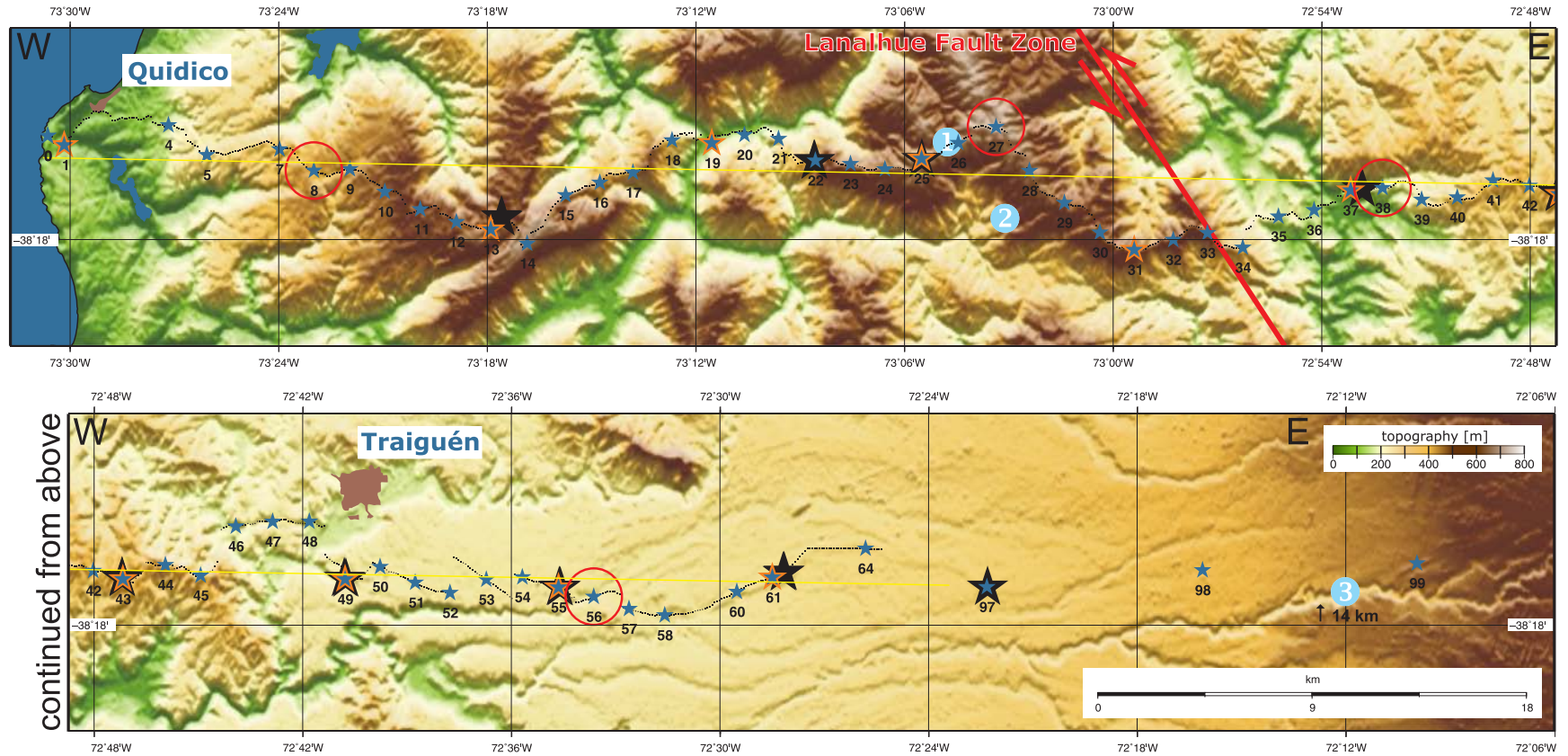
Figure 2.5.: Profile map of the controlled source seismic experiment geometry. Receiver positions are given as small black squares. The instruments were deployed from east to west with a spacing of 100 m with respect to the CDP-line, shown in yellow. Stars indicate shotpoint locations and are color coded: NVR = blue, SH = orange, ESP = black. Shotpoints of the data examples shown in figure 4.1 are marked with red circles. The sinistral Lanalhue fault zone (LFZ) is marked by a red line (Melnick and Echtler, 2007). The blue '1' marks the relocated hypocenter of the 1960 great Chilean earthquake (Mw = 9.5) by Krawczyk and the SPOC Team (2003) at 73° 04,8' W and 38° 15,8' S (-73.0800°/-38.26338013°). This is within 4 km horizontal distance to the independently obtained relocation by Engdahl and Villaseñor (2002) marked with a '2' (73° 03' W/38° 17,4' S or -73.05°/-38.29°). In 1989, the main shock of the earthquake was placed to 72° 12' W and 38° 09,6' S (-72.20°/-38.16°) by Cifuentes (1989), 14 km north of the CDP line at position '3'. The DGM shows data from the SRTM mission by NASA and other space agencies (Farr et al., 2007).
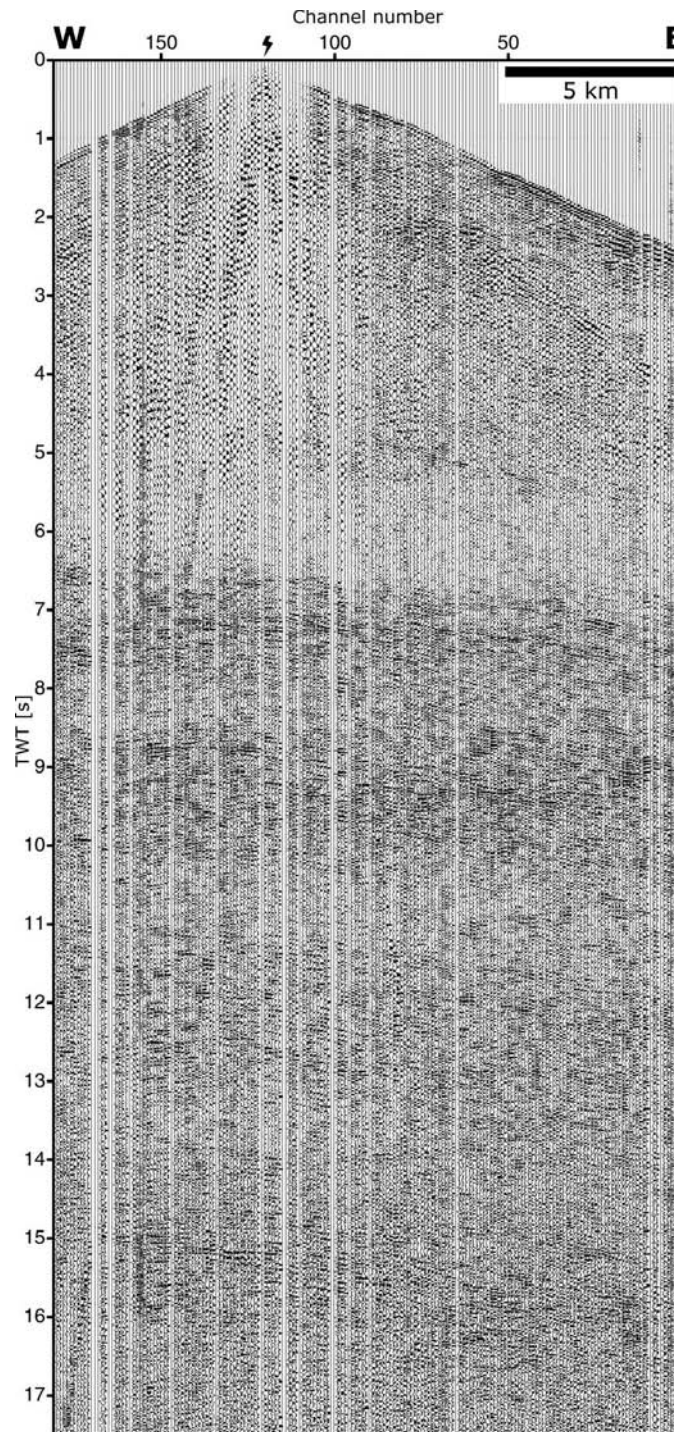
Figure 2.6.: NVR shot gather example of shot no. 56, marked by spark, for location see figure 2.5 (Groß, Micksch, and TIPTEQ Research Group, 2008). The section shows the vertical component of ground motion. It has only been bandpass-filtered and horizontally and vertically scaled, underlining the good data quality. The next chapter deals with the preprocessing of such shot gathers and gives details about the used bandpass filter or applied mutes to cleanse the data from unwanted noise.

3. Preprocessing

Raw field recordings (shot gathers) must be treated with several processing steps like data conversions, trace header assignment or bandpass filtering to prepare the data for the normal moveout (NMO) correction, the stacking and finally the depth migration.

The following sections and chapter 4 deal in some parts with more technical aspects having arisen during the processing and peculiarities involved with ProMAX. The *italic* job names correspond to the processing jobs in the NVR-line in the TIPTEQ area in ProMAX, names in quotation marks refer to ProMAX modules or programs/shell-scrips. ProMAX version 2003.12.1 is used for the processing of the data.

3.1. miniSEED to SEG-Y

The EDL units record in miniSEED (IRIS, 2008) data format and the recordings must be converted into SEG-Y (SEG, 2008) for further processing in ProMAX. The raw field data can be found in the project folder `/tipteq/rohdaten` and are sorted after recording-day/ instrument-ID_HD-ID.

The first or last recorded files may get corrupted when using non-continuous recordings. Unfortunately, if one 30 min recording file is damaged somehow, the whole trace is not converted in the following conversion steps. Scripts and visual inspections help to check and clear the data from faults. Lists of the receivers and sources for each deployment/day help to create shot gathers from the single traces. The scripts and a quick walkthrough (HOW2SEGY.TXT, see B.1) can be found in `/tipteq/SEGY`. A time window of 102 seconds was cut out of the daily ≈ 6 hour recordings, starting with a lead time of 2 s before the shots. The created shot gathers are merged to three 'day-files' for each component to be imported into ProMAX.

3.2. Trace header assignment and file preparation

Each day-file for all three components was loaded into ProMAX into a separate job and header values were remapped to other positions in the data header, e.g. source/receiver coordinates or elevations. Additional trace header values were assigned with 'trace header math' e.g.

flags for NVR/ESP/SH, ProMAX specific header values like 'shot_pt' or a CDP number was calculated from other header values (e.g. *u_ day_ 15c1*). The day files were rewritten to disk and combined to one file for each component containing all 104 shots (e.g. *u_ merge_ c2*).

The data headers contain a sort of preliminary geometry from that step on to be used for editing jobs or picking mutes. The real field geometry was loaded into ProMAX in a later step to create the geometry database which e.g. allows plots of all header values for visual plausibility checks. One might try to set up the ProMAX geometry database as earliest as possible to avoid problems e.g. with already picked mutes which use the receiver coordinates as secondary key. Differences in the two geometries change the coordinates very little but may result in an inoperative or partially inactive mutes.

3.3. GPS timing errors

Problems with some of the GPS cards inside the EDLs lead to timing errors of the respective traces. This time shift was a random value but constant for one recording period/day. These traces ($\approx 2\%$ of all 18720) were searched by hand in each shot and shifted about a mean value according to the neighboring traces. The error was often greater than the potential variations of the first breaks due to topography along the line, thus easy to detect. Traces which are not obviously disturbed, but belong to EDL numbers which showed timing problems before, were also checked and smaller shifts could be fixed as well. The affected traces needed to be shifted between -2.515 and +1.805 s. Figure 3.1 shows an example of FFID 81 (Shotpoint 14), pegnumber 706. The associated ProMAX job is called *u_ fbtimes_ correction*.
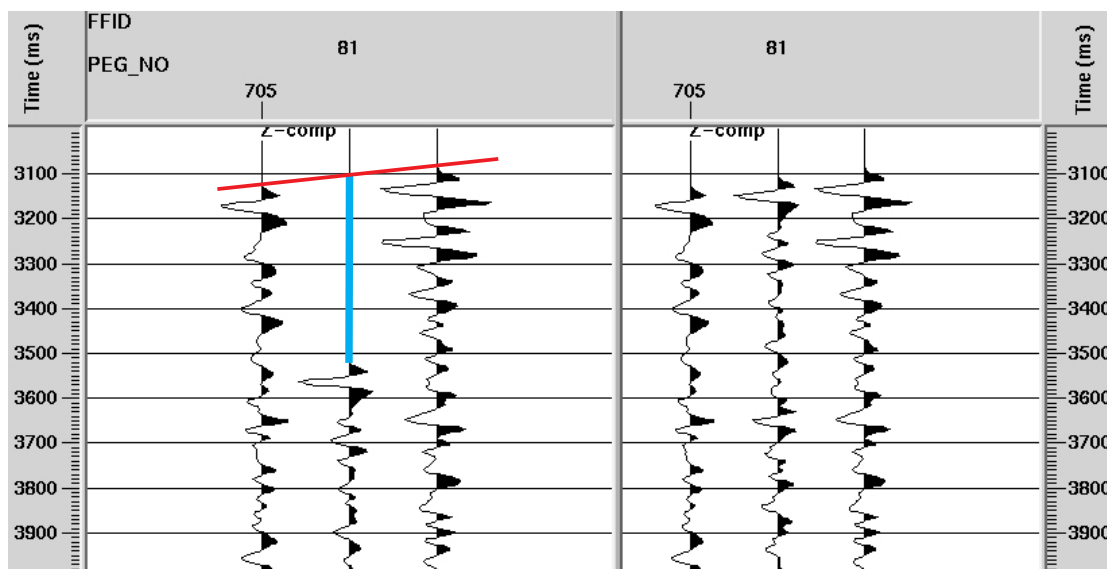
Figure 3.1.: The mean first-break time calculated from neighboring traces gives the new first-break time (red line). The blue line marks the time the trace needs to be shifted.

3.4. Trace muting: airblast

The blasting agent was detonated in boreholes of about 20 - 30 meters depth for the TIPTEQ shots. Boreholes are generally tightly sealed with bentonite to minimize the dissipation of the released energy to the air. A blowout is observed if this seal breaks and bentonite and soil is thrown into the air (see figure 3.2). A sort of trailing banner of sonic noise is created beside the bang of the explosion from the ejection of the explosion gases and soil, thus lengthening the airblast signal. Tightly sealed boreholes also produce airblast signals from the conversion of seismic waves to sonic waves at the earth's surface, but much sharper in appearance in the seismic data.

Figure 3.2.: Image of a blowout at shotpoint 49. Image courtesy of L. Rabenstein.

The sonic waves travelled along the active spread (18 km offset for NVR shots) and were recorded on all geophones, even though they are buried up to 40 cm deep. The airwave signal is sharp in appearance and not dispersive (for audible sounds air is a non-dispersive medium), it is only altered by topography producing reverberations, or lengthened by blowout exhausts. ESP shot 33 (FFID) at shotpoint 25 (cf. map in figure 2.5), with a charge of 150 kg, produced an airwave which was recorded over an offset of 33.5 km (see figure B.1a). There, the cutout trace length of 100 s after the shot time limits the further observation of the airblast signal of FFID 33 as well as for all other shots. Longer cutout windows allow an observation up to ≈ 36 km (see figure B.1b). Thybo et al. (2006) observed an airblast of a marine shot close to the coast (charge of 300 kg) up to 100 km inland on equally deep buried geophones. The authors believe that this wave was propagated so far as a reflected wave from an atmospheric reflector and note that only few observations are available of such far-travelled airwaves.

Scientific curiosity lets one estimate the air temperature at the shotpoint of FFID 33 at the time of the explosion early in the morning ($\approx$ 6 o'clock local time). The knowledge of the maximal offset (33.5 km) and time of 100 s lets one calculate the sonic speed c_{air}. From that, the air temperature at the shot time is calculated using a practical formula for the speed of sound for dry air (Wikipedia, 2008b): $c_{air} = 331.3 + (0.606 \cdot \vartheta)\ m \cdot s^{-1}$. The air temperature, ϑ, results to $\approx 6.1°$ C.

The *u_pick_airblast* job in ProMAX removes the airblast with the help of a surgical mute. A LMO correction was applied to the data with an average sonic velocity of 333 m/s to flatten the airblast for a convenient picking. This also needs a bulk shift of the data in time, depending on the greatest offset, to lengthen the traces. The time window of the airblast signal is shifted out of the traces by the LMO otherwise without this extra time. Figure 3.3 shows examples of different airblast mutes. The picked mute times must be recalculated to unreduced times. This calculation is offset dependent and must be carried out outside ProMAX using e.g. shell-scripts and AWK. The result is re-read into ProMAX, and can then be used to cancel out the airblast noise. Some obstacles within ProMAX can make this procedure tricky and cumbersome. A walkthrough on how to pick an airblast can be found in /tipteq/metadata/misc (How2pick-an-airblast.txt, see B.3).
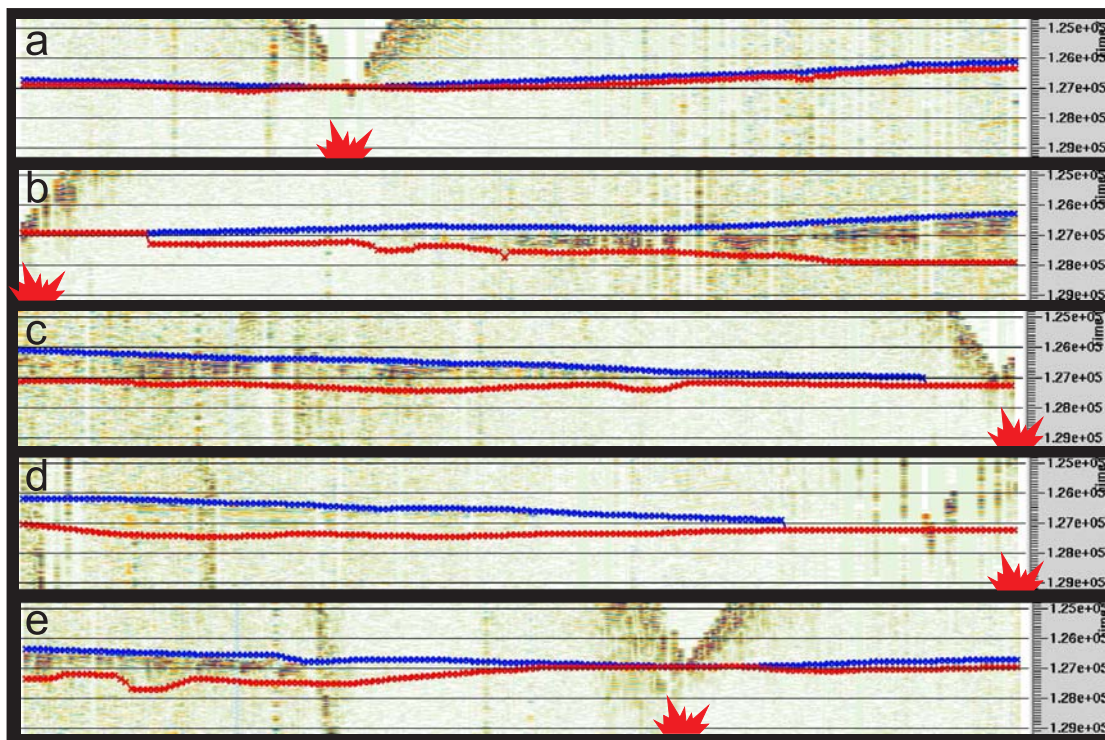
Figure 3.3.: Representative airblast mutes for five TIPTEQ shots. Almost no airblast disturbance (a), a gradually widening mute to greater offsets (b/c) or the widening starts at a certain offset (d/e). Shotpoints are marked with red symbols along the whole active spread of 18 km, the length of the time window is $\approx$ 4 s.

3.5. Trace muting: cars and trucks

The receiver line was chosen along small local and backcountry roads and some part led through properties of a local forestry company, especially in the western part of the profile. The shot times were early in the morning, but traffic was still recorded along the 18 km long active spread.

The amplitude of the generated noise by a car passing by a receiver station rises and declines again. Here, the critical part is to cut out the car noise when its amplitude exceeds the normal noise or signal level. The data was displayed in variable density color mode with no filtering or AGC. Several amplitude scaling settings and colormaps were tested with control samples along the profile to find a setting which satisfies all shots to quickly find the noise generated by cars. The chosen trace scaling factor was 0.001, used together with the 'rev_sw_strat.rgb' colormap. Surgical mutes were used to remove the disturbing sections from the traces (ProMAX job *u_pick_carnoise*). Further mutes were created when two or more cars were found on one trace (see figure 3.4). Two cars following each other and cars turning around on the road can be identified and the size and velocity of the cars might be distinguishable and calculated from the observed noise pattern. A taper can be added to the mute when it is applied later in the migration flow (see section 4.1), if the picks were not accurate enough due to the colormap or scaling. The most disturbed data was found in the western half of the profile (shots with FFID 64 - 88), where roads are frequently used by forestry companies and around the tiny commercial centers and housing areas like Relun situated at shotpoint number 19 (FFID 65).
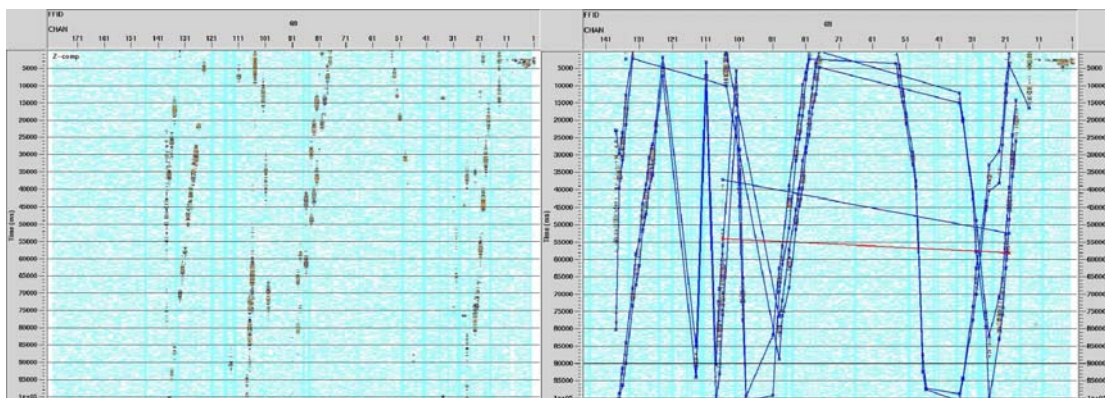
Figure 3.4.: The left side of this figure shows the unfiltered data of FFID 69, the colored streaks are the noise patterns produced by cars. Up to 4 surgical mutes are needed to cut out all disturbances (right).

3.6. Ground roll

Ground roll is coherent noise generated by low-velocity, low-frequency, high-amplitude Rayleigh waves and can obscure signal and degrade overall data quality (Schlumberger, 2008). F-k filtering and a surgical mute were tested to reduce the interferences of the ground roll, but none of them brought any improvements. Bandpass filtering (cf. section 3.8) reduced the low frequency ground roll significantly.

3.7. Top mute

Top mutes are used to eliminate high amplitudes at the beginning of the seismic signal, e.g. the first arrivals and related source-generated noise, e.g. guided waves (Roth et al., 1998; Robertsson et al., 1996). The first-breaks usually have the highest amplitudes along a seismic wave train and would, if not removed, decrease the following useful signal amplitudes if a trace scaling is applied along the whole trace in later processing steps. Top mutes can be applied automatically, but hand picking can be more effective. The mutes for all shots of the TIPTEQ experiment were picked with *u_ pick_ top_ mute*.

3.8. Bandpass filter

The 'interactive spectral analysis' tool in ProMAX was used to examine the frequencies contained in the data at different times and offsets to construct a bandpass filter. The aim was to suppress low frequency ground roll and high frequency noise (cf. figures 3.5, 3.6 and 3.7). Most energy seems to be contained in frequencies between 20 - 35 Hz in all shots. An Ormsby bandpass filter with corner frequencies of 6 - 10 - 35 - 50 Hz was finally chosen (see figure 3.8).
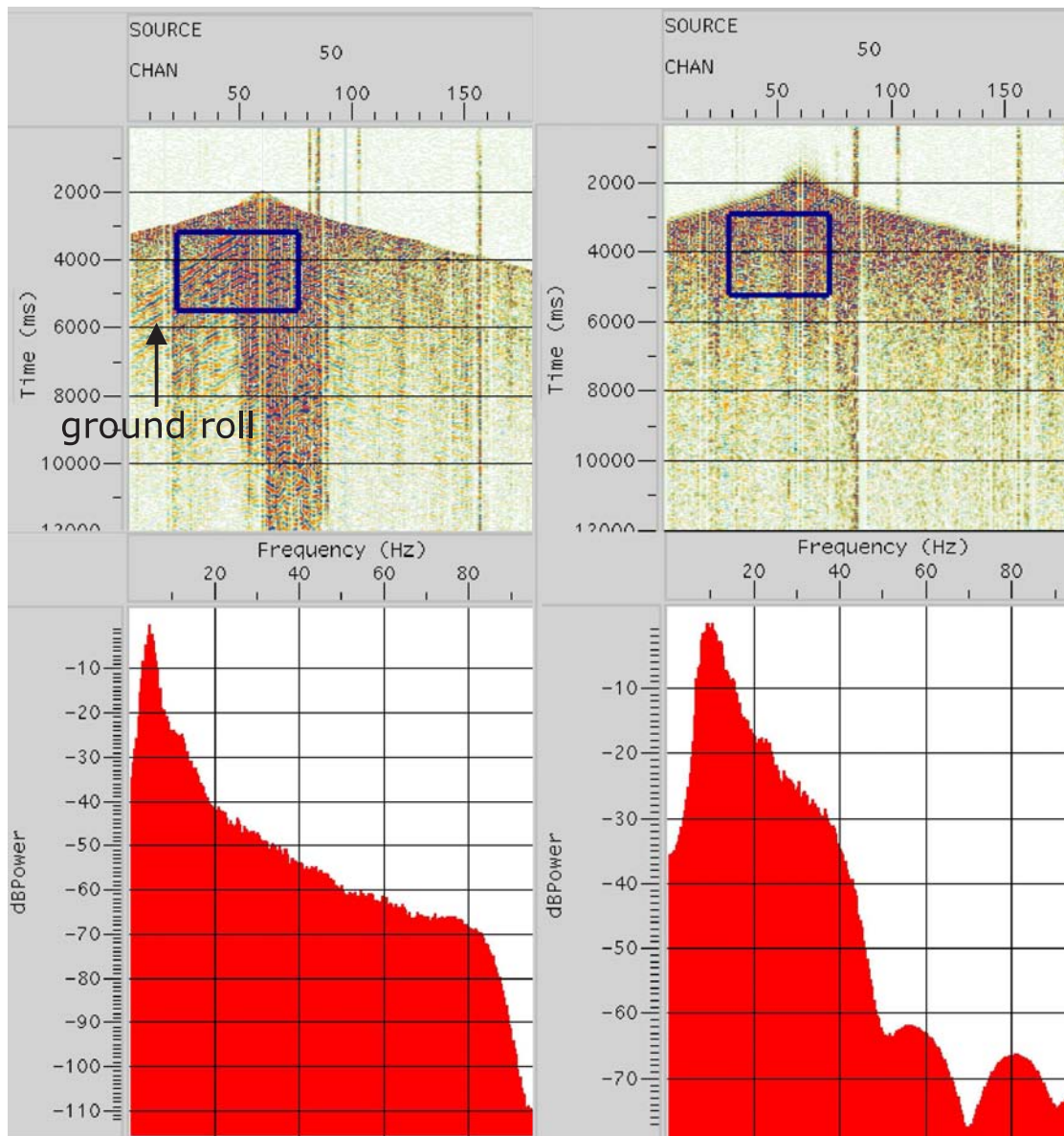
Figure 3.5.: Unfiltered (left) and filtered data (right) of FFID 50. The respective frequency spectra calculated in the blue boxes are shown in the lower part of the figure. The black arrow points to the typical parallel, low frequency ground roll signature. An example filter rejecting low frequencies ($<= 10$ Hz) reduces the ground roll significantly.
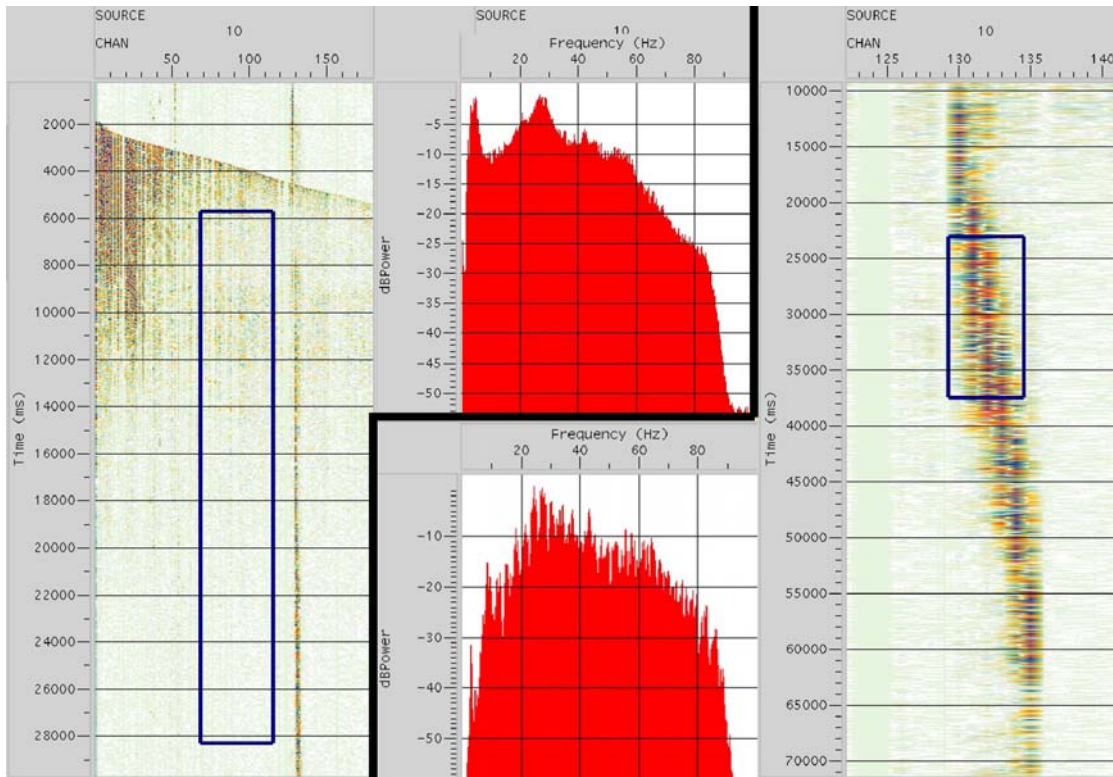
Figure 3.6.: Two frequency spectra examples from FFID 10, blue boxes in the shot data show the areas where the frequencies are calculated from. The left part shows a spectrum of most likely useful subsurface information. Frequencies below 10 Hz are attributed to ground roll. The spectrum from the car noise on the right shows no distinctive peak or plateau and looks more or less similar to the spectrum of the useful data, above. So, a surgical mute is the preferred method to get rid of the car noise instead of frequency filtering.
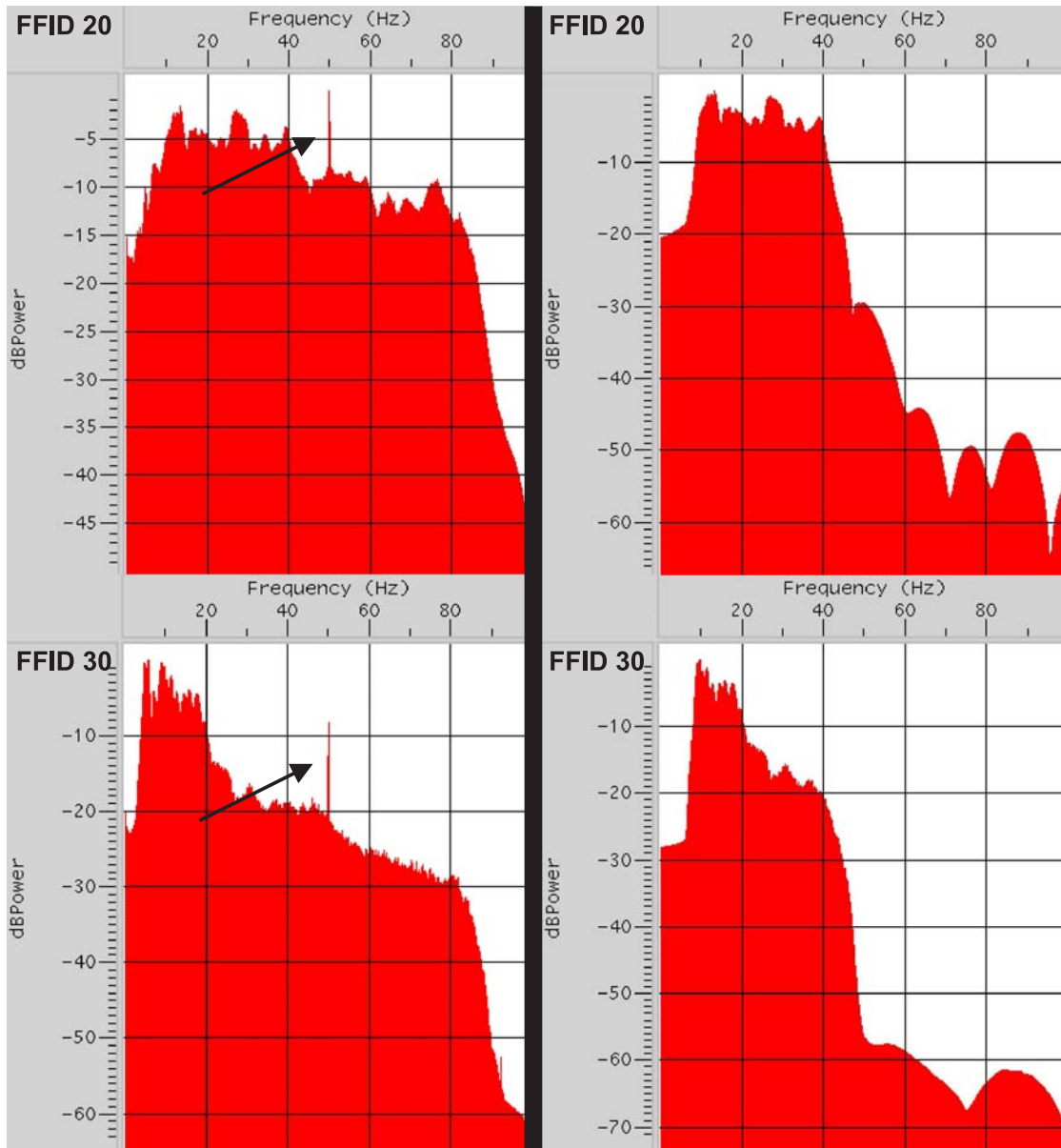
Figure 3.7.: Examples of unfiltered (left)and filtered frequency spectra. Several shots exhibit a distinct maximum at 50 Hz which is the typical alternating frequency for electrical AC currents (arrows in figure) inducing this frequency in the cables of the geophone. The right part of the figure shows the effect of the finally chosen Ormsby bandpass filter with corner frequencies of 6 - 10 - 35 - 50 Hz.
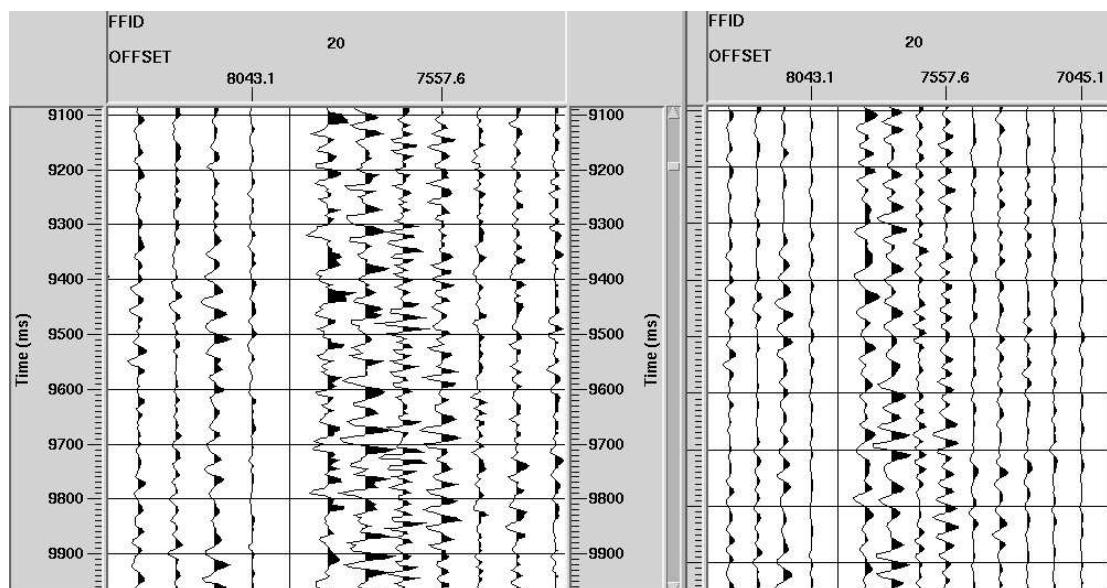
Figure 3.8.: Data example of unfiltered (left) and filtered data (right) of FFID 20, where we can observe a lack of high frequencies in the traces.

3.9. ProMAX geometry setup and database

3.9.1. Geometry assignment

The geometry for the TIPTEQ profile is set up with the 'crooked line geom spreadsheet' macro in the flow *u_geometry*. The global configuration of the survey is asked first, like the types of shots, the receiver interval or the measurement units (meter or feet). The following buttons (receivers, sources, pattern) open spreadsheets where the coordinates, the FFIDs or shothole depths have to be listed or read from ASCII files. The 'Bin' button opens the crooked line binning window, where 4 subitems have to be executed consecutively by ticking them off and clicking on 'ok' afterwards. First, all midpoints of the sources and receivers are calculated from the data entered in the steps before. The binning grid is defined in the next step via a graphical interface, where the midpoints and the limit of the survey must be plotted first. A track (CDP-line) can be defined next by hand via picks on the screen or can also be read in from an external calculation. The used TIPTEQ 'CDP line' was calculated beforehand from the receiver coordinates with a least square regression calculation (Wikipedia, 2008a). Finally the 'Bin' pull-down menu is unlocked and the bins can be parameterized and plotted. Save all items separately and exit to the former menu. The third subitem allows the binning of the midpoints, the database can then be finalized in the last step. Exit this window counterintuitively via cancel to get back to the main 'crooked line geom spreadsheet' macro. The ProMAX help manuals (e.g. 'geometry_assignment.pdf', (ProMAX, 2003)) are in great detail on setting up different kinds of survey geometries.

3.9.2. The ProMAX database

The database is populated with a lot of values like absolute offsets or the nearest geophone to a shot, which derive from the geometry calculations. The values are stored in corresponding ordered parameter files like TRC (trace), SRF (surface) or CDP. These values can be manipulated (database math, spreadsheets, or by moving points with the mouse) and plotted (2–D, 3–D) in many ways. An extensive documentation can be found in the 'DBTools.pdf' help file. It is necessary to check the database for plausibility and errors. This can be done relatively fast with the 'older' 'XDB database display' tool. Here one can plot e.g. CDP versus fold (see figure 3.9) or just check if the FFID plot shows an ascending line, as expected. The normal 'DBTools' are preferred for 3–D plots and selecting parameters in 3–D.
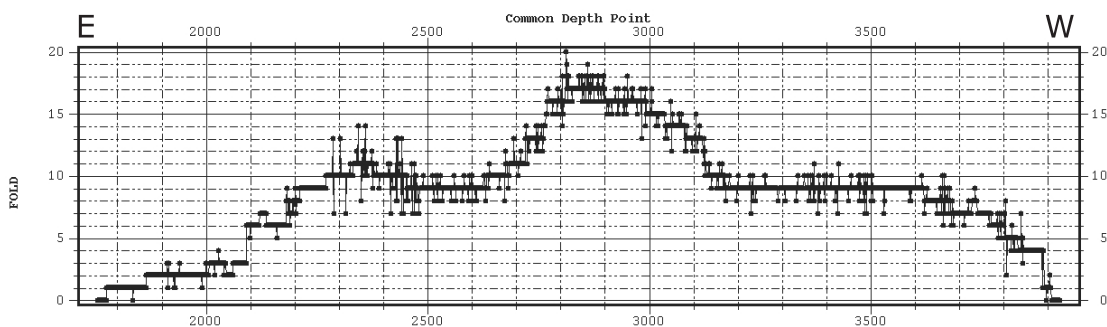
Figure 3.9.: 'XDB database display' plot of CDP versus fold of all 104 shots. The ESP shot configuration raises the fold in the central part of the profile from the nominal eightfold NVR configuration.

3.9.3. Matching the geometry to the data files

The next step is to match the newly created geometry to the data files, which is also done in the *u_ geometry* flow with the module 'Inline Geom Header Load' (read flow comments). The data files are written to disk afterwards with the new geometry, so it is not necessary to load the stored geometry in each following flow. Some old important header values like receiver coordinates or FFID number, which are overwritten in this process, can be optionally stored in new ones with 'trace header math' for revision. 'Geometry written to the trace headers match the database' should now be present in all job protocols.

3.9.4. Errors in the database

Two errors were noticed in the TIPTEQ database. The relation between CDP and 'NEAR_SRF' (nearest peg/receiver to CDP) showed wrong values at the eastern end of the profile. The three shots off the line would produce CDPs with the same nearest receiver value (1001) up to the second receiver, but for the first tenths of CDPs, a value of 1064 was assigned. This error could be corrected manually by setting the correct values.

The second error occurs for three shots, all fired at one shotpoint location (SP 1, FFID 99) close to the coast at the same day. The corresponding trace offsets show the wrong algebraic sign (see figure 3.10). Other database values which make use of the offset parameter showed the same conspicuousness.
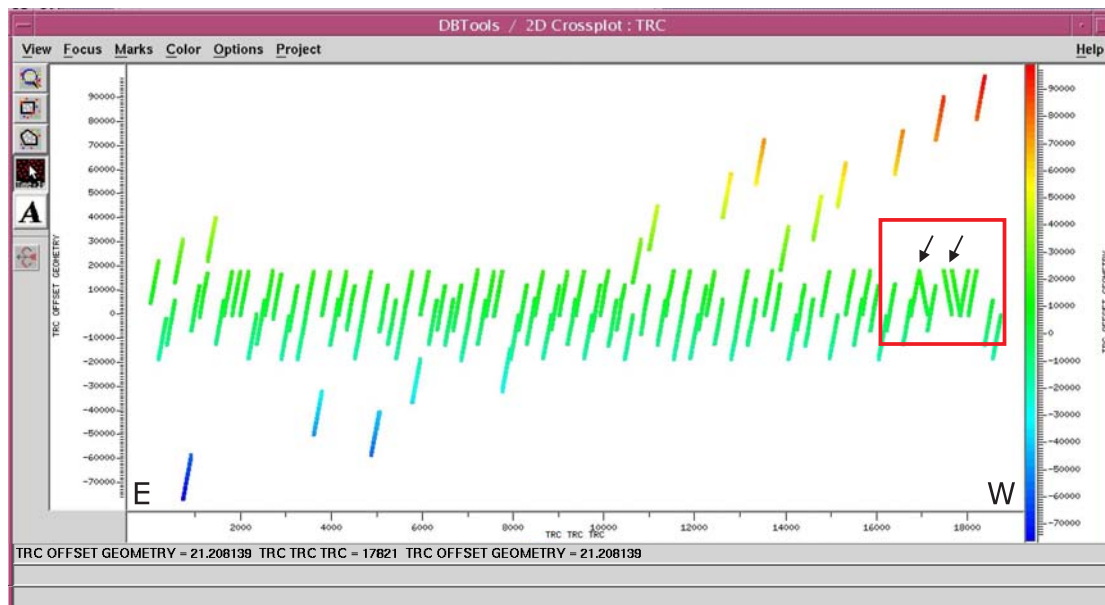
Figure 3.10.: DBTools 2–D Crossplot of all traces versus trace offset. The red box and the arrows point to the 3 shots with the wrong algebraic sign. The NVR and SH shots can be seen in green colors, other colors show ESP shots.

Several approaches were tried to correct the offset values. The offsets were changed during the header assignment in the first steps of the preprocessing (see section 3.2) or it was tried to manipulate the values in the database later on. This changed the offset, but not the appearance of other linked parameters, and no satisfying solution could be found. It is not finally clear if the error really comes from a wrong offset calculated by ProMAX or from another database fault and how it affects the stacking or migration process.

The stacked and migrated images of the NVR data set presented in this thesis use only one shot of the three shots in question (FFID 99). The other two shots belong the the SH component of the experiment. Two test stacks one with and one without FFID 99 are shown in figure 3.11. We see that FFID 99 shows the correct alignment as expected for this shot with the correct offset values. The shotpoint is located at the western end of the receiver spread, the onset of the first signals must therefore increase towards the east. The curved onset of the shot data comes from the first-break top mute, and shows that the mute is also applied correctly. So, this shot was not excluded from the further processing steps, since it is correctly aligned in the data. Shot spacing is also sparse in the area around shotpoint 1 because of the pueblo of Quidico and two misfires at shotpoint 9 and 12.

No other flaws could be found in the database, so the shot gathers were ready for the processing described in the following chapter.
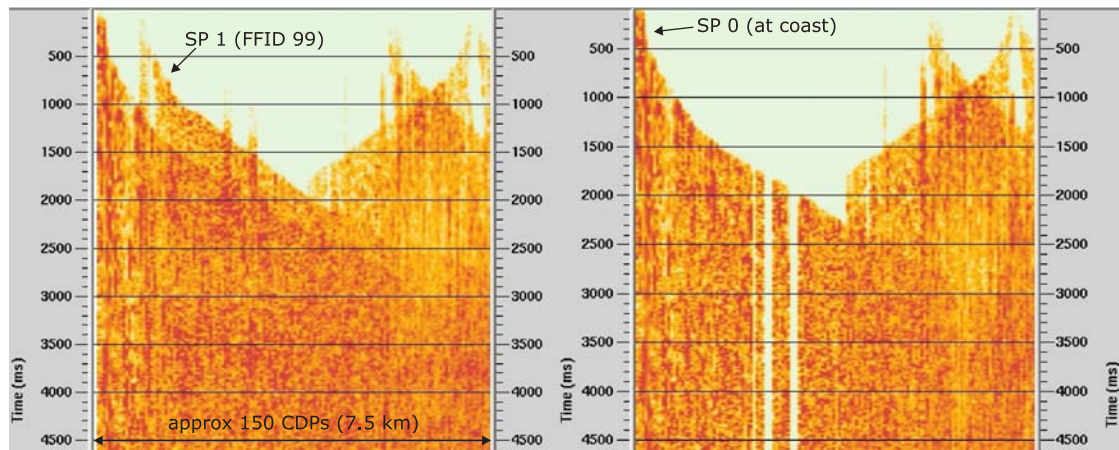
Figure 3.11.: Two test stacks one with (left) and one without FFID 99 (right) demonstrate the correct alignment of the shot with the suspicious offset values in the ProMAX database.

4. Processing sequence

The processing sequence applies edits and mutes from the preprocessing to the data. The data is also filtered and energy losses are tried to be recovered. The main step is to stack and then migrate the data into depth. See the whole processing sequence in table C.1 in the appendix (C) and ProMAX job *u_stack_migration* in the NVR-line in the TIPTEQ area in ProMAX.

4.1. Processing steps I

Disk data input The z-component of all NVR shots with the applied geometry was loaded. Only the NVR shots were loaded to achieve an equal fold along the profile.

Trace length The trace length was then shortened from 102 to 60 s.

Trace DC removal The DC bias or offset of the input traces was calculated by the mean of the samples and is removed.

Trace Kill/Reverse Traces with obviously no useful data due to a broken soldering joint or disconnected geophone cable were searched visually and marked in a parameter file to be neglected during the processing.

Airblast signal The recalculated mute times of the airblast picks were stored in a parameter file and then loaded from the database. A 30 ms ramp was added before and after the mute times (see section 3.4).

Car noise Four surgical mutes were applied subsequently. It showed that a long, gently increasing mute ramp of 15 s was needed to minimize the disturbances produced by passing cars and trucks. The mute picks were set only around the highest amplitudes in the central part of the car noise with the parameters chosen during the preprocessing (see section 3.5).

Hand statics Static corrections for individual traces were used to account for the time shift error produced by malfunctioning GPS cards.

Header statics Two seconds were removed then from the traces at the beginning. This additional time before the shot time was helpful during the picking of the mutes and correcting the GPS time error.

Top mute The picked top mute was applied to the data.

Bandpass filter An Ormsby bandpass filter with the corner frequencies of 6 - 10 - 35 - 50 Hz was used.

True Amplitude Recovery The sound wave generated by the shots loses energy due to inelastic damping, transmission and spherical divergence as it propagates. This spherical divergence causes a decrease in the energy density, because the energy of the wave must be distributed over an ever-increasing surface with radius r. This happens in a dependence of $1/r^2$. The amplitude of the wave decreases in a ratio of $1/r$.

To cope with the loss, each trace is multiplied with a time variant amplitude scaling function $(1/(t \cdot v)^2)$, meaning every sample of the trace is scaled depending of the radius r of the spherical wave at this time. Two offset dependent velocity-depth functions were used, changing them at an absolute offset value of 1500 m.

Ensemble Balance This module computes and applies a single scalar for each input ensemble of traces (for each shot): New amplitude value = Old amplitude value / Scalar. In this way, variations in amplitude between ensembles are reduced (ProMAX, 2003). The time gate where this scalar is calculated from was picked by hand for all 104 shots.

Automated Gain Control (AGC) A further way of enhancing seismic data is the use of an automatic gain control, which scales the seismic traces depending on the e.g. RMS amplitude of all non-zero samples in a given time window, that slides along the trace sample per sample. The amplitude in the center of the window is then multiplied by a scalar, depending on the RMS amplitude. The visual result depends strongly on the window length: Long windows retain the character of the input data, whereas too short windows boost weaker signals, but also the noise, levelling the amplitudes. By applying an AGC to all the traces of a shot gather, the signal amplitude for increasing offsets is amplified, making up for the loss of energy of the seismic wave. A sliding window length of 4 seconds was used.

Trace Equalization This processes works like the ensemble balance module, but just for one single trace. Within the same picked time window a scalar is calculated and applied to the whole trace, reducing amplitude variations between traces. This equalization is applied several times to the data in the processing sequence (see table table C.1).

Infill Data Infill Data uses a limited aperture Tau-P forward and inverse transform to fill in missing data. This applies to killed or missing traces of one shot and/or for surgical mutes. Several aperture sizes and dips were tried to infill missing traces and cut-out data, but no really satisfying parameters were found. The missing parts in the data is interpolated from neighboring traces, so there is always the trade off to generate 'new' data which might not produce constructive interferences during stacking.

F-X Decon This deconvolution process is used to suppress random noise. The data is transformed from time and distance to frequency and distance, with a Fourier transform

applied to each trace - a time slice is converted to a frequency slice. Events with similar dips appear as a sinusoidally complex signal along a given frequency slice. That is, they can be described in the form: $\cos \omega t + i \sin \omega t$. Therefore, this signal is predictable. In the F-X deconvolution process, a complex prediction filter is used to predict the signal one trace ahead, across the frequency slice. Any difference between the predicted waveform and the actual one can be classified as noise, and is removed (ProMAX, 2003). The inverse step transforms each resulting frequency trace back to the time domain.

Blend Blend copies the input data for the following processing tool and blends it with the processed output of that tool with a given ratio, e.g. 3:5 (data processed by next tool:input data to that tool).

Dip Scan Stack Dip Scan Stack uses a limited aperture Tau-P transform to enhance the coherent seismic events. The process transforms the input x-t traces to a selected range of dip, or slant, stacked traces. Sample by sample, each dip trace is weighted by the semblance along that dip. These dip traces are then inverse Tau-P transformed back to x-t space. The stronger, coherent events, independent of dip, have greater weights and contribute proportionally more to the inverse transform (ProMAX, 2003). This module was used together with the blend module (see item above) to avoid an overbalanced coherency enhancement.

4.2. Example of shot gathers

Figure 4.1 shows four shot gathers of single shots between the coast and the Central Valley (SP 8, 27, 38, 56). All shot gathers give the vertical component of the 3-component recordings. The data are bandpass filtered and a horizontal and vertical scaling is applied. Missing traces are interpolated and then filled, using the wavefield of the surrounding traces for this display job. A NMO correction is applied at last (see section 4.4).

The seismic data show distinct reflections and broad reflectivity bands, e.g. between 3 - 4 s and 6 - 7 s TWT at shotpoint 8 near the coast. These bands can be correlated with those observed at shotpoints more inland and dip towards the cordillera. The overall data quality can be rated as good. A first glimpse of the downgoing oceanic plate may be visible in each section, e.g. at ≈ 8 s TWT at the coast and at 17 s TWT under the Central Valley.

Such processed shot gathers are the input for the stacking process explained in section 4.5.
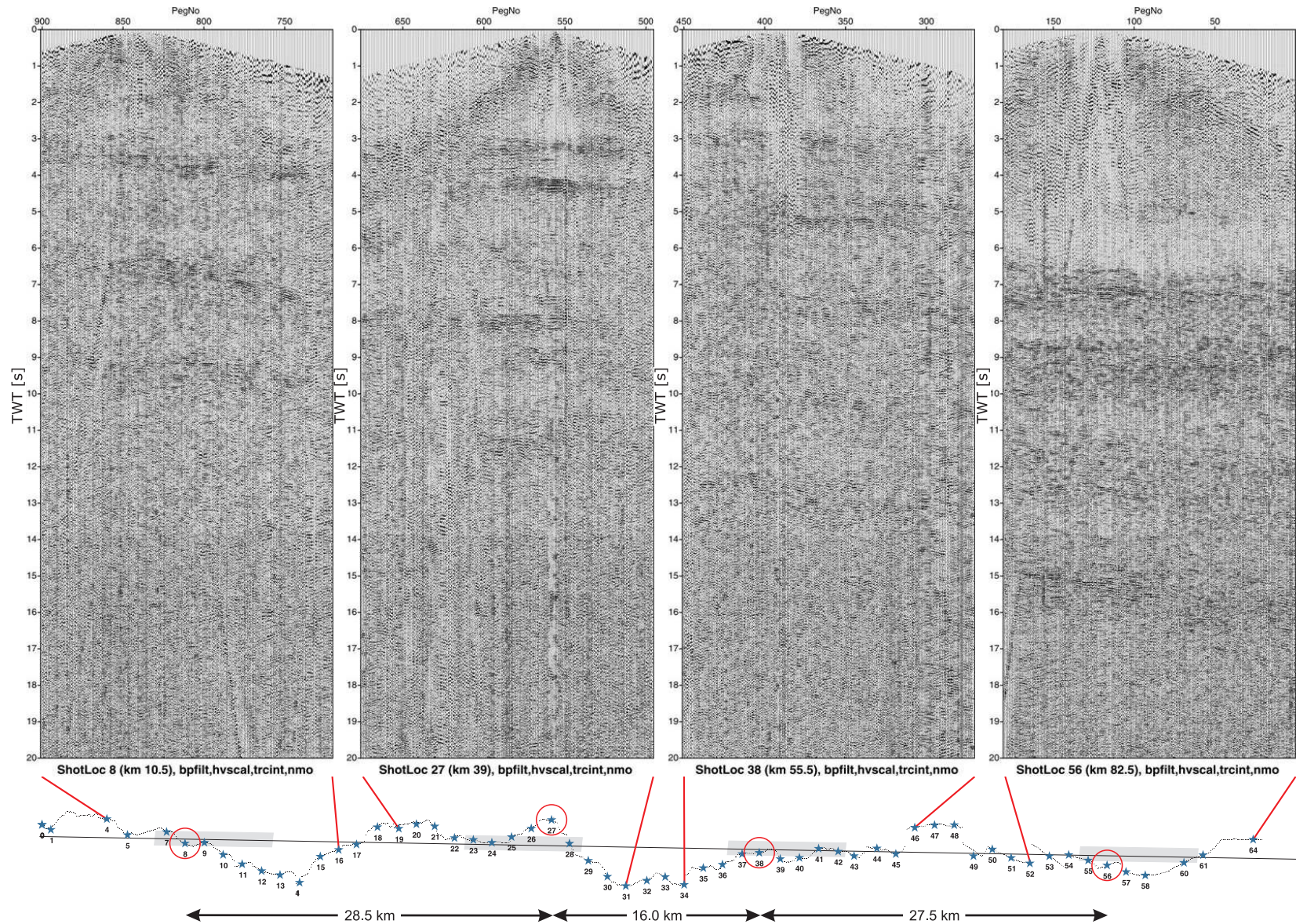
Figure 4.1.: Example of 4 partly processed shot gathers. The lower part of the figure shows the position and corresponding covered subsurface along the profile (black dots = receivers, numbered stars = shotpoints, circles = example shots shown above, grey rectangle = subsurface coverage). Confer profile map on page 14 (figure 2.5) for shotpoint locations (red circles).

Figure 4.3.: Time vs. offset sketch, see text for details.

This equation is a 2–D approximation of that for 3–D wave propagation through an elastic medium, valid for a horizontally layered half space. x is the distance from source to receiver, z the depth of the reflector. $\tilde{v}$ is the RMS velocity and a measure for the bending of the hyperbola and is given by (Forkmann, 1987):

$$\tilde{v} = \sqrt{\frac{\sum_k d_k v_k}{\sum_k \frac{d_k}{v_k}}} = \sqrt{\frac{\sum_k v_k{}^2 t_k}{t_0}} \tag{4.2}$$

d_k is the thickness and v_k is the velocity of the k-th layer.

The correction term, $\Delta t_{NMO} = t_R - t_0$, depends on the depth of the reflected layer and the RMS velocity of the layers above ($\tilde{v}$). The deeper the reflectors are situated, the flatter the hyperbola.

For a horizontal layered medium, the correction term can be written as (Forkmann, 1987)

$$\Delta t_{NMO} = \sqrt{t_0{}^2 + \left(\frac{x}{\tilde{v}}\right)^2} - t_0. \tag{4.3}$$

If this correction is applied to all shots, using the velocities from the SPOC velocity model, all horizontal reflectors should show up as horizontal lines in the CDP gathers, but diffracted waves and multiple events are still bent. Dipping reflectors which produce asymmetric hyperbolas appear also still bend and can be be treated with a dip moveout (DMO) correction.

4.5. Stacking

After the NMO correction, all seismic traces that share a CDP bin can be summed up, whereby signals in phase are amplified, and incoherent noise is damped statistically, increasing the signal to noise ratio. Diffractions and refractions are also reduced. A n-fold stack results in a $\sqrt{n}$-times improvement of the initial data (Schmöller, 1987). In the TIPTEQ case, a CDP fold of 8 results in a ≈ 3 times improvement in data quality (see figure 4.4). This method equals a simulated zero-offset experiment for all corresponding receivers. If strong lateral velocity gradients are present, the hyperbolic assumption may not be appropriate for some reflectors (Yilmaz, 2001).

Summing up over the binned traces is also a kind of data reduction without great losses, but with data improvement. For example, the file size of the TIPTEQ SEG-Y day files to be read into ProMAX of one component sum up to 1.28 Gb. The compiled ProMAX day file with the assigned geometry amounts up to 880 Mb. The stacked data occupies just 50 Mb.

The SPOC wide-angle velocities were converted from a 'interval velocity in depth' table to a RMS velocity table ('stacking velocity') with the module 'velocity manipulation' in the job *u_vel_editor*.
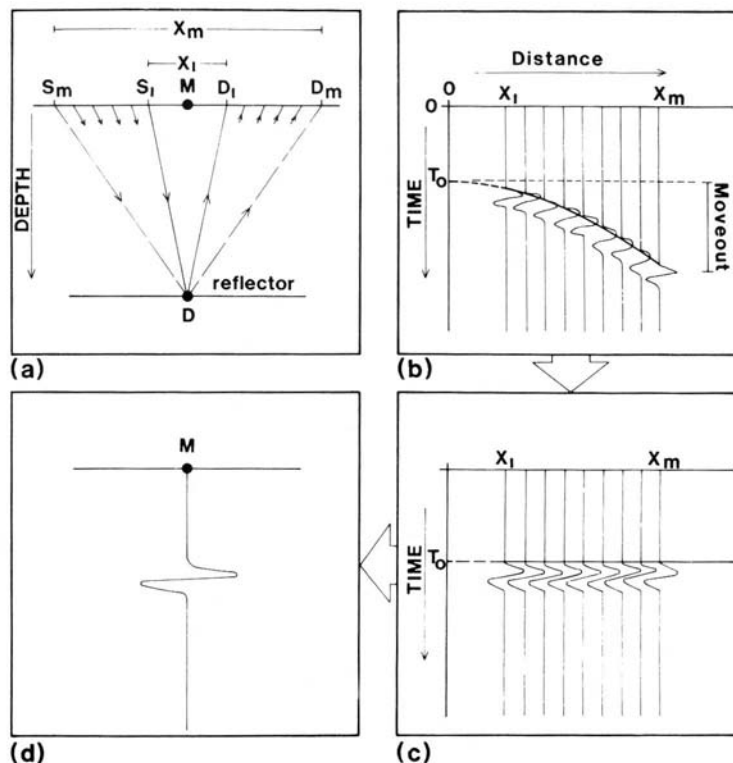
Figure 4.4.: The process and result of CDP sorting (a), NMO correction (b/c) and stacking (d) (Beaumont and Foster, 1989).

4.6. Kirchhoff depth migration

Here, only a short overview of the Kirchhoff (depth) migration is given, for a detailed background the reader is referred to Bancroft (2007) and references therein, Yilmaz (2001), chapter 4 and 5, Schneider (1978), or other relevant literature.

The possible candidates for reflector locations which are imaged by a pair of source and receiver lie all on a ellipsoidal surface, considering a constant velocity earth (see figure 4.5). The travel-time observed for a single event on the seismic trace is the same for all reflective points on that ellipsoid. In a zero-offset experiment the ellipsoid changes to a sphere (2–D case: ellipsis changes into circle). Migration smears the energy of this single event over the ellipsoidal surface (figure 4.5, right).
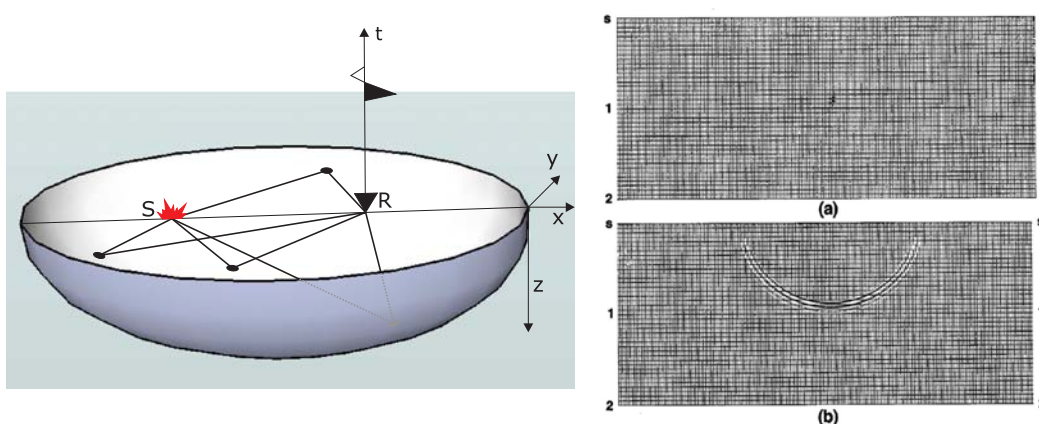
Figure 4.5.: Reflection surface ellipsoid of possible reflector locations with the same travel-time (left). Migration principle on smearing (right). (a) An unmigrated zero-offset section, consisting of a single non-zero sample on the central trace. (b) Migrated section, showing that the spike gets smeared onto the locus of possible reflection points – for this constant-velocity zero-offset 2-D example, a semicircle (Yilmaz, 2001).

Given a different sample, perhaps on a different unmigrated trace, migration would similarly spread that sample onto an ellipsoid of its own. Kirchhoff migration works by repeating this process for all samples on all input unmigrated traces, summing each resulting ellipsoid's contributions into the output image as it goes (Gray et al., 2001). Constructive interferences create the migrated image. Too little subsurface information (small fold) results in 'smiles', which develop if there are not enough neighboring ellipsoids to interfere with.

An example for the migration principle based on diffraction summation is shown in figure 4.6. For every migrated sample, energy is summed along the diffraction, or hyperbolic path, on the input section. The summed value becomes the amplitude value at the output location (Bancroft, 2007).

Kirchhoff depth migration computes the shape of the diffraction from a depth/velocity model
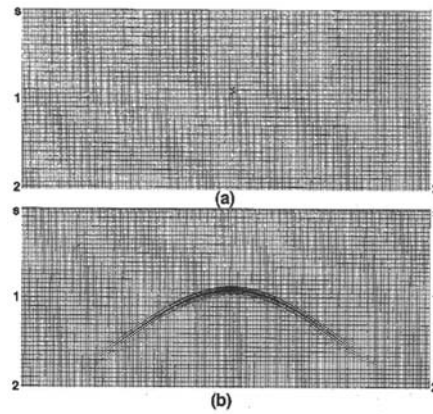
Figure 4.6.: Migration principle based on diffraction summation. (a) An idealized cross section, consisting of a single point scatterer in an otherwise homogeneous earth. (b) The zero-offset response to the cross section, consisting of a single diffraction curve (for this constant-velocity zero-offset 2–D example, a hyperbola). Kirchhoff migration performs a weighted sum of the amplitudes along the diffraction curve and places the sum at the scatterer location (Yilmaz, 2001).

using a precomputed travel-time map. This can be done by using ray-tracing or solving an expression such as the Eikonal equation.

The TIPTEQ and all other 2–D data sets contain energy coming from a 3–D environment, meaning that the energy in the shot gathers can also come from out of plane reflections (sideswipes), oblique reflectors, and as seen in figure 4.5 of non-unique reflector positions. This is not considered in the 2–D implementation of the Kirchhoff depth migration, and may lead to variations in dip an depth of reflective elements. A 3–D survey setup and/or 3–D migration can eliminate this adulteration.

4.7. Processing steps II

Normal Moveout Correction The NMO correction was applied together with a stretch mute of 30 %. The NMO actually operates by stretching the traces. This effect is most prominent at shallow times and at the far offsets, e.g. visible as low frequencies with high amplitudes from the first breaks. This will degrade the stack and distort the frequency content of the shallow data. Any data point whose sample interval is altered by a percentage greater than the specified value will be muted (ProMAX, 2003).

Resample/Desample The data is resampled to a coarser sample rate to make data processing quicker and decrease the amount of disk space required to store data. This does not have a significantly adverse effect on signal data quality, unless the data's frequency content is greater than the Nyquist frequency. That means, the frequencies of the seismic data must be below the Nyquist frequency in order to resample the data without aliasing effects.

The new output sample rate was set to 10 ms which equals 100 Hz (input sample rate 5 ms). The Nyquist frequency is defined with $f_{Nyquist} = \frac{1}{2}f_{sample\ rate}$, resulting in 50 Hz for the resampled data. The condition $f_{max\ (data)} < f_{Nyquist}$ is just fulfilled, the upper border of the used bandpass filter for the TIPTEQ data is 50 Hz (refsec:bandpass). The highest frequencies might just show minor aliasing effects, so the anti-alias filter of the 'Resample/Desample' module was used to minimize aliasing effects.

Trace Math Transform The 'reflection strength' transformation was applied, which computes the complex amplitudes of the trace or the trace envelope as input for the stacking process.

CDP/Ensemble Stack The 'straight mean stack' method was used to sum up the samples. The sum is divided then by the number of traces in one CDP bin. Other methods like 'median stack' where the median of the traces is put in the output trace are also feasible.

Pad Traces At the beginning and the end of the stack section additional CDPs (traces with no data) were created. This guarantees enough room at the ends of the profile for subsurface reflectors to migrate to. Our first CDP with 'real' coordinates is e.g. 1775 (first midpoint between shotpoint 99 and first receiver; see figure 4.7). Existent header values are not extrapolated over these new traces. The x- and y coordinates off all CDPs from 0-1774 are the same ones as for CDP 1775. If header values of the padded CDPs are needed for any reason, they must be calculated externally.
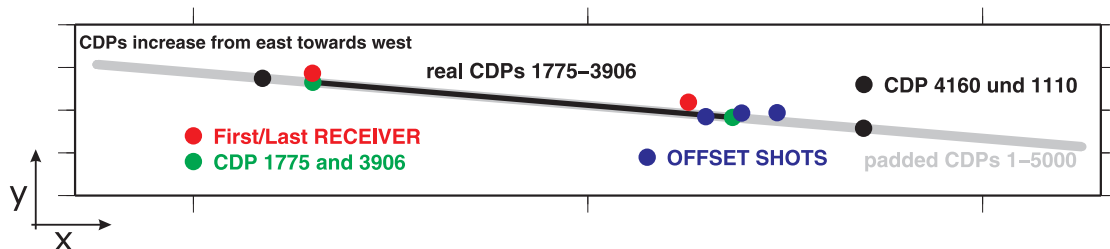
Figure 4.7.: Map of the CDPs and the padded CDPs together with the offset shots and first/last receiver for orientation. Black dots mark two CDPs which become relevant in chapter 10.

Kirchhoff Depth Migration The 'implicit Eikonal solver' method was used to produce the Green's functions. This method provides fair to good results, compared with the other two possible calculation methods (maximum amplitude ray tracing and multiple arrival ray tracing), and is 2/9 times faster (table mig_overview.pdf, ProMAX, 2003). Nevertheless, a complete migration job needed 2 days minimum of full CPU runtime on a SUN Ultra-60 workstation (512 Mb RAM), if no other user/jobs were working/running on the same machine.

4.8. Resolution of the seismic data

Seismic resolution is defined by how close two reflective features can be together and yet still be seen as two unique events in the data. This depends strongly on the used frequencies and therefore, also on the used source and energy. The results of the example calculations, given below, apply for the TIPTEQ data.

4.8.1. Vertical resolution

A quarter of the main wavelength can be seen as a minimum distance between two reflectors to be recognized as two events. This can be altered through a noisy recording to larger ratios (Yilmaz, 2001). The main frequencies (f) of the explosive shots of TIPTEQ (75 kg, 20 m depth) was not investigated, but generally, a wide range of frequencies should be generated. The goal of imaging deep crustal structures up to 60 km depth requires low frequencies. The used bandpass filter (see section 3.8) – with the corner frequencies of 6 - 10 - 35 - 50 Hz – limits the range of frequencies to $\approx$ 10 - 40 Hz for resolution calculations.

Seismic velocities (v) for the crustal rocks were picked from the used SPOC velocity model and range between 5.8 to approx. 7.2 km/s close to the plate interface. With the following equation, this results in wavelengths (λ) between 145 and 720 m, assuming this two velocity extremes:

$$\lambda = \frac{v}{f}. \tag{4.4}$$

Therefore a vertical resolution of 36 to 180 m is possible for the reflection seismic data set at minimum (see table 4.1).

v [km/s]	5.8	7.2	5.8	7.2
f [Hz]	10	10	40	40
λ [m]	580	720	145	180
$\lambda/4$ [m]	145	180	36.25	45

Table 4.1.: Vertical resolution of the TIPTEQ data.

As the seismic energy (and contained frequencies) decreases with increasing depth due to inelastic damping, absorption and diffraction, the vertical resolution reduces as well (spherical divergence).

Figure 4.8 shows a model with a wedge, illustrating layer thicknesses and demonstrates the limits of vertical resolution and its dependence on wavelength. The model is convolved with a kind of ricker wavelet and the synthetic response is shown the lower part of the figure. Spikes indicate the position of the model boundaries and resemble also a single frequency source signal. At 10 ms TWT wedge thickness, the two boundaries can not be seen as separate events.
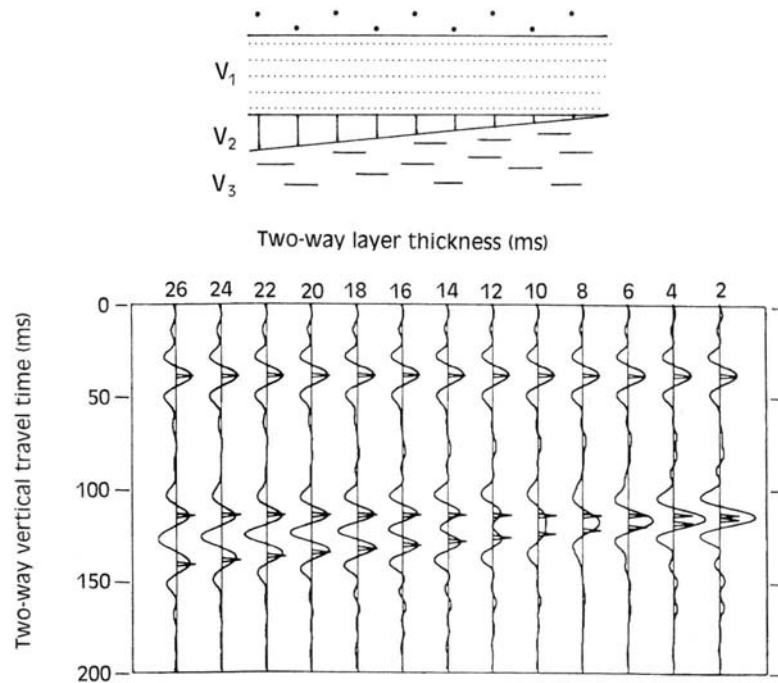
Figure 4.8.: Example of the dependence of wavelength and layer thickness, the two sketches are not the same scale (Jones, 1999).

4.8.2. Horizontal resolution

The horizontal resolution also depends mainly on the frequency. A seismic wave front is not reflected instantaneously from one single point but instead from an area over a short time interval. Hence, signals from reflectors close-by, that come to the receiver in that time-frame can't be distinguished from each other and interfere. For a given frequency, energy arriving at the receiver inside the time window resembling half of the wavelength ($\lambda/4$, one way travel-time) interferes constructively and enhances the signal (Yilmaz, 2001). The area where these reflections originate is called the Fresnel zone, or first Fresnel zone (see figure 4.9) and reflections from inside that zone are not separately resolvable.

High frequencies (short wavelengths) result in narrow Fresnel zones. The smaller the Fresnel zone, the easier it is to differentiate between two reflecting points. Hence, it is a measure for lateral resolution (Yilmaz, 2001).

The radius (r) of the Fresnel zone is given by Schmöller (1987), according to the following equation:

$$r_{fres} = \sqrt{\frac{1}{2}\, z \cdot \lambda} = \sqrt{\frac{1}{2}\, z\, \frac{v}{f}}, \tag{4.5}$$

in which z is the depth of the reflector and λ the dominant signal frequency. The horizontal resolution decreases with increasing depth and with increasing wavelength.
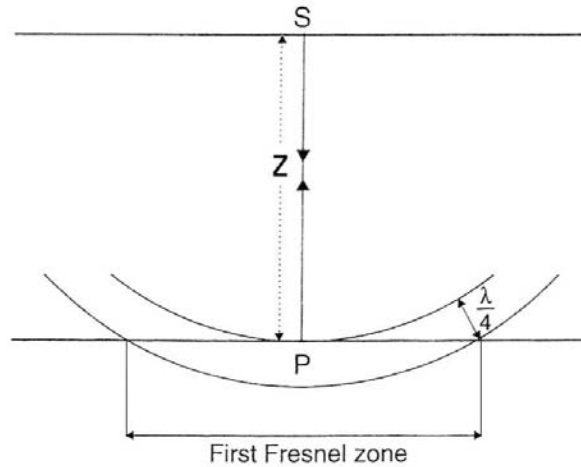
Figure 4.9.: Geometry of the Fresnel zone (Jones, 1999).

For a 40 Hz signal the radius of the Fresnel zone amounts to 2.32 km at 60 km depth (constant $v = 7.2$ km/s), 10 Hz result in a 4.65 km radius (see table 4.2). From that, 9.3 km may be an upper limit for the size of the Fresnel zone, since the average crustal velocity is lower than 7.2 km/s. These radii may be still considered small compared to the distance to the shotpoint (here 60 km).

v [km/s]	5.8	7.2	5.8	7.2
f [Hz]	10	10	40	40
λ [m]	580	720	145	180
$r_f res$ [m], z = 20 km	2408	2683	1204	1342
$r_f res$ [m], z = 40 km	3406	3795	1703	1897
$r_f res$ [m], z = 60 km	4171	4648	2086	2324

Table 4.2.: Horizontal resolution of the TIPTEQ data. Radii of the first Fresnel zone for different depths. The diameter of the zone gives the horizontal resolution.

Figure 4.10 shows the horizontal and vertical resolution up to a depth of 60 km for the minimum and maximum frequency of 10 and 40 Hz. As resolution depends on the seismic velocities, a mean crustal velocity was recalculated every 10 km (black line), derived from a 1-D velocity depth function of the SPOC wide-angle velocity model at profile kilometer 110 (grey line). In this way, a better subsurface resolution is calculated than using only the extreme velocity values as shown above in table 4.1 and 4.2. Smaller shot spacings do not increase the resolution of the data, they mainly increase the fold of the data and therefore the signal-to-noise ratio (SNR). Changing the distance from the source to the receiver or frequency content of the source reduces the radius of the Fresnel zone. An example for marine seismic profiling in figure 4.11 shows the increase in resolution if the source or/and receiver is towed close to the seafloor instead at the sea-surface. More information on lateral resolution can also be found in the course notes of Bancroft (2007).
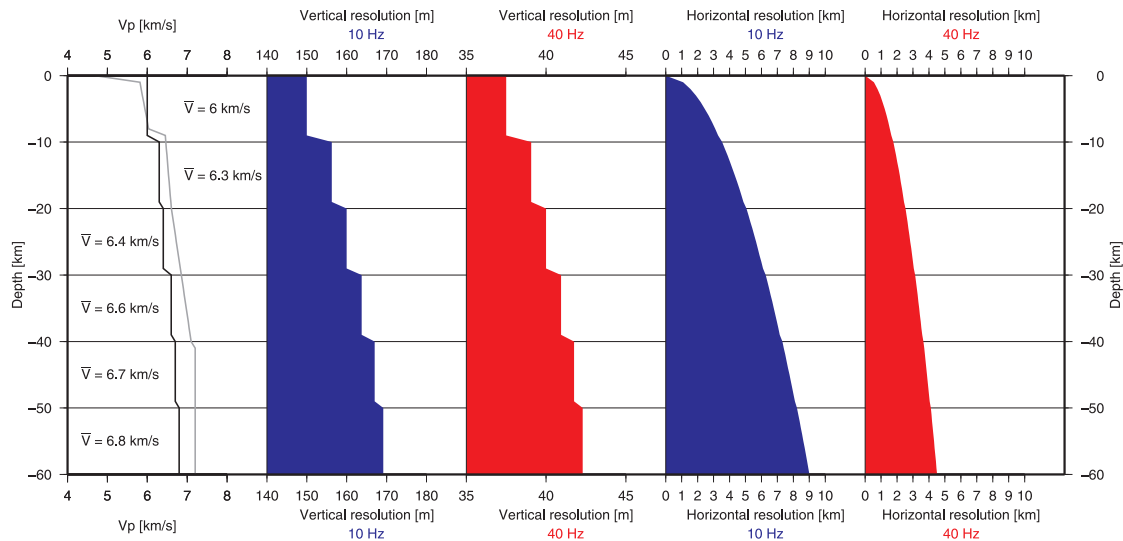
Figure 4.10.: Horizontal and vertical resolution up to a depth of 60 km for the TIPTEQ data set. The black line shows a mean crustal velocity recalculated every ten kilometers derived from a 1-D velocity depth function of the SPOC wide-angle velocity model (grey line). These mean velocities were used in the calculations shown in red and blue. The smooth curves of the horizontal resolution result from a depth dependency of the Fresnel zone (cf. equation 4.5).
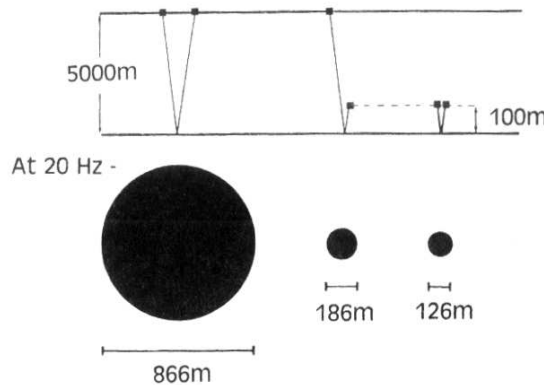
Figure 4.11.: Approach to minimize Fresnel zones. The black circles demonstrate the relative size of the Fresnel zone for different marine source/receiver configurations at the surface and using a deep-towed source and/or receiver (cf. equation 4.5). For the speed of sound in water a velocity of 1.5 km/s was used, the source frequency is 20 Hz (Jones, 1999).

4.9. Problems with ProMAX

Several problems with ProMAX made parts of the processing tedious and time consuming. Minor problems occurred because of display, network and computer configuration incompatibilities - together with different ProMAX versions - at the beginning of the PhD studies and could partly be solved. Certain interactive tools like the 'Interactive Vel Editor' or the 'Interactive Spectral Analysis' did not run at all on the local machine, and had to be used on different workstations.

The export of data out of ProMAX, besides SEG-Y or other similar seismic data formats, is dissatisfying, especially when the seismic section should be plotted besides earthquake, fault or other geoscience data e.g. with the open source program package 'GMT' (Wessel and Smith, 1991) or 3–D visualization tools. SEG-Y plotting of large sections is not convenient with GMT and using PS plots generated by ProMAX results in absurd large files, difficult to handle further on in publishing software like CorelDraw. CGM files did also not satisfy the needs. Screenhots proved to be the best solution to export seismic images from ProMAX. Section 9.3 shows a way how to convert the seismic data from the screenshots into ASCII data with longitude, latitude and depth to be plotted very easily alongside earthquakes, velocity interfaces and grid data with GMT or as point data in 3–D visualization software like Fledermaus. Printouts from ProMAX are directed to a printer using thermal paper like a FAX machine. The resolution is quite good, but the paper is very sensitive to sunlight, pencils, or felt tip pens making it difficult to work with.

Errors of unknown reason occurred during several ProMAX job in connection with the 'topmute'. Display jobs of shots e.g. produced an error and stopped, if the topmute was commented out, which was active in runs before. A workaround was to pick a dummy mute and load it to show data without a topmute.

Database errors and other mute problems were already discussed in chapter 3: Preprocessing (section 3.4: Airblast mute and subsection 3.9.4: Database errors)

The worst problem arose during the stacking and migration of the data. It first showed in September 2006 and became a really steady feature in spring/summer 2007 with the result that it was not possible to stack and migrate even single shots let alone the whole NVR data set any more. Therefore it was not possible to enhance the seismic images further or to produce more than a nasty brute stack of the horizontal components.

During the run of the stacking and migration flow, probably just before the data is written to disk an error occurs. This happens randomly and is totally unpredictable in respect to the amount of users working on the machine, for example. The error states that there is no diskspace to write the data to, even though several gigabytes are available on the partitions used by ProMAX (see figure 4.12). Sometimes, files were written in spite of the error message, sometimes it was possible to continue the job and a file was written to disk, but mostly no

file was produced at all. This error message is independent of the amount of data (number of shots) or the trace length, and no other correlation to this error message could be found. This impeded the production of migration images. A migration job of all NVR shots which should take ≈ 2 days of full CPU time lasted at minimum 2 weeks, because of several job aborts, if producing a file at all. Unfortunately, this issue remains unsolved so far.
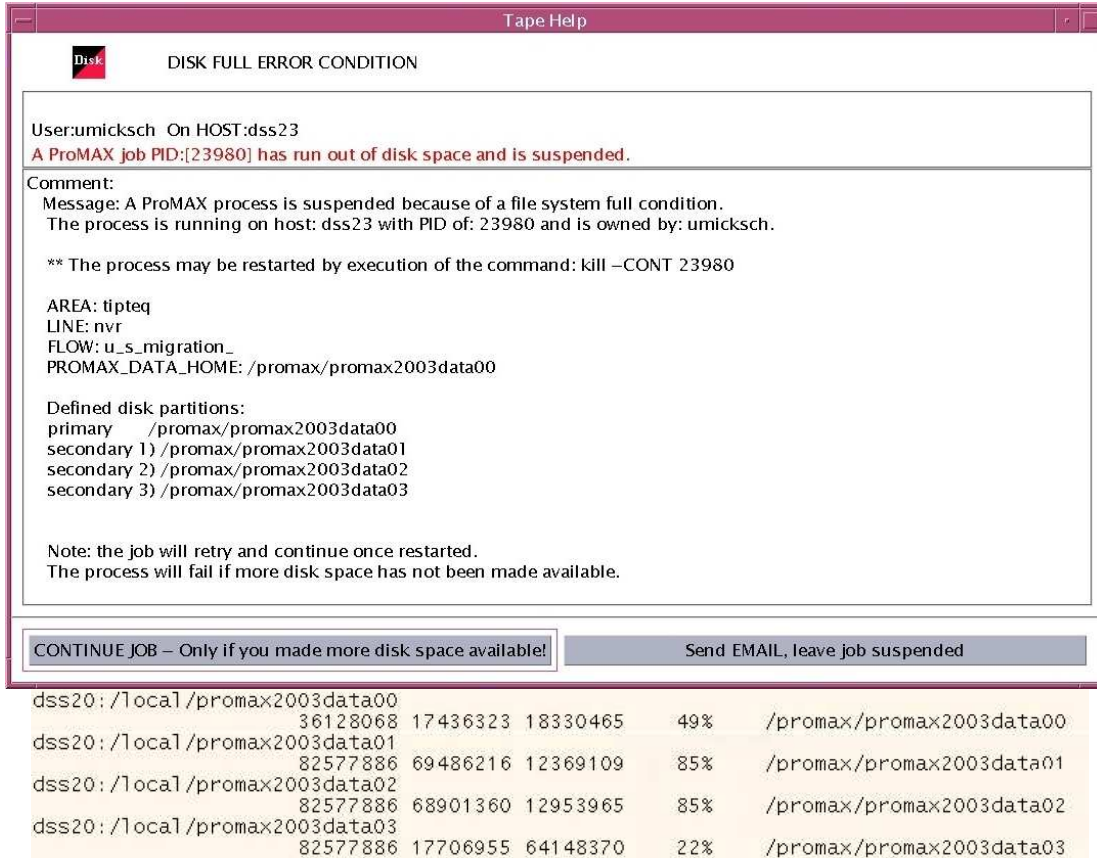
Figure 4.12.: Error message occurring during migration. The free diskspace is shown in the lower part of the figure.

5. Stacked and migrated images

Here, I present the seismic images after the processing, evaluate them, and describe features related to the processing sequence. A geological interpretation is given in chapter 10.

5.1. The CDP stacked time section

The time section including airblast and first-break noise is shown in figure 5.1. We see coherent reflections and broad, arching reflectivity bands with a duration of 1 - 2 s TWT up to a depth of $\approx$ 10 s TWT. These distinct bands are structurally continuous for tens of kilometers distance. We observe strongly horizontal events, e.g. at 5 or 7 s TWT and dipping events, both, in east and west direction. A prominent continuous reflector band is visible at 8 s TWT at the coast down to 17 s TWT under the Central Valley. On might speculate that the origin of this reflector comes from the downgoing plate or is otherwise connected to the plate interface (cf. also single shot gathers in figure 4.1). Below that, no real coherent reflectivity is observed, except for an enigmatic reflection (a), which is present below 15 s TWT in the eastern half of the section. This reflector seems to cut through the potential plate interface right at the eastern end of the profile. The noise from the airblast (b) and the high amplitudes resulting from the first breaks (c) are dominant in the first few seconds. They interfere in such way that an observer could mistake them for 'real' reflectors, especially between profile kilometer 10 - 30, thus showing the need to cancel these unwanted signals from the data. The signal from the high amplitudes of the airblast is still visible in depths between 15 - 25 s TWT e.g. near profile km 50 (d). In the central part, just around 50 km (in all depths) and at x = 70 km in a depth of $\approx$ 10 - 15 s TWT the seismic image appears to be blurred and less reflective than the neighboring areas.
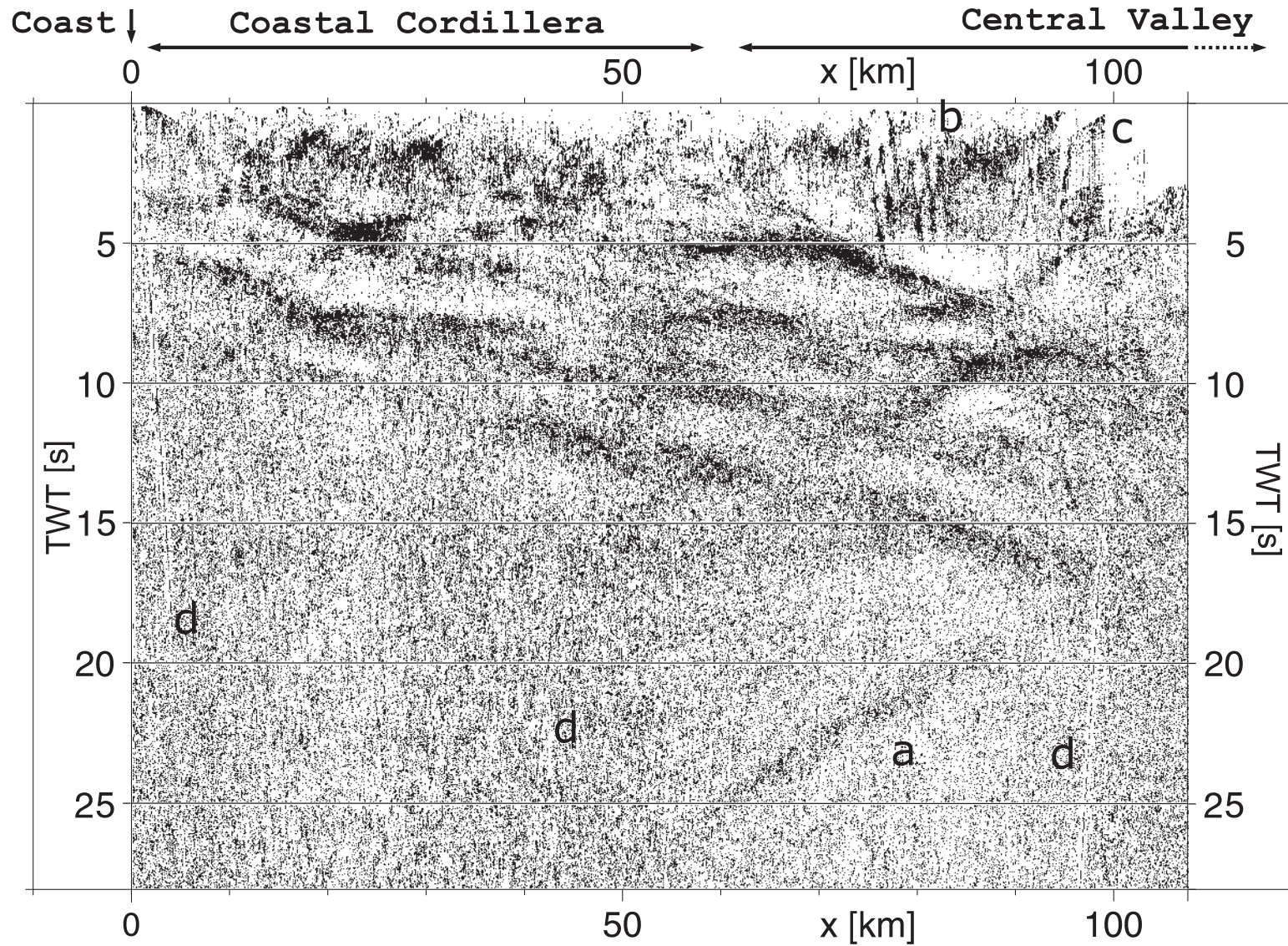
Figure 5.1.: Stacked time section (based on SPOC velocity model), see text for details (Groß, Micksch, and TIPTEQ Research Group, 2008).

5.2. Migrated image

5.2.1. Migration with unmuted data

Figure 5.2 shows part of a migrated section where no airblast mute or muting of the first breaks was applied.
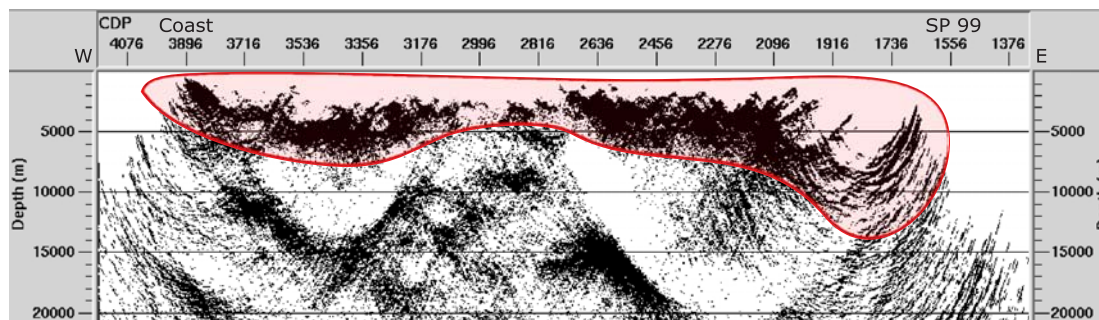
Figure 5.2.: The first kilometers of an example migration with airblast and first-break noise still contained in the data (red mask).

Between 0 - 7 km, we observe a highly reflective, detailed structure, even though it is only attributed to the sonic wave or first breaks. In the eastern end of the section we see artifacts resulting from migration, clearly visible migration smiles from the first breaks. They appear so prominent because of a coarser CDP fold at the eastern end of the profile.

Of course, if this unwanted noise is removed we loose also some important data from the subsurface, especially in the first kilometers, but the main goal was to image the crustal structure down to the plate interface at a depth of 50 - 60 km. A different experiment setup and/or processing technique would be needed to carry out studies of the near subsurface.

Close to both ends of the profile we see two major zones of almost no reflectivity expect the two mentioned sources of interference. In the middle part, where we did observe a diminished reflectivity in the stacked section (see figure 5.1), we observe also less prominent reflections of the airblast and first breaks, as we would expect from the sides of the section. One can't help but think that this is a) subsurface related: weaker shots or bad coupling of the receivers because of the particular subsurface, or b) is caused during the processing because of equalizations over all shots, which are affected by the changing of a transparent to a non-transparent zone (cf. section 10).

5.2.2. Migrated image

The final migrated image using the SPOC wide-angle velocity model (cf. figure 1.6) is shown in figure 5.3. We recognize a similar distribution of reflectivity bands in the continental crust like in the stacked section in figure 5.1. Reflectivity, which can possibly be attributed to the plate interface or oceanic plate is visible at 25 km below the coast to 55 km depth beneath the Cental Valley. The first few kilometers appear transparent at both ends of the section, a) because of the different applied mutes ($\approx$ 1 - 6 km) and b) because of the seismically transparent zones. No vertical or horizontal exaggeration is used. Again, for a complete interpretation of the seismic image please see chapter 10. The reflectivity pattern also shows similarities to the two-fold NVR SPOC profile (Krawczyk and the SPOC Team, 2003) (see figure 1.5) in the overlapping part from the coast to $\approx$ 50 km along profile (see figure 10.2).
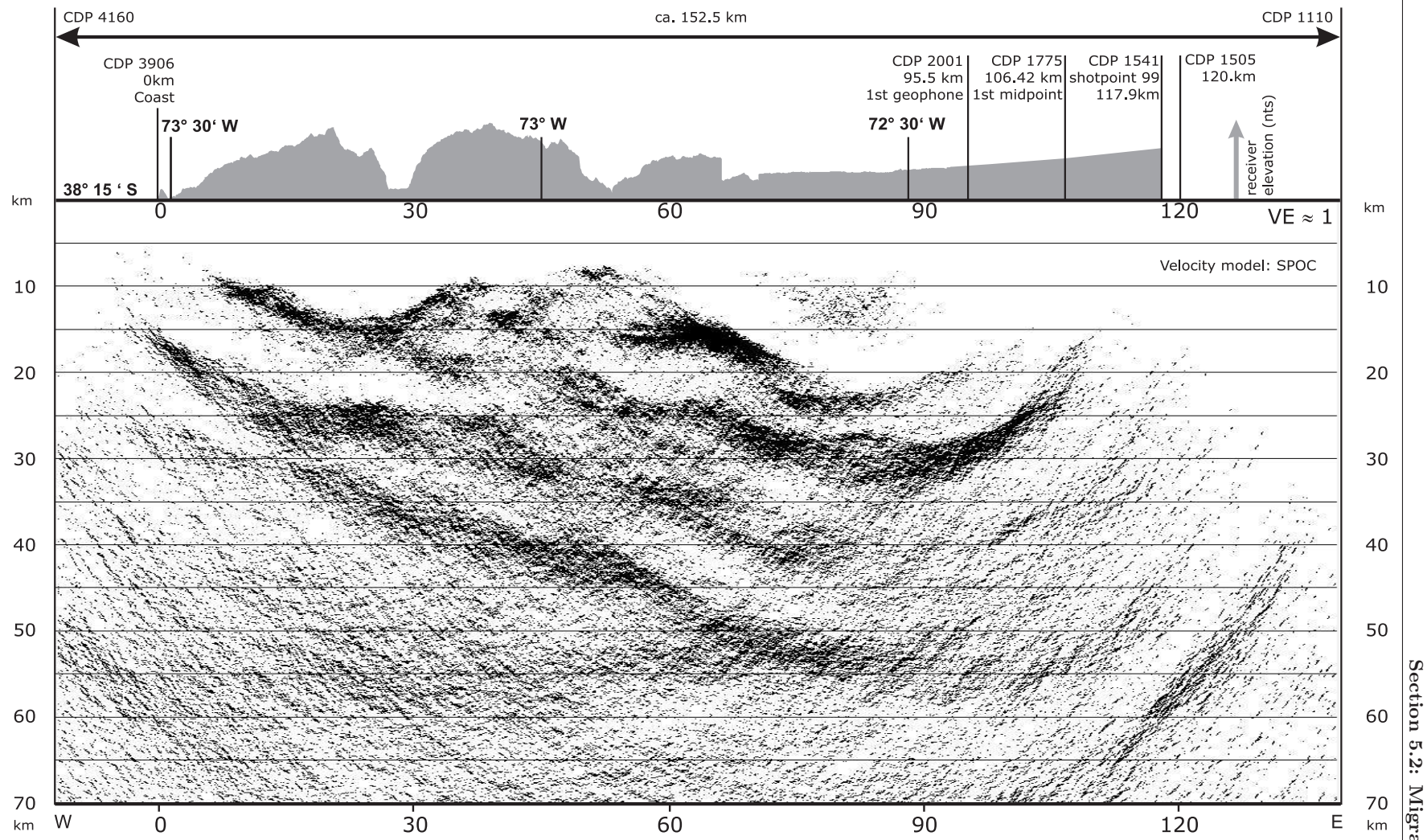
Figure 5.3.: Migrated depth section (based on SPOC velocity model), see text for details.

5.2.3. Migration artifacts and geometrical effects

Of course, we observe typical migration artifacts like smiles in some parts of the section, but the 'obvious', big smiles at the ends of the section are also contributed to the setup and subsurface geometry.

Figure 5.4b shows a schematic sketch comparable to the eastern end of the TIPTEQ line. We see a spread of receivers with two shots at each end of the spread. This spread moves towards the west. The rectangle marks a subsurface area considered here east of the easternmost receiver.
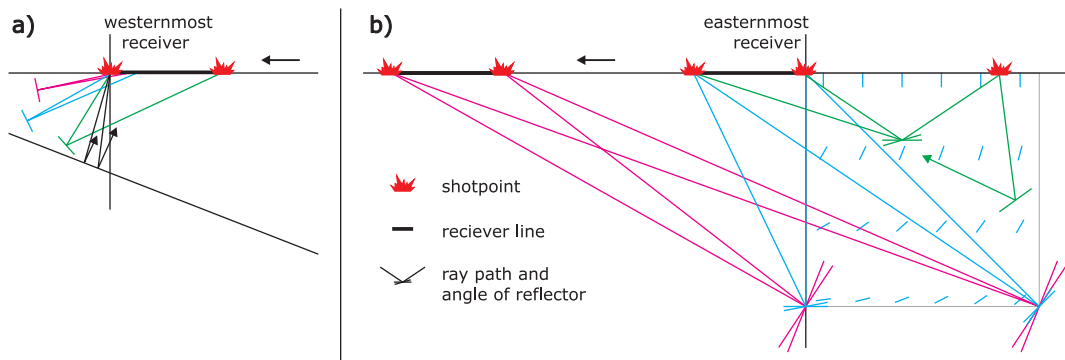
Figure 5.4.: Preferred imaging of steep dips at the ends of the profile.

The ray paths shown in green belong to a shotpoint off the line in the east. This geometry records mainly horizontal events, the possible reflector dip steepens for reflector positions towards the shot and east of it, almost vertical features can be imaged. The recordable dip angle of one reflective features at one certain x, z position depends on the length of the spread. The blue rays belong to shots at the end of a spread which is located just at the beginning of the profile and demonstrate the possible angles of reflectors, which reflect the seismic energy back into the spread. The short blue lines represent the mean reflective angles for the western shot of this setup. Horizontal, or quasi horizontal reflections are only possible in depth and close to the first receiver. The farther east a reflective event is situated, the steeper must be its dip to be recorded. There is also a maximal-depth and spread-length depending dip of a reflective element on a certain subsurface position to be recorded, because too steep dips reflect energy in front of the spread. Finally, the magenta lines represent shots from a moving spread in westerly direction. We see, we need a very steep minimum reflector angle to reflect data back into the spread from the subsurface within the rectangular area. The dip of the reflectors we can image steepens the farther we move away from the beginning of the profile.

In the TIPTEQ case, we can record onsets of the enigmatic reflector, labeled a in figure 5.1, up to profile kilometer 50 from the first receiver at 95.5 km. This equals ≈ 34 shots which image only steep dips off the end of the profile versus 3 shots (Shotpoint 97, 98 and 99) off the end of the line, which image mainly horizontal events. This imbalance obscures any recorded horizontal events off the end of the profile and we see only the steep events. Within the area

covered by the moving spreads, the effects of reflections from outside the current spread is reduced, due to the greater fold of the data because of overlapping spreads. The westward dipping reflector in figure 5.1 at a depth of $\approx$ 10 s TWT at profile kilometer 80 - 90 km might be a candidate to migrate towards steeper dips east of the profile – like the enigmatic reflection – and come to place around profile km 100 at a depth of 25 km in the migrated section (see figure 5.3).

Towards the western end of the profile, we record subsurface information from in front of the current spread. This is due to a similar effect as described above and a given dip in the subsurface (see figure 5.4a). Seismic waves travelling ahead of the last receiver are reflected back into the spread because of the dipping plate interface and connected similar dipping layers. Quasi horizontal reflections can be imaged close to the last receiver, and again, further from that, only steep reflectors can be recorded.

An angle of incidence dependent processing could be carried out for the shot recordings near the ends of the profile to overcome the problem of recording mainly steep dips there.

A more appropriate way to show the image of the subsurface might be to limit the migrated section only to the parts covered by receivers as shown in figure 5.5. Be aware of this discussion while reading chapter 10 about the interpretation of the depth section.
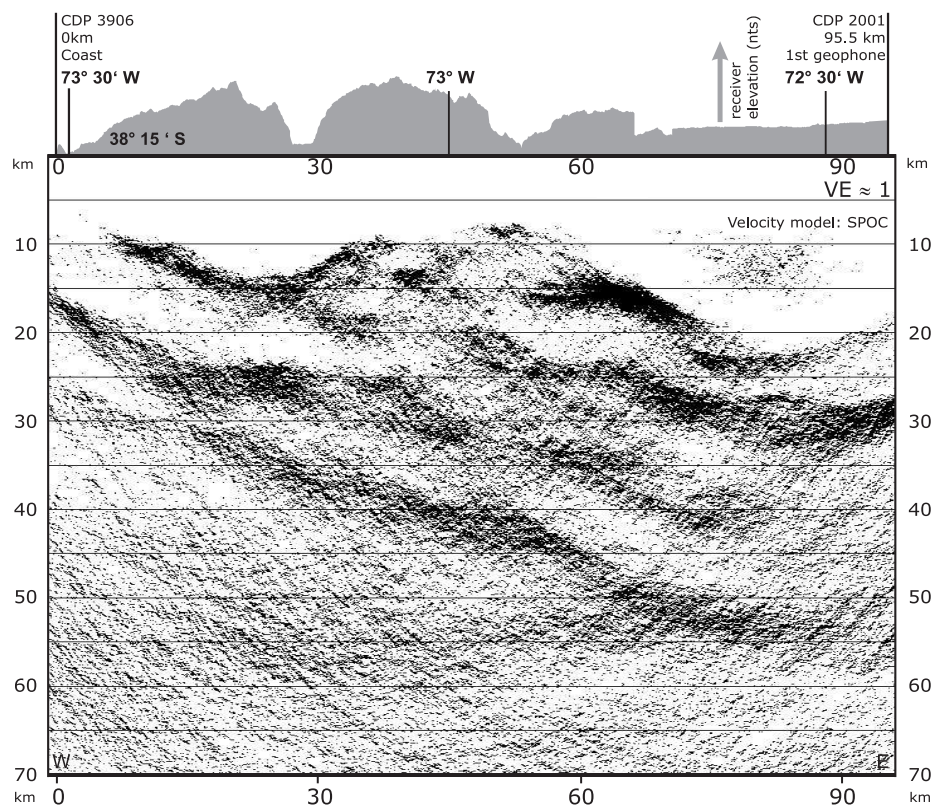
Figure 5.5.: Depth migrated section covering only the extend of the receiver line.

We see a broad horizontal reflection at a depth of 50 - 60 km in the western part of the depth section. There is no known geological expression for such a feature, so a artefact of the processing might be its cause. This depth corresponds to ca. 16 s TWT in the stacked time section, if we correlate this via the end of the last downgoing band. Here, we see also darker tinge in the data. This might be caused by the end of a scaling or equalization window, where we might have an abrupt change in amplitude.

The used SPOC wide-angle velocity model has technically a coarse resolution, resulting in a smooth velocity model. In the next steps, a near-surface velocity model by means of a first-break tomography is constructed. This model is merged with the SPOC wide-angle velocity model for further migration jobs, probably resulting in a more realistic depth image. This gives also an opportunity to test the influence of near-surface velocity structures (< 5 km depth) on deep crustal structures (≈ 40 - 60 km depth).

5.3. Seismic image and resolution

Figure 5.6 shows a direct comparison of the seismic image with results of the resolution calculations. The graphs on the sides of the seismic section show the calculated vertical and horizontal resolutions (cf. section 4.8 and figure 4.10).

The graph in the central part shows the horizontal resolution every ten kilometers in the same horizontal scale as the seismic image for a direct comparison. A calculated horizontal resolution of just below 4 km in a depth of 40 km for a frequency of 40 Hz seems acceptable. This requires that the source energy is great enough to allow seismic waves with frequencies of 40 Hz to reach such depths and back to the surface without great losses because of absorbtion, damping, and scattering.

The vertical scale is the same for all graphs and seismic data. Vertical resolution of the seismic data is governed by the vertical pixel resolution of the background image of 89.7 m. This causes a loss of resolution power for high frequencies (≤ 40 Hz), but resolution power is sufficient for low frequencies (≥ 10 Hz). The vertical resolution is good enough for this crustal scale investigation with a best value of ≈ 90 m. The thickness of the black inset in the lower right of the vertical resolution graph on the left gives a vertical scale of 200 m for the seismic data.

Figure 5.6.: Direct comparison of the seismic image with results of the resolution calculations. The graphs on the sides show the calculated resolutions (cf. section 4.8 and figure 4.10). The graph in the central part shows the horizontal resolution every ten kilometers in the same horizontal scale as the seismic image for a direct comparison. The vertical scale is the same for all graphs and seismic data.

6. First-break tomography – Preparation, procedure and model setup

Tomographic images in earth science – based on travel-times – show subsurface velocity distributions and can be used for depth migration of reflection seismic data (Guo and Young, 2004), to resolve crustal structures (Asch et al., 2007; Daly et al., 2008), or to image the depth extend of subducting slabs into the earths mantle (Zhao et al., 1994). Classically, travel-time tomography was used to construct global earth models from earthquake travel-times (Sengupta and Toksöz, 1976; Aki et al., 1977; Bijwaard et al., 1998; Romanowicz, 2001). They are constructed from an inversion of P- and/or S-wave travel-times obtained from earthquakes, crosshole profiling, or controlled source experiments like TIPTEQ. The source/receiver geometry and the appropriate wavelength bandwidth limit the resolution and depth extend of the tomographic images. Vp/Vs ratios from tomographic inversions can be used for the petrophysical characterization of the subsurface rocks.

Here, the tomographic image is constructed to trace the found surface geological features into depth by the inverted velocity contrasts. In addition, a tomographic image is merged with the SPOC–South velocity model in a subsequent chapter, to compare the impact of that merged model on the depth migration.

I used the program package FAST (3-D First Arrival Seismic Tomography programs) by Colin Zelt (Zelt and Barton, 1998) for the tomographic calculations. This program is available at `http://terra.rice.edu/department/faculty/zelt/fast.html` for free. FAST is capable of 3–D tomographic inversions, but only 2–D calculations were used. The TIPTEQ data set has no real 3-D information, even though the profile is crooked, because there are no seismic cross-lines. All related program and data folders can be found in `/tipteq/TOMO`. The calculations were carried out in folders in 'my' home directory, therefore, it might be necessary to adjust path settings to rerun some jobs. First-break travel-times, the geometry of receivers and shotpoints, and a starting velocity model are the three basic inputs needed for FAST. The preparation of these inputs, the procedure of using FAST and some theoretical aspects are explained in the next sections.

6.1. First-break picks

Travel-times were picked in all 104 TIPTEQ shots with ProMAX. The recorded traces were displayed with a reduced travel-time t* = t - offset/vred (vred = reduction velocity = 6000 m/s),

so that the first-breaks are aligned more or less on a straight line for a more convenient picking. 104 shots times 180 receivers result in 18720 possible travel-times. 15471 travel-times (> 80 %) could be picked. Stations with no data because of disconnected geophones or stolen hard-disks, as well as noisy traces or small amplitudes e.g. of ESP (offset) shots limited the number of picks. First-breaks on traces close to a shot were also difficult to pick. The energy of the exploding chord which failed to ignite the blasting agent at the two misfires (shotpoints 9 and 12) still produced first-breaks on channels with small offsets. The amplitudes were very small and hard to detect, so the 360 traces of those two shots were omitted. First-breaks can be picked in any 'trace display' job, the used flow in ProMAX is called *u_ pick_ firstbreaks*. Figure 6.1 shows some examples of first-breaks of shots along the profile.
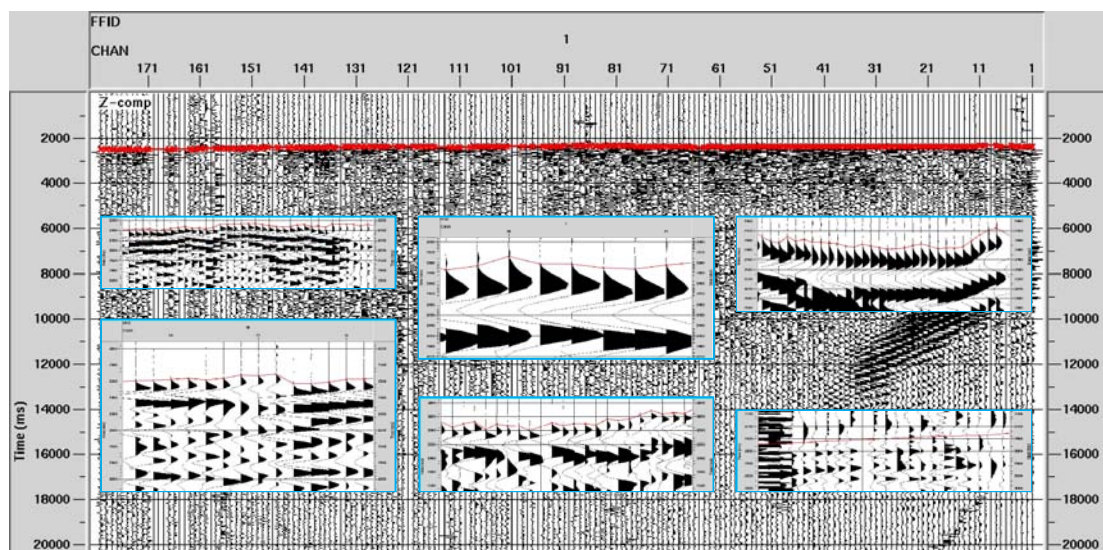
Figure 6.1.: The background image shows the flat onset of the first-breaks of FFID 1, because of the reduced travel-time (LMO). The insets show different characteristics of the first-breaks of shots along the profile, mainly of good quality. The inset in the lower right shows first-breaks more difficult to pick.

6.2. Preparation of the input files

Two scripts were used to prepare the data and parameter input files for FAST. The scripts can be found in the directory `/tipteq/TOMO/tiptomoprep*`. 'tiptomoprep' is the basic preparation folder, whereas the other preparation folders are needed for special pickfiles or pickerror studies.

6.2.1. projection.scr script

The receiver line followed local roads because of a pronounced topography and land usage, and was therefore not a straight, east-west trending line. This crooked receiver line must be

projected on a straight 2-D profile, from which the receivers and shotpoints have the smallest possible deviation. This is done with a least square regression calculation, like the calculation of the CDP line (see section 3.9.1) and results in a coinciding regression line. The shotpoints are then moved orthogonally onto that straight line. The original distance from the shotpoint to the receivers is kept and the new receiver coordinates are marked on the regression line in that corresponding distance (Zelt, 1999). There are other ways of projecting the sources and the receivers, but, e.g., moving all the receivers orthogonally on the regression line and calculating the new shotpoint coordinates would result in a nearly identical final tomographic image (Trond Ryberg, GFZ, pers. comm.). The geographical coordinates are exchanged with local coordinates, for a convenient use of 'kilometers' as model units for x and z direction. The last receiver position (955) at the coast was used as origin of the subsurface models.

One needs to prepare 2 files beforehand containing shotpoint and receiver information like latitude, longitude and elevation, confer 'receivers4ProMAX.asc' and 'shots4ProMAX.asc' in `/tipteq/TOMO/tiptomoprep*`. The script itself sorts in the first part the shot and receiver coordinates, calculates the new local coordinate and geometry files. The second part deals with the calculation of the regression line and calculation of the input files for FAST. Figure 6.2 shows the real sources and receivers together with the projected shotpoints and regression line for the eastern part of the profile. The maximal deviation of the profile to the regression/CDP line is 3 km.
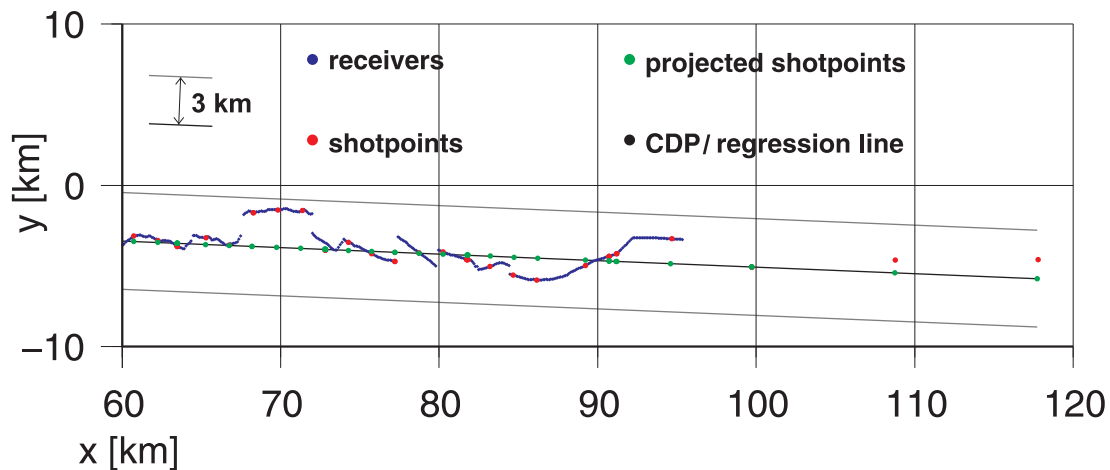
Figure 6.2.: Part of the receivers and shotpoints together with projected shotpoints and regression line (local coordinates). See appendix D for a map of the whole profile.

6.2.2. prep_data script

One needs to export the travel-times out of the database of ProMAX as well as information like offset, trace elevation, and FFID of each trace for each travel-time. The best common key to match each data entry is the trace number (1 - 18720). Four ASCII files (*.a_db files) were exported for each item together with the trace as number out of the TRC OPF.

The strange number of '33999999521443642490773241379936429670400' indicates that the database of ProMAX has no entry at that position, meaning explicit NAN. This number is written in the exported ASCII files instead of '0' for no first-break pick on a trace, because '0' can have a meaning, e.g. 0 samples or 0 s. ProMAX assumes that this ridiculous high number does never occur for any entry.

The script 'prep_data' in `/tipteq/TOMO/tiptomoprep*` prepares in the first part a file called 'fb_all.dat' from the four 'a_db' files with 'FFID offset time elevation'. The reduction factor is also removed from the travel-times in this step. It might be necessary to change file names, the lead time before a shot, the reduction velocity and pickerror. The second part of the script addresses the generation of parameter files as well as ASCII travel-time input files for each shot, which are converted into binary file inputs for FAST. The output from the 'projection.scr' script is used for this generation as well as the just generated file fb_all.dat. The structure of the travel-time files consists of 6 columns, which stand for the x, y, z coordinates along the profile, the travel-time, a given pickerror, and a flag (-1/1) indicating a shotpoint or a receiver with a travel-time.

If one follows the folder and filename structure as in `/tipteq/TOMO` the procedure to run both scripts is summarized below. One must convert the created binary pick files from UNIX binaries to LINUX binaries in a last step, because I changed from a UNIX compiled version of FAST to a LINUX version (shorter runtime of inversions). The new preparation of the input files is not needed for each run of FAST or after changing inversion parameters, it is only needed if the number of picks and/or the travel-times change.

export of the four a_db files and preparation of the list files

$\Downarrow$

projection.scr (UNIX)

$\Downarrow$

prep_data

$\Downarrow$

convert-unix-linux.scr (LINUX)

$\Downarrow$

copy all new pick and created parameter files in folder where the inversion is executed, e.g.
`/tipteq/TOMO/tipteq_1`

The files to copy should include all ASCII 'fd????.asc' and binary 'fd????.picks' files containing the first-break travel-time as well as the freshly created files f.in and r.in.

Figure 6.3 shows the picked travel-times for the 15471 first breaks vs. profile kilometer. Between 0 - 3.5 s we see the travel-times of the NVR and SH shots. The travel-times from the 3 shots off the line start at 95.5 km at ≈ 1 to 8 s. Other travel-time picks above 3.5 s belong to the ESP shots with offsets up to 95 km. The greatest pick density is observed between 0 - 1 s. Between x = 0 - 20 km, pick density is decreased in the same time frame because of a wider shot spacing within the village of Quidico and two misfires at shotpoints 9 and 12 (≈ km 13 and 18). Battery problems and vandalism lead to the gaps at kilometer 85 and 78.
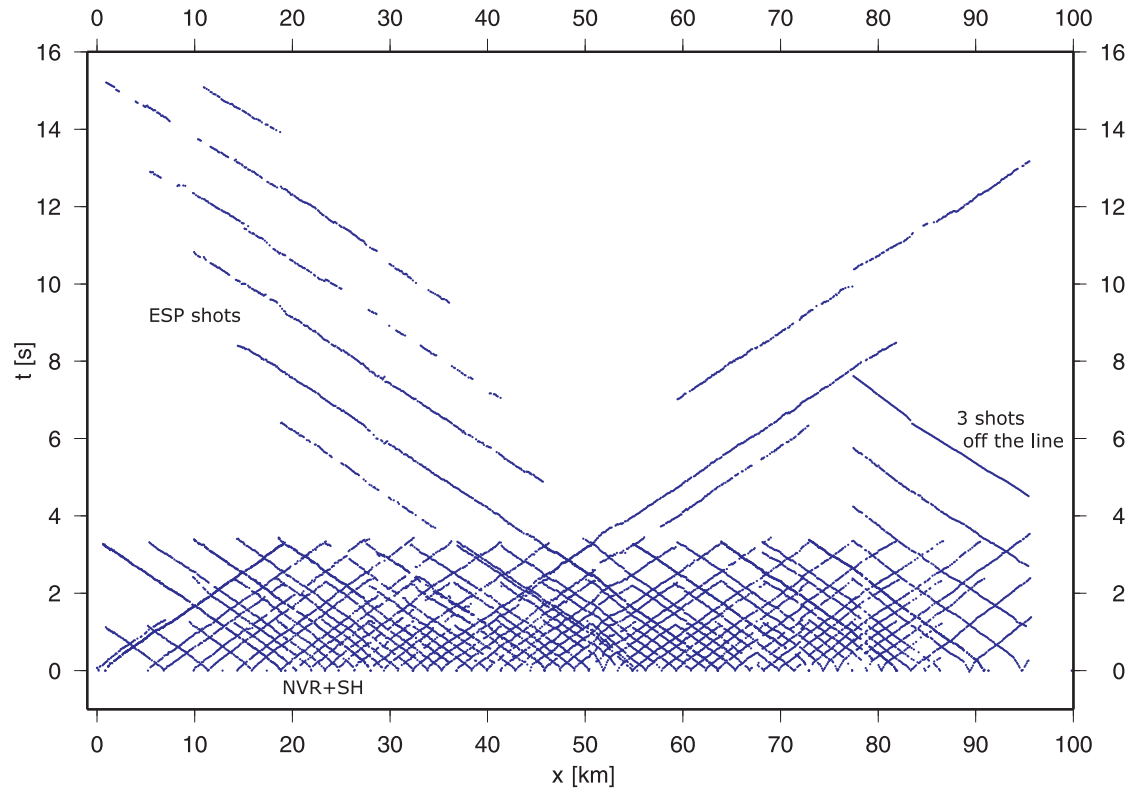
Figure 6.3.: All picked travel-times vs. profile kilometer.

Figure 6.4 shows all travel-times vs. occurring offsets. All picks lie more or less on a straight line. Deviations of travel-times of some shots can be explained because of mispicked phases or an error in the geometry arising from the shotpoint projection. Shots fired in sedimentary basins can also increase travel-times because of low seismic velocities. The travel-times marked in red originate from FFID 8 (Shotpoint 99) east off the line in the Central Valley. Other delayed travel-times e.g. at x = 30 km or 65 km also belong to shots in the Central Valley, arguing that these delayed times are caused by sediments.
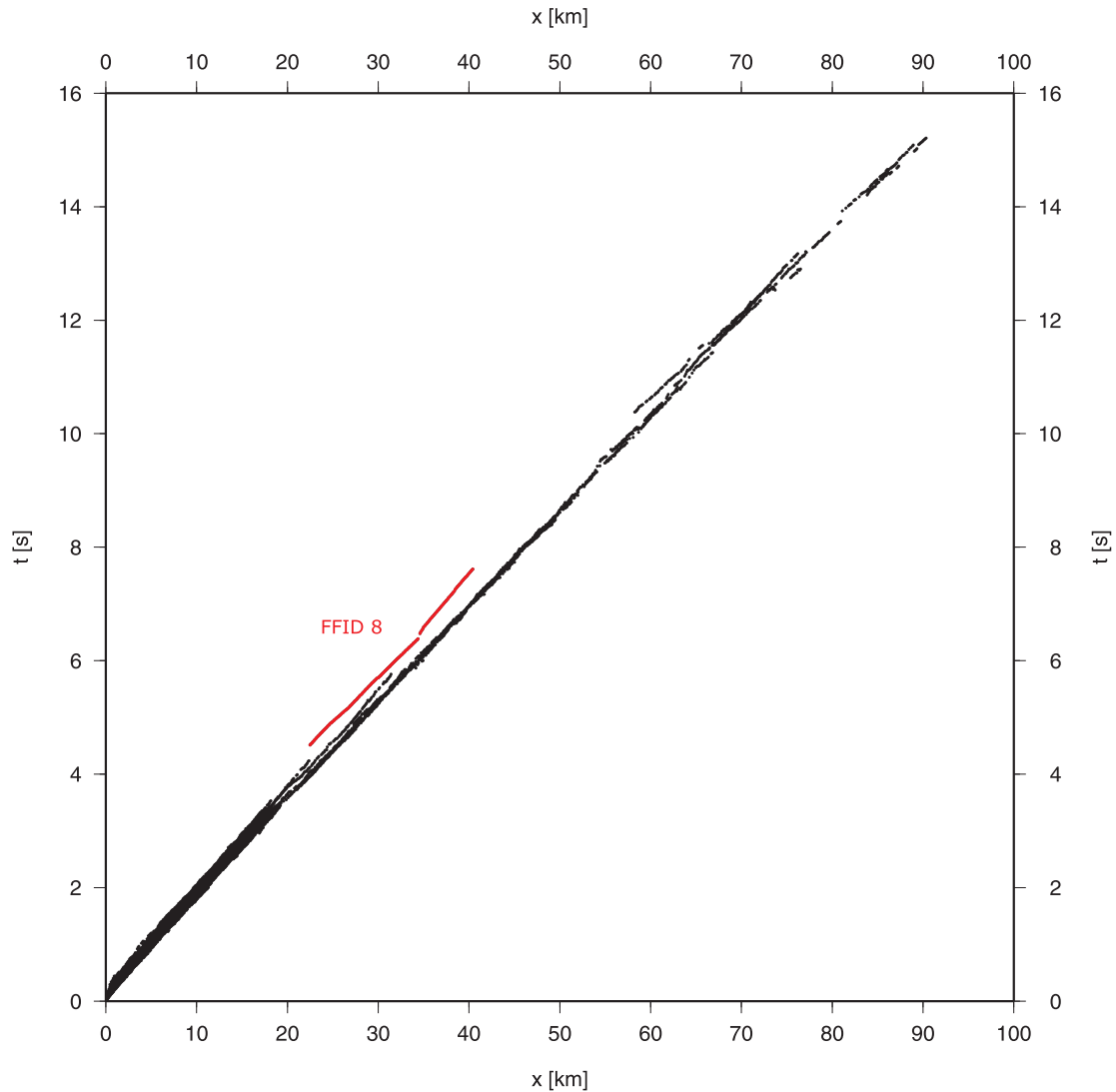
Figure 6.4.: All picked travel-times vs. occurring offsets.

6.3. Forward and inverse calculations in FAST

Seismic tomography, as implemented by FAST, uses a given subsurface velocity starting model and calculates synthetic travel-times from that using the input source/receiver geometry and created model parameter files (forward modeling). These travel-times are then compared to the picked travel-times. In following inversion steps, the subsurface velocity structure is altered in that way to minimize the differences between measured and repeatedly calculated travel-times. This is achieved by dividing the model space into cells, each with an own velocity. A detailed description of the used techniques in FAST and field examples can be found in the paper of Zelt and Barton (1998) and references therein.

6.3.1. Forward modeling

A wave travelling through the earths interior can be described with the eikonal equation (equation 6.1), which is a high-frequency approximation of the wave-equation and relates the gradient of the travel-time to the velocity structure (Vidale, 1990). t is the travel-time, the Cartesian coordinate axes are x, y, and z, and s is the slowness (inverse of velocity).

$$\left(\frac{\delta t}{\delta x}\right)^2 + \left(\frac{\delta t}{\delta y}\right)^2 + \left(\frac{\delta t}{\delta z}\right)^2 = s^2(x, y, z) \qquad (6.1)$$

The approximation is only valid if the gradient of the velocity is a great deal smaller than the frequency (Červený et al., 1977):

$$grad\ (v) \ll f$$

FAST solves the eikonal equation by finite differencing to calculate the first-arrival travel-times on a uniform grid after a method presented by Vidale (1990). Zelt and Barton (1998) include improvements for a faster runtime or inclusions for head wave operators (Hole and Zelt, 1995). The ray paths are obtained by following the steepest gradient of the time field from a receiver back to the source (Vidale, 1988).

6.3.2. Regularized inversion

Regularization is an approach by which constraints, in addition to the data, are applied to an inverse problem to treat the underdetermined part of the solution (confer also papers of Scales et al. (1990) and Phillips and Fehler (1991)).

Artifacts which arise from the underdetermined part of the model are damped, so that they do not influence the part of the model with has a good subsurface representation. Not only the residuals between observed and calculated travel-times are to be minimized, but also the variability of the inverted model parameters (Holliger, 2003). The objective function Φ minimized at each iteration is (Zelt and Barton, 1998)

$$\Phi(m) = \delta t^T C_d^{-1} \delta t + \lambda[m^T C_h^{-1} m + s_z m^T C_v^{-1} m] \tag{6.2}$$

where m is the model vector and δt is the data residual vector. C_d is the data covariance matrix, which is a a diagonal matrix with elements σ_{ii}^2, where σ_{ii} is the prior uncertainty of the ith travel-time. C_h and C_v are the horizontal and vertical roughening matrices, respectively, which include smoothness and flatness conditions. A model is considered smooth and flat if the changes in parameters of neighboring points in the model are marginal. For ray-based travel-time tomography it makes sense to minimize model roughness, e.g. infinite-frequency ray methods are valid for smooth media only (Zelt and Barton, 1998). Flatness corresponds to a minimization of the gradient (first spatial derivative) of an objective function, whereas smoothness corresponds to the minimization of the curvature of that function (second spatial derivatives of the inverted velocity model). s_z determines the relative importance of maintaining vertical versus horizontal model smoothness/flatness. λ is the trade-off (damping) parameter between minimizing the residual between observed and calculated travel-times and the wish to produce a model of minimum structure. No damping is present if $\lambda = 0$, requesting that the model is over-determined. There is no rule to set $\lambda = 0$, and it must be determined empirically. As a rule of thumb can be considered: the larger the under-determined parts in the model the greater must be λ. If λ is too large, the model is damped to much, resulting in a very smooth/flat model with the effect that structural detail is lost, and the travel-time data is not fitted very well (see below for parameter studies).

Equation 6.2 leads to the system of equations of (Zelt and Barton, 1998)

$$\begin{bmatrix} C_d^{-1/2}L \\ \lambda C_h \\ s_z\lambda C_v \end{bmatrix} \delta m = \begin{bmatrix} C_d^{-1/2}\delta t \\ -\lambda C_h m_0 \\ -s_z\lambda C_v m_0 \end{bmatrix} \tag{6.3}$$

where L is the partial derivative matrix with elements l_{ij} equal to the length of the ith ray in the jth cell (Humphreys and Clayton, 1988; Zelt and Barton, 1998, section 4). m_0 is the current model, δm is the model perturbation, and $m = m_0 + \delta m$. This system is solved using the LSQR variant of the conjugate gradient algorithm (Nolet, 1987; Paige and Saunders, 1982). According to equation 6.3, there are two free parameters, λ and s_z. However, s_z is held fixed for all iterations leading to a final model, whereas a range of λ values are tested at each iteration and that which gives the smallest data residual $\delta t^T C_d^{-1} \delta t$ is selected; for the last iteration we determine the value of λ that gives a normalized misfit of 1. This makes s_z the only free parameter (Zelt and Barton, 1998).

A stopping criteria for the inverse calculations is given by the pick error. The residual values are normalized by the accuracy of the travel-time picks. Calculations stop when the observations have been fitted to within one standard deviation-in a RMS sense (Scales et al., 1990). Rodriguez-Tablante et al. (2006) state that a good estimation of pick uncertainties is required. The use of values that are too high results in models lacking information that could be resolved by the data, and values that are too optimistic may cause artifacts in the velocity field as a consequence of data overfit.

The advantage of regularized inversion is the ability to include prior information, such as solution simplicity, so that it can provide the "minimum structure" model for a given level of fit to the data. The disadvantages of regularized inversion are its computational and memory requirements and the arbitrariness of the parameter values that determine the trade-off between data fit and the solution of the prior constraint equations (Zelt and Barton, 1998).

6.3.3. Comparison of FAST to other programs and methods

Backprojection is another method used for inversion calculations. It produces very similar results and performs nearly as well as the regularized inversion approach (Zelt and Barton, 1998). Hole et al. (2006) also compare both methods and state that results show similar structures. There, the regular inversion provides a higher resolution of near-surface structures, but contains high frequency artifacts in deeper parts of the model ($z_{max} \approx 6$ km).

Rodriguez-Tablante et al. (2006) compare FAST to PStomo_eq (confer Benz et al., 1996; Tryggvason et al., 2002). The programs use basically the same forward and inverse algorithms, but differ in how smoothing is applied. Besides investigating the cutbacks resulting from the projection of a crooked line to a straight 2–D line, the authors use synthetic and field data to show that FAST produces smoother models than PStomo_eq. The synthetic calculations show that FAST better models regions with smooth changes in the velocity field. PStomo_eq showed better performance in the resolution tests by giving a better recovery than FAST in checkerboard tests. PStomo_eq also appears to show thin geological structures, like dolerite dikes, much better than FAST when using field data (z_{max} of the used subsurface model $\approx$ 0.4 km).

Malinowski et al. (2005) present two velocity models, one produced with FAST the other produced with JIVE3D (Hobro, 1999; Hobro et al., 2003) which conducts a combined refraction–reflection tomography with different mathematical methods than FAST. Both models are fairly similar, they reproduce both the same important features for that study. JIVE3D produces a smoother velocity field than FAST, because of the required model parametrization of JIVE3D.

Different methods and implementations seem to produce similar images, especially in those parts of the model that are constraint very well. They differ in the amount of smoothness or in the detail of the inverted structures. Rodriguez-Tablante et al. (2006) conclude that the

choice of which program to use depends on the additional information available, the expected results, and what the model will be used for. The smoother models of FAST may therefore not be the best choice for a near-surface geological comparison of the first 200 - 300 m, or to image dyke-like features, but are sufficient to be used for migration of reflection seismic data in a crustal scale.

6.4. The usage of FAST

The source code of FAST was altered to be able to use more than 99 sources (Trond Ryberg, GFZ, pers. comm.). Compiling the source code creates $\approx$ 60 executables in the folder `/tipteq/TOMO/FAST/bin` for 2-D and 3-D calculations to produce the resultant tomographic images. The relevant programs use the created input files and are linked via various shell scripts and are executed in a project folder, e.g. 'tipteq_1'. It is advised to copy the folder `/tipteq/TOMO/tipteq_1` into a new project folder if one intends to conduct an own tomographic calculation, since the folder contains all important scripts and files needed by FAST. Parameter files need then only minor adjustments and one must supply the own created input files (see section 6.2). It is also feasible for the sake of clarity to copy the project folder into a new one if one changes e.g. the pickerror or the model size.

A second improvement of FAST is achieved by a loop of 5 single inversion runs, whereupon each run the inversion cell size is reduced successively (Ryberg et al., 2007). The output velocity field of the former inversion is used as the new starting model for the current run. This results in an iterative improvement of the subsurface velocity model. One model calculation only with large cells results in a coarse velocity field, which does not justify the number of rays passing through the blocks. The result might be quantitatively comparable to the iterative approach, especially in shallow depths with a high ray coverage. Small cells on the other hand exhibit a smooth velocity field, but not necessarily of a better quality. In areas of little ray coverage, especially in the deeper layers, the rays of one shot tend to focus in one 'single beam' with unrealistic velocities (too smooth, too fast) along the travel path. The five inversion cycles contribute to the independence of the final tomographic model from a reasonably chosen starting model (see below for comparison studies).

The needed scripts as well as the parameter and input files can be viewed with 'nedit' (linux-version) by the execution of the script 'all' in the project folders, which gives a tabbed view of the involved files for convenience.

The main script is the file 'xxinv', which first creates a basic starting velocity model. It also contains the loop around the inversion script, which is called with 'inv' together with the number of inversion iterations, the number tests with a decreasing λ and the name of the starting velocity model. The script 'maskieren', which is executed after the inversions, masks areas in the five velocity models that are not covered by rays. 'prepgitter' creates velocity grid files that include the masks created before. The final script 'dvn' plots the five masked

velocity grids for the decreasing cell sizes with GMT (cf. figure 6.5). The complete calculation needs ≈ 40 minutes (minimum) of full CPU power to run on a Intel Pentium 4 CPU with 2.00 GHz and 1 GB of RAM (Linux system), 35 minutes are needed for the 5 inversions alone.
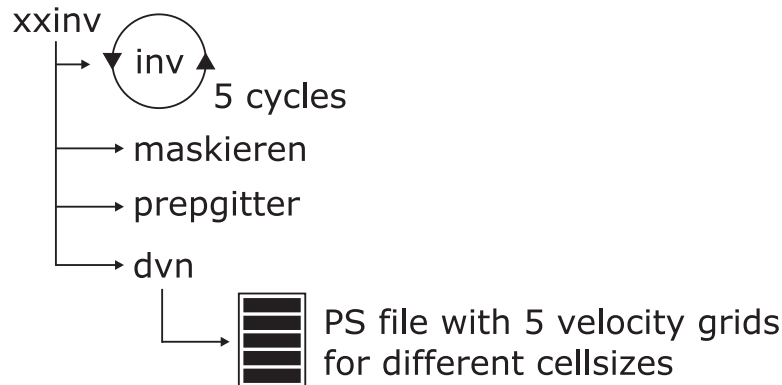
Figure 6.5.: Order of execution of scripts to create the tomographic images.

The resultant velocity distributions may contain areas, which are not constraint by rays and are therefore masked out. A switch set at the end of the 'prepgitter' script may interpolate these NAN areas. The resultant ray coverage and velocity information from the second cycle of inversions is used for this purpose. The models with the greater cells have a coarse but likewise velocity structure compared to the models with finer cell sizes. The blocky look is dissolved by the finer sampling of the relevant grid, smoothing the contact of the two grids. This interpolation is valid, since one uses velocity information of cells, rays have actually been travelling through. The interpolation results must always be compared to the results without interpolation. The greater cells of the first cycles tend to extend the final interpolated model into depth, compared to the ray image of the last cycle. This results in an interpolation below the depth covered by rays in the last cycle. One has no velocity constraints from neighboring cells and the interpolation could construct a false structure. Here, it is necessary to limit the extrapolated image to the depth of the deepest ray coverage in the last of the five images. The shot-receiver distribution can also limit the validity of the interpolation, e.g. at the ends of the profile. Small offsets limit the depth penetration of the rays there.

Other parameter files to govern the inversion itself are listed below, the main switches and important values to be set are described in brief:

f.in This file contains the parameters for the finite difference eikonal solver. A flag (1/0) which is set behind 'isource' in a list representing all shotpoints states if the shot is included or not in the calculations.

r.in Parameters for ray path an data kernel calculations are set in r.in. 'itrace' lists the shots to be used, simply delete numbers to exclude shots. 'tmax' gives the maximal time to be used to calculate travelpaths.

for.header The limits of the model are set in this file. One has to state minimum and maximum values on the coordinate axes in km, the spacing of the nodes in km, which divide the subsurface in cells and the number of nodes in each Cartesian direction, which is basically the corresponding length divided through the nodespacing plus one.

inv.header The number of nodes which make up the cell size for the inverse grid are given in 'inv.header'. This file is updated during each loop with finer cell sizes for the inversion from the file 'i.dat'

i.dat This file contains the values for the five inversions conducted with varying inversion cell sizes.

i.in 'i.in' contains the parameters for the inversion itself. 'sz', for example, gives the relative importance of maintaining vertical smoothness/flatness versus horizontal smoothness/ flatness (cf. equation 6.2).

l.in The initial lambda value to try for the first non-linear inversion is given here as well as the reduction factor of lambda to use for the following inversion steps. The number of lambdas to try is given at the start of the 'xxinv' script.

See also the FAST documentation contained in `/tipteq/TOMO/FAST` for further information on parameters used in the files listed above.

Log files provide a lot information on the current calculation. The number of the used sources, the number of calculated rays, or the values of λ, etc., are written in log.0 - 4. Additional copies of 'r.in' and 'f.in' with different shot lists, e.g. for all western shots or every second/third shot, as well as '.org' files are convenient and easily copied into 'f.in', 'r.in' for experimenting.

The resultant velocity model for each cycle is written in the binary files vel-0 - 4. The hitcounts, the number of rays in each cell, are recalculated for each cycle in the script 'maskieren' and written in the binary file num.cell. These two binary files are converted to xyz ASCII files useable with GMT with the FAST program 'gmtslice' at the end of the 'maskieren' script. As mentioned above, 'prepgitter' creates the masked grid files for plotting with GMT in the script 'dvn'. The grids are plotted together with a mask covering the model cells above the topography. This masks ray paths above the sources and receivers which are inside the model boundaries (zmax = 2 km asl), but would lie in the 'air'.

6.5. Model setup and used parameters

A similar field experiment like TIPTEQ was conducted in the Karoo Basin, South Africa within the joint research project 'Inkaba ye Africa' (Bräuer et al., 2007). The experiment geometry, which is comparable to the TIPTEQ NVR setup geometry, resulted in tomographic images up to a depth of 1.5 km. The TIPTEQ ESP shot configuration uses greater offsets

than 18 km (offsets up to 95 km) and one can expect therefore a deeper ray penetration of the subsurface.

The TIPTEQ inversions were started with a main model size covering 30 km in depth and 140 km in east-west direction. The origin is receiver 955 at the Pacific coast. The model starts at -10 km before the coast, at -2 km above sealevel, therefore reaching actual depths of +28 km (z direction is reversed). A simple 1-D Vp velocity/depth function based on the SPOC wide-angle model served as starting model, which was extended into 2-D by FAST with the module 'velbuild'. The used 1-D velocity function is shown in table 6.1; the starting model is shown in figure 6.6. No vertical exaggeration is used in this and the following images. All available shots of the NVR, SH, and ESP configuration result in 15471 usable travel-time picks. A generous pickerror of 0.03 s was assumed. Test-runs with different forward and inversion cell sizes determined the cell sizes to start with. The cell size of the subsurface blocks for the forward and inverse calculation are listed in the following tables (see table 6.2 and 6.3 and files 'for.header' and 'i.dat'). The cells of the forward grid must have the same length in the Cartesian directions and must always be finer than the inversion grids. λ was chosen to be 1000. The parameter 'sz' was set to 0.25, thereby setting the relation of horizontal versus vertical model roughness to 4:1 (see below for parameter studies).

z [km]	Vp [km/s]
-2	4.5
10	6.0
25	7.0
30	8.0

Table 6.1.: 1-D velocity input model for FAST (linear interpolation between the given constraints).
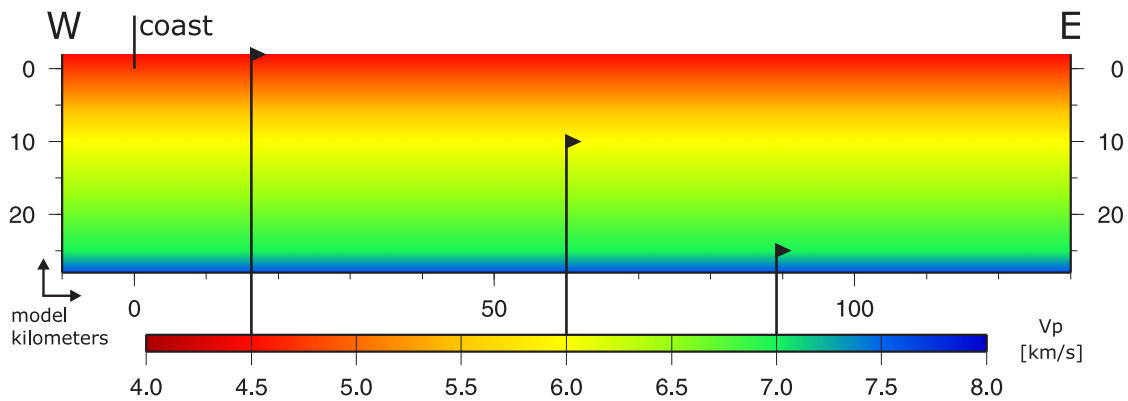
Figure 6.6.: Model setup and starting velocity model.

cell size [km]	no. of cells in x	no. of cells in z
0.1	1400	300

Table 6.2.: Cell size and number of cells for the forward calculation.

cycle	no. of cells in x	no. of cells in z	cell size in x [km]	cell size in z [km]
1	8	3	17.5	10
2	16	4	8.75	7.5
3	35	8	4	3.75
4	70	15	2	2
5	280	60	0.5	0.5

Table 6.3.: Cell sizes and number of cells for the inverse calculation.

7. First-break tomography – first images and validation

Inversion results are non-unique and need to be confirmed with several approaches, e.g. checkerboard tests, variations of the number of picks, or by changing the inversion cell size. Suspicious structures, paired with high velocities in the TIPTEQ inversion results required extensive validation tests to prove them real or just artifacts. The structures under question lie in the deeper part of the resolved subsurface and relate to the ESP shots with greater offsets. First-arrival picks from the explosive shots recorded with the seismological network of TIPTEQ on stations close to the profile (Haberland et al., 2006) were incorporated to improve the subsurface images.

Figure 7.1 shows the technical features of the following figures. The model size is 30 x 140 km, starting at y = -2 km to 28 km in depth. No vertical exaggeration is used. The receiver line is a thick black line above the surface, the shotpoints are plotted with red triangles. The modelspace below shows the tomographic images. The RMS value in the lower right corner always shows how good the synthetic travel-times fit to the picked travel-times, based on the given pickerror. The inversion should produce a RMS value of the same value as the pickerror (here 30 ms). The RMS (root mean square) values of the five inversion cycles converge towards the given pickerror. The difference of some ms in the RMS value of the last inversion cycle to the given pickerror can be attributed e.g. to errors resulting from the projection of the crooked receiver line onto the straight 2–D profile. In most figures the result of the fifth inversion cycle is shown only.
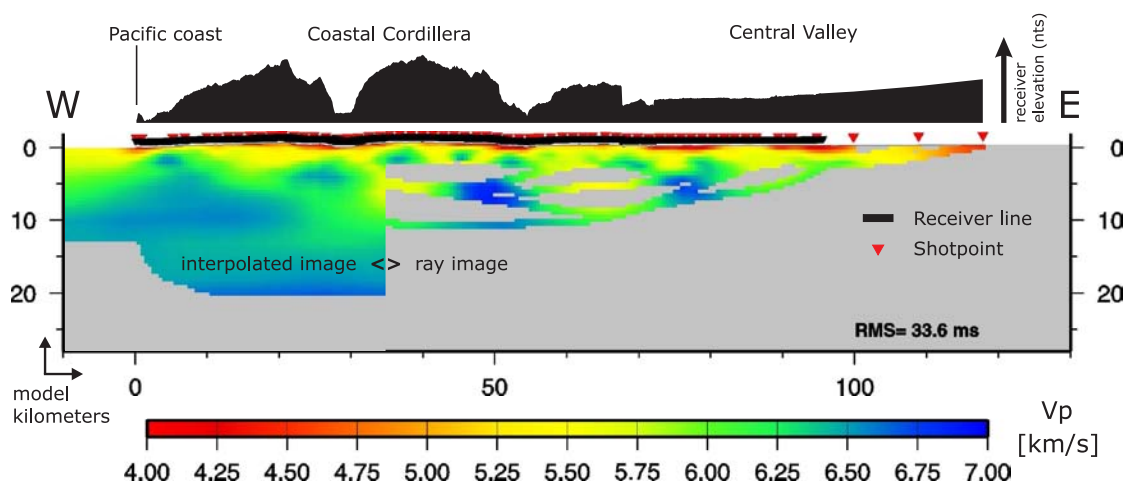
Figure 7.1.: General features of the tomographic images, see text for details.

7.1. Inversion result of all shots

Figure 7.2 shows the results of the inversion of 15471 travel-times of all available TIPTEQ shots (NVR/ESP/SH).

Panel 7.2a shows the final image of the five inversion cycles. We observe ray coverage along the whole profile from the Pacific coast up to the easternmost shot off the line at model kilometer 117.8. The deepest ray penetration of ≈ 11 km can be found in the central part of the profile (x = 40 - 60 km). Between 3 to 11 km depth we see the raypaths of the 15 ESP shots, the greater offsets result in deeper subsurface penetration.

The velocities range from 3.36 km/s to 6.95 km/s. Velocities ≤ 4 km/s occur on only 91 entries of the total of 17141 entries in the velocity grid file (x4.grd, 281*61 entries in x and z direction). They are found in the model above the topography and are therefore masked out. Four to five velocity entries at x = 52 - 53 km, z = 0 km show velocities below 4 km/s, but above 3.9 km/s. They are attributed to interpolation errors and therefore errors in the topography mask, because at that position the difference of the crocked line to the projected line reaches almost the maximum value of three kilometers, paired with a steeply declining topography to a horizontal one at x = 52 km (cf. figures 6.2 and 7.1). Maximum velocities greater 6.9 km/s occur in ≈ 15 cells at 48.5 - 50 km in a depth of 6 - 7.5 km. The range of the colormap to code the velocities covers therefore 4 - 7 km/s. A detailed plot showing the areas of the minimum and maximum velocities and a histogram of the velocities ≤ 4 km/s can be found in the appendix in figure E.6.

Panel b of figure 7.2 shows the corresponding velocity model with interpolation. Within the area covered by rays, the interpolation seems reasonable. Small changes in the input velocity model produce varying raypaths for the ESP shots, imaging similar structures at various depths, thus creating the same image as with interpolation, if virtually combined (see figure E.7). Velocity information below the lowermost rays must not be considered valid. There, we observe no fine velocity structures, rather a smooth distribution. The image might show a reasonable trend in the velocities, since velocity information of a former inversion cycle is shown, where actually rays have travelled through these areas.

Part c of figure 7.2 shows the ray image and interpolated results of each of the five inversion cycles with decreasing cellsizes (cf. table 6.3). Each cycle uses the resultant velocity model as input for the current inversion calculations, starting with the velocity model shown in figure 6.6. The quality of the image increases towards later cycles, also apparent in the RMS values. They decrease from 93.2 ms down to a value of 33.6 ms. The chosen pickerror was set to 30 ms.
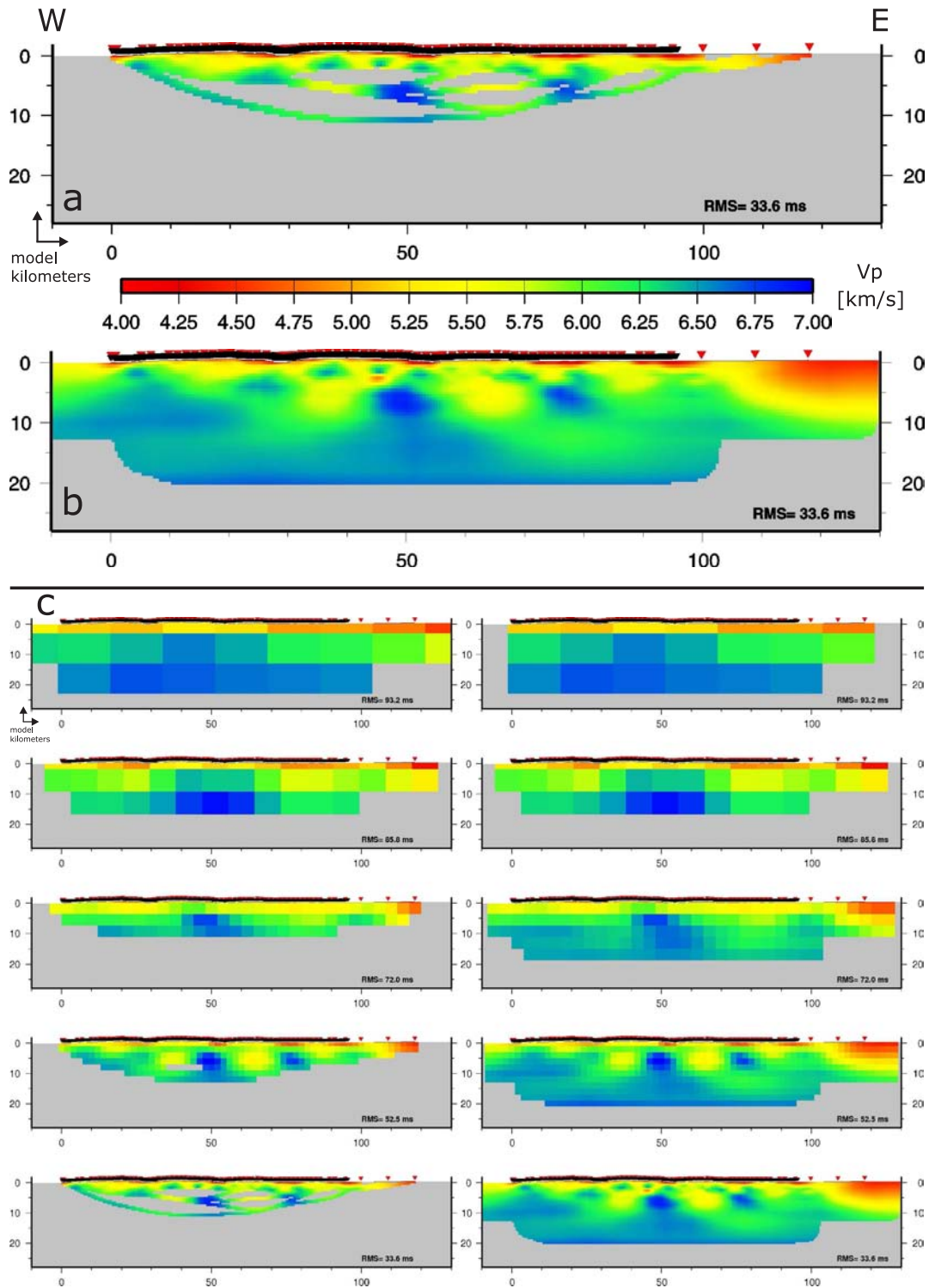
Figure 7.2.: Tomographic results of all available shots along the TIPTEQ profile (NVR/ESP/ SH). Panel a shows the final image of the five inversion cycles, panel b shows the corresponding interpolated image. Part c of the figure shows the results of each of the five inversion cycles with decreasing cellsizes (cf. table 6.3). The velocity scale is valid for all tomographic images of that figure.

Figure 7.3 shows the resulting interpolated image together with a mask limiting validity into depth constructed from the ray image in figure 7.2a.
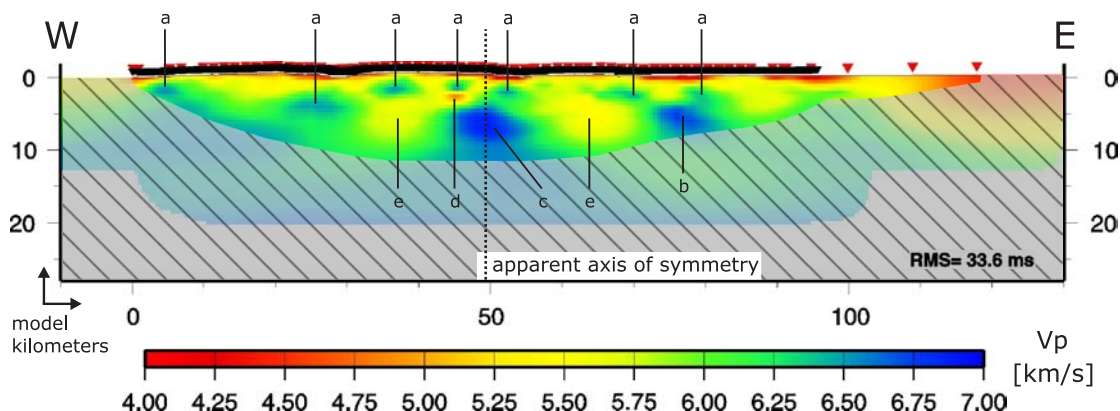
Figure 7.3.: Tomographic results of all available shots, the masked area must not be considered valid. See text for more details on the annotations.

The first thing one notices are zones of very high velocities greater than 6.4 km/s at very low depths ($<$ 10 km depth). These lens-like zones occur along the whole profile, marked with 'a' in figure 7.3. Notable are also two large high velocity structures at profile kilometer 78 and 50 between 5 and 10 km depth with velocities up to 6.95 km/s (b and c, dark blue colors). At x = 45 km and z = 3 km, a small red patch (d) shows velocities of 4.9 km/s close beside two zones of high velocities in blue. This structure may be an artefact, since it first appears in the last inversion cycle with interpolation (cf. figure 7.2c) and is not visible in the ray image without interpolation or in the results from previous cycles. The overall velocity structure also exhibits a roughly symmetrical distribution with a vertical axis of symmetry at x $\approx$ 50 km. The two great patches (e) beside the high velocity body marked 'c' also contribute to the symmetrical appearance. The most common velocities range between 5.25 - 6.25 km/s, coded in yellow to green colors, which is typical for upper crustal velocities up to depths of 10 km (Christensen and Mooney, 1995). The velocities at the surface start at 4 km/s (bright red colors) and can be attributed to sediments, especially in the eastern part of the profile in the Central Valley (cf. the three shots off the line). Less sediments are observed in the western part of the profile. The velocity structure below 2 - 3 km appears highly questionable because of the symmetrical and recurring velocity structures, paired with zones of very high velocities at those shallow depths. To validate the results and to test the robustness of the calculations, several approaches were conducted which are presented in the next sections.

Parameter studies of e.g. a changing λ (damping) or s_z (smoothness relation) which lead to the used values, were conducted to illustrate their impact on the inversion results and are presented in the appendix E.1 and E.2. Inversion calculations with only one inversion cycle were conducted with varying inversion cellsizes. The results can be found in the appendix E.3.

7.2. Ray coverage

Figure 7.4 shows a plot of the hitcounts, which are the number of rays that pass through a particular cell. The more often a cell is hit by rays, the better constraint is the determined velocity of that cell, resulting in a better final subsurface velocity model. Two arrows point to cells which belong to two ESP shots which have less than 20 and 40 hitcounts, respectively. These two shots also show the deepest subsurface penetration (greatest offsets), showing the need to check the resultant velocity information for these depths. Dark red colors follow next for the remaining ESP shots with hitcounts below 150. The ends of the profiles also contain mostly cells with hitcounts between 200 - 300. The black rectangle outlines the area with a hitcount value between 300 and 800, resulting from the regular shot spacing of 1.5 km with offsets up to 18 km, not achieved at the ends of the profiles. Above a hitcount of 800, the number of cells with more hits than 800 drops radically. The hitcount maxima with 1172 counts can be found in several cells between 42 - 52 km along profile, marked by an ellipse (dark blue colors). The average hitcount value for all sampled cells amounts to 188. Figure E.8 in the appendix shows two inversion results where only cells with more than 10 or 30 hitcounts are used to create the velocity image.
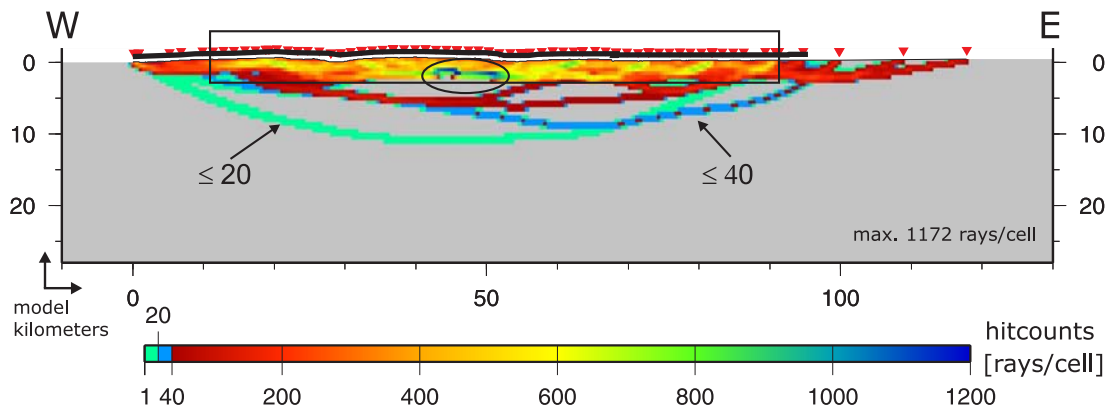
Figure 7.4.: Plot of the hitcounts for the inversion using all available shots. The black rectangle outlines the area with a hitcount value between 300 and 800, the hitcount maxima with 1172 counts is marked by an ellipse.

7.3. Checkerboard tests

A commonly used approach to test the spatial resolution power of tomographic images are 'checkerboard' tests (Ryberg et al., 2007; Van Wagoner et al., 2002). Regular, harmonic perturbations (anomalies) are superimposed over a simple starting velocity model. A forward calculation is conducted with the perturbated model to calculate synthetic travel-times using the shot and receiver geometry of the field experiment. Random noise of the same level as the pickerror uncertainty of the real data set is added to the synthetic data. Inversion of the synthetic travel-times, using the same starting model, should then recover the perturbated velocity model. By subtracting the starting model in the last step, only the recovered perturbations are shown in the final image. An assessment of the recovered anomaly pattern yields an estimate at each point in the final model of its ability to resolve features with a length scale equal to the spacing of the anomaly grid (Zelt, 1998). Where the ray coverage is insufficient to resolve the local structure (perturbations), the regularization will act to smooth the model towards lateral homogeny (Zelt and Barton, 1998). Perturbations must not only be harmonic, they could be any shape, e.g. elongated forms in a more homogeneous background can be used to assess the recovery power for dyke like features.

Figure 7.5 shows a schematic workflow example for the TIPTEQ checkerboard calculations. They start with the generation of perturbated velocity models of the standard starting velocity model shown in figure 6.6. The perturbation pattern is of a sin(x) times sin(y) functional form and the peak anomaly value is ±5 per cent of the starting velocity model. Up to seven harmonic perturbated models with different anomaly sizes were created to assess the spatial resolution of the data (cf. table E.1 in appendix E.8). The forward calculation uses the TIPTEQ shot and receiver coordinates to compute rays through the perturbated models resulting in synthetic travel-times. A random number equal to or less than the pickerror (here 30 ms) was added to the travel-times. The random number is calculated using the 'rand' and 'srand' capabilities of AWK starting with a seeding number derived from the nanoseconds of the system time. Random generators use al-
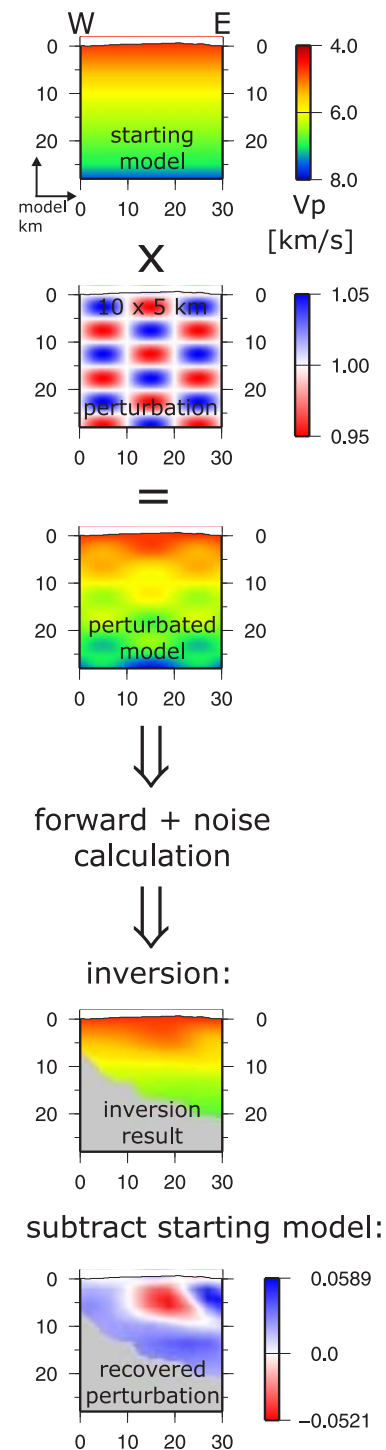
Figure 7.5.: Checkerboard calculation workflow.

gorithms to create pseudo-random numbers that are repeatable, unless the numbers are seeded with an unique value. The inversion is conducted next, using the standard starting model and the synthetic picks. The resultant velocity distribution shows visibly only minor variations to the starting model (cf. inversion result in figure 7.5 at x = 25 km and z = 5 km), so the starting model is subtracted from the result. The final checkerboard image shows then the recovered perturbation, colored with a polar color palette table. The script to generate the perturbated models can be found in the folder `/tipteq/TOMO/checker/MKCHK`, and `/tipteq/TOMO/checker/CHK1` contains the three scripts for the forward, noise and inversion calculation (forward, add_noise, xxinv).

Figure 7.6 shows two results of the checkerboard calculation with anomaly sizes of 10 x 5 km and 5 x 5.25 km. Anomalies deeper than 5 km can not be recovered in both images for these two anomaly sizes. Great irregular positive (blue) and negative (red) patches develop in these areas of low or no ray coverage (cf. figure 7.4), because the smoothing regularization of the tomographic method produces a smooth, non-alternating model there (Zelt, 1998). In the upper panel (a) of figure 7.6, between z = 0 and 5 kilometers, the individual anomalies are not delimited clearly and tend to smear with each other. This happens in areas of limited resolution power (ray coverage) for the given size of the structure to be resolved. In panel (b) of figure 7.6 the perturbation pattern can not be recovered well. The anomalies smear to linear structures, the peaks of the individual anomalies are difficult to point out. The areas in both panels where recovered structures or smeared anomalies can be observed coincide with the proposed mask in figure 7.3. The checkerboard tests show that smaller structures than the size of 10 x 5 km can not be resolved deeper than 5 km depth. The consequence would be to neglect the rays from the ESP shots using the great offsets, in order not to falsify any interpretation.
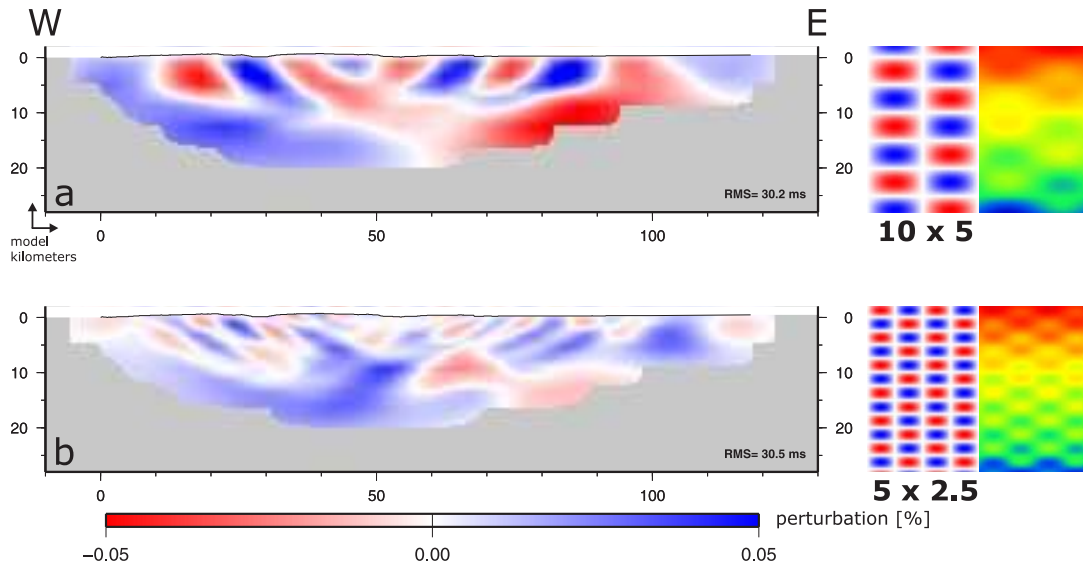
Figure 7.6.: Two checkerboard examples with anomalies of 10 x 5 km (a) and 5 x 5.25 km (b) in size, the anomaly pattern and perturbated velocity model are shown on the right. The elevation along profile is represented by the thin black line.

Smaller anomaly patterns can not be resolved at all, the images just show irregularly smeared patches of red and blue (see appendix E.12). Greater anomalies than 5 x 10 km in size can be recovered in spite of the low ray coverage in the deeper parts of the model. There, the resolution seems to be sufficient to identify rough velocity trends (see appendix E.12).

The shotpoint and receiver interval of only 1.5 and 0.1 km, respectively, should produce a better resolution than 10 x 5 km. For ideal data (all travel-times picked correctly on all possible traces and a minor pickerror) a lateral resolution of no worse than the shot spacing should be possible throughout most of the sampled area (Zelt, 1998). Most of the central part of the TIPTEQ profile shows a very good ray coverage in the first few kilometers together with a high hitcount value ($\approx$ 400-700, cf. figure 7.4), so a good recovery power and resolution should be anticipated at least there. One measure to increase the resolution could be to decrease the conservative pickerror of 30 ms to a reasonable lower one, to force the inversion to a better fit.

7.4. Robustness of the inversion

The robustness of the results can be assessed by reducing the number of travel-times used for the inversion calculations. One can use a random operator to select the travel-times, or use every xth line of the travel-time file, like it was done here. Figure 7.7 shows two example results using every second and fifth line. More test runs with also drastically reduced travel-times can be found in the appendix E.7.
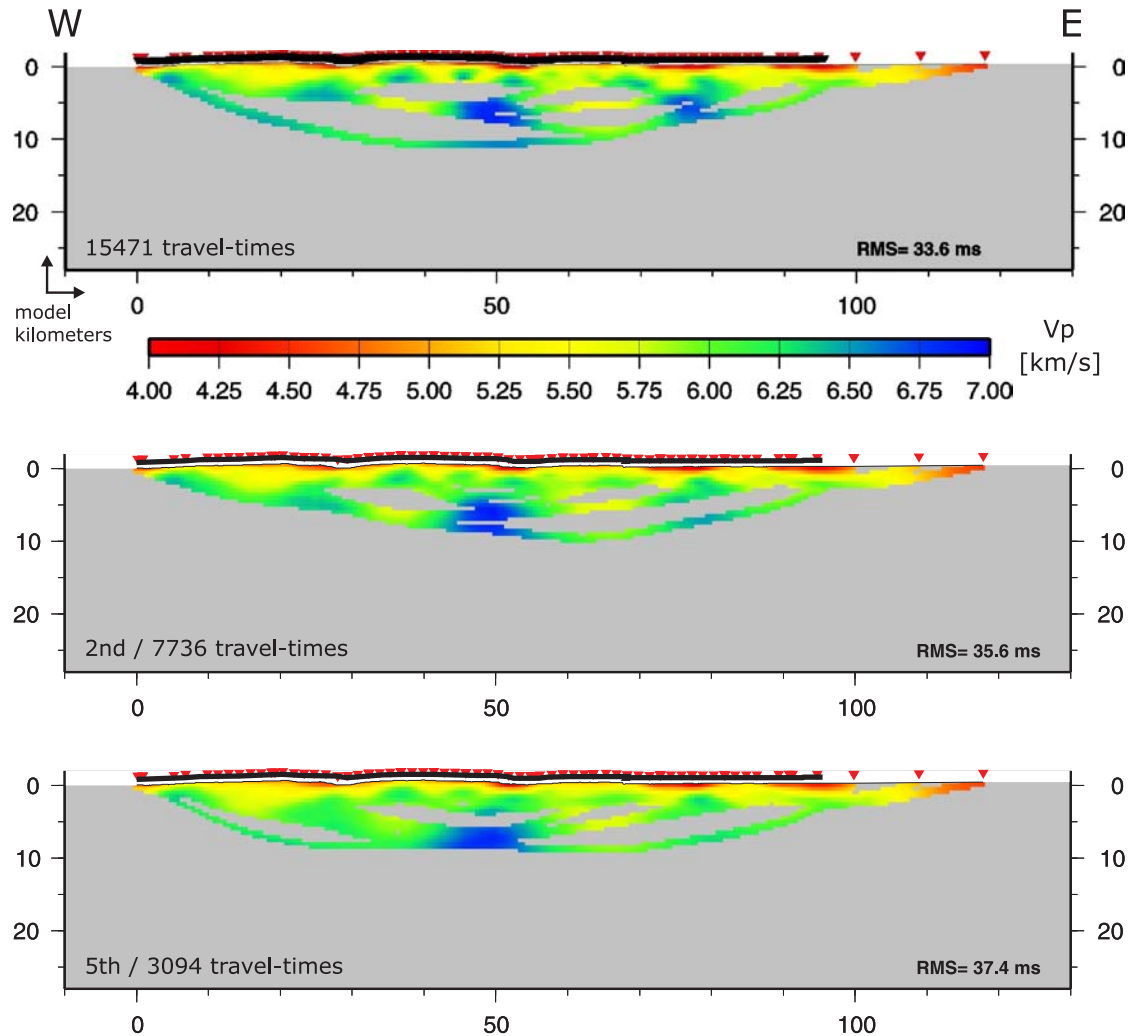
Figure 7.7.: Inversions with a reduced number of travel-times using every second (middle) and fifth line (lower) of the travel-time file in comparison to all travel-times (upper panel).

The images with the reduced travel-times reproduce the general features of the inversion with all travel-times. Detail of the fine structures is lost for each travel-time reduction. The reduction acts like a low-pass filter, where the upper cut-off frequency is reduced for each reduction of the travel-times. The high velocity zone at x = 50 km is present in all plots with reduced traveltimes (see also E.7). This may lead to the assumption that it is a real feature.

7.5. Variations in the number and positions of shotpoints

The reduction of shotpoints and inversions with parts of the shotpoints produce a rather non-satisfying result in order to assess the validity of the deeper parts of the model. This is because of the ESP shot configuration, which uses increasing offsets only towards the ends of the profile. Inversion results of shots from the middle part show therefore only a limited depth penetration although, one high velocity structure is just situated in the middle of the profile.

Each of the 3 panels in figure 7.8 shows an inversion result using approximately only one third of the shots along the profile (west, middle, east) defined by the increasing FFID number from east towards west. By that, some ESP shots from other thirds of the profile are interspersed in between. The corresponding receivers are also distributed along the whole profile, because ESP shots in the far west were fired when the receiver line was at the profile beginning in the east (and vice versa) to achieve the long offsets.

All three inversions reproduce the shallow part of the model in their section, if compared with figure 7.3. The western shots, e.g., reproduce the structures for the first few kilometers up to x = 50 kilometer quite reliably. One ESP shot at x = 25 km illuminates the deeper part of the model and shows part of the high velocity structure at x = 50 km. The 'middle' part shows no deep penetration, whereas the eastern shots show a deep ray coverage resulting from several ESP shots. These ray paths show also high velocity structures, but neither in the same place nor of the same magnitude, e.g., at the western high velocity structure at x = 20 km.
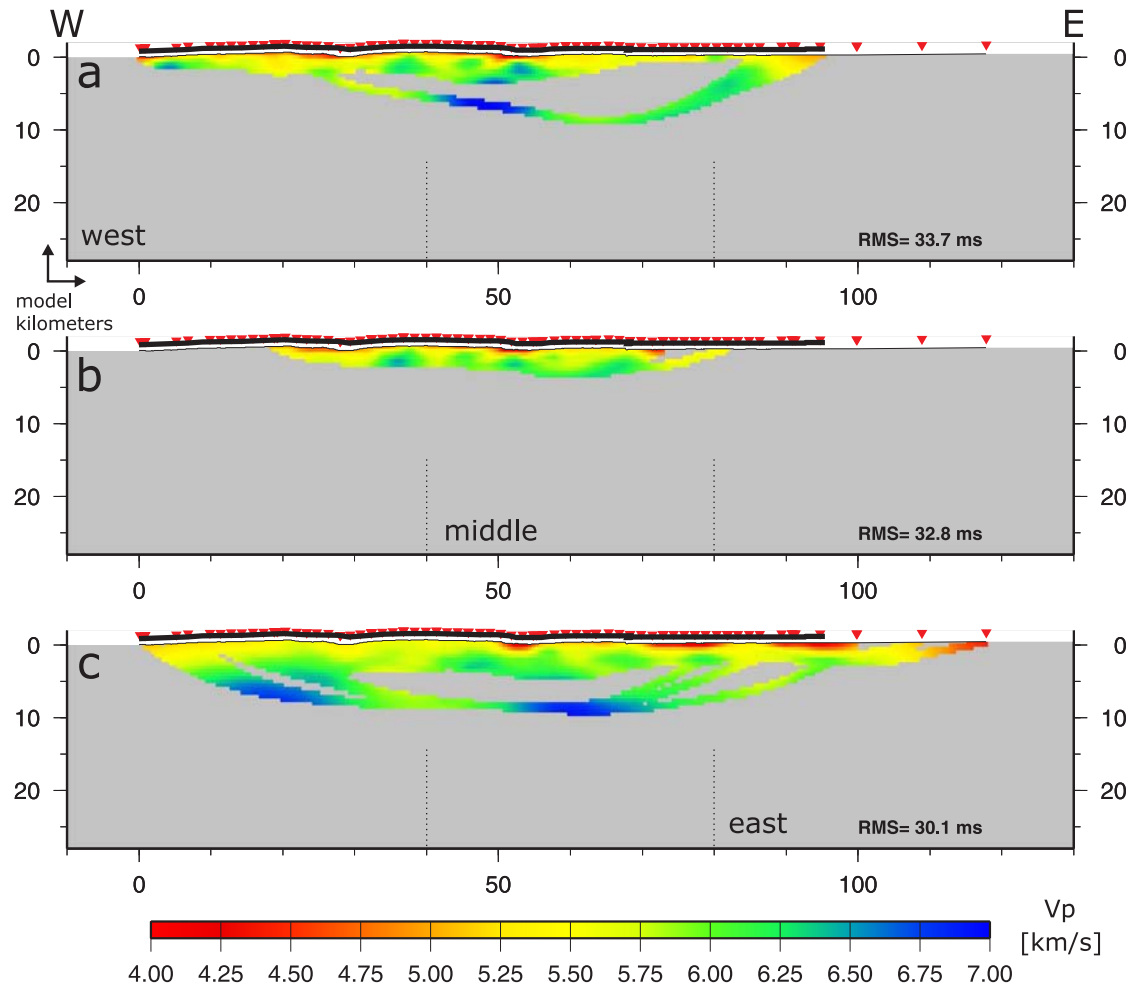
Figure 7.8.: Inversion results using a reduced number of shotpoints. In panel a, only the western third of shots is used (including ESP shots along the whole profile), panel b presents the result using only the middle part of the shots, c shows the resultant inversion image using only the eastern third of shotpoints.

7.6. Variations in the starting model velocities

The inversion should be independent from a reasonably chosen starting model. This was e.g. shown by Ryberg et al. (2007) using starting models with $\pm 10\%$ of velocity variations.

Figure 7.9 shows results from inversions with different starting velocity models as listed in table 7.1. The changes are ± 10 % of the normally used velocity model (cf. section 6.5). A -10 % starting velocity model with a low velocity zone (LVZ) at 25 km depth was also tested.

z [km]	Vp$_{standard}$ [km/s]	Vp - 10% [km/s]	Vp + 10% [km/s]	LVZ [km/s]
-2	4.5	4.05	4.95	4.05
10	6.0	5.40	6.60	5.40
25	7.0	6.30	7.70	3.30
30	8.0	7.20	8.80	7.20

Table 7.1.: Variations of 1-D velocity input models used for inversion shown in figure 7.9. All velocities are in km/s.

The raypaths from the ESP shots travel through different depths, but sample the same structures along the profile. The images show great similarities, especially for the first few kilometers. The inversion result with the low velocity zone also fits to the other plots. The low velocity zone is only visible in the result from the first inversion cycle (see insets in figure 7.9). The following inversion cycles (2 - 5) lack this low velocity layer.

This strongly demonstrates that the independence of the used starting velocity model is also valid for the TIPTEQ data set. Especially the improvement of FAST by Ryberg et al. (2007) to conduct five inversion cycles in a row using the former resulting velocity model as the new input model contributes to this independence. The effect of unreasonable starting velocity models, e.g. using a drastic low velocity layer is already removed in the second inversion cycle. Confer also figure E.7 in the appendix showing more examples using varying starting models.

From the point of the velocity variation tests, the inversion result is robust and the observed structures may therefore be reliable, also in the deeper parts of the model. The RMS value is also equally low for the different starting velocity models.
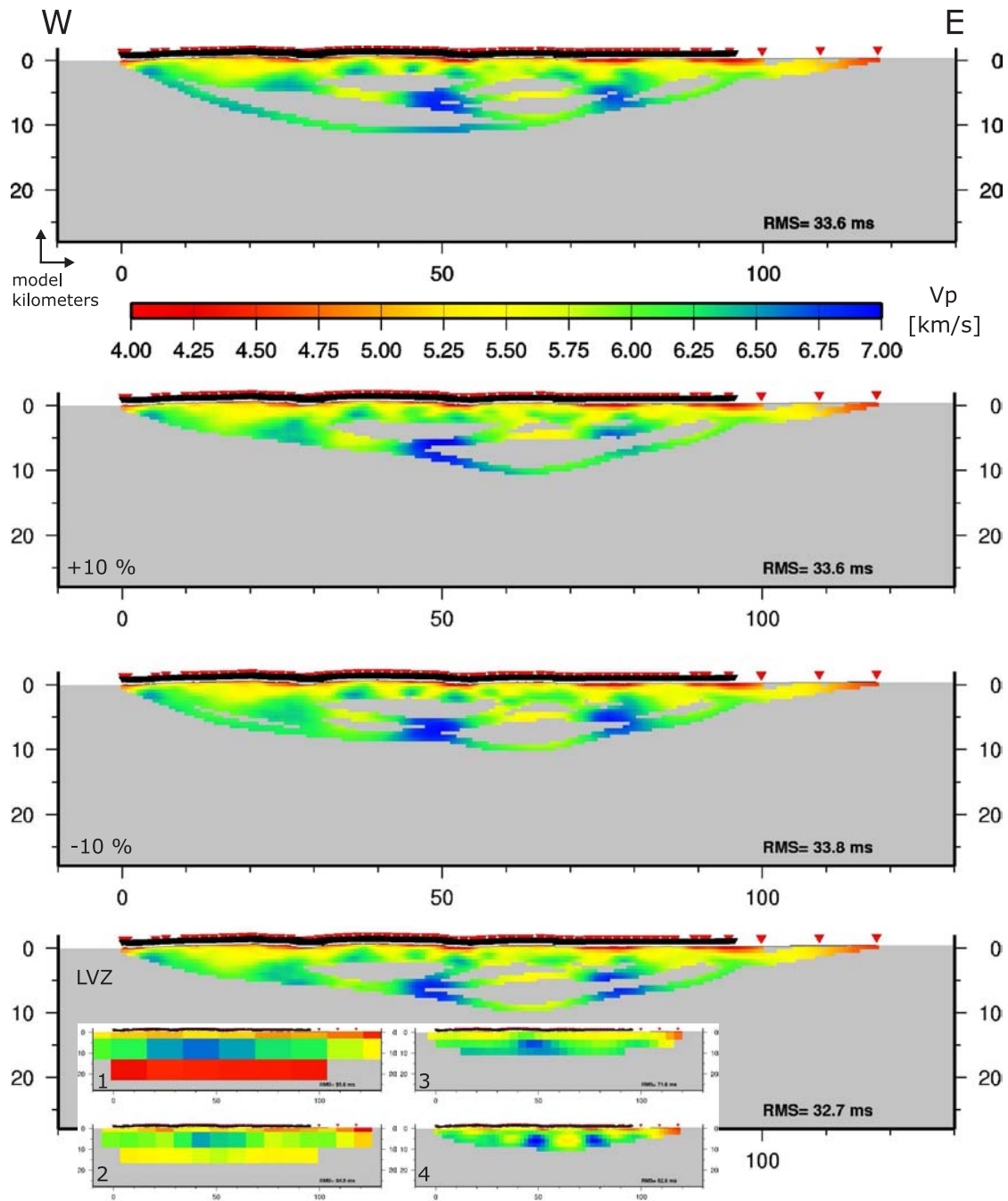
Figure 7.9.: Inversion results calculated from different 1–D starting velocity models as shown in table 7.1. The insets in the lowermost panel show the results of the first four inversion cycles. The LVZ is only visible in the inversion result of the first cycle (lowermost red layer).

7.7. Incorporation of first-breaks recorded on seismology stations

The seismological network of TIPTEQ (Rietbrock et al., 2005; Haberland et al., 2006; Haberland et al., 2008) used a denser spacing in its central part, the vicinity of the TIPTEQ reflection seismic line (see figure 7.10). At the end of the controlled source experiment in February 2005, part of the stations used there were used to densify the central part of the seismological network even more (yellow triangles). The red squares show seismic stations which were active during the seismic profiling.
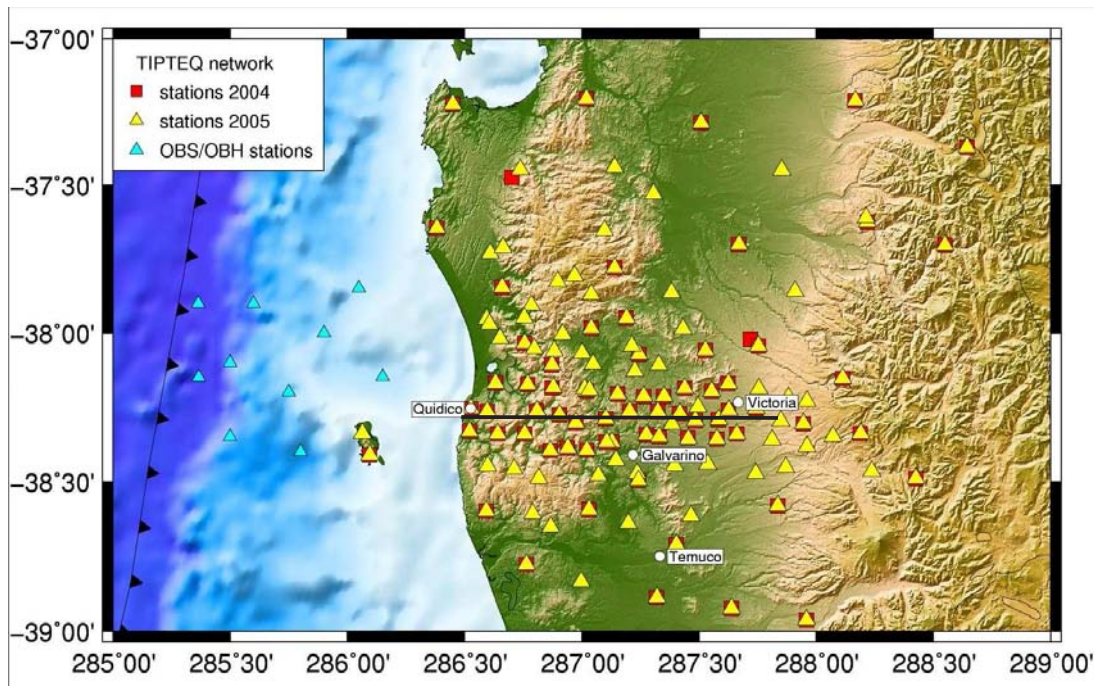
Figure 7.10.: The northern seismological network of TIPTEQ. The black line shows the extent of the TIPTEQ reflection seismic line (modified after Rietbrock et al. (2005)).

In some of the recordings of seismology stations close to the seismic reflection profile, first-breaks from the explosive shots could be identified. These travel-times were kindly provided by Christian Haberland (University of Potsdam/GFZ). It was tried then to improve or confirm the inversion image in the deeper parts of the model by additional ray paths from the additional travel-times. Since the seismological stations in the Central Valley did also record signals when the receiver spread was e.g. at the cost, they do provide greater travel-times or longer offsets and therefore, a deeper penetration, than the 'standard' offsets of 18 km of the active experiment.

Several criteria must be fulfilled by the seismological stations, for that the first-breaks can be included into the tomographic inversions. First, the stations which recorded shots must not lie more than 10 kilometers off the profile in a north-south direction. The same reference point as

for the tomographic inversions was used, which is the last receiver station (955) at the Pacific coast. This reference point slightly favors relevant northeastern seismology stations, because the profile is slightly tilted of about 2°. Second, the distance of the recording station to the shot must be at least twice the 'standard' offset of 18 kilometers ($>$ 36 km) to decrease the geometrical error introduced from stations far from the profile. This allows that the well covered upper model kilometers are not biased by errors, and favors deeper ray penetration. Figure 7.11 shows the used and discarded seismology stations. The scripts to prepare the seismology data can be found in `/tipteq/TOMO/tiptomoprep-incl.seismologie/shotsseismologie`. The standard model size (cf. section 6.5) was doubled in x - direction for the inversions. The number of inversion cells in x direction was also doubled respectively, to achieve the same cell dimensions as in the inversions before. The corresponding files and results can be found in the folders `/tipteq/TOMO/tipteq_1-groesser-SEISMOLOGIE*`.

Figure 7.12a shows the picked and seismology travel-times vs. profile kilometer. We can use 208 additional travel-times that fit our criteria out of a total of 1425 travel-times from stations that recorded the explosive shots. 924 travel-times come from stations that lie within the 10 km limit north and south of the profile. The restricted travel-times start at $\approx$ 6 seconds. The easternmost station that recorded shot signals is station D403 at $\approx$ x = 150 km. This does not necessarily create usable offsets in the same range. Figure 7.12b shows the travel-times vs. all occurring offsets. The maximum offsets from the seismology stations are in the same range like the maximum offsets created by the ESP shots. Deviations from the trend of the travel-time curve partly originate from geometrical errors caused by the crossline offset of the seismology stations. Another cause for delayed travel-times are certainly $\approx$ 6 recording stations that lie in the sediment rich Central Valley (cf. travel-times in figure 7.12a at x $>$ 90 km).
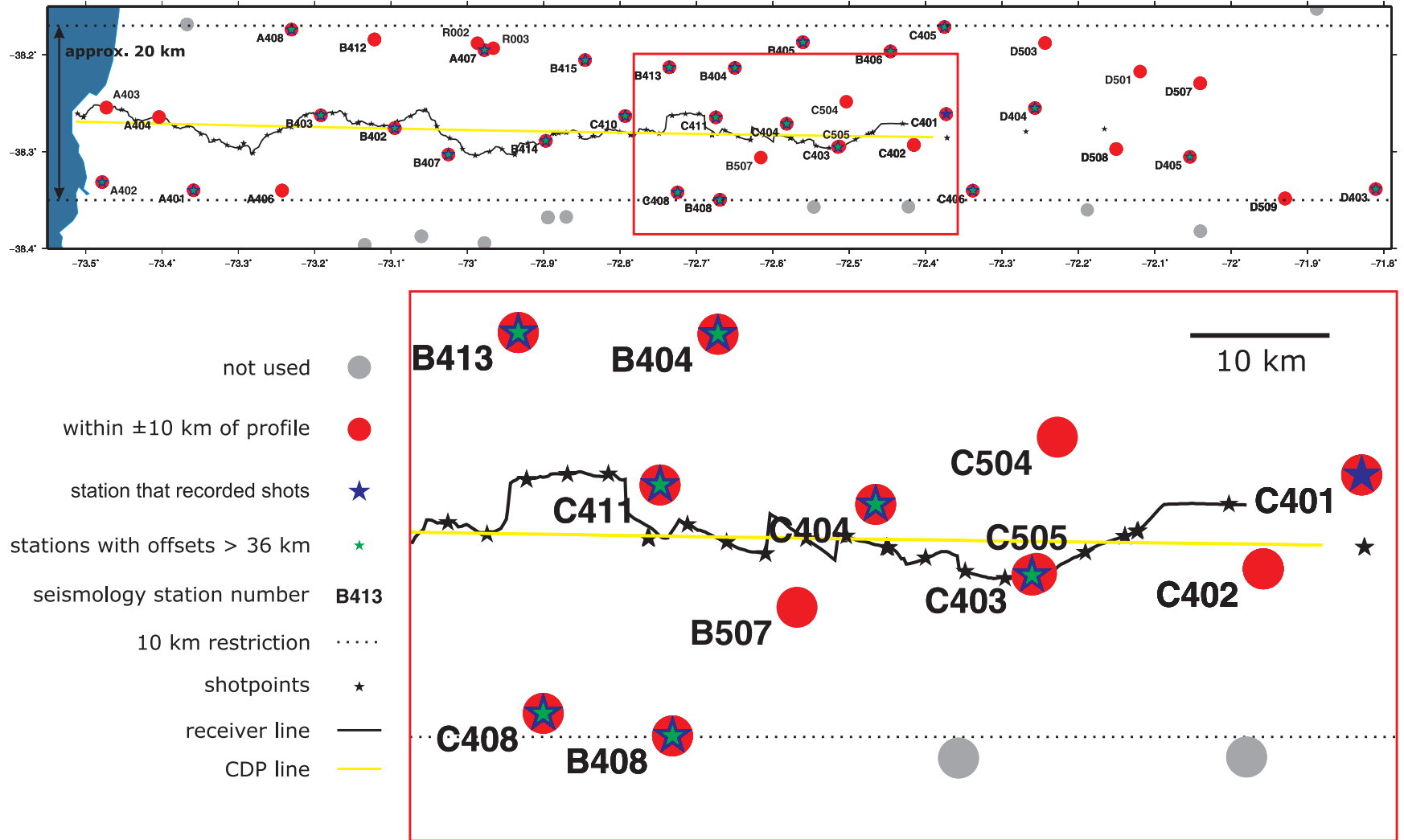
Figure 7.11.: Distribution of the used seismology stations along the TIPTEQ profile with labels for each exclusion criteria.
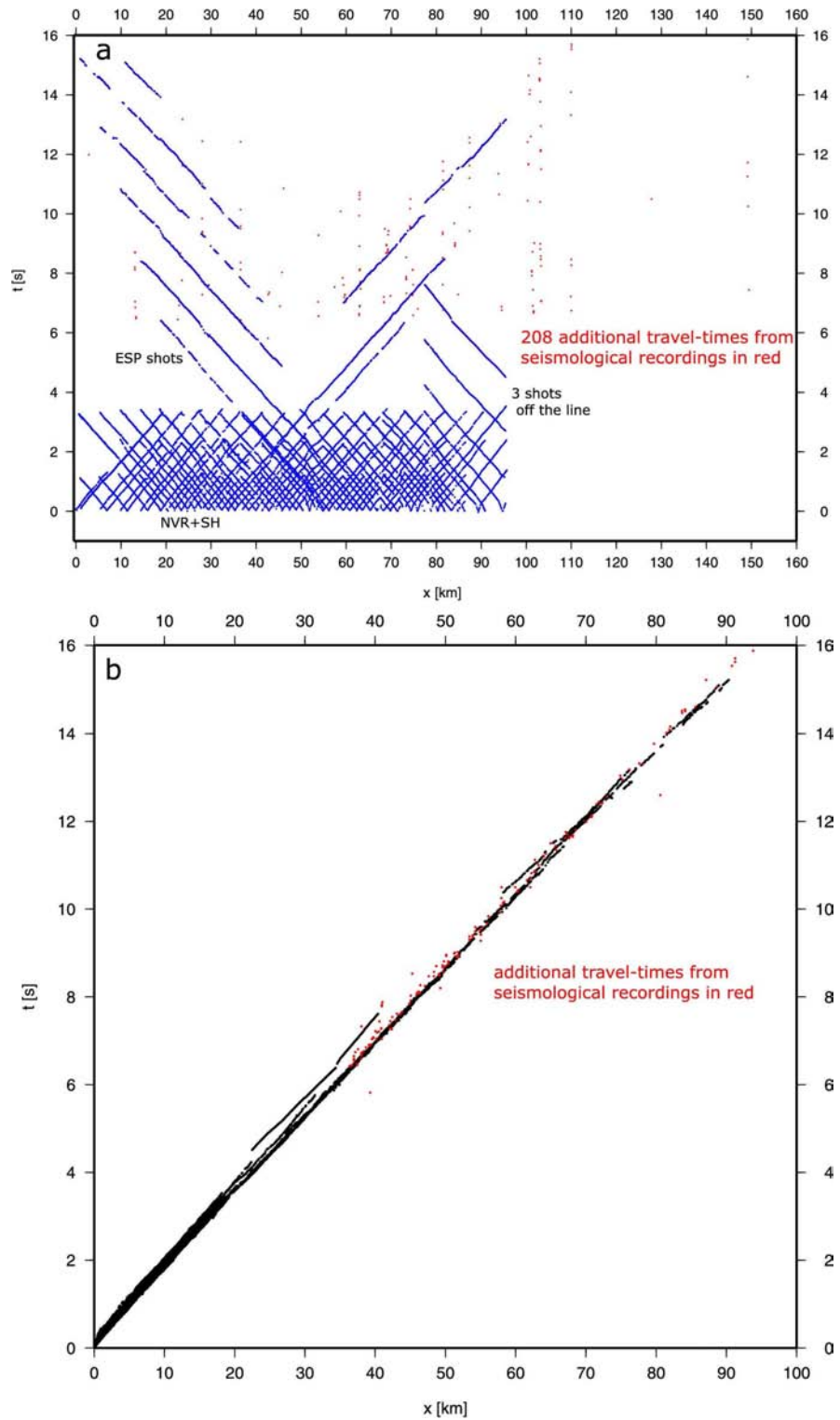
Figure 7.12.: All picked travel-times vs. profile kilometer (a) and travel-times vs. occurring offsets (b), including additional seismology picks (cf. figure 6.3 and 6.4). See text for details.

The result of the inversion with additional travel-times from seismological stations is shown in figure 7.13. The desired effect to improve and constrain the deeper layers of the model is missing. The observed suspicious structures and high velocity zones seem to localize even more. Between x = 50 - 100 km the deeper structures appear repetitive. Unfortunately, no new information is gathered. The first few kilometers show resemblances to the other presented figures, e.g. figure 7.3. The main problem of the inversion with seismological travel-times seems to be the errors emerging from the geometry, because we calculate in two dimesnions but use a 3–D source/receiver array. This calculation emphasizes the need to place the receivers on a straight line very close to the shotpoints.
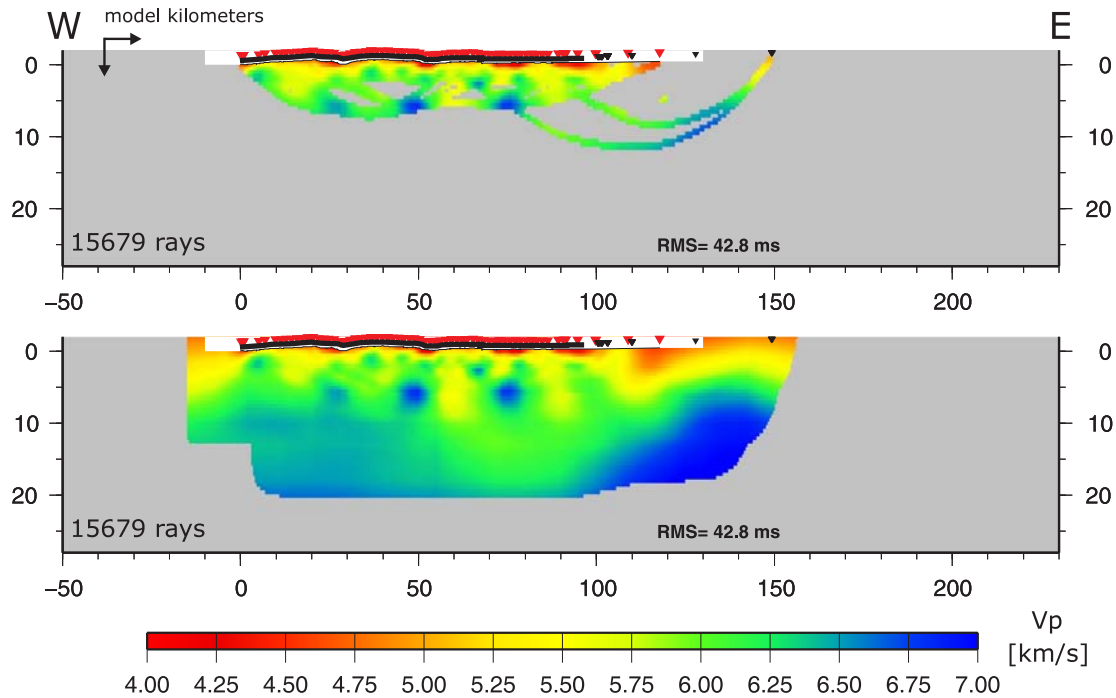
Figure 7.13.: Inversion result including seismological travel-times (ray and interpolated image).

The variation in results by using additional seismology first-break picks is also shown by four inversion presented in figure E.13 in the appendix. Inversion results with and without the minimum offset restriction of 36 km are shown, resulting in a total of 924 travel-times. In addition, the seismological travel-times are inverted alone. The additional picks provide more ray paths and therefore a better coverage, but as mentioned above, do not clarify the suspicious structures. A best RMS value of 42.8 ms is reached, when the minimum offsets are restricted. No offset restrictions (more rays) do not improve the RMS value (62.1 ms), proving the offset limitation to be neccesary.

7.8. Variation of the inversion cellsizes

The diversity of the tomographic images in a depth greater than 3 km lead to an investigation with deviant inversion cellsizes to the standard ones listed in table 6.3. A sensitivity towards changing cellsizes was noticed e.g. in the results of the inversions using only one inversion cycle or in results using the additional seismology picks, where several different inversion cellsizes were tested with the double sized model (cf. section 7.7). More than 30 additional inversions were conducted to find a connection between cellsizes and resultant image or the relation of the quotient of the number of cells in x and z direction and the inversion result. The nature of that quotient (integer or fraction number) or the relation of the cell dimensions was also investigated. The interpolated inversion images are shown for a better visualization of the variations in velocity structure.

Figure 7.14 shows six inversion results where the number of cells in z–direction is changed for the fourth inversion cycle for each subfigure (numbers in red). The number of cells in x–direction is kept fixed. The most prominent changing feature is the high velocity zone in the central part of the models. With increasing cell numbers in the fourth cycle, the high velocity structure vanishes first and then shows up again. These dramatic changes happen by increasing the cellnumbers by just one. Then, the high velocity anomaly slightly fades out.

Small changes in the number of cells result in great changes if models are compared with each other. This effect is independent of the inversion cycle number. Figure 7.15a shows a second example, where three inversion differ slightly (numbers in red) from a reference model, the cellnumbers in x-direction are kept fixed again. Part b of figure 7.15 shows two inversion results, the upper one with a rather low number of cells, whereas in the lower one the cellnumbers increase rapidly. High cellnumbers cause narrow, smooth rays as seen in figure E.5, and therefore result in a smooth interpolated image. A low number of cells (large cells) preserves high or low velocity zones much better, and might be more realistic, because small cells tend to be under-determined. This is not inconsistent with the observation that the inversion is very much independent from the chosen starting model, or the velocity model of former inversion cycles (cf. section 7.6). This observation is valid for each inversion run, only the comparison between inversions with a different sequence of cellnumbers shows variations.
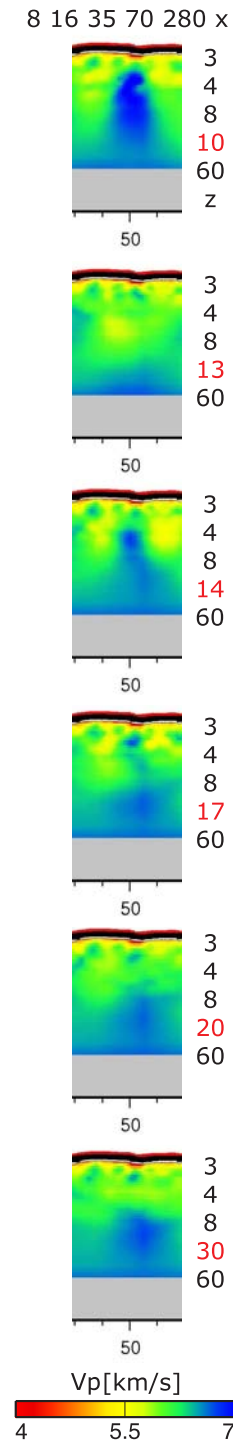
Figure 7.14.: Variation of the inversion cellsizes, part I.
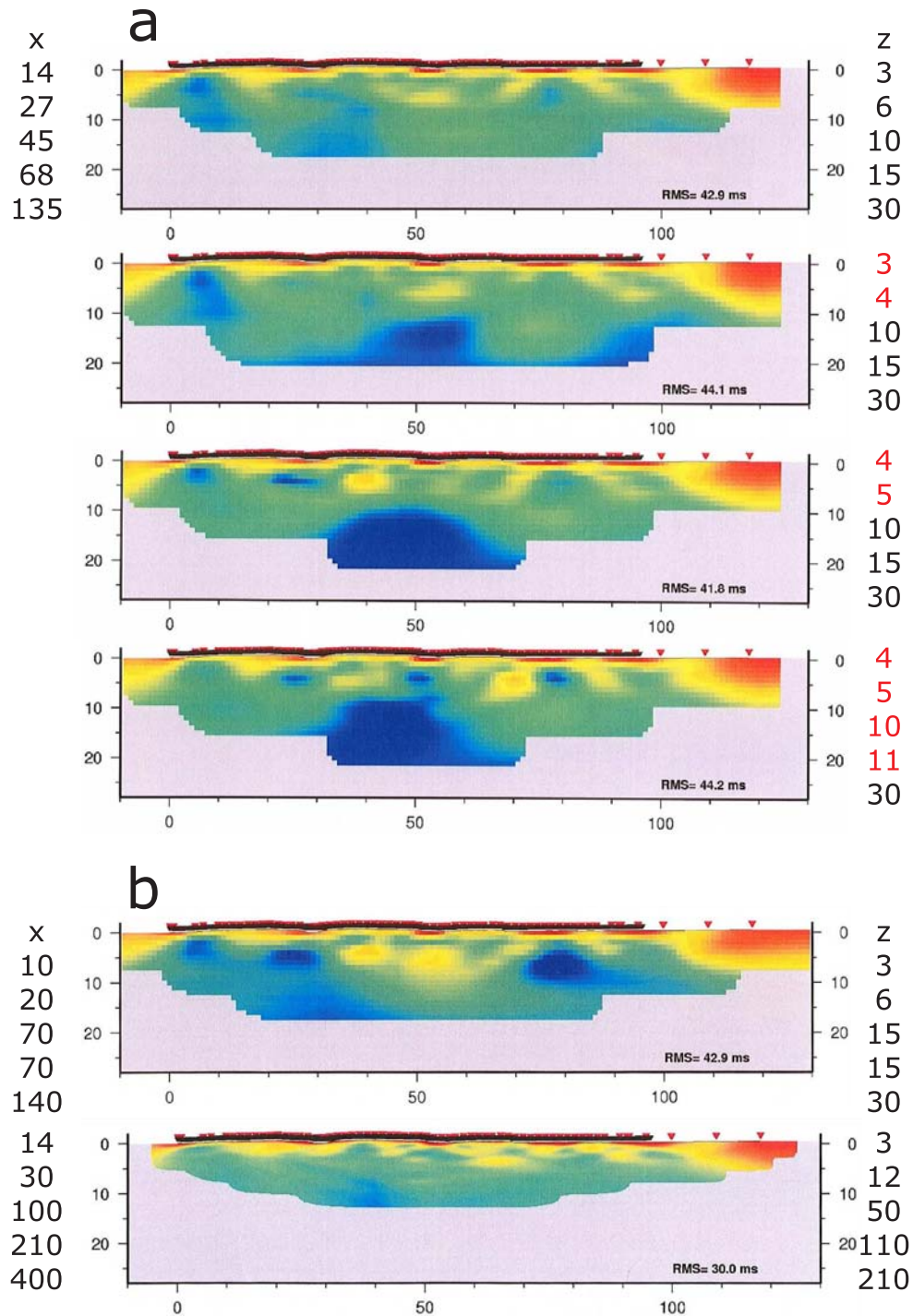
Figure 7.15.: Variation of the inversion cellsizes, part II. Panel a of the figure compares small changes in the number off cells in z–direction. The cellnumbers in x–direction are kept fixed. Part b shows the effect of rapidly increasing cellnumbers.

7.9. Limiting the inversion input

The tests and the incorporation of additional travel-time information presented in the last sections demonstrate that the deeper layers of the velocity model must not be considered valid. Tests like the variation of the starting velocities or in the number of picks showed the power of the used method and robustness of the resultant images, but it is not possible to constrain or gather more information in the areas of low ray coverage with the applied approaches. Near-surface structures ($< 3km$) show only very little deviations in each of the previous shown inversions, only in their resolution (blocky appearance) due to the used cellsizes. Consequently, the next step is to run inversions without the travel-times from the ESP shots. It is important to calculate the inversions without the information of the ESP shots, and not only to limit the velocity grid to a certain depth, so that the result is not biased. Figure 7.16 shows an inversion using only the 15 ESP shots (2851 rays, marked in yellow) with the standard values (cf. section 6.5). Some ESP shotpoints were used several times, confer figure 2.3 for shot and receiver layout. No high velocity structure in the central part and a high RMS error also justify the omittance of the ESP shots.
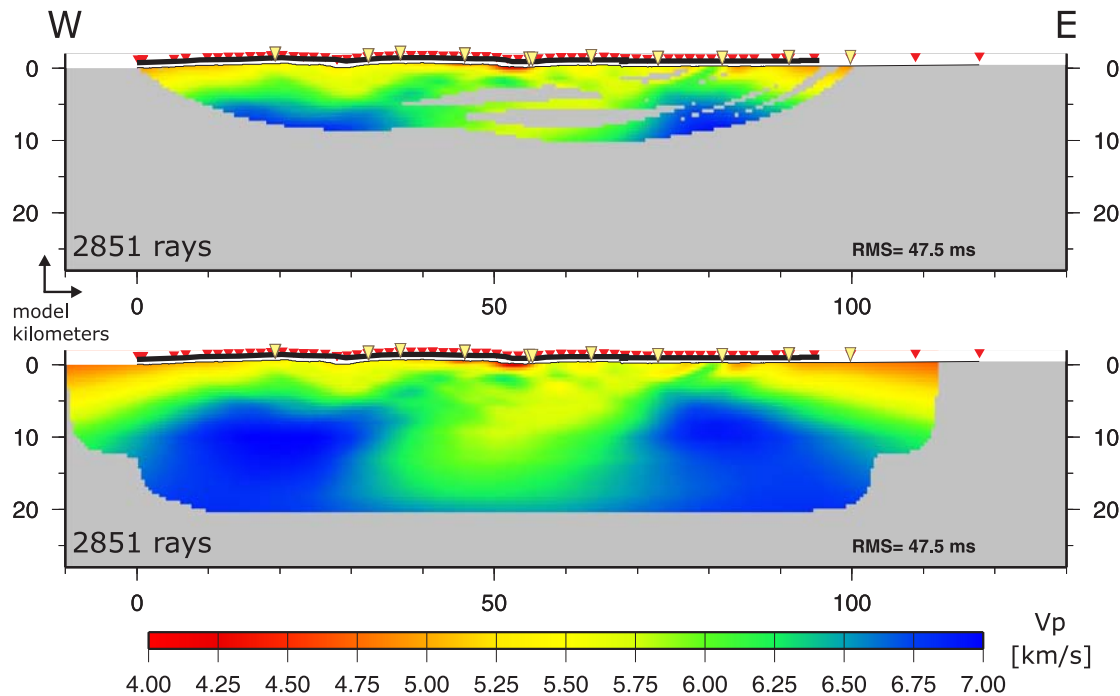
Figure 7.16.: Inversion result using only ESP shots, shotpoints are marked with yellow triangles (ray and interpolated image).

The appendix contains further images and investigations related to the inversion of all usable shots. Comparison plots of the picked and synthetically calculated travel-times are shown as well as a comparison of the synthetic travel-times with the recorded data. Studies to determine the minimum pickerror, or plots of the RMS values of each shot or receiver along profile, start page 206 in section E.10.

8. First-break tomography – NVR and SH shots only

Structures and velocities below a depth of $\approx$ 3 kilometers can not be considered valid in the tomographic inversions shown in chapter 7. By using only the NVR and SH shots, the maximal offset is 18 km, resulting in a depth penetration of $\approx$ 2 kilometer from topography. The cellsizes, as well as the pickerror, must be reduced to resolve finer structures in these depths, but this may again produce problems in terms of ray coverage and resolution which must be tested. Smaller cells account for fewer rays passing through the individual cells.

8.1. Model setup with NVR and SH shots only

The model space was limited in z direction to 7 km, with a maximal depth of 5 km below sea level. The extend in x direction is kept (140 km) to allow the incorporation of the three NVR shots east off the line. The origin is again receiver 955 at the Pacific coast, the model starts 10 km west of the coast, at -2 km above sealevel. The same simple 1-D Vp velocity/depth function based on the SPOC wide-angle model is used as before as starting model, resulting in a velocity of $\approx$ 5.4 km/s in 5 kilometer depth (cf. figure 8.1). A vertical exaggeration of $\approx$ 4.3 is used in this and the following images.
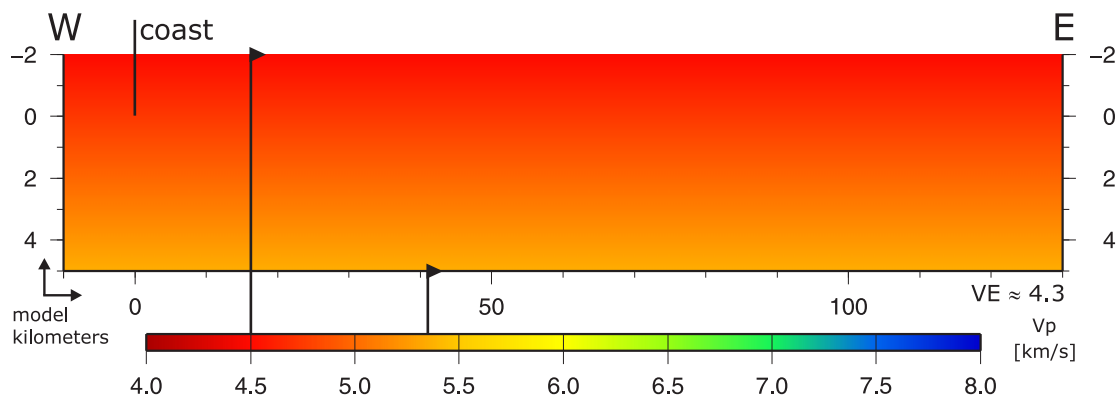
Figure 8.1.: Model setup and starting velocity model used for the inversion of the NVR + SH shots only. The velocities range from 4.5 - 5.375 km/s.

73 NVR, 13 SH shots, which are basically additional NVR shots, and the three shots off the line result in 16020 possible travel-times (89 shots times 180 receivers). Approximately 76 % (12124) could be used in the inversion calculations. A pickerror of 0.01 s was chosen after test runs. The cell size of the subsurface blocks for the forward and inverse calculation are listed in the following tables (see table 8.1 and 8.2 and files 'for.header' and 'i.dat' in the project directory /tipteq/TOMO/tipteq_1-NVR-smallercells+pickerror0.01). λ (damping) was chosen to be 1000, 'sz' (smoothness relation) was set to 0.25 which proved to be the optimal values in the parameter studies conducted in chapter 7.

cell size [km]	no. of cells in x	no. of cells in z
0.05	2800	140

Table 8.1.: Cell size and number of cells for the forward calculation using only NVR and SH shots.

cycle	no. of cells in x	no. of cells in z	cell size in x [km]	cell size in z [km]
1	28	14	5	0.5
2	56	28	2.5	0.25
3	140	56	1	0.125
4	280	70	0.5	0.1
5	560	140	0.25	0.05

Table 8.2.: Cell sizes and number of cells for the inverse calculation using only NVR and SH shots.

8.2. Inversion result of all NVR and SH shots

Figure 8.2a shows the ray and interpolated inversion image using only the NVR and SH shots. Part b of the figure shows the same inversion including the three shots off the line in the east.

The two inversions (a and b) look similar up to an extremely high degree. We observe a complex velocity pattern along the whole profile. Depths up to 2 km are reached, which is in agreement with results of similar experiment setups (cf. Bräuer et al., 2007). At x = 40 - 50 km in a depth of 1.5 - 2 km we notice zones of high velocities of up to 7 km/s in the lowermost part of the velocity images. These zones differ in appearance and show rather unreasonable high velocities for such low depths. It must be investigated if these zones are in areas of low ray coverage or if structures from that area can be recovered using checkerboard tests. Several linear features are visible, e.g. at x = 50 or 20 km in a depth of $\approx$ 0.5 - 1 km. It must also be verified that these structures are not related to ray paths or zones of very high or low ray coverage. Figure F.1 in appendix F shows an example of all 5 inversion cycles.
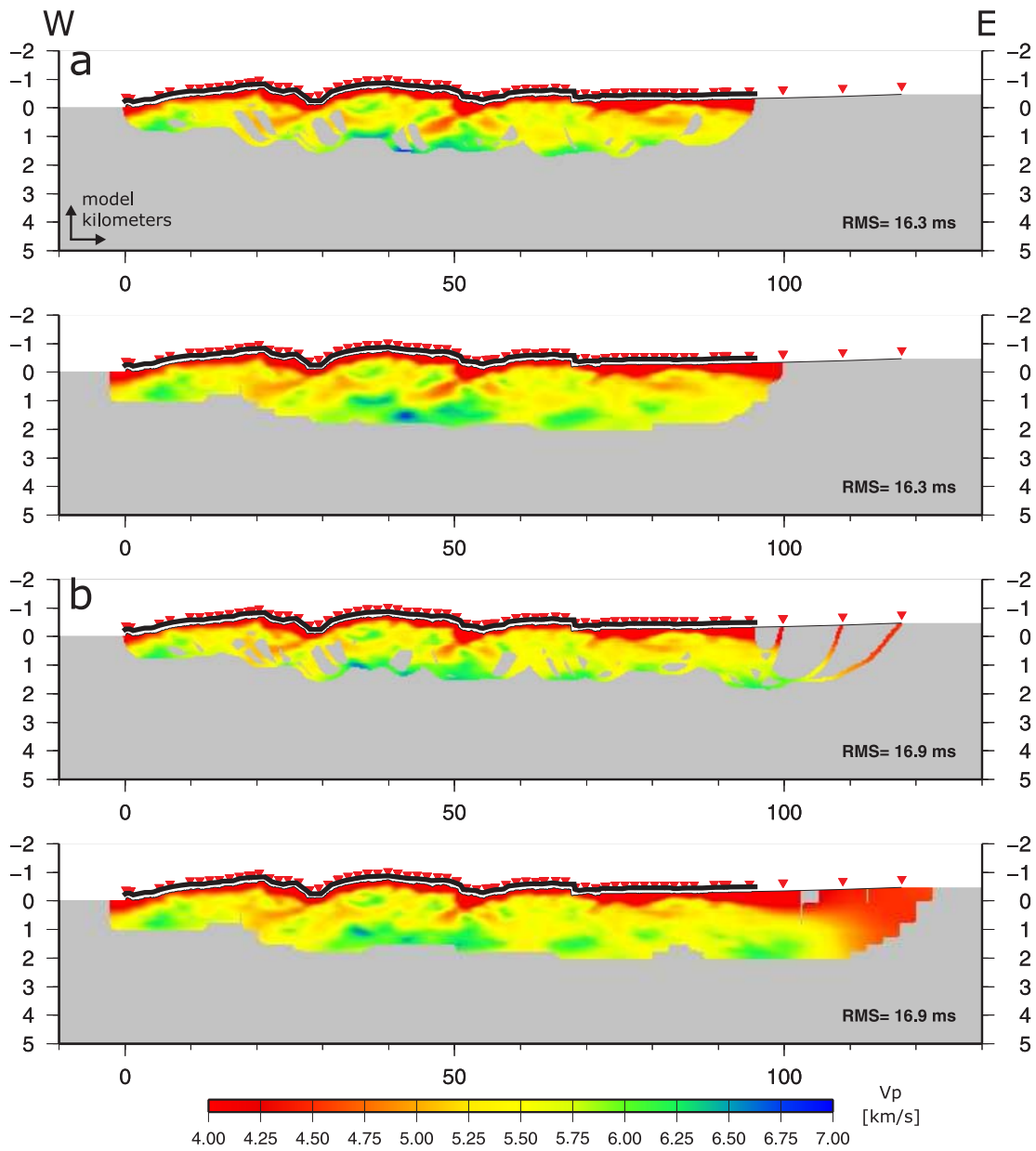
Figure 8.2.: The two uppermost pictures show the ray and interpolated image of the tomographic results of NVR and SH shots (a). Part b shows the same inversion including the three shots off the line in the east. See text for more details.

The seismic velocities range from ≈ 2.5 km/s at the surface to a maximum of 6.74 km/s, the shown color scale, also in the following images, starts at 4 km/s, to be comparable to the pictures shown in the chapter 7 before. Velocities below 4 km/s are found in the sediments of the Central Valley, the sediment filled valleys along the profile, and close to the surface and are also shown in the darkest red. To start this color scale with lower velocities would broaden the range of velocities used for similar shades of one color, resulting in an image lacking contrast which is needed for comparisons during the validation process. Most velocities range between yellow and green, 5.2 - 6.3 km/s, respectively, and would otherwise be shown in one color. The final image used for the interpretation (cf. figure 8.7) and the plots without vertical exaggeration (e.g. figure F.13) use a different color scale to take account of these low sediment velocities.

The depth penetration of the velocity model is too shallow to compare the velocity image with the reflection seismic image shown in figure 5.3 on page 51. The top-mute hinders a direct comparison and without it, the uppermost part of the seismic image is obscured by unwanted noise such as the airblast and the high amplitudes of the first-breaks. The complex velocity pattern may be decoded and interpreted using a local geological map, which will be presented in chapter 10.

8.3. Ray coverage

The number of rays passing through the inversion cells are shown in figure 8.3. Cells below a depth of ≈ 0.5 km show a lower hitcount number in general. Very low hitcount numbers are reached at the ends of the profile or at several parts along the profile, e.g. at x = 40 km. White cells show a hitcount number above 180 rays per cell.
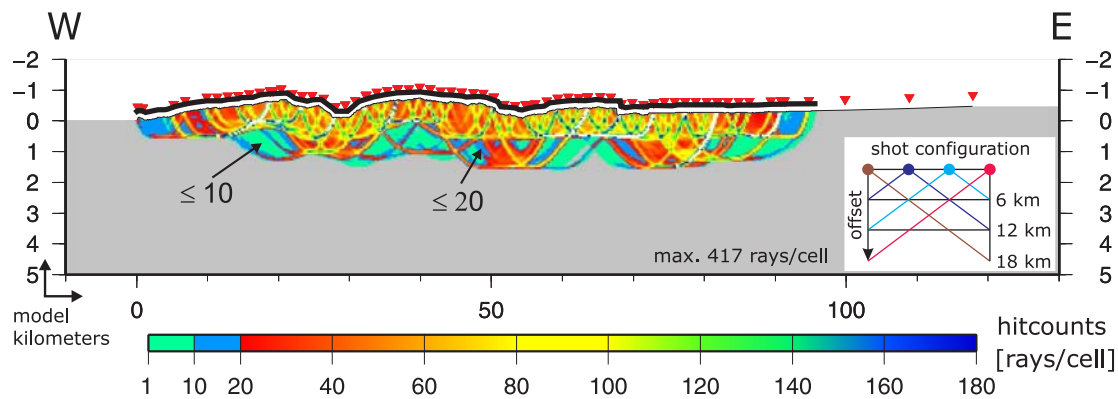
Figure 8.3.: Hitcounts for NVR and SH shots only. White colors account for hitcount values greater than 180. The inset on the right shows the four possible shot configurations, see text for more details.

Even though a constant shot spacing of 1.5 kilometer was used, we observe a change in the hitcount image at ≈ 0.5 km below topography. This may result from the used experiment setup. Four types of shot-receiver configurations were used within each spread spanning 18 kilometers, whereas two are just mirrored configurations (cf. inset in figure 8.3). Two shots, fired at the ends of the profile provide offsets up to 18 kilometers. The other two shots fired within the spread provide only offsets up to 12 km, and therefore less depth penetration. Increased hitcount values in the lower part may result from a thicker sedimentary cover at the surface in valleys at x = 27 and 55 km and the Central Valley at x = 85 km. This sedimentary cover shows a shallower gradient in velocity increase into depth than the surrounding rocks. The traced rays are possibly less refracted in the sediments and might therefore reach deeper layers.

A comparison of the linear features shows that there is no correlation with high or low hitcount numbers, or to a thick/thin bundle of rays (cf. figure 8.4). Parts of one linear feature are distributed across zones of high and low hitcount values. A correlation with cells showing a hitcount value greater than 180 could also not be confirmed. In the depth range of the linear features the ray density drops rapidly along the profile (z > 0.5 km). This general drop may also not be the cause of the linear features, since the observed features cross this border obliquely, e.g. at x = 25 km. The distance of the shots and receivers to the ideal 2-D profile cause no obvious influence to the velocity or hitcount distribution.
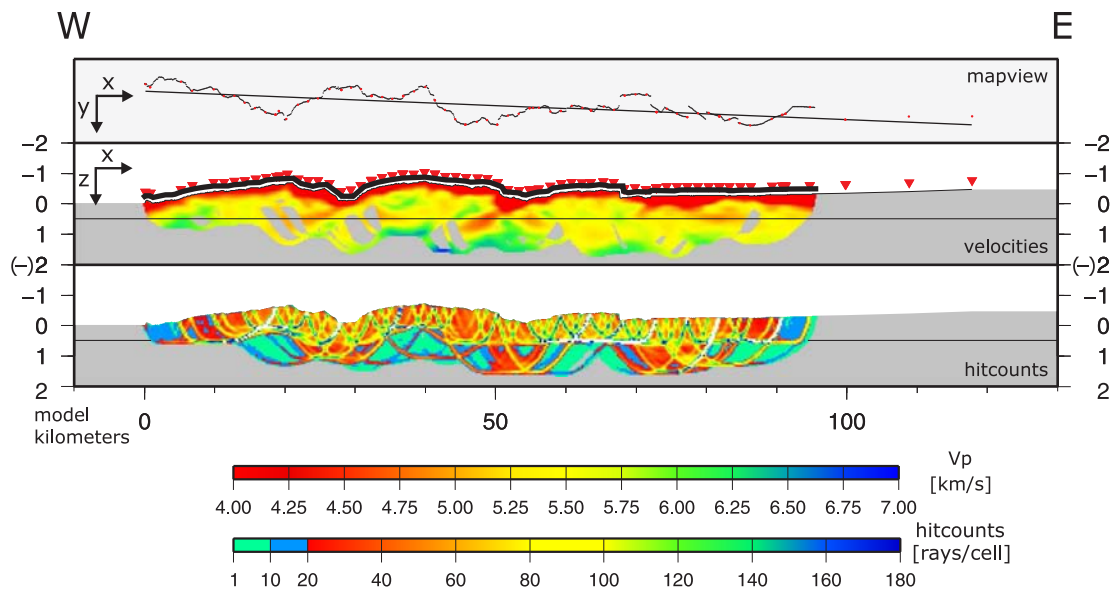
Figure 8.4.: A direct comparison of the geometry, velocity model, and hitcount results.

8.4. Checkerboard tests

Figure 8.5 shows two results of the checkerboard calculation with anomaly sizes of 4 x 0.5 km and 2 x 0.25 km. The checkerboard structure is recovered quite well along the whole profile in part a. The deeper layers just start to smear in zones of low ray coverage, because of the smoothing regularization of the tomographic method (Zelt, 1998). Panel b shows that the input anomaly size is too small to be recovered at all. Structures up to the range of 4 x 0.5 km can be considered in the interpretation along the whole profile. The results of all five conducted checkerboard calculations can be found in figure F.2. Further information on the process of checkerboard calculations are given on page 76 in chapter 7.3.
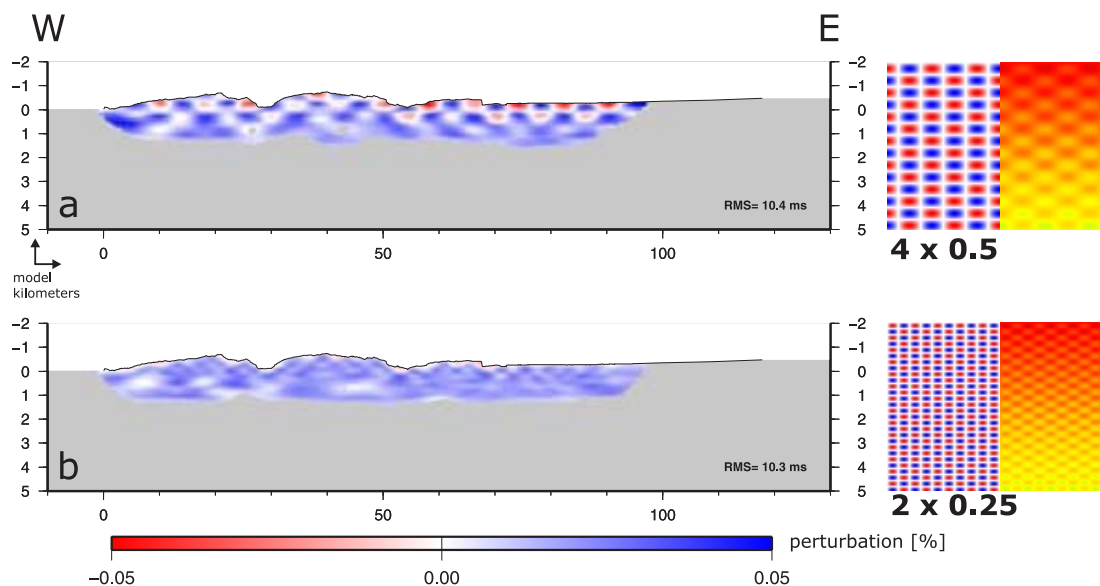
Figure 8.5.: Two checkerboard examples (NVR + SH shots) with anomalies of 10 x 5 km and 5 x 5.25 km in size, the anomaly pattern and perturbated velocity model is shown on the right.

8.5. Further tests

Variations in the number of picks, in the number and position of shotpoints, and in the starting velocities were incorporated into the inversions in the next step. The resultant images are presented in the appendix F, starting page 215. Test results of velocity variations, for example, showed the same robustness like results using the standard values and entire data set. The lower central part (x = 40 - 50 km, z = 2 km) shows variations in size and position of the structures with velocities greater than ≈ 6.4 km/s in several tests. The checkerboard tests do not reveal problems in that area, but the hitcount study shows a poorer ray coverage there. Tests of cellsize variations, which proved crucial in the inversions using all 104 shots, produce minor deviations in general. Figure F.7 shows the results of a pickerror study. The smaller

cells used in the inversion with only NVR and SH shots provide a better resolution of the subsurface, but only if a smaller pickerror is used. A realistic visual pickerror of 10 ms proved to be appropriate, resulting in a best RMS value of 16.3 ms. A comparison of 4 inversions, using different cell sizes, pickerrors, and shots, is shown in figure F.8 and demonstrates the increase in structural detail towards finer cells and smaller pickerrors. One even observes some coarse similarities in structure to the results of the inversion including the ESP shots (cf. figure F.8a/b).

Figure F.9 in the appendix shows inversion results of all available shots (including ESP shots), but using the small inversion cells and pickerrors of 0.03 and 0.01 like it was used for the inversion lacking the ESP shots presented in this chapter (see table 8.2). The results show clearly artifacts or high RMS errors, attributed to the included ESP shots and give further support to omit the ESP shots from the calculations.

Other plots to assess model quality in terms of how good the data is fitted are found in figure F.10. The fit of the data is much better than that of the inversions including the ESP shots. The RMS errors of the 89 shots along profile or RMS values of the individual receivers are much lower. This is strikingly visible in a comparison of the picked an modeled travel-times together with shot data, presented in figure 8.6, which underlines the quality of the inversion without the ESP shots.
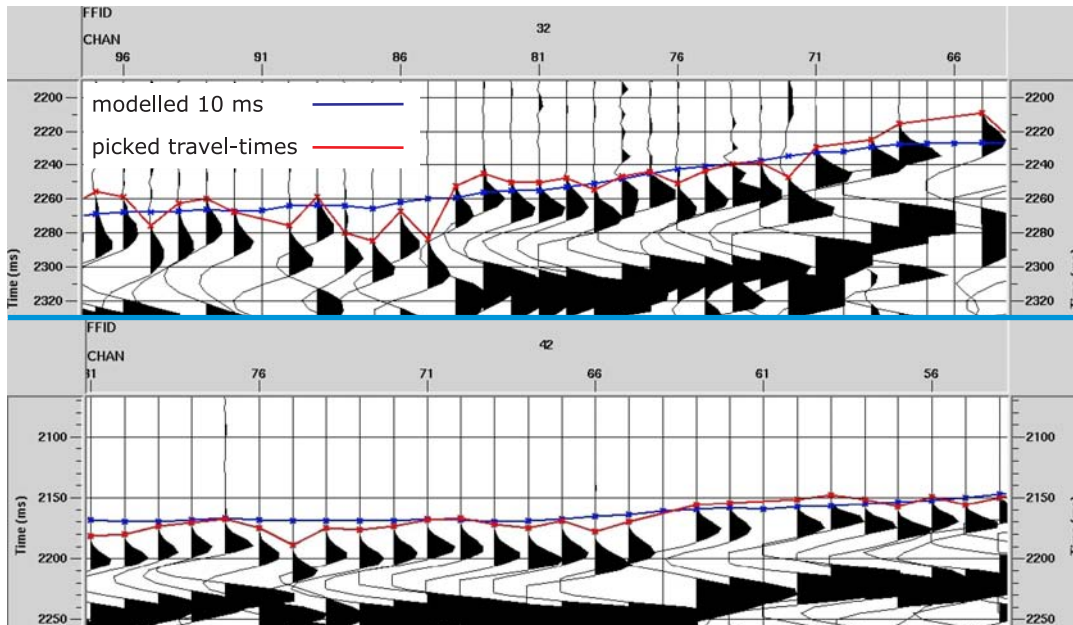
Figure 8.6.: Synthetic and picked travel-times together with shot data. The blue line belongs to the synthetic first-breaks with a pickerror of 10 ms, the red line shows picked travel-times. A very good fit is achieved, showing the quality of the inversion without the ESP shots. A comparison of the modeled travel-times calculated with both used shot configurations is provided in the appendix in figure F.11.

8.6. Final tomographic images

Figure 8.7 shows the final tomographic image of the inversion using only the NVR and SH shots. The range of the color palette was expanded to include sediment velocities which start with values close to 2.5 km/s at the surface. The lower panel of that figure shows part of the profile without vertical exaggeration, to show the real dimension of the imaged structures. We observe the transition from the coastal cordillera to the sediment covered Central Valley at approximately x = 70 km. The appendix shows further images without vertical exaggeration of the whole profile (with and without interpolation), including the three shots off the line in the east (cf. figures F.13 - F.16, page 225 - 228).
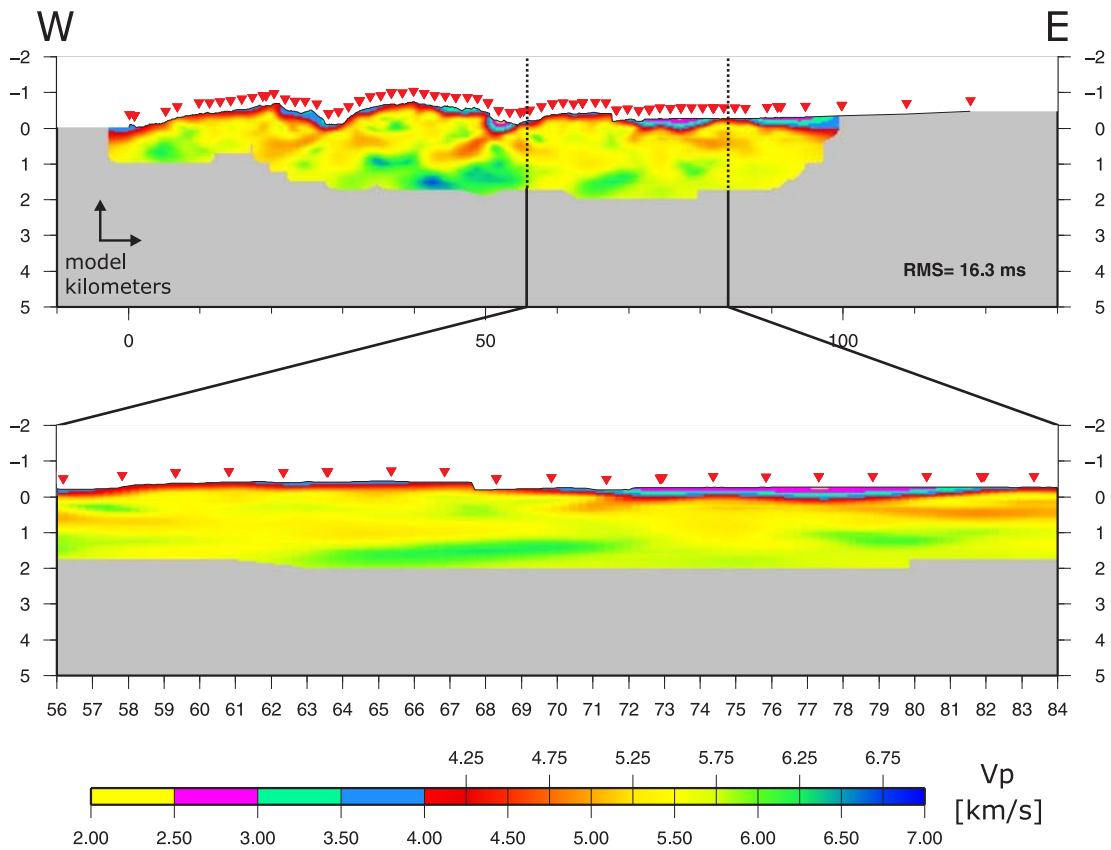
Figure 8.7.: Final tomographic image using NVR and SH shots. The lower part shows a detail along the profile without vertical exaggeration, to show the real dimension of the imaged structures. The sediment covered Central Valley starts at approximately x = 71 km.

An interpretation of the resulting structures and velocity distributions will be given in section 10.3, where the tomographic image is compared to local geological maps and fault data.

9. Migration tests with different velocity models

This chapter deals with the migration of the reflection seismic data set and the influence of different velocity models on the migrated image. Two further velocity models are available, that are not derived from the reflection seismic data set: one crustal-scale model was provided by the seismology group of TIPTEQ (Haberland et al., 2008), the other results of a combination of the SPOC (Krawczyk et al., 2007) wide-angle model with the inversion result of all shots. This inversion proved to be unstable and inaccurate, but provides a velocity model with extreme values and strong variations close to the surface, which could influence the depth position of the imaged structures.

9.1. Merging of the SPOC and tomographic velocity models

The merging of the SPOC and tomographic velocity models was conducted with MATLAB, which is a high-level programming language and interactive environment (a open source clone of MATLAB is called Scilab). The advantage to use MATLAB for the conducted calculations is that the velocity field is treated as a matrix where manipulations of the data set can be conducted very fast and easily.

Velocity grid files of the SPOC model (see figure 1.6) and the tomographic result shown in figure 7.2b were first converted into ASCII files. The interpolated, unmasked image of the tomographic result was used, to obtain a smooth transition between the two grids without greater steps in velocity. Both ASCII files were read into MATLAB, and were trimmed to the extend of the TIPTEQ seismic line ($\approx$ 120 km). Then, they were adjusted to use the same origin at the coast. The models need to be interpolated to use a common grid spacing and are merged by exchanging the corresponding values of an empty background matrix. The resultant velocity field was then exported into an ASCII data file. CDP values were assigned to the x-y-v data via shell-scripts, to be able to import the velocity field into a ProMAX velocity table. The 'interactive velocity editor' module of ProMAX was used to extrapolate the velocity structure of the oceanic plate to remove the sharp step in velocity at the eastern end of the model at a depth of 60 kilometers. In addition, the model was extended to a total depth of 150 kilometers with a constant velocity of 8 km/s. The model was smoothed within the 'interactive velocity editor' using 75 CDPs in x- and 500 m in z-direction as smoothing

parameters (see figure 9.1). This final model was then stored as an 'interval velocity in depth' as well as a 'stacking velocity' model (see figure G.1a) to be used in the migration job. The MATLAB code to merge the models can be found in the appendix, section G.1.
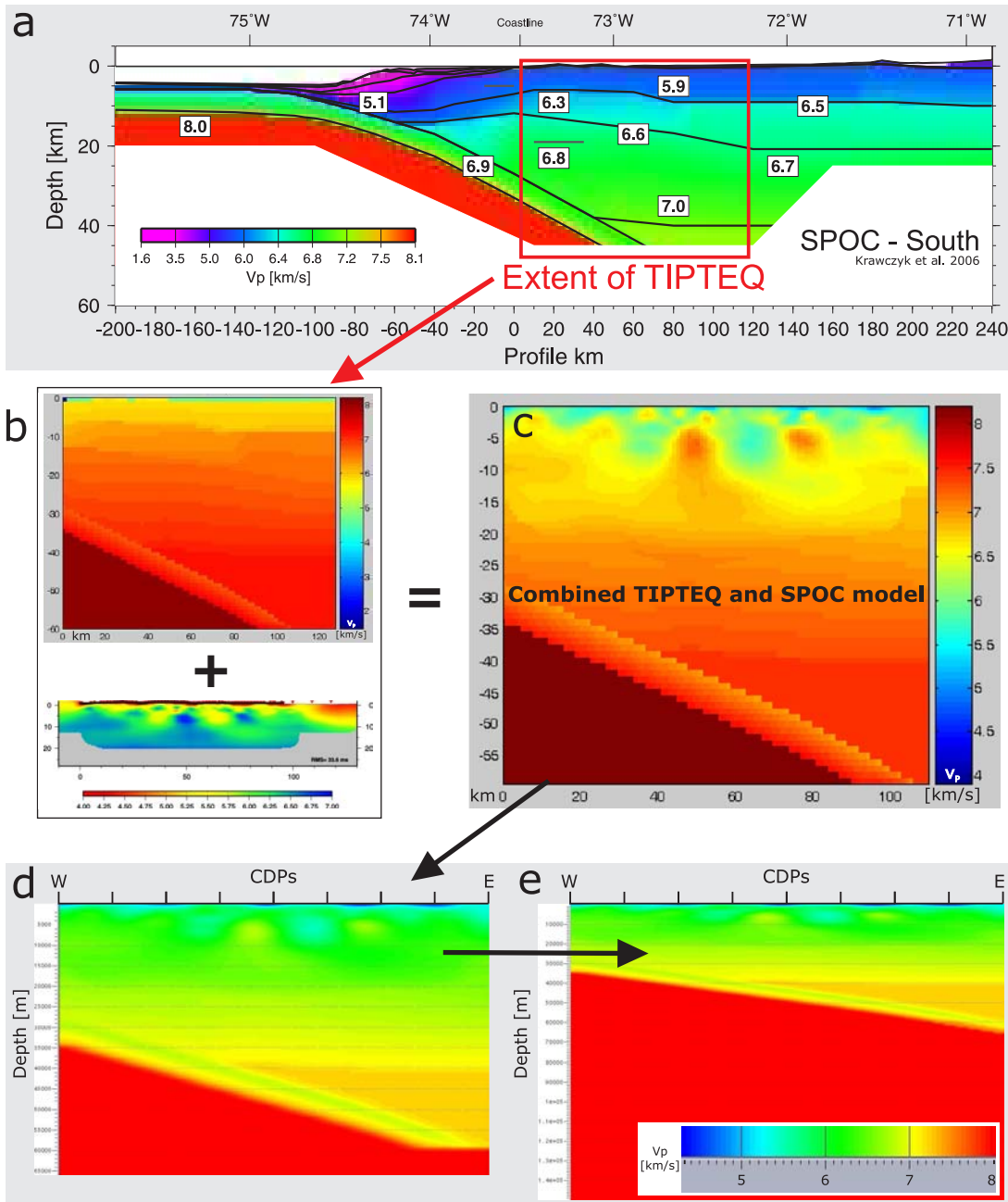
Figure 9.1.: The SPOC model (a) was imported into MATLAB and merged with the interpolated tomographic model calculated from all shots (NVR/SH/ESP; b/c). The CDPs were assigned to the resultant velocity model, to be able to import it into ProMAX. There, it was further altered and smoothed to cope with steps in velocity and model size (d/e).

9.2. Preparation of the seismological model

The seismology group within TIPTEQ provided a 2–D cross section of their 3–D velocity model obtained from the northern seismological network (cf. figure 7.10) at the latitude of the seismic line at $\approx 38.2°$ S (Christian Haberland, University of Potsdam/GFZ, pers. comm). CDP values were again assigned with shell-scripts to import the model into a ProMAX velocity table for migration. Figure 9.2a shows the tomographic velocity model with masks covering the less constraint areas, part b shows the ProMAX velocity model, where an unmasked version of the velocity model was used.
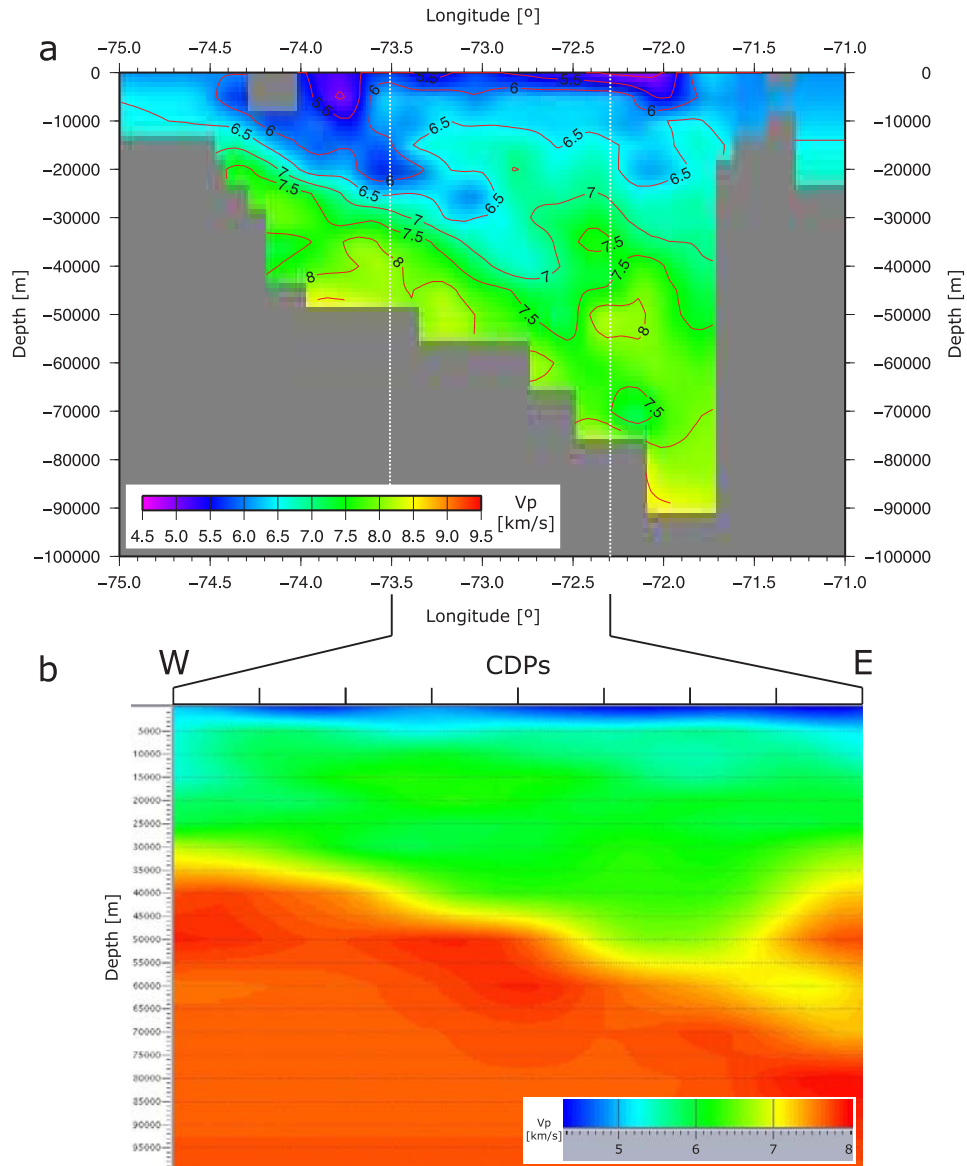
Figure 9.2.: Tomographic model at $\approx 38.2°$ S from seismology data (Haberland et al., 2008). Part b of the figure shows the ProMAX velocity model along the TIPTEQ transect. Confer figure 9.1d to compare differences in the velocity models).

9.3. The conversion of seismic images to ASCII point data

The digital output of seismic data from ProMAX, besides SEG-Y or other similar seismic data formats, can be very unsatisfactory. Two better possibilities are CGM or postscript files. They proved not to be appropriate when the seismic image is needed to be plotted with grid files, faults, or earthquakes with GMT or 3–D visualization software like Fledermaus. Further processing and editing of the PS-files with publishing software (CorelDraw, Photoshop) is not convenient, since almost every wiggle on a seismic traces is treated as one single element, resulting in a vast amount of elements which slows down the program tremendously. Tests with CGM files did also not satisfy the needs.

A good way to work with different classes of geoscience data and seismic images was to take screenshots of the seismic sections displayed in ProMAX. Combining these screenshots with GMT plots in publishing software like CorelDraw works excellent, but leads to problems in terms of referencing both plots accurately. Using the pixel image of the seismic profile in GMT with 'psimage' has in turn the disadvantage that the seismic image must again be trimmed and positioned by hand to the respective range of e.g. the east-west range of a pixel image showing the receiver functions. Both GMT modules 'segy2gmt' and 'pswiggle' produce unsatisfying results for seismic sections with large, crustal-scale dimensions.

The solution is to convert the screenshots of the seismic data into ASCII data files with longitude, latitude and depth for each 'black' pixel. This innovative approach makes it possible to combine the seismic results with all sorts of data in a suite of programs in one single figure. The main part of the conversion was conducted with MATLAB. The screenshots were read into MATLAB as black and white PNG files and the pixels in x and z direction defined the size of the image matrix. Dimensions in x (CDP) and z (m) of the image are known, because they were set in ProMAX for the display job beforehand. Depth values for each pixel could be calculated from that very easily. The coordinates for each pixel in x direction were calculated after a linear equation with the origin at the respective westernmost CDP of the image, the slope results from the slope of the TIPTEQ CDP line. The distance of the calculated position of the easternmost pixel to the respective CDP coordinates should be minimal and ranged 170 and 260 m, which is ≈ 2 ‰ of the total distance of 106.55 and 152.5 km, respectively. Pixel coordinates were calculated using local coordinates and are exported next to be converted into longitude/latitude values, e.g. with the program 'utm' on a UNIX machine. The reloaded values into MATLAB are then matched to the depth values and written to disk including a flag indication a black or white pixel. AWK is finally used to create a file consisting of longitude, latitude, and depth for each black pixel representing a tiny part of a seismic reflector. An example MATLAB script can be found in the appendix G.3.

Four ASCII seismic images were converted in the described way, where two use the merged velocity model of the SPOC and tomographic image and differ in the number of CDPs and processing steps. The other two images differ in the used velocity model for migration (see table 9.1).

With this method, vertical resolution is lost for high frequencies (≤ 40 Hz), but resolution is sufficient for low frequencies (≥ 10 Hz). The horizontal resolution is not affected at all (cf. figure 4.10). Overall, the resolution of the ASCII data is adequate for crustal scale plots and investigations.

no.	file	velocity model
1	seismic4psxyz1775-3906.asc	SPOC + tomography
2	seismic4psxyz1110-4160.asc	SPOC + tomography
3	seismic4psxyz1110-4160–LUETH.asc	SPOC
4	seismic4psxyz1110-4160–SEISMOLOGIE.asc	tomography (seismology)

no.	x [km]	z [km]	pixel in x	pixel in z	resolution in x [m]	resolution in y [m]
1	106.55	70	1767	777	60.3	90
2	152.5	70	1437	669	106.1	104.6
3	152.5	70	1050	780	145.2	89.7
4	152.5	70	1050	778	145.2	90

Table 9.1.: Sizes and resolution per pixel of the ASCII converted seismic images.

9.4. Migration tests with different velocity models

The next figures show a direct comparison of the migration results with the same CDP range, using the three different velocity models discussed in the sections before. This direct comparison is only possible because of the transformation of the seismic data to ASCII files. The resultant migration using the SPOC velocity model serves as a reference model, and was already discussed in chapter 5.

Figure 9.3 shows the resultant migrations for the SPOC (black) and the merged velocity model (SPOC + tomographic model; red). Both migrations are highly comparable in their major structures, the noisy pattern of small-scale reflective features obscures this observation. The shallow velocity pattern of the merged model has only little influence on the overall picture. High velocities in the central part of the model might account a for slightly lower reflection pattern in the central part of the seismic image at a depth of ≈ 8 - 15 kilometers.

Figure 9.4 shows migrations using the SPOC (black) and the velocity model derived from seismology data in blue. Again, the images are highly comparable, the reflective structure of the migration using the seismological velocity model appears to be deeper (< 1 km). This difference increases slightly towards depth and towards the east (cf. the enigmatic reflection at -72.2°, z = 45 - 70 km).

Overall, the results are very similar and sufficient alike, greater divergences are partly observed in the deeper parts of the sections, where the used velocity models differ (cf. figures 9.2b and

G.1b). The plotting of earthquake hypocenters from the TIPTEQ seismology group within the reference seismic section (SPOC velocity model) is possible without greater errors induced from the varying velocity models. This also supports the credibleness of the subsurface velocity images, where two independently recorded data sets of two experiments (SPOC/TIPTEQ), in addition treated with different methods (wide-angle modeling/tomography), come to the same results. Figure 9.5 shows a combination of all three migrated sections, figure 9.6 shows each seismic image for comparison.
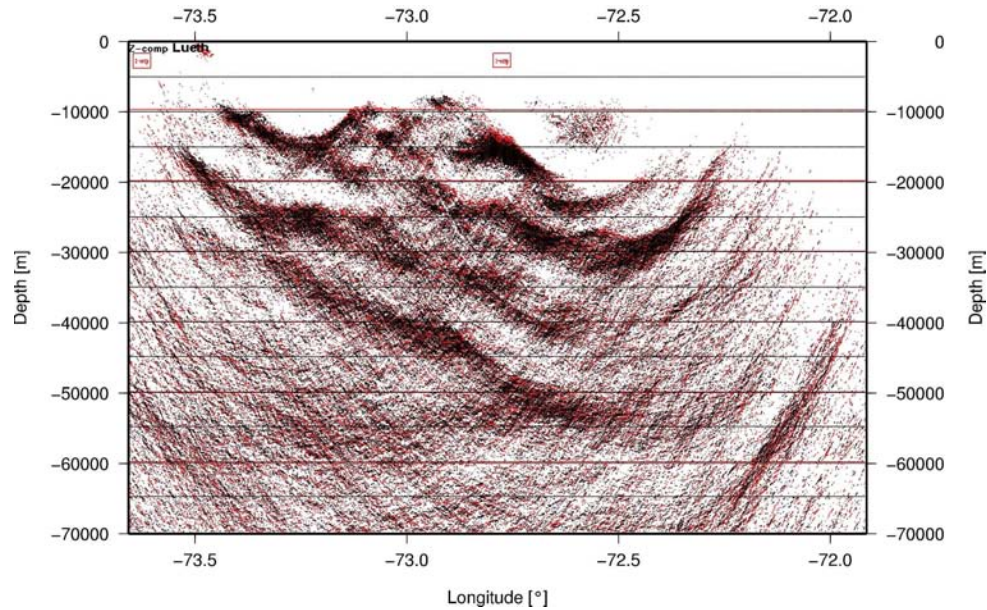
Figure 9.3.: Comparison of migrations of the reflection seismic TIPTEQ data using the SPOC (black) and merged velocity model in red (VE ≈ 1.5).
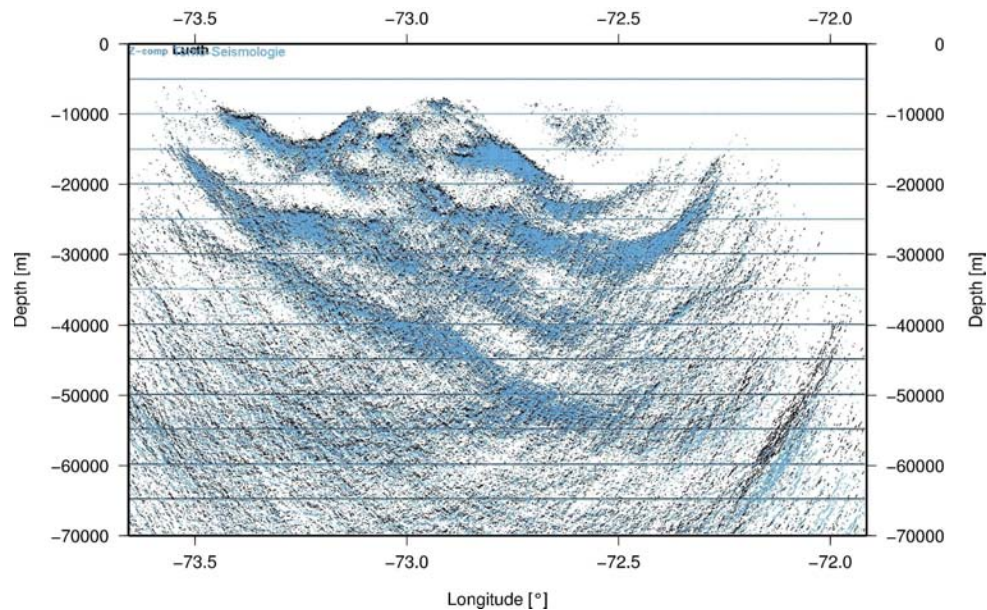
Figure 9.4.: Comparison of migrations of the reflection seismic TIPTEQ data using the SPOC (black) and seismology velocity model in blue (VE ≈ 1.5).

106
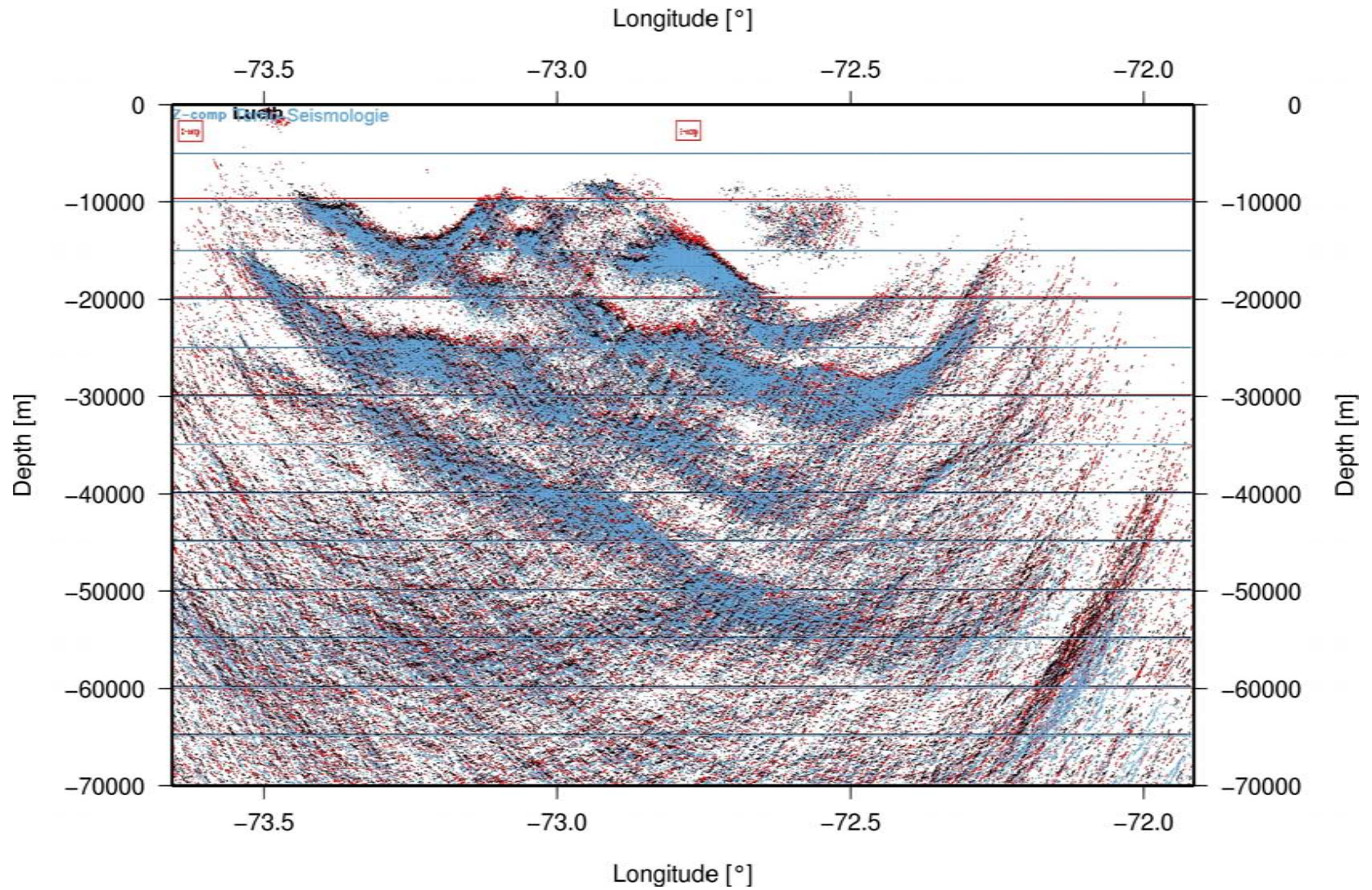
Figure 9.5.: Comparison of all three migrations. The one using the SPOC velocity model is shown in black, the merged velocity model in red, and the seismology velocity model in blue (VE ≈ 1.5).
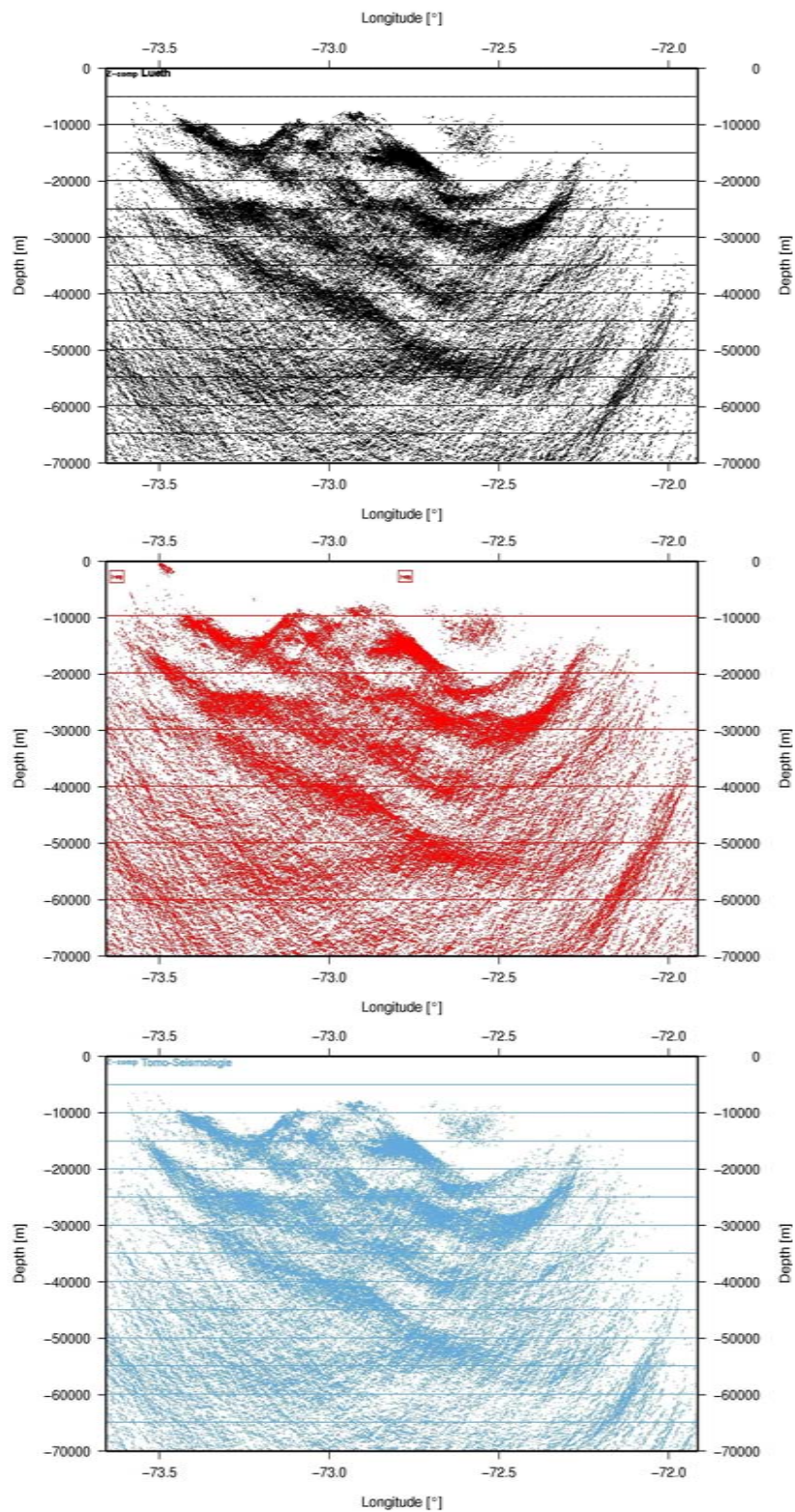
Figure 9.6.: Comparison of all three migrations (VE $\approx$ 1.5). The one using the SPOC velocity model is shown in black (top), the merged model in red (middle), and the seismology model in blue (bottom).

10. Interpretation and discussion

This chapter discusses the interpretation of the final reflection seismic structural image of the TIPTEQ data as well as the derived tomographic velocity model in terms of their geological and geodynamic significance. The findings are compared to the results of other TIPTEQ groups and of former experiments in the study area. Comparisons with other subduction zones, such as Casacadia, find similarities and differences in structures and processes active at a subduction zone. The crustal architecture and related issues like transparent zones or the nature and dimension of a possible subduction channel are addressed first, followed by a comparison of the seismic data with findings of other TIPTEQ groups.

A great advantage for these comparisons is the conversion of the seismic sections to 3–D ASCII data (cf. section 9.3). This allows a combined plotting of the seismic data with grid data, earthquakes, or pixel images accurately and geo-referenced in GMT-PS-files (see example scripts in `/tipteq/GMT/plots`). These vector format files (mixed with pixel images) are further editable and can be easily converted in any format. There is no need to shift, stretch or apply transparencies in publishing software like CorelDraw or Photoshop to create a combined figure. A direct and fast comparison of the seismic data with results of other TIPTEQ groups is possible with this approach in a variety of programs. 3–D views of the subduction zone and related data were realized with the software Fledermaus by IVS3d (see 3–D model in `/tipteq/fledermaus`). More information on the visualization of the seismic and related data in 3–D with Fledermaus and Google Earth are found in the appendix H.

The seismic data used for the figures in this section were migrated using the reference SPOC wide-angle velocity model and range from CDP 1110 - 4160 (cf. figure 4.7, black dots). The east-west range of the seismic data was adjusted for some figures to account for the extend of the used background data, e.g. a pixel image of receiver function results. The latitude of the following figures corresponds to $\approx 38.25°$ S ($38°$ 15' S) where $0.5°$ equal ≈ 43.8 km (see figure 10.1). Figure 10.2 shows a map of the profile area. Experiment geometries of former studies, e.g. the SPOC experiment, are plotted together with the TIPTEQ source and receiver geometry and CDP line. Main features of the forearc that are needed for the discussion, such as the Lanalhue Fault Zone or the Coastal Cordillera, are introduced.

Some results presented here are published in a joint paper:

K. Groß, U. Micksch, TIPTEQ Research Group, Seismics Team (2008) The reflection seismic survey of project TIPTEQ - the inventory of the Chilean subduction zone at 38.2° S, Geophysical Journal International 172 (2), 565 - 571, doi: 10.1111/j.1365-246X.2007.03680.x, URL: `http://tinyurl.com/6ynwm4`.

The TIPTEQ Research Group, Seismics Team consists of:

Groß, K., FU Berlin, Germany (a)

Micksch, U., GFZ Potsdam, Germany(b)

Araneda, M., SEGMI, Santiago, Chile (c)

Bataille, K., Universidad de Concepción, Chile (d)

Bribach, J. (b)

Buske, S. (a)

Krawczyk, C.M. (b)

Lüth, S. (a, b)

Mechie, J. (b)

Schulze, A. (b)

Shapiro, S. A. (a)

Stiller, M. (b)

Wigger, P. (a)

Ziegenhagen, T. (b)
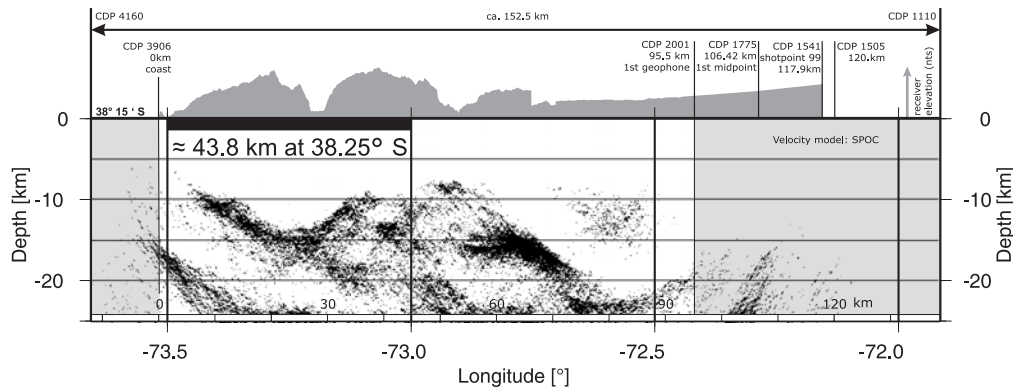
Figure 10.1.: Geographic frame and CDP setting of the seismic images in this chapter. Areas outside of the receiver geometry at the ends of the profile are covered with masks to delimit the confidence area (cf. section 5.2.3).
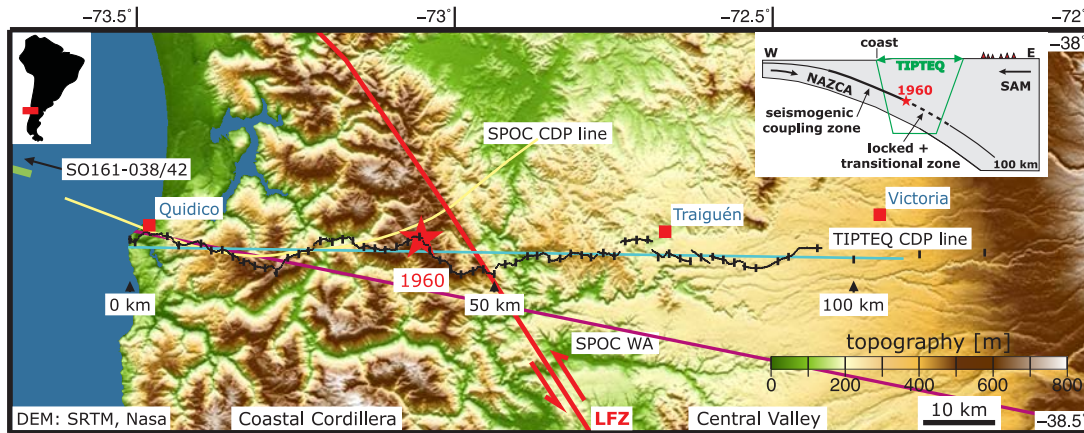
Figure 10.2.: Location map of the active-source seismological experiment of project TIPTEQ (for acquisition details see table 2.1). Black line - receiver line, black ticks - shot locations, blue line - CDP line, red star - hypocentral area of the 1960 earthquake. The yellow and magenta lines mark the CDP line of the SPOC onshore seismic reflection profile and the SPOC wide-angle refraction profile, respectively (Krawczyk et al., 2007). The green line marks the eastern end of the marine seismic reflection profile SO161-038/42 acquired by RV Sonne in 2002 (Reichert and Schreckenberger, 2002). The red line maps the surface trace of the Lanalhue Fault Zone (LFZ; after Melnick and Echtler (2007)). NAZCA and SAM label the Nazca and South American plates in the inset. (Groß, Micksch, and TIPTEQ Research Group, 2008).

10.1. Interpretation of the TIPTEQ poststack reflection seismic image

Figure 10.3 shows the seismic section at $\approx 38.25°$ S including colored velocity interfaces from the SPOC wide-angle experiment (Krawczyk et al., 2007) and the relocated hypocenter of the 1960 earthquake marked with a red star (Krawczyk and the SPOC Team, 2003). The inset labels the reflective bands (R1 - R3). The colored dots mark hypocenters of earthquakes recorded with the local seismological network (Haberland et al., 2006). Earthquakes between -38.7° and -37.9° S are shown in magenta (≈ 90 km clip area), light blue dots belong to earthquake hypocenters in a corridor of 40 km around the profile (20 km north and south of the profile line). Orange dots represent earthquake hypocenters within 5 km north and south of the profile. Earthquakes which occurred at depths shallower than 25 km can be associated with crustal faults e.g. the cluster close to the coast as well as the earthquakes at x = 60 and 105 km which do not belong to the seismic reflectors seen close by. Two other zones of seismicity are observed. Seismicity below 45 km depth may be attributed to the Wadati-Benioff zone (Haberland et al., 2006; pers. comm.). The seismicity directly above the plate interface up to x = 40 km is discussed in more detail below. Figure 10.6 shows an interpretation of the TIPTEQ reflection seismic data modified after figure 4 of the paper by Groß, Micksch, and TIPTEQ Research Group (2008). The seismic background image was exchanged with the resultant image of this study and some interpreted features were adjusted accordingly.

The seismic image of the NVR data set of project TIPTEQ shows the subducted oceanic Nazca plate below the segmented forearc and a highly reflective overriding South American plate. High reflectivity directly above the plate interface is suggested to be associated with the existence of a subduction channel with a varying thickness of 2 - 5 km down to a depth of at least 38 km. It might continue towards depth. Local seismicity possibly defines the upper bound of the subduction channel. The continental Moho is not clearly imaged. However, one possible location is at 38 - 40 km depth given by the 1960 earthquake hypocenter. The Moho may be continued eastwards to a depth of 35 km where a prominent structure is imaged. This reflector coincides with the modeled Moho interface from a 3–D density model along the Chilean margin. The reflectivity east and above of the 1960 hypocenter area may exhibit alternative eastward continuations of the continental Moho. The position and extent of the continental mantle wedge changes accordingly. Major forearc features such as the crustal Lanalhue Fault Zone and a strong west-dipping reflector perpendicular to the plate interface can be observed.

Figure 10.3.: The migrated depth section of TIPTEQ is plotted together with velocity interfaces modeled after wide-angle data from the SPOC experiment. The epicenter of the 1960 Chile earthquake is marked with a red star, colored dots show earthquake hypocenters located with the northern TIPTEQ seismological network. A proposed subduction channel is shown by a grey mask on top of the oceanic crust marked in green. The inset labels the reflective bands R1 - R3. See text for details and references.

10.1.1. The position of the oceanic crust

The wide-angle data of the SPOC–South profile define the position of the oceanic crust in the TIPTEQ section (solid and dashed green and red lines in figure 10.3) with a possible vertical error of 2 - 3 km. The dashed lines extend the crustal interfaces from the confidence region of the velocity model up to a depth of 60 km (Stefan Lüth, GFZ, pers. comm., cf. section 4.3). The top of the oceanic plate in the SPOC wide-angle velocity model was inferred from the clearly observed oceanic Moho and the thickness of the oceanic crust imaged by marine seismics close to the coast (Rauch, 2005).

At first glance, the top and bottom interfaces of the oceanic crust seem to cut through the lowermost reflective band (R1) which might itself represent the downgoing oceanic crust. If the two wide-angle interfaces of the oceanic crust are slightly tilted eastwards and shifted upwards for about 2.5 - 3 km within the given error bars, the interfaces would embrace the lowermost reflective band (R1) which might then be interpreted as the oceanic crust. A depth migration of the reflection seismic data with an independently derived velocity model (seismological tomography) results in a very similar migration result like the one using the SPOC velocity model (cf. chapter 9). This observation, in turn, supports the depth positions of the SPOC velocity interfaces and the reliableness of the SPOC velocity model. As a consequence, the strength of reflectivity varies within the oceanic crust which is addressed below. Seismicity below 45 km is interpreted to be intra-plate seismicity in the Wadati-Benioff zone (Haberland et al., 2006; pers. comm.), and argue for a slightly steeper plate dip in depths between 40 - 60 km. This is implemented in figure 10.6.

10.1.2. The reflectivity of the oceanic crust

The oceanic crust imaged by the TIPTEQ depth section (cf. figure 10.3) exhibits a varying intensity of reflectivity which increases with depth. The oceanic crust can be traced down to depths of 55 km below the Central Valley. Almost no reflectivity in the crust is observed from beneath the coast up to x = 20 km (z = 35 km). This lack of reflectivity is also observed in the SPOC NVR seismic profile (see figure 1.5). The SPOC NVR profile coincides with the TIPTEQ NVR seismic line in the first 50 - 60 km (cf. figure 10.2). The smooth increase of reflectivity in the oceanic crust just west of the hypocenter of the 1960 earthquake is not observed in the SPOC NVR seismic image perhaps because of the low CDP fold (1 - 2) of the SPOC data.

The decreased reflectivity in the oceanic crust correlates roughly with the transition from the seismogenic coupling zone to the transitional zone (cf. figure 10.2; for definition see e.g. Hyndman and Wang (1993), Tichelaar and Ruff (1993), or Flück et al. (1997)). Hoffmann-Rothe et al. (2007) compiled a large data set of along-strike variations in parameters defining the Nazca–South America subduction margin between 14° and 48° S. The coupling depth estimation is based on elastic dislocation modeling of GPS data (Khazaradze and Klotz, 2003).

At the latitude of the TIPTEQ profile the end of the fully coupled zone occurs at ≈ 43 km depth and the downdip end of the subsequent transition zone at 62 km depth. The earthquake hypocenters located with recordings from the TIPTEQ seismological network (see figure 10.3) cumulate above the plate interface above a depth of ≈ 31 km. Only few earthquakes are observed along the plate interface deeper than 31 km. This decrease in seismicity coincides with a change in the reflectivity pattern in the oceanic crust and might argue for a seismogenic coupling zone at shallower depths. No apparent change of reflectivity and structure is observed in the overburden above the Nazca plate interface west and east of x = 20 km in figure 10.3. This fact favors the assumption that the observed change of reflectivity is attributed to processes active in the oceanic crust which change the material properties.

During the process of subduction the water content in the oceanic crust and overlain marine sediments is decreased in several stages. Dewatering starts with the sediment porosity collapse immediately after subduction. Accretionary prisms often show mound-like structures or active venting of fluids, e.g. found and investigated at the convergent continental margin off Costa Rica and Nicaragua (Hensen et al., 2004). The source of the venting fluids is most likely within the subducted sediments since the fluid isotope geochemistry points to clay-mineral dehydration and temperatures between 85° and 130° C. Temperatures above 50° C are not reached within the sediment cover of the upper plate. The fluids migrate upwards from depths of 12 km along deep-seated faults which were mapped in reflection seismic sections (Hensen et al., 2004).

Temperatures at the end of the seismogenic coupling zone reach approximately 350° C (Hyndman and Wang, 1993). Between 200° and 400° C the porosity collapse in basalt in the oceanic crust releases trapped fluids (Hyndman and Peackock, 2003). This process might cause the increased reflectivity in the subducting oceanic crust at and below depths of 35 km in the TIPTEQ seismic section (cf. figure 10.3). Heat flow investigations within project TIPTEQ resulted in a modeled temperature of 250° C at the plate interface in 26 km depth at 36° S (M. Heesemann, University of Bremen, pers. comm.).

In northern Chile (21° S), the seismic sections of the ANCORP experiment also show sparse reflectivity in the oceanic crust below 25 km depth (The ANCORP Working Group, 1999; Asch et al., 2003). Here, the onshore reflection seismic sections are extended offshore by stacked wide-angle results and migrated wide-angle CMP reflections of the CINCA experiment (Patzwahl et al., 1999). The onshore seismic sections also show a reduced reflectivity (z $\approx$ 40 - 50 km) at the coast. A distinctive increase of reflectivity is observed below 55 km depth. The continental mantle above this crustal section is interpreted to be hydrated which in turn first needs a dehydration probably of the underlying oceanic crust. The breakdown of reflectivity in the oceanic crust at 77 km depth suggests that fluids are no longer retained in the crust and that progressive dehydration (eclogitization) of oceanic crust has largely destroyed the impedance contrast with the overlying mantle peridotite (The ANCORP Working Group, 1999). The reflectivity in the oceanic crust in the TIPTEQ reflection seismic section can be followed down to 55 km depth. It can not be concluded if the same process as suggested for

the ANCORP section causes the observed rapid decrease in reflectivity. The decrease is most likely related to the experiment geometry. It is not possible to image the eastward dipping plate interface east of x = 85 km, because the seismic energy is reflected farther east, away from the receiver spread.

10.1.3. The continental Moho

The continental Moho (blue dashed line, figure 10.3) of the SPOC wide-angle model is drawn where velocities over 7.2 km/s occur in the SPOC velocity model. This is based on upper mantle velocities found along the ISSA-2000 transect one degree south of the onshore TIPTEQ/SPOC profile (Lüth et al., 2003).

A clear structurally imaged boundary marking the position of the continental Moho could not be found in the TIPTEQ NVR data. The dewatering of the downgoing oceanic crust might lead to serpentinized forearc mantle material that reduces the velocity contrast between continental crust and mantle and thus hampers the formation of an explicit Moho reflection in the seismic image. This phenomenon is also observed in receiver function data from the Cascadia subduction zone (Bostock et al., 2002; Nicholson et al., 2005) and Alaska (Abers et al., 2006). Unfortunately, constraints from a thermal model, such as isotherm geometries and phase transitions, are not available for the TIPTEQ transect.

Even though the existence of the continental Moho within the overriding plate is not directly evident in the seismic image, two possible delineations and intersections of the continental Moho with the oceanic plate can be considered. The first scenario assumes the hypocenter of the 1960 Chile earthquake, as shown in figure 10.3 (red star, z ≈ 38 km). Krawczyk and the SPOC Team (2003) relocated the hypocenter using the continental Moho from the SPOC wide-angle velocity model together with the assumption that the hypocenters of mega-thrust earthquakes initiate at the down-dip end of seismogenic coupling zones (Oleskevich et al., 1999; Peacock and Hyndman, 1999). Engdahl and Villaseñor (2002) relocated the 1960 earthquake epicenter independently at almost the same location (within 4 km horizontal distance) using an improved global velocity model (ak135) and a new location procedure (EHB method). The reflection pattern directly east of the 1960 hypocenter gives no evidence of the expected Moho, possibly attributed to the discussion above.

A second major reflective band (R2) above the plate interface can be traced from the coast (z = 15 km) to a depth of 43 km at x = 70 - 80 km. This crustal reflector pierces the SPOC Moho interface slightly (cf. figure 10.3) and is not observed in greater depths. A continental Moho could rise from just below the earthquake hypocenter to ≈ 35 km depth and embrace the second lowermost reflective band (cf. figure 10.6, red solid line). Density modeling within project TIPTEQ (Paolo Alasonati, University of Kiel, pers. comm) shows a Moho interface which coincides with a short oblique reflector segment at x = 100 - 105 km in a depth of 35 - 40 km (see figure 10.4). The preferred Moho interface, coded by the red solid line, is

connected to that reflective element. The gravimetrical model depicts a Moho rising up to a minimum depth of 33 km at x ≈ 130 km (72° W). This undulating Moho and the plate interface delimit a zone of sparse reflectivity and outline the possibly hydrated mantle wedge. In a velocity model obtained from local earthquake tomography studies within the ISSA-2000 experiment a P-wave velocity anomaly at 72° S supports the rising Moho interface towards the east (Bohm, 2004). Moho and slab interfaces were kindly provided by Paolo Alasonati (University of Kiel). More information and comparison of a density model and the seismic data is given in subsection 10.2.5.

Above and east of the 1960 hypocenter, horizontal structures argue for an other possible continental Moho interface (cf. figure 10.6), e.g. a Moho rising up to a depth of 34 respectively 27 km. The highest position would coincide with the interpretation of Yuan et al. (2006) based on receiver function studies at ≈ 39° S. These Moho interfaces seem to be unlikely since several prominent reflective bands must be crossed and the interface would need a complicated, interleaved 3–D structure.

The second scenario is, that the continental Moho is not directly imaged, because it encounters the oceanic plate at depths greater than 55 km. Horizontal or east dipping structures can not be imaged with high coverage in these depths east of profile-km 85 - 95 because of the experiment geometry. This would imply that all of the reflectivity above the plate interface is attributed to the continental crust and the location of the 1960 earthquake is not at the intersection of the continental Moho with the oceanic crust. However, a continental Moho depth of 55 km or more would be highly surprising. The continental Moho, if anything, tends to shallow towards the coast from the present-day topographically high, volcanic arc of the Andes. Here, the Moho does not reach depths of more than 40-50 km between 37° and 39° S (Krawczyk et al., 2007). If the continental Moho were to intersect the oceanic plate at depths greater than 50 km, then crustal material should have been added to the base of the crust in this region. As a consequence, one would expect this region to uplift due to isostasy. However, presently this region occupies the western part of the topographically low Central Valley. Thus it seems unlikely that the continental Moho intersects the oceanic plate at depths greater than 50 km.

10.1.4. The subduction channel

The reflectivity from x = -12 - 40 km directly above the plate boundary can be associated with the existence of a subduction channel (Lohrmann, 2002; Krawczyk and the SPOC Team, 2003; Lohrmann et al., 2007) with a thickness of 2 - 5 km (cf. figure 10.3, grey mask).

The subduction channel as defined by Cloos and Shreve (1988a, 1988b) is a zone with varying thickness above the oceanic crust in which material being transported downwards, exhibits a velocity gradient with respect to both plates. The material flowing within the subduction channel is derived from trench deposits, off scrapings from the base of the upper plate by
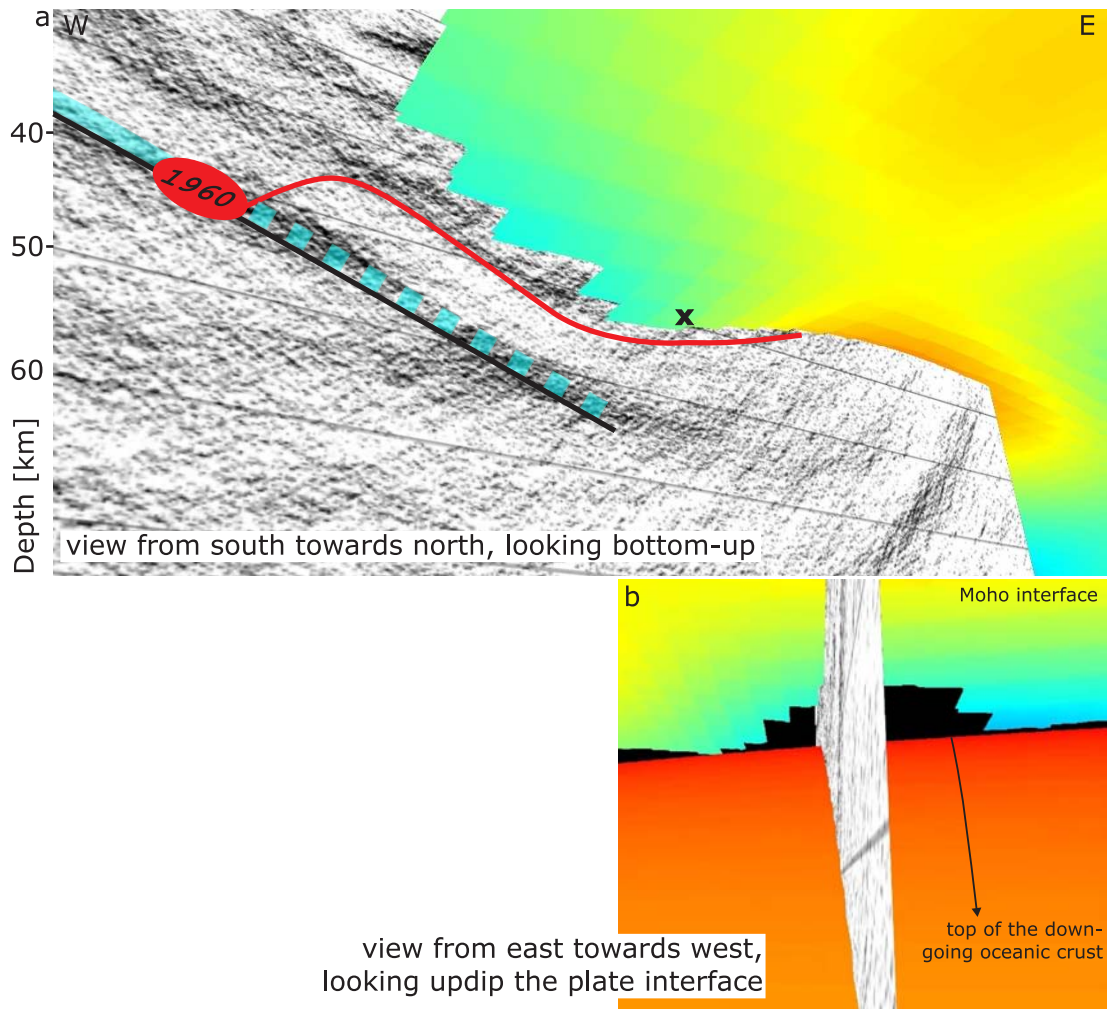
Figure 10.4.: 3–D view of the seismic section and Moho interface from a 3–D density model (Paolo Alasonati, University of Kiel, pers. comm). The red line shows the continental Moho interpreted from the seismic image (cf. figure 10.6 and gravimetrical constraints. The gravimetrically derived Moho in the 3–D model does not intersect the downgoing slab or the seismic section in all places (see panel b) because of filtering and smoothing which was applied to the 3–D interface. Where the seismic profile cuts the Moho interface, a huge window is observed in the Moho. The position where the Moho starts to intersect the profile is marked by an x in panel a. The Moho interface was kindly provided by Paolo Alasonati (University of Kiel).

tectonic erosion, or from the top of the downgoing plate at depth. Following this concept, the subduction channel and the transition zone may be expected to be highly reflective, as material here differs from its surroundings, thus inducing a strong impedance contrast. An additional process leading to high reflectivity may be the dewatering of sediments carried down in the subduction channel and the migration of fluids into the continental crust. Currently the thickness of the subducting sediments at the Chilean convergent margin at 38° S is 2.2 km at the trench (Rauch, 2005), but this is neither expected to be continuous along the entire subduction channel nor through time.

The thickness of 2 - 5 km of the subduction channel observed onshore is an upper bound. Seismic images may not distinguish material within the subduction channel from freshly accreted material or material that is moving with the oceanic plate. According to Cloos and Shreve (1988a) a narrowing of the subduction channel leads to an upflow of material, and thus causes a thickening of the channel further up-dip. This process is one possible explanation for basal accretion. Such a thickening of the channel (> 2 km; x = 5 - 30 km, cf. figure 10.3) is observed below the Coastal Cordillera, where uplift is observed at the surface (Rehak et al., 2008). Glodny et al. (2005) conducted a detailed study in the Valdivia area using isotope tectonochronology and sandbox modeling. This study shows that the intercalated metasediments and metabasites which build up the Coastal Cordillera at the surface were once basally accreted and consist of material that was transported from the offshore trench to depth along what is thought to be the subduction channel. In the seismic section, a strongly segmented upper plate is observed, showing horizontal and arched reflector elements that characterize the internal structure of the Permo-Triassic accretionary wedge (cf. figure 10.6), tracing at depth the sequences mapped and dated at the surface.

The mélange in the subduction channel that is subducted further down undergoes dehydration and embrittlement and may lead to the observed reflectivity at x = 45 - 90 km at depths of 40 - 60 km (cf. figure 10.6). Local seismicity studies (Haberland et al., 2006) show moderate seismic activity along the plate interface (cf. figure 10.3). The earthquake hypocenters may delimit the upper bound of the subduction channel. Orange colored hypocenters are within 5 km north and south of the profile line. Four hypocenters are located within the proposed subduction channel (x ≈ -12, 3, 12, and 62 km), indicating recent activity within the channel.

10.1.5. Reflectivity changes along the plate interface

Changes in reflectivity along and some kilometers above the plate interface can be observed, e.g. within the proposed subduction channel. Two stronger reflective patches are found at x = 20 and 50 km right above the oceanic crust (see figure 10.6). Such changes are also reported from other subduction systems. In Cascadia, Nedimović et al. (2003) suggest a correlation between reflectivity and coupling along the plate interface. According to their interpretation, a thin reflective zone less than 2 km thick indicates the coupled section of the plate interface. This zone broadens to 2 - 4 km in a transitional zone at the down-dip end

of the seismogenic coupling zone. A broad reflection band more than 4 km thick (E-layer) marks the beginning of the zone of aseismic creep. For south central Chile a similar thickness variation is observed in the TIPTEQ data in the reflective zone along the plate interface. The thickness varies from an average thickness of 2 - 3 km in the coupled zone at 24 - 38 km depth to more than 4 km in the zone of aseismic creep at 38-45 km depth downdip the hypocenter of the 1960 earthquake (see figure 10.6). Below 45 km depth a less reflective zone is again observed down to a depth of 55 km where again a stronger patch of reflectivity exists.

In Cascadia the reflections from the E-layer vanish where the oceanic plate encounters the mantle wedge (Nedimović et al., 2003). In the preferred interpretation of the TIPTEQ seismic data, with the onset of the continental Moho just below 40 km depth, the reflectivity corresponding to the E-layer starts at the beginning of the mantle wedge. This reflectivity can be attributed to the continuation of the subduction channel towards depth below the mantle wedge. A similar observation is reported by Calvert et al. (2003) for Cascadia where a lobe of subducted material and sheared crustal rocks, up to 15 km thick, underplates the serpentinized mantle wedge.

The origin of the E-layer in the Cascadia subduction zone was addressed by several authors. Green et al. (1986) interpreted the laminated structure of the E-layer as the lowermost layers of lithified sediments and possibly the uppermost crystalline layers of the oceanic crust underplating the base of the overriding plate, whereas Nicholson et al. (2005) attribute the E-layer to fluids in the upper part of the oceanic crust. A migration of these fluids into the continental crust can explain variations in the thickness of the layer. This is in agreement with Kurtz et al. (1986) who modeled a zone of high electrical conductivity at the depth of the seismic E-horizon caused by saline fluids in the pore spaces of sedimentary and mafic materials of the upper oceanic crust. All three papers place the E-layer at the plate interface between the upper part of the oceanic crust and the base of the continental crust and connect it with processes active at the plate interface. These findings from Cascadia support the interpretation of the reflective band at the plate interface as the seismic signature of the fluid-filled subduction channel in south central Chile. Other studies in Cascadia argue that the E-layer reflection is caused by fluids trapped at a boundary in the continental crust at least 10 km above the plate interface (Hyndman, 1988). This is further supported by receiver function analysis (Cassidy and Ellis, 1993) and a 3D compressional wave velocity model constructed through tomographic inversion (Ramachandran et al., 2005). In this interpretation the top of the oceanic plate is correlated with a thin reflective band (F-layer) below the E-layer. With the available TIPTEQ data for south central Chile the depth of the plate interface is well constrained. The E-layer as interpreted above might then correspond to strong subhorizontal reflections in the continental crust (e.g. from x = 10 - 50 km, z = 24 - 33 km in figure 10.6).

Sato et al. (2005) observed a change in reflectivity in central Japan beneath the Tokyo metropolitan area where the Philippine Sea plate is subducted. Here, a change to reduced reflectivity at the upper surface of the Philippine Sea plate is related to the coseismic slip distribution occurred during large thrust events. Comparisons of the TIPTEQ reflection seismic

section with the slip distribution of the 1960 Chilean earthquake calculated by Barrientos and Ward (1990) did not reveal a connection of changes in reflectivity and slip distribution.

10.1.6. Structure of the continental crust and associated reflectivity

The crustal structure of intercalated metasediments and metabasites is overlain by two great transparent zones close to the surface towards both ends of the profile. The uppermost 8 km appear transparent along the entire profile because of the applied mutes (cf. section 3). The seismic image appears blurred or less reflective in the central part of the profile between x = 47 - 58 km, at all depths down to the plate interface (cf. figure 10.3).

The varying pattern of reflectivity and transparency observed in the overriding plate can be explained in the context of local geology (Hérve, 1988) and morphotectonic segmentation of the region (Mpodozis and Ramos, 1989; Melnick and Echtler, 2007). At x = 47 km the profile crosses the sinistral strike-slip Lanalhue Fault Zone, LFZ (Glodny et al. (2008), see figure 10.2). Its continuation to depth can not be observed in the first few kilometers of the reflection seismic section because of the applied mutes. At about 8 - 10 km depth, the LFZ might be inferred by a lateral change of reflectivity (see figure 10.6). The granitoid Coastal Batholith (Melnick and Echtler, 2007), covered by sediments occurs east of the LFZ and the Eastern Series (ES, Hérve, 1988) and causes an almost transparent image down to 23 km depth where an east-dipping reflector indicates a change to highly reflective material. This high reflectivity may be caused by fluids trapped just below the granite or simply by a change in the lithology. Krawczyk et al. (2007) state that the sediment basins at the surface, comprising interbedded sedimentary and volcanic strata of late Oligocene to early Miocene age have a maximum thickness of no more than 3 - 4 km (Tašárová, 2004). An east-dipping fault plane of the LFZ instead of a purely vertical strike-slip fault is supported by the seismic image and by cross sections shown in Glodny et al. (2008) and two Diploma theses of Chilean students (Ardiles Araya, 2003 and Burón Muñoz, 2003). The proposed subsurface extrapolation of the LFZ is shown with a green and black dashed line in figure 10.6. Some kilometers west of the dashed black line in depths between 8 - 15 km reflector segments with similar dip as the black dashed line are observed (green arrows). This reflectors could be an alternative fault plane for the depth continuation of the LFZ. Test migrations of single or a small suite of shots in the vicinity of the LFZ did not provide further constraints.

The reduced reflectivity in the central part of the profile (x = 47 - 58 km) is bordered by the LFZ to the west. The lateral width of this zone of ≈ 11 km can also be observed in the test migration including the airblast and first-break noise (cf. figure 5.2). Here, the airblast and first-break noise have a different appearance and amplitude than along the other parts of the profile. The reduced reflectivity is also visible in the stacked time section in figure 5.1.

Figure 10.5 shows the local geology along the central part of the reflection seismic profile. The Carboniferous - Triassic Eastern Series high T(emperature) metasediments (Melnick and

Echtler, 2007: unit Pz2, see figure 10.5 and 10.6) which are a Carboniferous - Permian forearc fold and thrust belt (Glodny et al., 2007; SERNAGEOMIN, 2003) correlate spatially with the zone of reduced reflectivity. This unit is followed eastward by a Triassic marine/continental sedimentary unit including volcanic sequences (SERNAGEOMIN, 2003; Melnick and Echtler, 2007: Tr) with an east-west extend of $\approx$ 5 km along the profile. Farther east, an outcrop of the Paleozoic - early Triassic Coastal Batholith was mapped for $\approx$ 5 km before the structures are covered by Quaternary sediments (Melnick and Echtler, 2007: Pzg, Qs). The Coastal Batholith with its intrusions mainly accounts for the observed transparency explained above in the eastern part of the TIPTEQ profile.

The Western Series (WS, Aguirre et al., 1972) is made up of chlorite schists which are exposed towards the coast (Hérve, 1988). They belong to a late Carboniferous - Triassic accretionary wedge (basal accretion, Glodny et al., 2005) which consists mainly of high P(ressure) metasediments and ultramafics (Melnick and Echtler, 2007: Pz1). Both, the schists (WS) and the granite body (ES), are favorable for deep seismic imaging along the profile.

10.1.7. The enigmatic reflector

The nature and the origin of the enigmatic west-dipping reflector at the eastern end of the profile at 40 - 70 km depth (x $\approx$ 120 km, cf. figures 10.3 and 10.6) is not yet clear. Only the west-dipping elements of that feature can be imaged because of the source/receiver geometry (cf. section 5.2.3). The spatial coincidence of its extrapolation to the surface and the trace of the Liquiñe-Ofqui Fault Zone which is a transpressional feature at the magmatic arc (Hérve, 1994; Rosenau et al., 2006; Cembrano et al., 1996), is notable. One might speculate that this bright reflective feature is related to a possible ascent path for melts (partially molten oceanic sdiments/crust) towards the volcanic arc.

High-resolution numerical modeling of a subduction zone setting by Gerya et al. (2006) suggests mixed and unmixed peridotitic plumes due to hydration of the mantle wedge by fluids released from the slab. The mixed plumes contain molten sediments and oceanic crust (molten wet peridotite), whereas the unmixed plumes consist of dry peridotite. The depths where these plumes originate in the numerical model ($\approx$ 80 km depth) correlate roughly with the position of the enigmatic reflection which might be a seismic representation of such a plume. The evolving models show laminated vortexes on top of these plumes which partly migrate underneath the upper plate towards the tip of the mantle wedge. Such vortexes might be an alternative explanation for the enigmatic reflection.

The position of the reflector also coincides with a local anomaly in the P-wave velocity model derived from local earthquake tomography (Bohm, 2004; Asch et al., 2007).
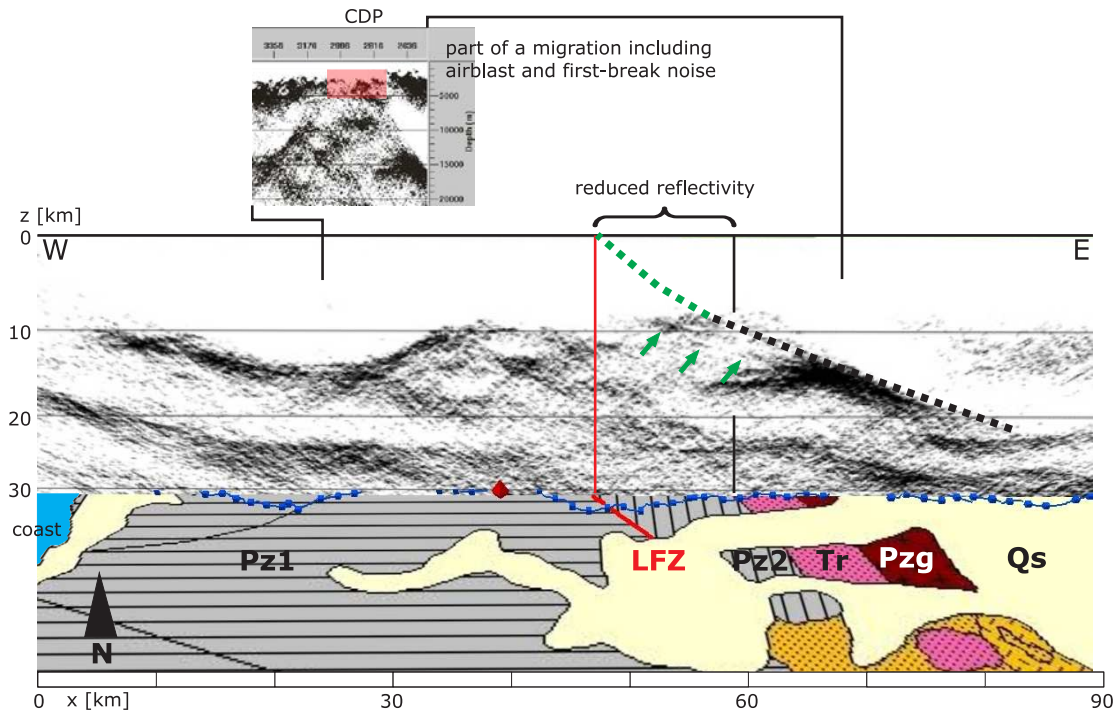
Figure 10.5.: This figure connects the seismic image with local geological units. In this 3–D view, the surface intersects the seismic image at a depth of 30 km. Blue cubes and the blue line represent the shotpoints and receivers south of the profile line. The red diamond marks the position of the 1960 Chilean earthquake. The cause for the less reflective part of the profile is shown as well, resulting from the unit labeled Pz2. The inset on top shows part of figure 5.2, where the reduced reflectivity of the airblast and first-break noise is marked by a red mask. Annotations of structures are the same as in figure 10.6. Geological units and fault data after Melnick and Echtler (2007). See text for details and references.

Pz1 - Western Series high P metasediments and ultramafics (Permian - Triassic)
Pz2 - Eastern Series high T metasediments (Carboniferous - Triassic)
Tr - Rift basins, marine, continental, and volcanic sequences (Triassic)
Qs - Undifferentiated sediments (Quaternary)
Pzg - Coastal Batholith and undifferentiated intrusions (Paleozoic - early Triassic)

reduced reflectivity

Lanalhue Fault Zone

	Pzg (subsurface)
	Qs (sediments)
	Pz2, Tr, Pzg (outcrops)

Eastern Series: Pz2
Western Series: Pz1
    chlorite schists (surface)

**Permo-Triassic
accretionary wedge**

oceanic crust

oceanic Moho

subduction channel

1960

top oceanic crust

hydrated
mantle wedge?

to volcanic arc ?

oceanic lithosphere

subduction channel
continental Moho

W

E

z [km]

z [km]

x [km]

0   50   100   150

Coast

Western Series **LFZ** **Eastern Series**
High P/T | **Low P/T**
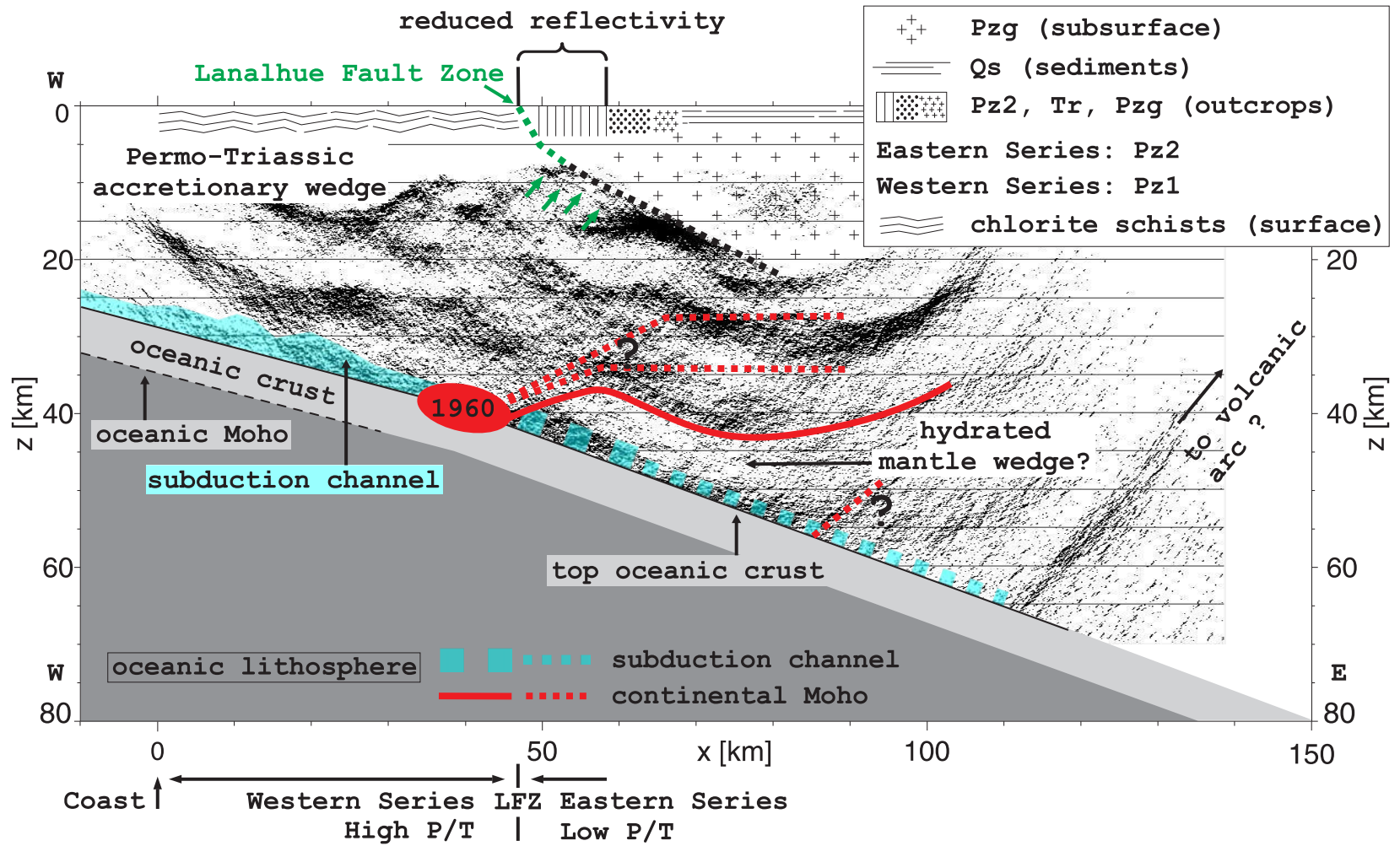
Figure 10.6.: Interpretation of the crustal structure and features at the plate interface for the TIPTEQ poststack depth migrated seismic section. The figure is modified after Groß, Micksch, and TIPTEQ Research Group (2008). See text for details and references.

10.2. Comparison of the seismic section with ...

10.2.1. Kirchhoff Prestack Depth Migration of the NVR data

The active source seismic experiment was carried out in collaboration amongst the GFZ and the geophysics department at the Free University of Berlin. The recorded data were shared and the FU Berlin used their own implementation of the Kirchhoff Prestack Depth Migration (KPSDM) to process the data. The KPSDM image is plotted together with the reference seismic section of this study in figure 10.7. The inset shows only the KPSDM image, high amplitudes are shown in red. Both of the seismic images use the same SPOC velocity model.

The first striking difference between the seismic sections are the depth positions of the otherwise very similar reflectors. Beside the depth difference, the same reflective features are imaged, but some appear more focused or more delimited in the KPSDM image. There is also no prominent reflector which can be attributed to the continental Moho. Figure H.3 in the appendix shows a large-scale version of the KPSDM image.

The prestack image was kindly provided by Kolja Groß (Free University of Berlin).

The following list gives similarities and differences between the prestack and poststack images. The capital letters correspond to the labels in the inset of figure 10.7.

A The same reflective bands with similar thicknesses are observed in the whole crust, in the central part between x = 30 - 60 km the reflective bands show reduced amplitudes in the KPSDM image.

B The same transparent zones are imaged close to the surface (B1, B2). The red bands (high amplitudes) close to the surface result from the high first-break energy still contained in the KPSDM image. The same sharp transition to a high reflective structure is observed at the lower boundary of the transparent zone B2. Here, an east-dipping change in color (bluish to green) might image the subsurface trace of the LFZ with a similar dip as interpreted in the images above.

C The same enigmatic reflection is observed in the east, which has an almost identical dip and length.

D The zone west of the enigmatic reflection also shows a reduced reflectivity and less prominent structures.

E The lowermost reflective band shows a very sharp lower boundary in the KPSDM image which is interpreted to be the plate interface. The oceanic crust shows no reflectivity or change in reflectivity at all, as observed in the poststack image. This sharp boundary fits to the interfaces from the SPOC wide-angle model remarkably well. The reflectivity above E1 is attributed to the subduction channel. A continuation of the subduction channel below 40 km depth might be constraint by the increased reflectivity above E2.
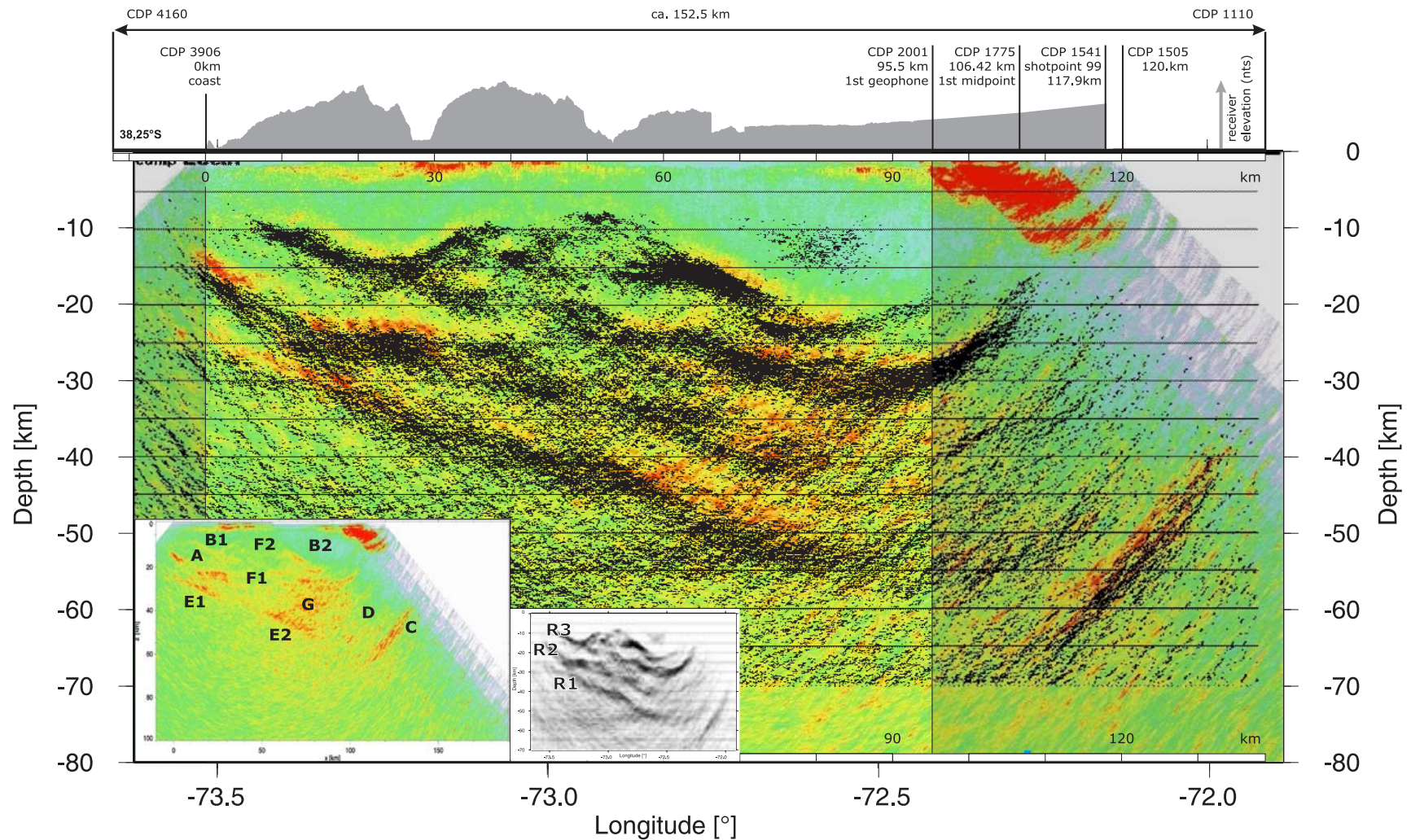
Figure 10.7.: This figure shows a comparison of the results of two processing techniques. The seismic section of this study (poststack processing) is compared to results of a Kirchhoff Prestack Depth Migration (Groß, 2008). The inset shows only the KPSDM image, capital letters label similarities and differences as described in the text. The prestack image was kindly provided by Kolja Groß (Free University of Berlin).

F The central part, between x = 30 - 60 km, shows a reduced reflectivity in the KPSDM image. The reflective bands are very faint (F1). This is attributed to heterogeneities in the eastern part of the Western Series, but this is not observed in the poststack image. At the beginning of the Eastern Series (x = 47 - 58 km) almost no reflectivity is observed in the KPSDM image above 20 km depth (F2). This may be comparable to the reduced reflectivity in the poststack section (cf. figure 10.5).

G No continental Moho onset is observed in both sections. Several horizontal or inclined reflector elements also suggest possible Moho interfaces in the KPSDM image. In between these horizontal structures, the reflectivity pattern is less transparent than in the poststack section.

The mismatch between both images is not a linear shift. The reflective elements in both images become aligned, if the KPSDM image is stretched towards depth (or the poststack image is bulged upwards). The best fit is achieved if the lower end of the KPSDM image comes to place at 84 - 86 km depth. This corresponds to a stretching factor of 1.05 - 1.075, illustrated in figure H.4 in the appendix.

The observed differences may be attributed to the differing processing methods, since the same velocity model is used for migration. First, possible sources for the differences could be different implementations of the Kirchhoff depth migration and the used ray-tracing algorithm to calculate travel-time files. A comparison of these files could provide answers on that, but this information is not provided as an output by ProMAX. Second, during the NMO and stacking applied in the poststack processing seismic traces are stretched in time to allow the hyperbolas of reflective elements to collapse in one point (cf. figure 4.4). To do so, the SPOC velocity model needs to be transformed from an 'interval velocity in depth' to a 'stacking velocity' model. The conversion of the velocity model and the stretching during the NMO could result in imprecise travel-times, resulting in the observed differing migration results. The KPSDM prestack method does not need an NMO or a stacked section, so one intermediate step where travel-time deviations could emerge is missing. Third, the TIPTEQ and all other 2–D seismic data sets contain energy coming from a 3–D environment, meaning that the energy in the shot gathers can also come from out of plane reflections (sideswipes), oblique reflectors, and as seen in figure 4.5 of non-unique reflector positions. The poststack migration is conducted in 2–D. 3–D effects are not considered and may lead to variations in dip and depth of reflective elements (cf. section 4.6). The prestack migration is carried out in a 3–D volume containing the crooked line geometry. This approach might then deliver different depth positions and appearance of reflective elements in comparison to the poststack approach.

The KPSDM migration produces a very similar image to the image using the SPOC velocity model, if the velocity model of the seismological tomography is used. This was also observed for the poststack approach (cf. section 9). So, each method proves internal consistency.

More information about the KPSDM image and related data processing can be found in a PhD thesis by Kolja Gross (2008).

10.2.2. Magnetotelluric (MT) resistivity image

The magnetotelluric experiment component of project TIPTEQ was conducted at the turn of the year 2004/2005 and consisted of a combined onshore/offshore experiment. The 30 MT stations covered an area from one degree west of the trench (at 74.5° W) to the Chilean - Argentinean border at $\approx 71°$ W. Onshore, the MT profile follows more or less the SPOC wide-angle refraction profile line, colored in magenta in figure 10.2. The amphibious approach of the experiment was designed to image the resistivity structure of the complete subduction zone including the presumably fluid-filled subduction channel. A comparison of the MT resistivity image and the seismic section of this study is shown in figure 10.8. The MT image ranges from the station 'QUI' close to the coast to station 'CUR' ≈ 145 km inland. The inset in figure 10.8 shows the complete onshore MT transect. The downgoing oceanic plate was put into the model as a priori information but calculations without the slab resolved similar structures.

The MT resistivity image was kindly provided by Gerhard Kapinos (Free University of Berlin).

Several structures of good conductivity (= low resistivity, colored yellow to red) are observed in the continental crust (cf. figure 10.8). East of the seismic reflection line (see inset), beneath the magmatic arc, two highly conductive patches can be related to melted material. Two highly conductive structures are also observed within the seismic transect. One good conductor is imaged between 80 - 90 km along the profile in a depth of 40 - 50 km. This coincides with the proposed hydrated mantle wedge (cf. figure 10.6). The source of the fluids could be from within the oceanic crust below (dehydration process). The maximum conductivity of the imaged low resistivity feature at the coast coincides with a strong reflective element in a depth of 10 km. This structure might be interpreted to be an accumulation of fluids emerged from the downgoing oceanic crust or rather the related sediments, from the area of the proposed subduction channel in depths above 25 km.

Very high resistivity (dark blue colors) is observed in the central part of the profile and just west of the enigmatic reflection. The low conductivity structure in the central part matches with the less reflective part of the seismic section, attributed to the geology of the western part of the Eastern Series (unit Pz2, see figure 10.5 and 10.6). The tip of that fin-like structure is close to a prominent crustal reflector observed at x = 60 - 70 km (z $\approx$ 15 - 20 km). It was argued before (cf. subsection 10.1.6) that this high reflectivity may be caused by fluids trapped just below the granite or simply by a change in the lithology (Groß, Micksch, and TIPTEQ Research Group, 2008). The high resistivity in the vicinity might rule out the fluids or just border that area of fluid accumulation in the crust. The zone of high resistivity just west of the enigmatic reflection (cf. figure 10.8, x = 100 - 120 km/z = 40 - 70 km) also correlates to a zone with less reflectivity, observed in both seismic sections (prestack and poststack). This might suggest that high resistivity correlates with low reflectivity but the seismic experiment geometry does not allow to image all potential structures in the area in question to confirm this idea (cf. section 5.2.3).

More information about the magnetotelluric experiment and related modeling can be found in a PhD thesis by Gerhard Kapinos (2008) and in Brasse et al. (2008).
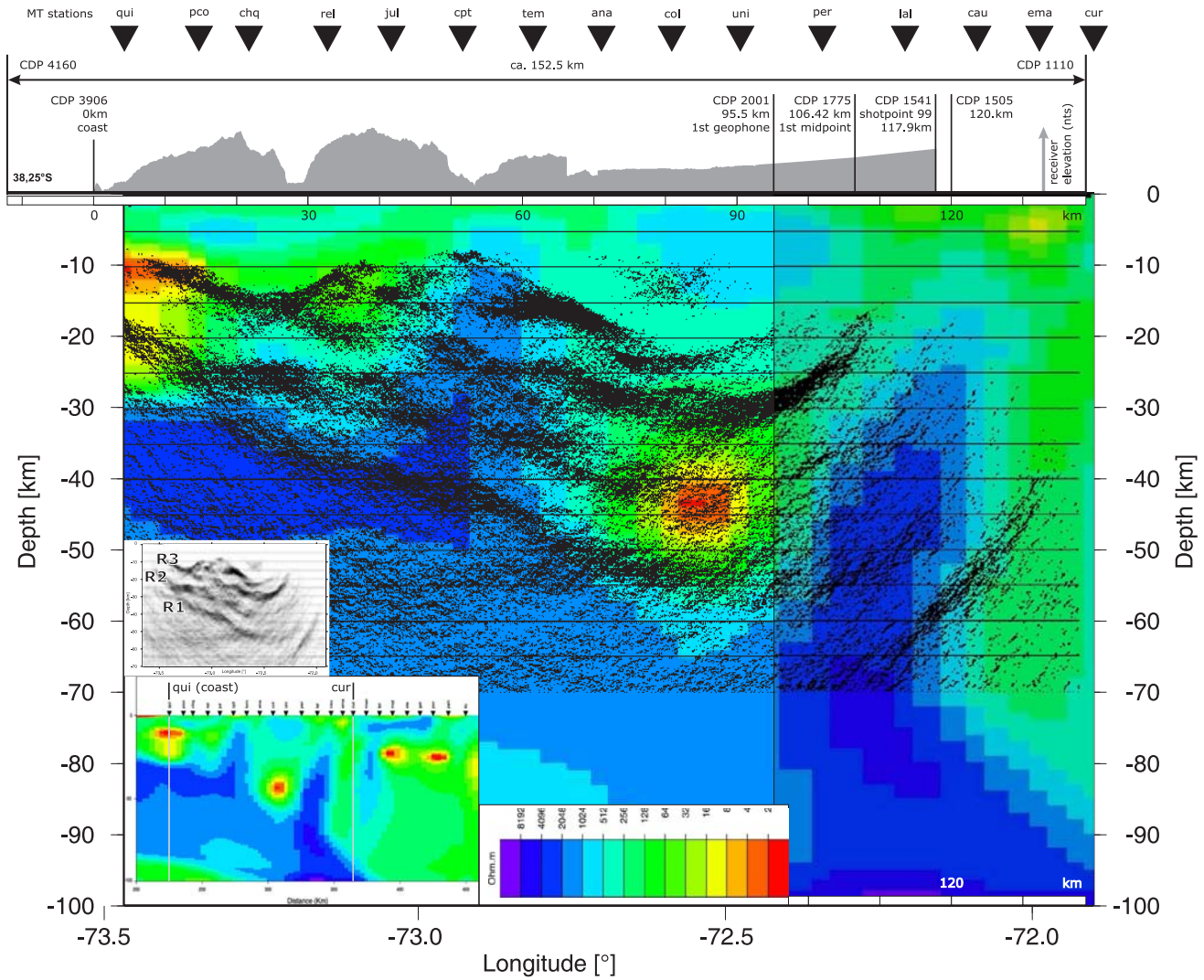
Figure 10.8.: This figure shows a comparison of the poststack seismic section and the TIPTEQ MT resistivity image. Two highly conductive structures are observed along the seismic transect and might be related to the accumulation of fluids. See text for more details. The MT resistivity image was kindly provided by Gerhard Kapinos (Free University of Berlin).

10.2.3. Seismological P-wave velocity model and Vp/Vs ratio

The seismological network of TIPTEQ (Rietbrock et al., 2005; Haberland et al., 2006; Haberland et al., 2008) consisted of 120 land stations and 10 OBS stations which recorded data over a 9 month period. The TIPTEQ reflection seismic line was the center of the network where a denser station interval of ≈ 5 km was used (cf. figure 7.10). Travel-times of 439 earthquakes and of 94 explosive shots from the active source experiment were used to invert for a 3–D P- and S-wave velocity model. The velocity data shown in the following two figures were kindly provided by Christian Haberland (University of Potsdam/GFZ).

The cross section of the seismological P-wave velocity model at 38.25° S was also used for a test migration of the reflection seismic data and resulted in an image almost identical to the reference seismic section using the SPOC velocity model (cf. section 9.4). Only a general vertical shift of less than one kilometer towards greater depths was observed. The reflectors at the lower eastern end of the profile, such as the prominent enigmatic reflection, show greater deviations because of larger differences in both velocity models (cf. figures in section 9.4).

Figure 10.9 compares the reference seismic section to the cross section of the seismological Vp velocity model. Contour lines were drawn every 0.5 km/s. White circles represent regional earthquake hypocenters (Haberland et al., 2006). The red star marks the epicenter of the 1960 Chilean earthquake (Krawczyk and the SPOC Team, 2003), black lines are SPOC velocity model interfaces by Krawczyk et al. (2007). Figure 10.10 shows the seismic image together with the Vp/Vs ratio at the profile latitude calculated from the 3–D P- and S-wave velocity model (Haberland et al., 2008).

The following list links observations by Haberland et al. (2008) in the Vp and Vp/Vs cross sections with the seismic image. The capital letters correspond to the labels in the insets of figures 10.9 and 10.10.

A The subducting plate is imaged by high P wave velocities (> 7 km/s). Yellowish colors (> 7.5 km/s) are aligned just below the lowermost, east-dipping reflective band (R1, cf. figure 10.3). The subducting oceanic crust is observed down to ≈ 80 km depth as a zone with low seismic velocities. The reflection seismic section allows to trace the crust down to ≈ 50 km depth. The oceanic crust shows a high Vp/Vs ratio down to 50 km depth which might point to hydration over a wide area, e.g. in the area of the observed increased reflectivity in the crust, starting at x = 20 km ('C', cf. figure 10.10).

B The velocities in the continental crust range mainly between 6 - 7 km/s. The thickness of the continental forearc reaches its maximum of 50 km at $\approx 72.7°$ W deduced from the velocity image. This is not observed in the reflection seismic section where the second lowermost reflective band (R2, cf. figure 10.3) ends in ≈ 40 km depth at this longitude. Below that band, the less reflective zone may argue for a hydrated mantle wedge (cf. subsection 10.1.3).

C An area in figure 10.10 labeled 'C' marks an increased Vp/Vs ratio (> 1.8) which is interpreted to be hydrated oceanic crust. This fits to the observed increase in reflectivity of the oceanic crust at and below 35 km depth in the reflection seismic section which was interpreted to be caused by the porosity collapse in basalt (cf. section 10.1.2).

D This low velocity zone is assumed to be oceanic crust (cf. figure 10.9) but it might also consist of a localized package of sediments and/or eroded continental crust which was transported down within the proposed subduction channel (cf. subsection 10.1.4). The enigmatic reflector is found just above this feature.

E This high velocity zone is observed along the Central Valley in the entire 3–D velocity model and was also found in earlier seismological experiments, such as ISSA (Bohm, 2004). It is attributed to continental mantle material. The enigmatic reflection is found in the area in question. Further constraints can not be given because the TIPTEQ active source experiment geometry limits the subsurface coverage in that area.

F The marine forearc shows reduced Vp velocities and an increased Vp/Vs ratio farther west. The reduced velocities can be followed along a broad reflective band (R2) in the seismic image down to 27 km depth, at $x = 40$ km.

G Low velocities up to 7 km depth are interpreted to be sediments of the Central Valley which are not imaged in the seismic section since these longitudes are not covered by the experiment geometry. The very smooth gradient between 'G' and the first receivers might be recognizable in results of the first-break tomography conducted in this study (cf. section 10.3).

H The high Vp/Vs ratio at 'H' might point to a local area of serpentinized mantle material. This area is characterized by a reduced reflectivity in the seismic section and correlates roughly with a zone of low resistivity in the MT image (cf. figure 10.8). It needs to be noticed that 'H' is spatially just above the eastern part of the zone labeled 'E'.
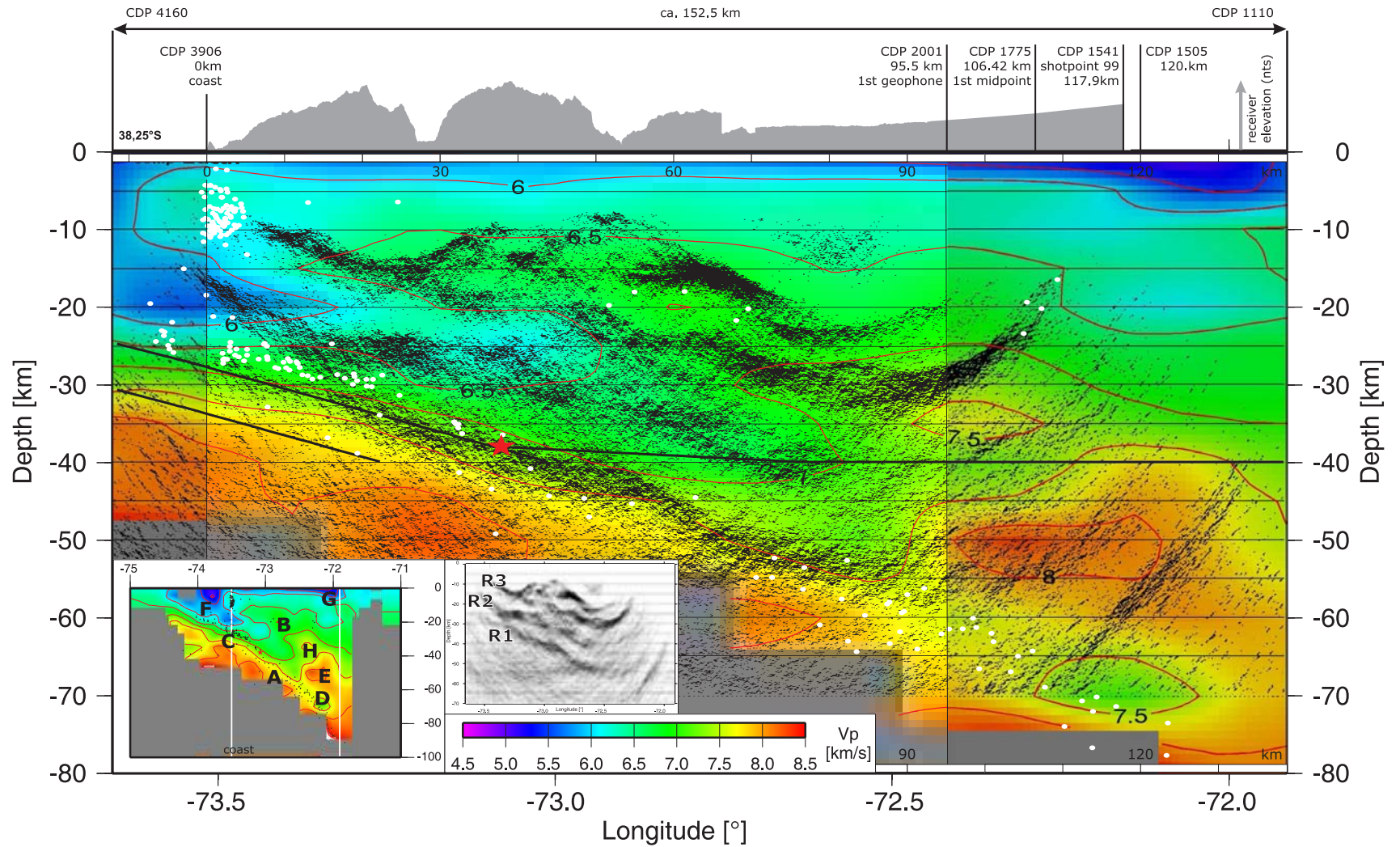
Figure 10.9.: TIPTEQ poststack section overlain on the velocity model derived from the inversion of seismological travel-times of local seismicity and shots from the active source experiment. See text for more details. The velocity data were kindly provided by Christian Haberland (University of Potsdam/GFZ).
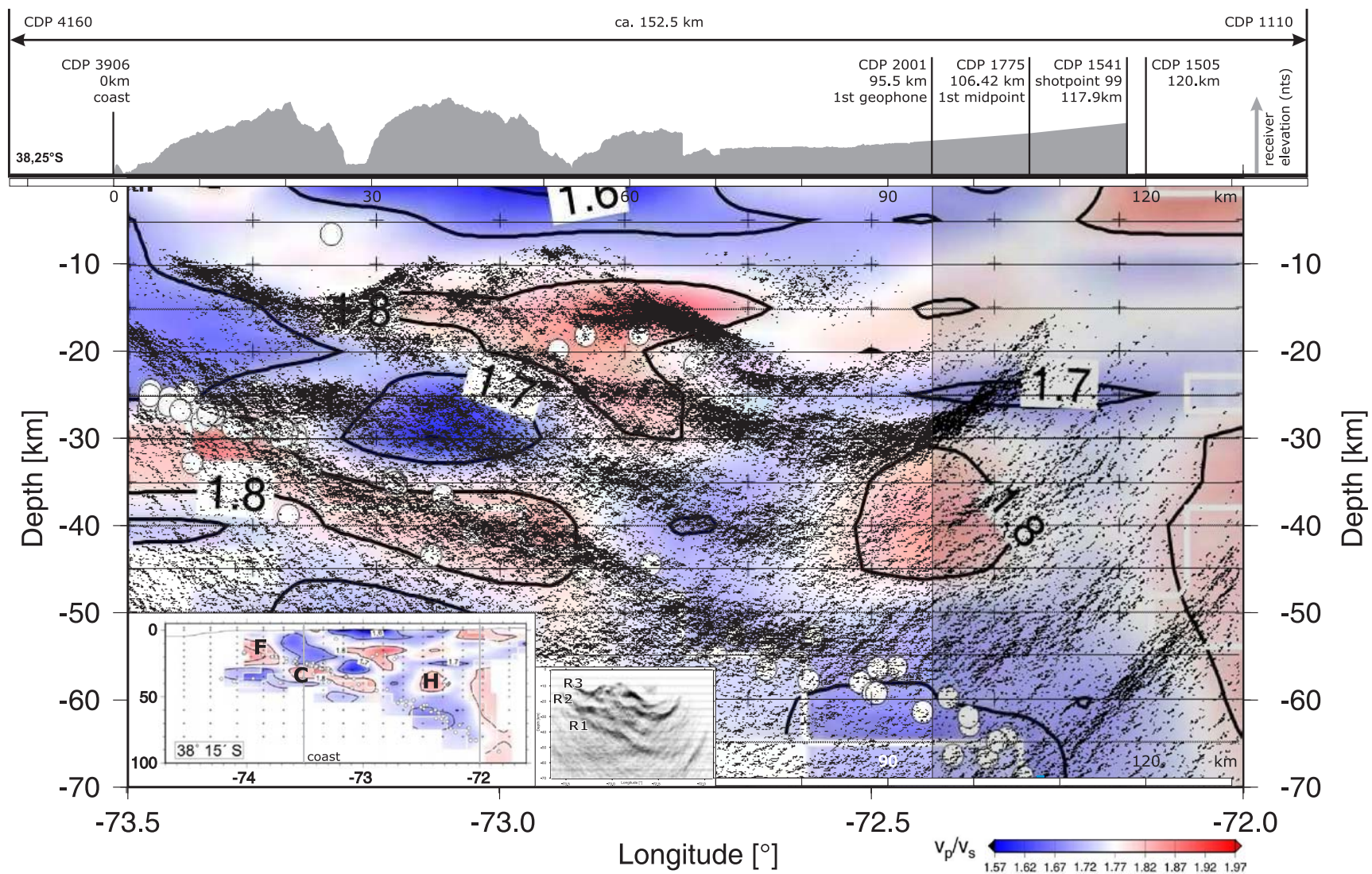
Figure 10.10.: Vp/Vs ratios are plotted along the poststack seismic section of this study. See text for more details. The velocity data were kindly provided by Christian Haberland (University of Potsdam/GFZ).

10.2.4. Receiver functions

Eight teleseismic events could be used for the calculation of 465 receiver functions (RF). The seismological velocity model provided velocities to migrate the receiver functions to depth. The resultant image and interpretation of the converters were kindly provided by Andreas Rietbrock (University of Liverpool, UK). A comparison of the receiver function image and the poststack seismic data is shown in figure 10.11. The RF resolve three converters which appear as red and blue bands. Red colors indicate a velocity decrease, blue colors a velocity increase, respectively. So, the change from red to blue colors in a depth of 30 - 50 km in the western part of the RF image is attributed to the oceanic Moho (see inset in figure 10.11). A faint band indicates the continental Moho below a stronger intra-crustal converter.

The lowermost reflective band (R1) is almost completely contained in the red band above the oceanic Moho proposed by the RF. This could imply that the depth of the interfaces of the SPOC wide-angle velocity model need to be adjusted. In turn, similar migration results with different velocity models support the SPOC model (cf. section 9.4). The faint continental Moho is interpreted to intersect the plate interface in ≈ 50 km depth. These depths seem very unlikely as it was argued in subsection 10.1.3 and by Groß, Micksch, and TIPTEQ Research Group (2008). No continuous reflective band or structure can be attributed to the intra-crustal converter. More information on receiver function in subduction zones settings can be found in papers of Yuan et al. (2006) and Bostock et al. (2002).
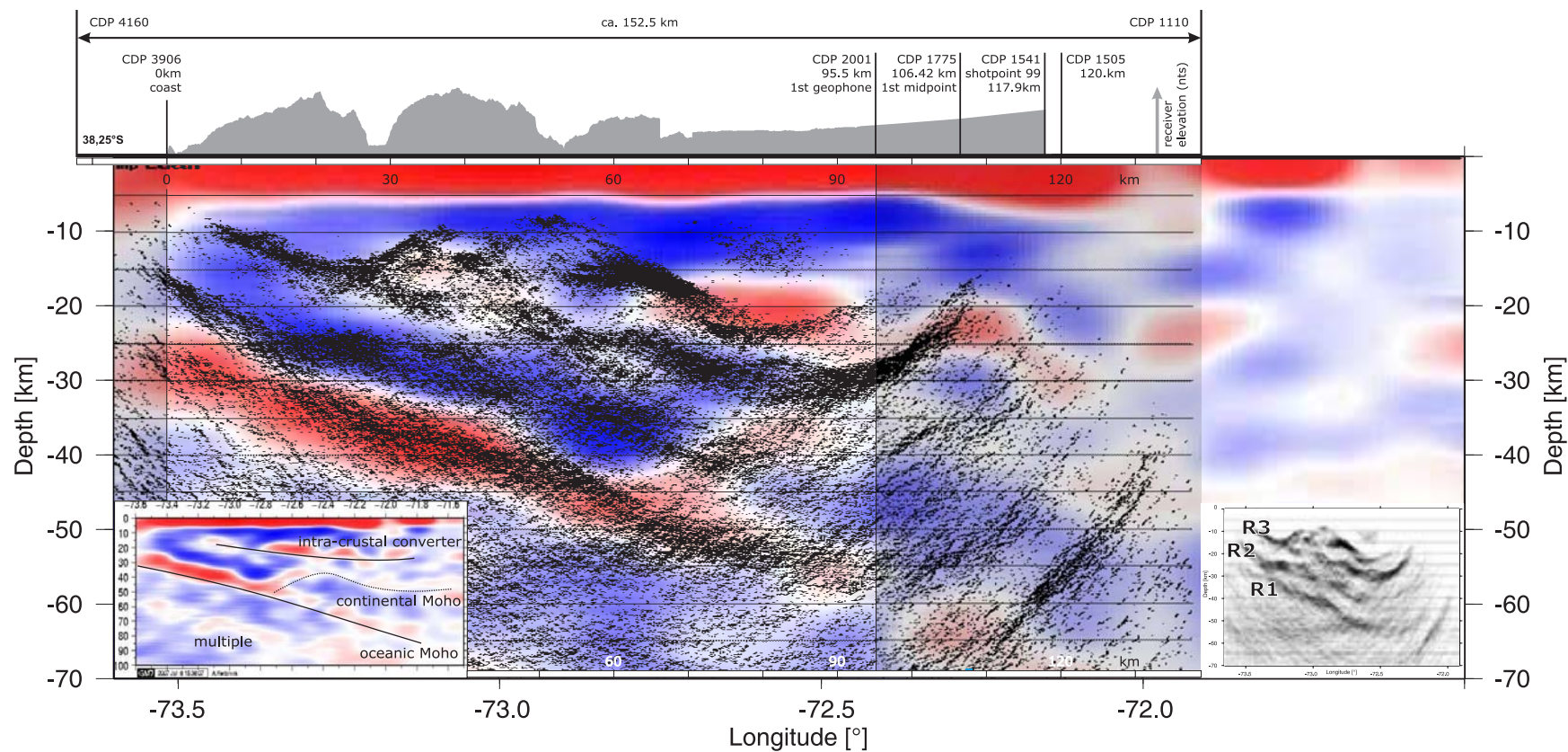
Figure 10.11.: Receiver functions and the poststack seismic image. Red colors show a velocity decrease, blue colors a velocity increase, respectively. See text for more details. The RF image and interpretation of the converters were kindly provided by Andreas Rietbrock (University of Liverpool, UK).

10.2.5. Gravity modeling

Several research projects investigated the gravity field in the study area during the last years, including project TIPTEQ. So, a huge onshore and offshore gravity database is available. The data basis, processing techniques, and modeling results are presented and discussed in a PhD thesis by Tašárová (2004), and in Tašárová (2007) and Krawczyk et al. (2007). Within project TIPTEQ the available 3–D density model was refined and extended. The 3–D plate and Moho interfaces as well as the modeled contact-line between the slab and the continental Moho were kindly provided by Paolo Alasonati (University of Kiel). The gravimetrically derived continental Moho in the 3–D model does not intersect the downgoing slab or the seismic section in all places because of filtering and smoothing applied to the 3–D interface. Where the continental Moho is expected to intersect the TIPTEQ profile – as observed in the 2–D density model – a huge window is observed in the 3–D interface (cf. figure 10.4b).

Figure 10.12 shows the TIPTEQ reflection seismic depth section superimposed on a 2–D density model at the latitude of the TIPTEQ profile as shown in Krawczyk et al. (2007), figure 8.9b. The black rectangle in the inset outlines the part which is shown together with the new seismic data. The red dot shows the piercing point where the 3–D modeled contact-line between the downgoing slab and the continental Moho crosses the seismic section (x = 80 km). The white line represents the cutting plane of the Moho interface from the 3–D model. A mismatch between the white line and the top (corresponding to the continental Moho) of the violet body with a density of 3.23 g/cm^3 is observed. This mismatch results from filtering and smoothing of the 3-D interface.

The short oblique reflector segment at x = 100 - 105 km in a depth of 35 - 40 km, is the preferred position the continental Moho interpreted from the reflection seismic data connects to (cf. figure 10.4 and subsection 10.1.3). This reflective element lies close to the top of the violet body with a density of 3.23 g/cm^3, which supports the course of the preferred continental Moho suggested from the seismic data.

One area of major interest is the brownish colored triangle west of the red dot and above the plate interface, labeled 'unidentified body' (Krawczyk et al., 2007) or 'A' in the inset of figure 10.12. It may be subdivided into two bodies with densities of 3.15 g/cm^3 (upper part) and 3.2 g/cm^3 in the lower part, respectively. The investigation by Krawczyk et al. (2007) revealed that this body is to a large extend responsible for the mismatch between the gravity-derived and refraction-derived positions of the continental Moho from the SPOC and ISSA-2000 experiments. The lower part of the 'unidentified body' may consist of highly hydrated and serpentinized mantle material with a mafic crustal material in the upper part. This mafic crustal material might originate from the intruded granitoids of the Nahelbuta mountains north of the profile. The SPOC wide-angle velocity model suggests a Moho at 38 - 40 km depth which is within the center of the 'unidentified body'.

In contrast, the earthquake catalogue of the ISSA-2000 experiment argues against serpentinized mantel material within the 'unidentified body'. Using the catalog data, the seismo-

genic coupling zone is interpreted to reach depths of 50 km (Bruhn, 2003). If the lower part of the unidentified body is serpentinized, the observed thrust events then occur between the slab and the serpentinite. Peacock and Hyndman (1999) suggested that the down-dip limit of subduction thrust earthquakes is controlled by the formation of serpentinite in the fore-arc mantle. This implies that the serpentinized mantle wedge and related continental Moho should then appear for the first time below 50 km depth. Further explanations for the origin of the unidentified body and the observed mismatch in Moho depths are given in the paper by Krawczyk et al. (2007).

Unfortunately, the TIPTEQ seismic image can not pinpoint an exact position of the Moho (38 or 50 km depth, cf. section 10.1.3 and figure 10.6), or identify structures that point to a divided body 'A'. A broad reflective band (R2, cf. figure 10.3) is positioned just above the unidentified body (cf. figure 10.12) from x = 10 - 30 km where a strong reflectivity is observed within the band. At x = 30 km the reflective band smoothly deepens into the area in question. The reflectivity of the band ceases at the eastern end of the body.

The shape of the density bodies above 25 - 30 km depth show a westward dipping border in the middle of the profile (cf. figure 10.12). This border cuts through prominent reflective bands and a large area of low reflectivity at the surface. In addition, the angle is in contrast to the proposed eastward dip of the Lanalhue Fault Zone (cf. subsection 10.1.6). Perhaps, this can be attributed to a density gradient within the granitoid body which is probably the causes of the eastern transparent zone up to depths of 26 km. The newly imaged geometry of reflective bands and transparent zones could be incorporated into the density model to adjust the borders of the bodies in question. This might result in new density constraints along the TIPTEQ transect.

In figure 10.13 the seismic image is shown together with the combined results of former experiments in the profile area as presented in figure 8.10 in the paper by Krawczyk et al. (2007). This figure includes the density model just presented above above, the unidentified body is outlined by white lines. The Vp tomographic velocity model from the ISSA-2000 experiment is shown above the density model (Bohm, 2004). Major interfaces from the SPOC refraction seismic velocity model are shown in thick black lines. The enigmatic reflector (cf. subsection 10.1.7) is visible at the lower eastern end of figure 10.13 in the vicinity of a local anomaly of high P-wave velocities, labeled 'B'. These increased velocities are attributed to 'normal' continental mantle in contrast to the hydrated mantle proposed west (Krawczyk et al., 2007).

Chapter 11.1 integrates the results related to the reflection seismic image and the conducted comparisons, the next chapter discusses the results from the first-break tomography.
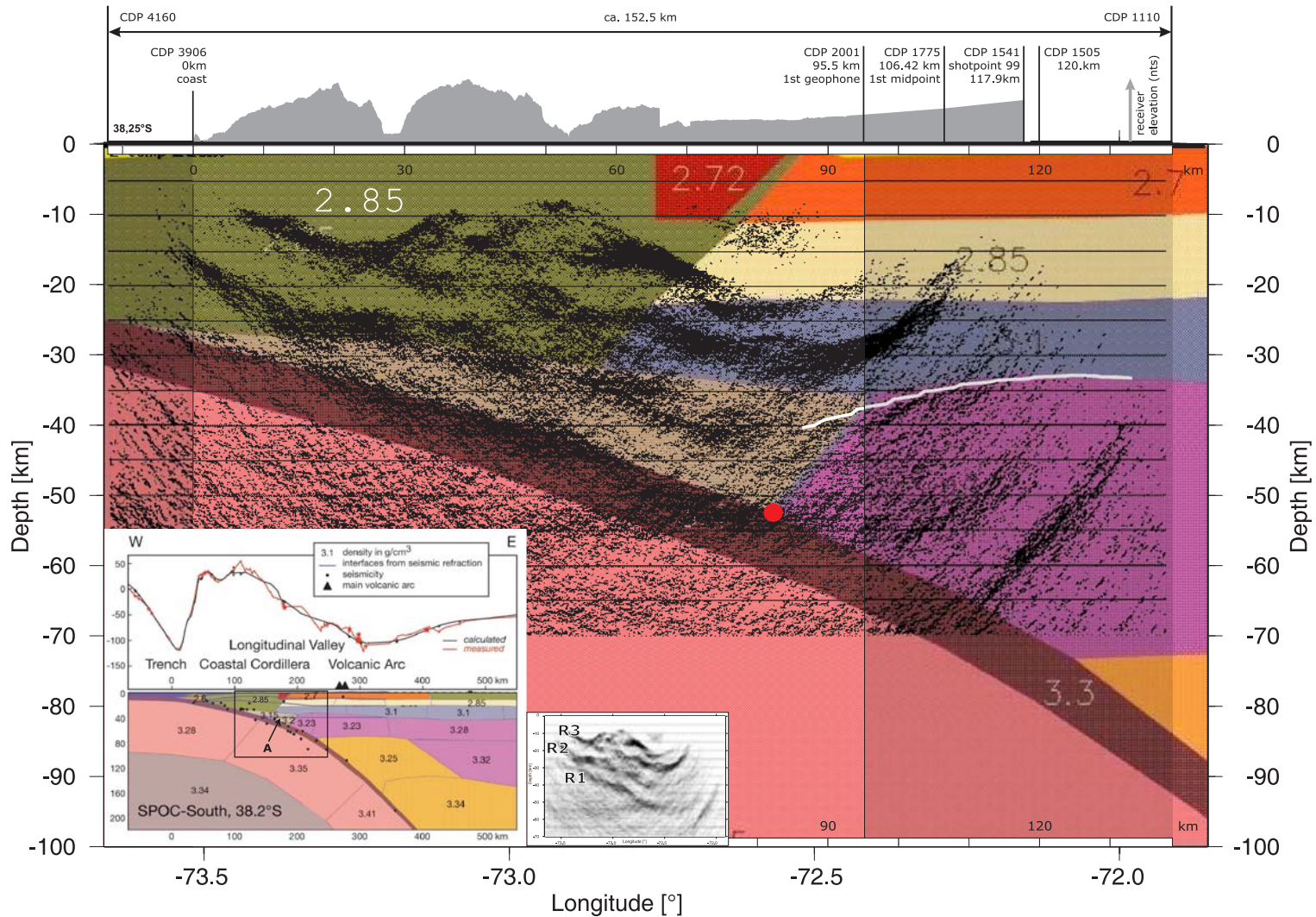
Figure 10.12.: This figure shows part of the available density model at the profile latitude. The inset displays the complete model extent. The black rectangle outlines the shown part of the model. Hydrated/serpentinized mantle might be found in the area labeled 'A' (Krawczyk et al., 2007). The red dot shows the point of intersection of the continental Moho with the oceanic crust obtained by 3–D density modeling, the white line represents the Moho interface from the TIPTEQ 3–D model. The 3–D plate and Moho interfaces as well as the modeled contact-line between the slab and the continental Moho were kindly provided by Paolo Alasonati (University of Kiel). Modified after Krawczyk et al. (2007), see text for more details.
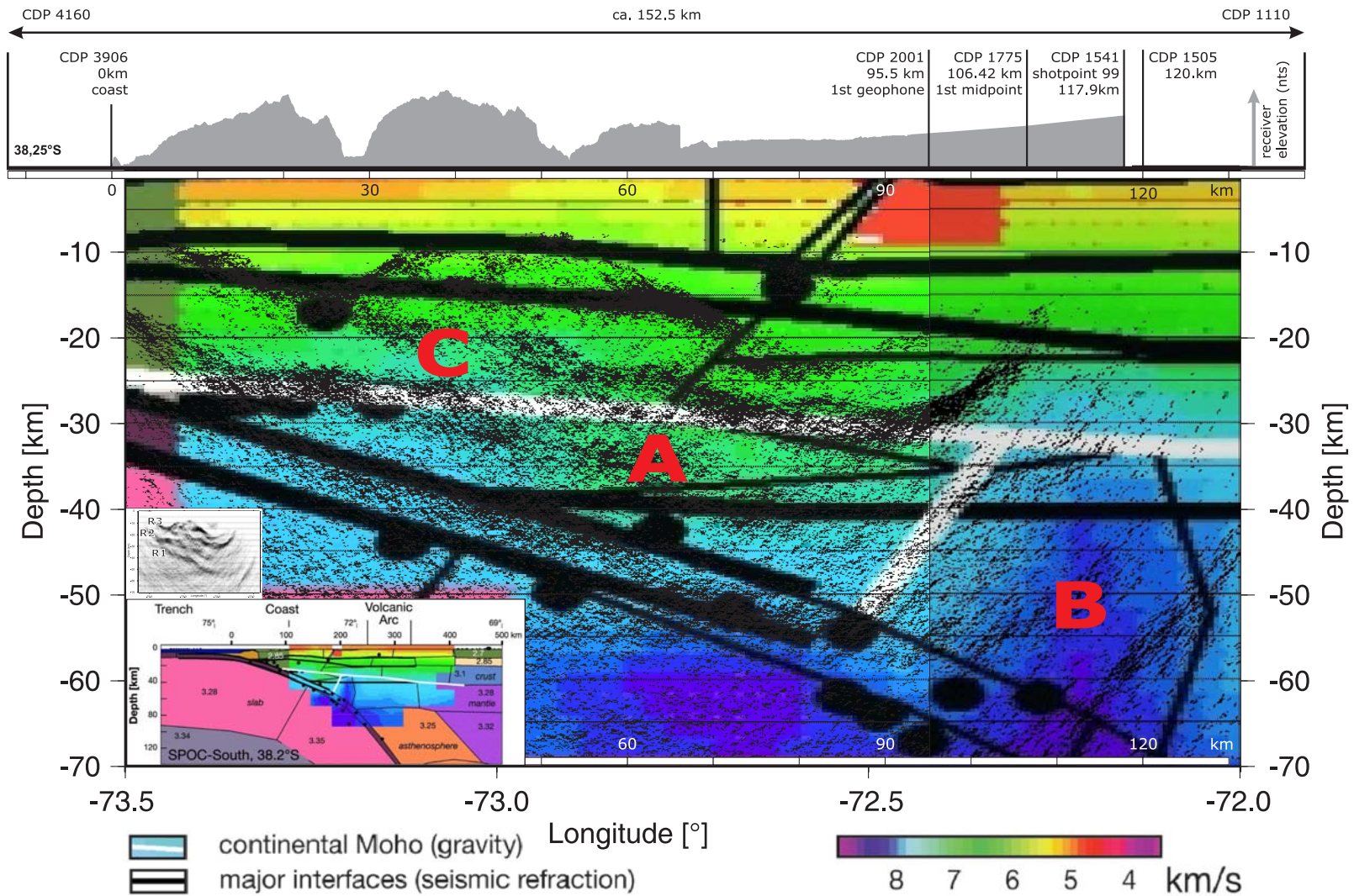
Figure 10.13.: This figure shows the seismic model underlain by the ISSA Vp tomographic velocity model and wide-angle velocity and density derived interfaces. A: Region of possibly hydrated/serpentinized mantle; B: Normal mantle; C: SPOC velocity model 7 km/s layer. Modified after Krawczyk et al. (2007), see text for more details.

10.3. Interpretation of the TIPTEQ first-break tomographic Vp image

After the interpretation and comparisons of the crustal scale seismic images, the interpretation of the near-surface first-break tomography is shown next. Chapter 6 - 8 describe the theory, the inverse calculations, and the important validation tests which were conducted to obtain the final images. The NVR and SH shots as well as the three shots off the line in the east were used for the inversion shown in figure 10.14, confer map in figure 2.5 for shotpoint locations. A vertical exaggeration of ≈ 4.3 is used in the image below whereas an exaggeration of 5 is used in the following 3–D views. Final inversion images without the shots off the line and corresponding figures without vertical exaggeration are shown in the appendix (cf. figures F.13 - F.16, page 225 - 228). Important parameters of the inversion such as cellsizes or starting velocity model can be found in the beginning of chapter 8.
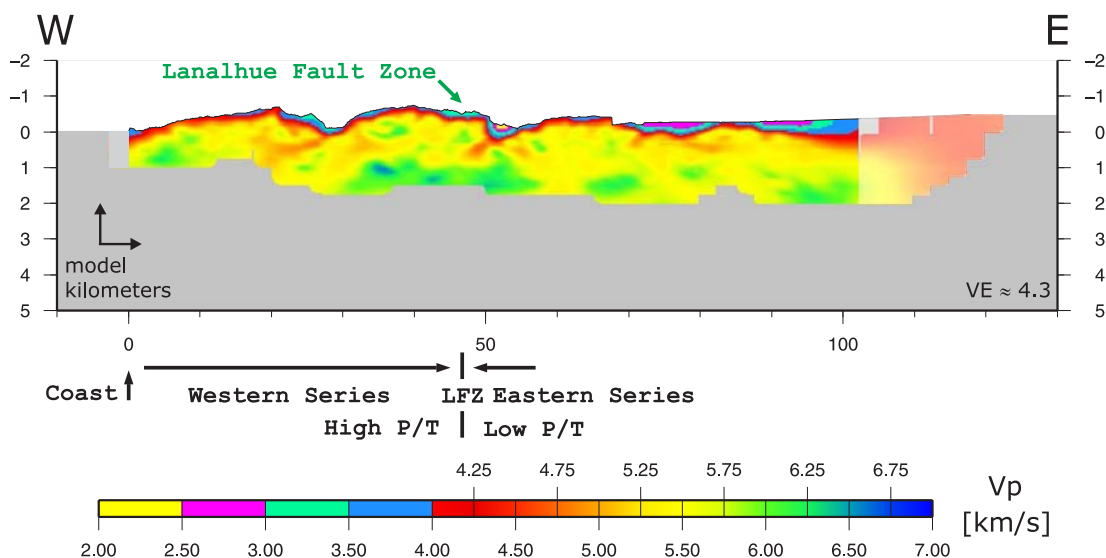
Figure 10.14.: Final tomographic image using NVR, SH shots and three shots off the line in the east. The sediment covered Central Valley starts at approximately x = 70 km.

The inverted velocities in figure 10.14 show a lively pattern with a lot of small scale structures. The eastern part of the section clearly exhibits more sediments than the Western Series (WS) west of the LFZ. The sediments may reach velocities ≤ 4.5 km/s (Brocher, 2005; Castagna et al., 1985). The onset of the sediments in the Central Valley is observed at x $\approx$ 70 km. The vertical step in the elevation at x = 68 km results from a north-southward change of the receiver line from the outcrops of the Coastal Batholith into the Quaternary sediments of the central Valley (Melnick and Echtler, 2007: Pzg, Qs). The velocity distribution below the two easternmost shots (x > 105 km) must be considered a general trend which suggests a thickening of the sediments. The confidence area ends at x $\approx$ 105 km.

The focus of the interpretation is on the eastern part of the tomographic section. This part of the Central Valley shows several separate units which now can be traced below the surface for the first time. The Western Series is mainly composed of one, but heterogenous unit, which makes it difficult to interpreted the subsurface velocity structures. The following figures show 3–D views of the survey area. The tomographic image is shown together with the local geological map after Melnick and Echtler (2007). The view on the TIPTEQ profile is approximately from the north towards south, in contrast to the figures shown before. This way, the link of the geological features towards depth can be illustrated more clearly due to the outcrop conditions north of the profile line. Spatial errors occur for obliquely striking elements due to the crooked line field geometry and the projection on a 2–D ideal profile line (cf. figure H.5 in the appendix).

Figure 10.15 shows the local geology above the tomographic section. The arrows indicate the coordinate axes and give the visible extend of the tomographic section in z and x direction. The Coastal Batholith (labeled Pzg) is observed beneath a sedimentary cover of ≈ 1 km in the east. Sparse sedimentation is observed on top of the Coastal Cordillera, except for sediment-filled river valleys. The x-position where the Lanalhue Fault Zone (LFZ) crosses the profile line is marked by a black arrow. Due to the crooked receiver line the piercing point lies east of the position indicated by the geological map (cf. figure H.5). The dipping green to yellow transition in velocities, marked by the white arrow, must not be considered the subsurface trace of the LFZ. The fault plane as interpreted in figure 10.6 reaches greater depth faster than the velocity isoline described above, thus needing a steeper dip.
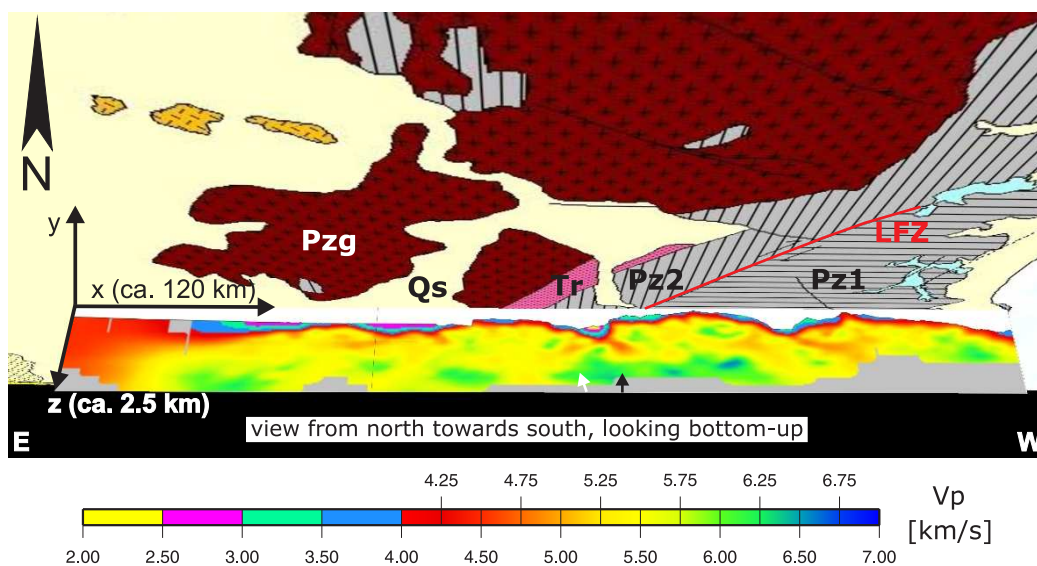
Figure 10.15.: Final tomographic model and local geology, see text for more details.

Pz1 - Western Series high P metasediments and ultramafics (Permian - Triassic)
Pz2 - Eastern Series high T metasediments (Carboniferous - Triassic)
Tr - Rift basins, marine, continental, and volcanic sequences (Triassic)
Qs - Undifferentiated sediments (Quaternary)
Pzg - Coastal Batholith and undifferentiated intrusions (Paleozoic - early Triassic)

The following figures 10.16 and 10.17 show details along the tomographic image from 'below' (a) and 'above' (b) the geological map which intersects the tomographic image at sea level. Structures above 4 x 0.5 km (x times z) can be considered in the interpretation along the whole profile (cf. section 8.4).
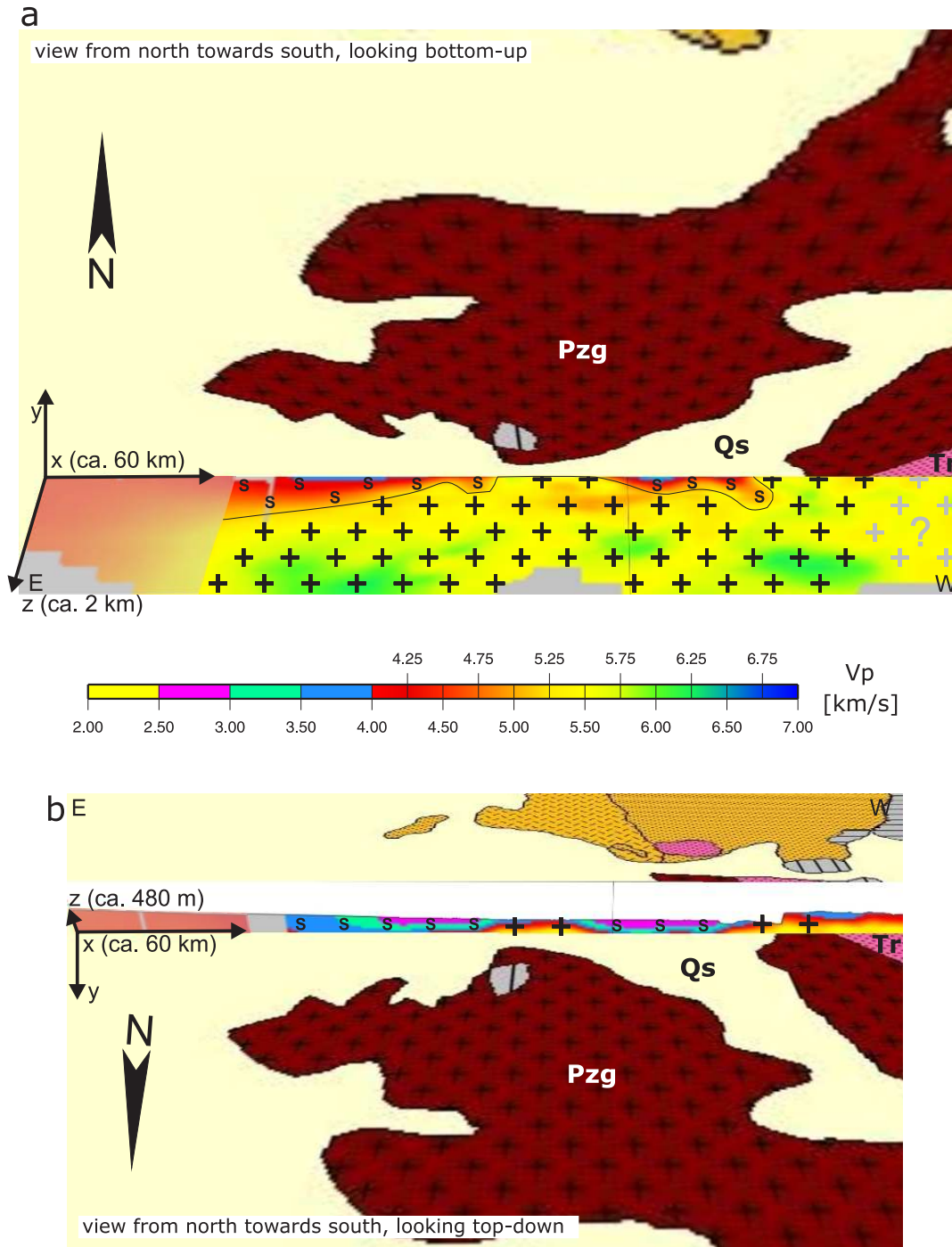
Figure 10.16.: This figure illustrates the subsurface continuation of the Coastal Batholith, Pzg (signature: +) and the Quaternary sediments, Qs (S). The thickness of the sediments reaches ≈ 1 km at the western border of the mask, which limits the confidence area.
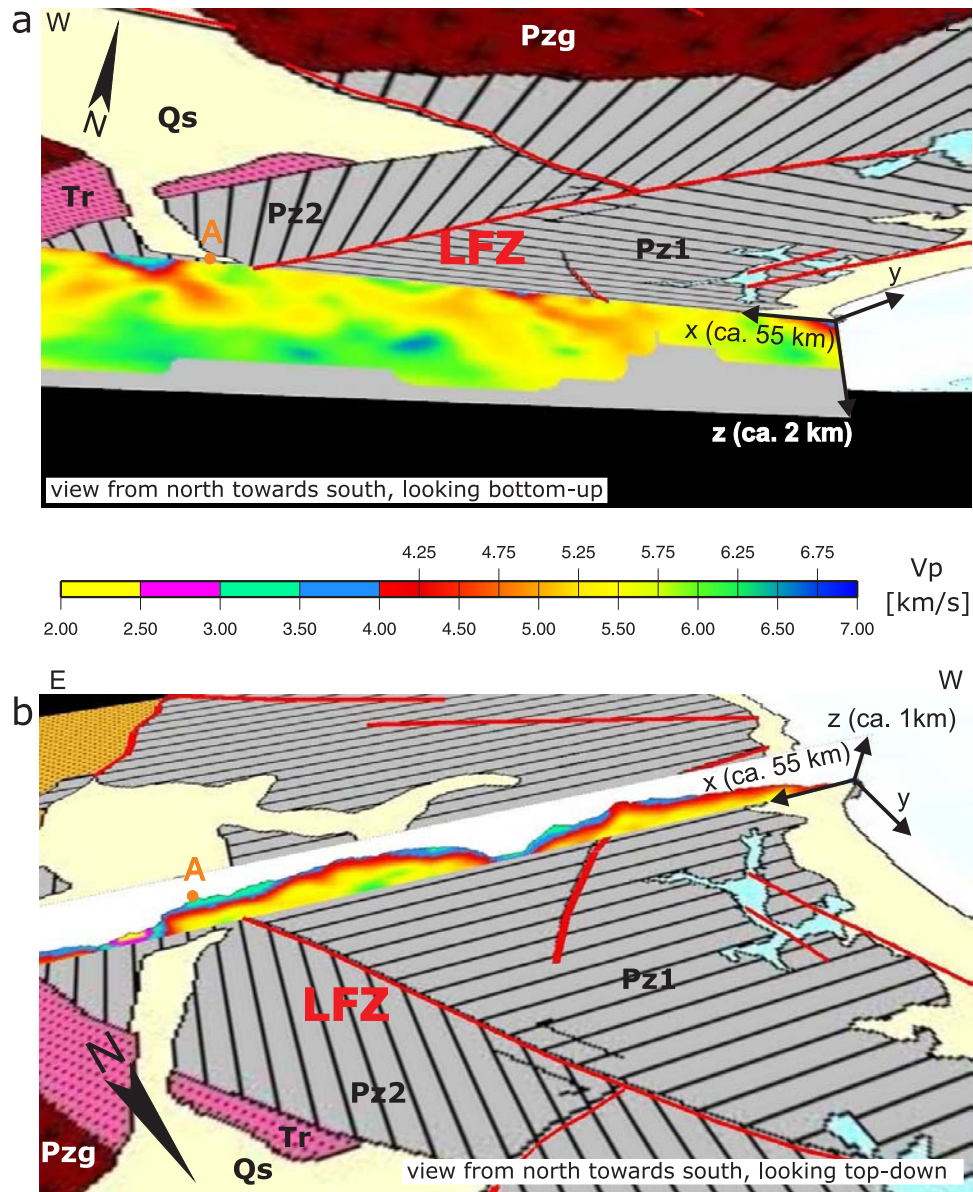
Figure 10.17.: No apparent, unambiguous correlation between velocities and mapped geology is observed in the Western Series (Pz1). A more detailed geological map might enable to trace surface structures towards depth. No particular velocity structure or change in velocities can be attributed to the LFZ. The crooked line geometry reaches its maximum deviation (< 3 km) in the vicinity of the LFZ, so the piercing point of the LFZ lies east of the position indicated by the geological map (marked A, cf. figure H.5).

10.4. Integrative Interpretation

Figure 10.18 shows an integrative interpretation of structures and processes active in the Chilean subduction zone along the TIPTEQ transect at 38.25° S. See section 10.1 and 10.2 for more details and references.

Starting below the coast and along the oceanic crust, the Vp/Vs ratio of the seismological velocity model (Haberland et al., 2008) shows an increased value along the east-dipping interface that coincides with the oceanic crust defined by the SPOC wide-angle model up to a depth of 45 km. This feature partly reaches into the suggested mantle wedge, with respect to the SPOC continental Moho. In the lower part of the high Vp/Vs zone an increase in reflectivity is observed in the continental crust below 35 km depth. This is interpreted to be related to the release of fluids due to the porosity collapse in basalt, which can occur between 200° - 400° C (definition according to Hyndman and Peackock (2003)). This range of temperatures may be assumed here, since a value of $\approx 250°$ C was modeled at 26 km depth along a datum on a profile at 36° S (M. Heesemann, University of Bremen, pers. comm.).

A clear structurally imaged boundary marking the position of the continental Moho could not be found in the TIPTEQ NVR data. The dewatering of the downgoing oceanic crust might lead to serpentinized forearc mantle material that reduces the velocity contrast between continental crust and mantle and thus hampers the formation of an explicit Moho reflection in the seismic image (Bostock et al., 2002; Nicholson et al., 2005; Abers et al., 2006). High Vp/Vs values are observed at the tip of the mantle wedge – considering the SPOC Moho interface at $z \approx 40$ km – but not within the wedge farther east. Several potential Moho interfaces may start in the vicinity of the relocated 1960 Chile earthquake hypocenter at the end of the seismogenic coupling zone (Krawczyk and the SPOC Team, 2003). The preferred Moho interface (red solid line) starts right below 40 km depth, rises to 37 km depth and continues underneath a broad crustal reflective band (R2) to the east. Here it connects to a short oblique reflective element that correlates with Moho interfaces from 2–D and 3–D density modeling (Paolo Alasonati, University of Kiel, pers. comm). The corresponding mantle wedge between the preferred Moho and the downdip continued subduction channel on the top of the oceanic plate is highly transparent in the poststack seismic section (see figure 10.18).

TIPTEQ transect at 38.25° S
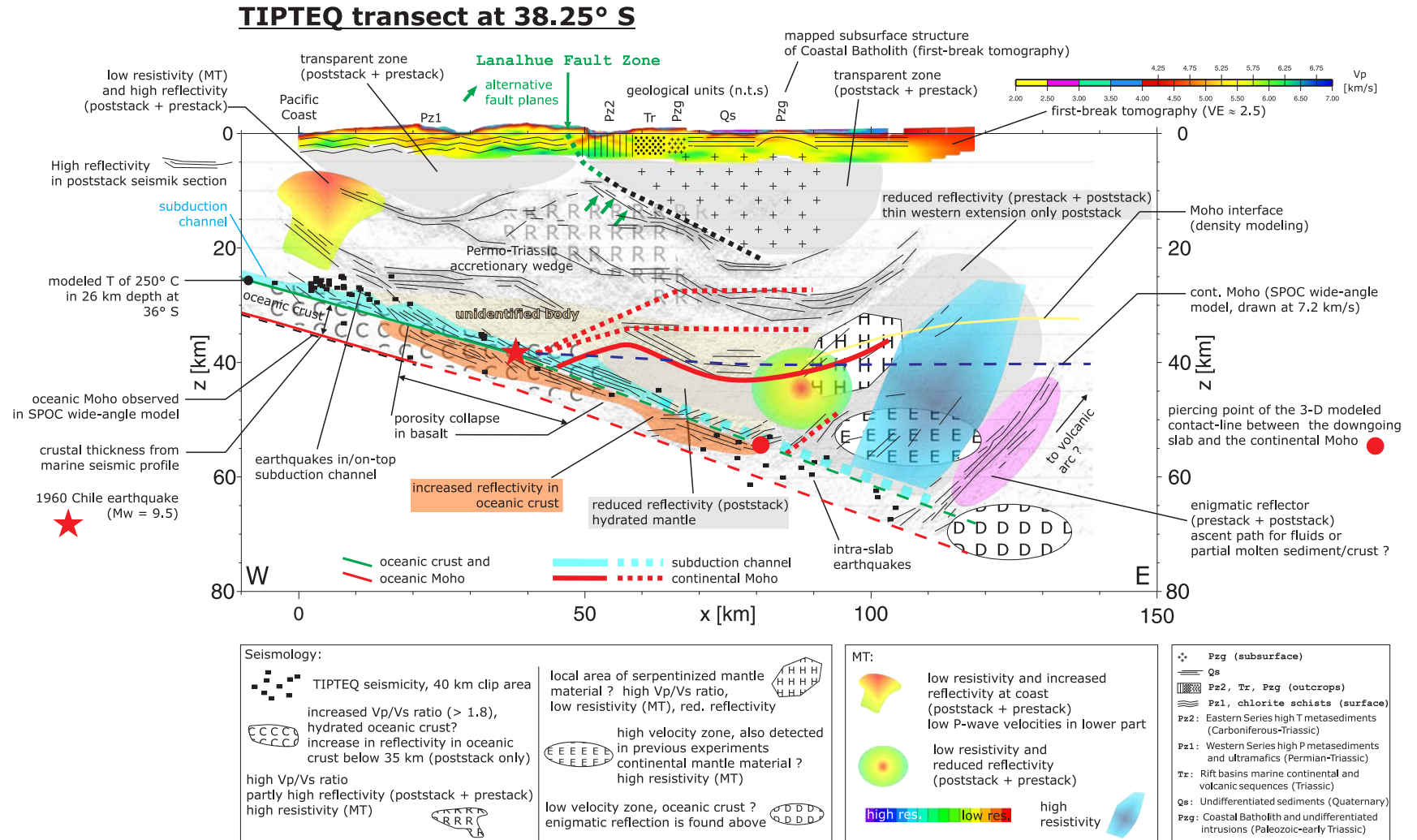
Figure 10.18.: Integrative interpretation of structures and processes active in the Chilean subduction zone along the TIPTEQ transect at 38.25° S. See text and section 10.1 and 10.2 for more details and references.

A second position where the continental Moho might intersect the oceanic plate may be in approximately 50 - 60 km depth. Here, the TIPTEQ reflection seismic data do not provide reliable constraints, because of low coverage at the eastern end and east of the receiver line. This part of the section is only illuminated by three shots within the Central Valley. Only a local patch of increased reflectivity ($z \approx 55$ km) is observed there in the seismic section. Other geophysical methods suggest an onset of the continental Moho on that depth range. The seismological tomographic velocity model (Haberland et al., 2008) suggests the crust to reach a thickness of 50 km at 72.7° W. The velocity isolines (e.g. 7.5 km/s), that follow the oceanic crust turn steeply upwards at $x \approx 90$ km, encompassing presumably continental mantle material (body labeled 'E') underneath. Density modeling (2–D and 3–D) results in a possible piercing point of the Moho in approx 55 km depth. In contrast, other intersections of the Moho with the oceanic plate are possible in density modeling, e.g. depending on the density composition of or within the 'unidentified body' (Paolo Alasonati, University of Kiel, pers. comm; Tašárová, 2007; Krawczyk et al., 2007). This 'unidentified' body could be a divided body with highly hydrated and serpentinized mantle material in the lower part, together with a mafic crustal material in the upper part. This interpretation would require the SPOC continental Moho to be drawn where velocities exceed 7.2 km/s, thereby supporting this model.

The continental Moho interpreted from the receiver functions (Andreas Rietbrock, University of Liverpool, pers. comm., cf. figure 10.11) is generally found in shallower depths. It might reach its maximum depth at the intersection of the slab and the Moho as given by the SPOC data. The clear change in amplitude which occurs at a firm change of crustal material with 'low' velocities to mantle material with 'high' velocities is biased by the presumably serpentinized continental mantle material. The serpentinisation reduces the velocity contrast between continental crust and mantle and thus hampers the formation of an explicit Moho signal along the highly hydrated tip of the mantle up to the plate interface. The expected phase reversal of crust to continental mantle vs. continental crust to oceanic crust should occur at the transition from continental Moho to oceanic crust, but here, it is smeared out.

Seismicity below 40 km depth is interpreted to occur below the plate interface (intra-slab), whereas the seismicity above 40 km is supposed to occur in the oceanic crust or above (Haberland et al., 2006). This interpretation implies, that the locked seismogenic coupling zone might end at ≈ 40 km depth, followed downdip by the transitional and free slip zone. This, in turn, places the intersection of the continental Moho to depths of ≈ 40 km.

To conclude, the position of the continental Moho is not observed clearly in any method, the hope to locate the continental Moho with the TIPTEQ high resolution reflection seismic profile was not fulfilled. Gravity modeling provides ambiguous results depending on the density distribution within the unidentified body. RF show only a faint, presumably biased signal due to smooth velocity variations within the serpentinized continental mantle wedge. The combination of results from former experiments (SPOC, ISSA) together with relocation of the 1960 earthquake, the TIPTEQ seismicity and the reflectivity distribution observed in the TIPTEQ

reflection seismic section point to a continental Moho depth of ≈ 40 km. Especially the SPOC velocity model where the oceanic Moho is clearly observed in the data, thus constraining the plate geometry, and the verification of the SPOC velocity model with a migration of the TIPTEQ reflection seismic data using the independently derived P-wave velocity model of the TIPTEQ seismology group argues for Moho depth of ≈ 40 km (cf. chapter 9).

The proposed subduction channel (Cloos and Shreve, 1988a) is interpreted according to the observed reflectivity above the plate interface (see figure 10.18). The mélange of trench deposits, off scrapings from the base of the upper plate by tectonic erosion, and of material from the top of the oceanic crust is expected to be highly reflective, as material here differs from its surroundings, thus inducing a strong impedance contrast. An additional process leading to high reflectivity may be the dewatering of sediments carried down in the subduction channel and the migration of fluids into the continental crust. High Vp/Vs ratios ('C') are also partly observed within in the subduction channel (e.g. at x ≈ 10 km or x = 40 - 50 km). Thickness variations may be attributed to the internal dynamics of the channel, where a narrowing of the subduction channel leads to an upflow of material, and thus causes a thickening of the channel further up-dip. This process is one possible explanation for basal accretion, and may be linked to the current uplift observed in the Coastal Cordillera (Rehak et al., 2008). Between x = 0 - 40 km the upper bound of the subduction channel may be delimited by the observed TIPTEQ seismicity (Haberland et al., 2006).

East of x = 80 km, different geophysical methods recognize different signatures of possibly related or similar processes, showing the complexity of the subduction zone system. First of all, a reduced reflectivity is observed (see figure 10.18). The shot/receiver geometry covers a subsurface from the coast to the first midpoint at 106 km. Reflective elements east of the first midpoints are imaged because their dip reflects seismic energy back into the 18 km long receiver spread. The more the spread moves to the west, the steeper inclined the reflectors must be to be enable to reflect energy back into the active spread. The depth migration moves the reflective elements to their true subsurface position. The lack of receivers east of 95.5 km causes the lack of e.g. horizontal structures, which might though still exist, and might also cause the reduced reflectivity. The other possible cause of low reflectivity is, of course, the properties of the subsurface material.

Results of the MT (Gerhard Kapinos, Free University of Berlin, pers. comm.) and seismological branch of TIPTEQ show strong anomalies or notable observations in the area in question. One good conductor (low resistivity) is mapped between 80 - 90 km along the profile in a depth of 40 - 50 km. This coincides with the proposed hydrated mantle wedge underneath the preferred Moho interface. Here, reduced reflectivity is observed in the the pre- and poststack reflection seismic sections. This area is still fairly imaged since the receiver line reaches up to x = 95.5 km. The source for this high-conductivity zone could be fluids from the oceanic crust below (dehydration). A high Vp/Vs ratio is observed in an overlapping area ('H') east and above this zone, interpreted to be a local area of serpentinized mantle. This interpretation argues against the preferred continental Moho interface (red line), because the area is cut by

the Moho. The high Vp/Vs ratio isoline (> 1.8) at 'H' suggest a Moho rising with a steeper angle towards 30 km depth. High P-wave velocities (> 7.5 km/s) are observed close to the upper limit of the area marked 'H'. The opposite is observed just east of these two anomalies. Rather low Vp/Vs ratios coincide with a high resistivity and high P-wave velocities ('E', $>$ 8 km/s). High P-wave velocities were also observed in a tomographic P-wave model derived of the ISSA seismicity. This zone is interpreted to be 'normal' continental mantle (Bohm, 2004; Krawczyk et al., 2007). The reflection seismic images (prestack + poststack) show no reflectivity pattern or structure to distinguish between the two zones described above. This is either due to a general low reflectivity or the geometrical aspect discussed above. The prestack image was kindly provided by Kolja Groß (Free University of Berlin).

The enigmatic reflector, the strongest and most continuous reflective element in the lower eastern part of the seismic sections (see figure 10.18, x = 110 - 120 km) delimits the area of high and low resistivity and opposed Vp/Vs ratios towards the east. Beneath the enigmatic reflection, 'D' marks a low velocity zone (< 7.5 km/s) in comparison to the surrounding velocities (Haberland et al., 2008). This zone is interpreted to consist of oceanic crust. The seismic images show no apparent reflectivity constraints.

The continental crust, characterized by broad arching, highly reflective bands exhibits high conductivity (low resistivity) below the coast. This low in resistivity might result from migrating fluids originating from the underlying subduction channel and/or oceanic crust. High, localized reflectivity paired with the described low resistivity is especially observed in the prestack seismic section but also contained in the poststack section at depths of 10 - 15 km beneath the coast (see figure 10.18). The corresponding P-wave velocities are rather low in the area in question, the Vp/Vs ratio reveal no anomalies. Farther east, in the central part of the seismic section, an increased Vp/Vs ratio is observed ('R'). This area is enclosed by highly reflective bands. The most prominent reflector which might be attributed to fluids underneath the granitoid body on the Coastal Batholith (x = 65 km) coincides with a maximum of the Vp/Vs ratio. The MT section shows a rather high resistivity in the corresponding area. This favors the assumption that the high fluid content – suggested by the Vp/Vs ratios – is not a connected conductor. The Coastal Batholith can be traced with the first-break tomography beneath the sediments of the western Central Valley up to depths of ≈ 2 km.

11. Conclusion and outlook

11.1. Conclusions

The Chilean subduction zone at 38.25° S with the subducting Nazca and overriding South American plate was investigates within the joint research program TIPTEQ. The first part of this thesis dealt with the preprocessing and processing of the TIPTEQ NVR seismic data. The preprocessing comprised considerably effort to reduce unwanted noise such as airblast disturbances and to provide an appropriate data set for further processing. Subsurface velocity information of the SPOC wide-angle experiment was used to stack and migrate the data applying a Kirchhoff depth migration.

A 2–D first-break tomography was conducted in the second part. Extensive tests and validation processes showed the limitations of the used data set and method. The included ESP shots with greater offsets yielded a subsurface coverage of up to 10 km depth. The resultant velocity image was dominated by small lenses of high velocities and two large zones of velocities close to 7 km/s, which are difficult to explain in a geological context. Parameter studies revealed unstable and conflicting results mainly related to areas with low ray coverage in the under-determined part of the model. The inclusion of seismological travel-times from stations which recorded shots from the active source experiment did not improve the subsurface image. The crossline offset of the stations to the 2–D profile line turned out to be too large, even though several criteria were used to find appropriate stations. The velocity image was stable and similar within the first three kilometers depth throughout the multitude of conducted tests. Limiting the inversion input to only the NVR and SH shots provided stable and well resolved subsurface models up to 2.5 km below topography.

Another purpose of the first-break tomography in the first place was to improve the SPOC wide-angle velocity model for an improved migration of the reflection seismic data set. The extremely high velocity values and densely spaced velocity variations in the unstable model provided the opportunity to test the influence of those near-surface velocity variations (up to 10 km depth) on a crustal-scale seismic image. Therefore, the unstable tomographic model was merged with the SPOC velocity model. A migration of the reflection seismic data set with that new velocity model was carried out subsequently to test the robustness of the final seismic section.

One further migration test comprised the migration of the reflection seismic data set with a crustal scale tomographic P-wave velocity model of the TIPTEQ seismology group derived

from the local seismicity. The comparison of all three migrations show great similarities. The comparison of the merged tomographic and SPOC model with the reference section (using only the SPOC model) differs only slightly in the upper central part (z = 10 - 15 km) where the velocity differences are largest in the first 10 km. This may imply that for the used stacking and migration methods, near-surface variations in velocity are less relevant for crustal scale sections. The largely seismically transparent upper parts of the TIPTEQ profile may favor this observation. Of course, this may be different for small-scale sections with higher frequency content or different subsurface structures and materials. The comparison of the migration using the seismological tomographic velocity model with the reference depth section shows a general downward shift of less than one kilometer. This resemblance allows the plotting of earthquake hypocenters from the seismology group in the seismic section without greater errors induced from the different velocity models. In addition, the SPOC velocity model is validated by the tomographic model since an independently derived subsurface model leads to the same migration result. Again, these observations may just be valid for crustal scale seismic sections, and certainly not for high-resolution hydrocarbon exploration. The direct comparison of the different migrations was made possible by the development of an innovative approach to convert screenshots from the migrated images into ASCII point data with lat/lon/z for each black pixel. This approach was very helpful for the combined plots of the seismic data with the results of other groups within TIPTEQ shown in the third part of the thesis, the interpretation and discussion.

11.2. Major results of the interpretation of the TIPTEQ data set

The resultant depth section shows the crustal architecture of the Chilean forearc from the coast up to 130 km inland for the first time in such detail. The 8-fold subsurface coverage provides a high resolution of the imaged structures down to 60 km depth.

It was possible to validate the velocity distribution of the SPOC–South wide-angle velocity model and the related plate geometry within the confidence area of the model (Lüth et al., 2003; Krawczyk and the SPOC Team, 2003). This step was important for the TIPTEQ interpretation, since the stacking and migration of the reflection seismic data uses this model as reference velocity model.

The oceanic crust shows a varying reflectivity which was related to the porosity collapse in basalt. Fluids are released from the oceanic crust into the subduction channel and then maybe further into the continental crust and mantle.

The subduction channel is inferred from the reflectivity distribution above the plate interface. The sediment thickness at the trench reaches 2.2 km (Rauch, 2005), but this is neither expected to be continuous along the entire subduction channel nor through time. The thickness and

curvature of the subduction channel might be outlined by the TIPTEQ seismicity between x = -10 and 30 km (cf. figure 10.3). The subduction channel might be traced farther downdip than the position of the 1960 Chile earthquake hypocenter (z ≈ 38 km).

The distribution of the reflective bands in the continental crust may provide further constrains for the modeling of gravity or travel-time data. Two large transparent zones are imaged in the upper part of the seismic section. The eastern one might be associated with the Coastal Batholith east of the Lanalhue Fault Zone. The first-break tomographic image allowed to trace the outline of the Coastal Batholith beneath the sediments of Central Valley for the first time in the eastern part of the profile. Here, the sediments reach a thickness of up to 1 km.

The continental Moho at the plate interface is interpreted to comprise a hydrated mantle wedge (which is highly transparent) starting close to the 1960 Chile earthquake hypocenter. The Moho is interpreted to follow a transition from reduced to little reflectivity towards the major reflective band labeled R2 in the former figures (cf. figure 10.3). This reflective band ceases to exist below ≈ 43 km depth at x = 70 - 80 km. The continental Moho is interpreted to be aligned underneath. Farther east, the Moho is connected to an oblique reflector segment at x = 100 - 105 km in a depth of 35 - 40 km whose position correlates with Moho interfaces derived from density modeling.

The integrated interpretation of results from other geophysical groups within TIPTEQ resolved a complex image of the South American subduction zone at depth (cf. figure 10.18). High Vp/Vs ratios paired with high conductivities argue for a highly hydrated mantle, whereas 15 km farther east, 'normal' mantle is interpreted to occur. A zone of high Vp/Vs ratio ('H', x = 90 - 100 km) is cut by the preferred TIPTEQ Moho interface approximately in half. The upper part of 'H' also exhibits high P-wave velocities (> 7.5 km/s) which argues against a continental Moho underneath. Velocities of 7.2 km/s were found in the uppermost mantle beneath the onshore forearc along the ISSA-2000 profile one degree south of the TIPTEQ transect (Lüth et al., 2003; Krawczyk et al., 2007). These diverse findings of different methods along one transect, or deviations with existing results close by, must certainly be bundled, balanced and brought further together.

In summary, processes like dominantly sediment subduction, moderate basal accretion and variable fluid release shape the accretionary wedge of the south central Chilean active plate margin. These processes are accompanied by forearc uplift in the updip part of the seismogenic coupling zone, and serpentinisation at its downdip end.

11.3. Outlook

The z-component of the TIPTEQ NVR data set was processed and migrated into depth. Test migrations of the horizontal components were also conducted, but the data was not crawled to the whole extent. The first breaks of the SH and ESP shots were used for the tomographic

inversions, but special processing techniques of the whole ESP and SH data sets could provide additional information. A further processing of the first seconds of the z-component data might resolve structures on top of the large transparent zones or could resolve the subsurface trace of the Lanalhue fault or other faults along the profile.

Within project TIPTEQ, further integrative studies of the collected data are possible between the individual groups to refine and link the existing results and geophysical images. Furthermore, a connection of the deep reaching geophysical data, such as seismic imaging or the tomographic inversion of seismological observation, with geological surface information must be sought after.

The depth position of the plate interface is crucial for the discussion of the extend and width of the subduction channel. Differences in reflector depths are observed between the prestack and poststack approach. This difference must be understood in more detail, because it leads to inevitable discussions about the depth position of the imaged structures. Synthetic data sets should be used as input for both methods to assess the occurring differences. Existing sections of former experiments where both methods were applied to the data should be reevaluated in search of similar depth variances and clues to solve this problem.

Recent studies by Bachmann (2008) in the Central Alps of Europe of an ancient subduction channel in the depth range of its former seismogenic zone comprised extensive fieldwork and dating techniques to reveal processes active at the former plate interface. Comparisons of the TIPTEQ geophysical data set with these findings should be fruitful.

The integrative interpretation showed that a lot of observations and suggested processes cumulate east of x = 70 km (cf. figure 10.18). High-resolution numerical modeling of a subduction zone setting by Gerya et al. (2006) shows highly dynamic structures even farther east. The TIPTEQ seismic experiment can not image the area in question in detail due to the field geometry. To asses the nature of the enigmatic reflector and surrounding processes it is highly recommend to extend the TIPTEQ transect farther east. Scientific background for such a survey is provided by former and the recent TIPTEQ experiments. A similar multidisciplinary approach should yield equally fascinating results.
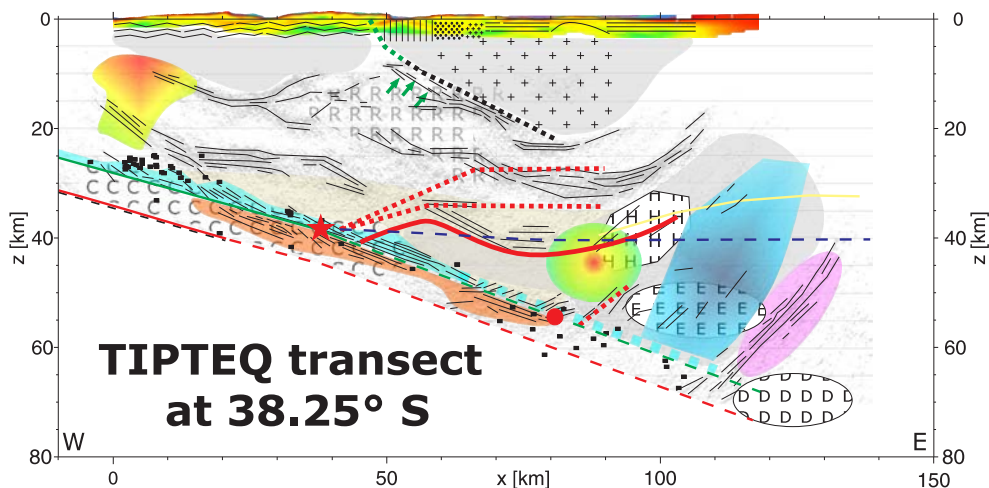
References

Abers, G. A., P. E. van Keken, E. A. Kneller, A. Ferris, and J. C. Stachnik (2006, January). The thermal structure of subduction zones constrained by seismic imaging: Implications for slab dehydration and wedge flow. *Earth and Planetary Science Letters 241*(Issues 3-4), 387–397. URL: `http://dx.doi.org/10.1016/j.epsl.2005.11.055`.

Aguirre, L., F. Hérve, and E. Godoy (1972). Distribution of metamorphic facies in Chile - an outline. *Krystalinikum 9*, 7–19.

Aki, K., A. Christoffersson, and E. S. Husebye (1977, January). Determination of the three-dimensional structure of the lithosphere. *Journal of Geophysical Research 82*(2), 277–296. URL: `http://www.agu.org/journals/jb/v082/i002/JB082i002p00277/`.

Angermann, D., J. Klotz, and C. Reigber (1999). Space-geodetic estimation of the Nazca-South America Euler vector. *Earth and Planetary Science Letters 171*(3), 329–334. URL: `http://dx.doi.org/10.1016/S0012-821X(99)00173-9`.

Ardiles Araya, M. E. (2003). La Serie occidental del basamento metamórfico, centro sur de la Cordillera de Nahelbuta, Chile, área Quidico-Capitán Pastene. Petrografía, mesoestructura y análisis microtectónico. Master's thesis, Universidad de Conceptión, Chile.

Asch, C., J. Mechie, X. Yuan, E. Lüschen, P. Giese, P. Wigger, S. Lueth, E. Scheuber, H. Götze, H. Brasse, et al. (2003, July). Seismic imaging of a convergent continental margin and plateau in the central Andes (Andean Continental Research Project 1996 (ANCORP'96)). *Journal of Geophysical Research 108*(B7), 2328. URL: `http://www.agu.org/pubs/crossref/2003/2002JB001771.shtml`.

Asch, G., B. Schurr, M. Bohm, X. Yuan, C. Haberland, B. Heit, R. Kind, I. Woelbern, K. Bataille, D. Comte, M. Pardo, J. Viramonte, A. Rietbrock, and P. Giese (2007, December). Seismological Studies of the Central and Southern Andes. In O. Oncken, G. Chong, G. Franz, P. Giese, H. Götze, V. Ramos, M. Strecker, and P. Wigger (Eds.), *The Andes - Active Subduction Orogeny*, Volume 1 of *Frontiers in Earth Sciences*, Chapter 21, pp. 443–457. Berlin: Springer Verlag. URL: `http://tinyurl.com/62va3w`.

Bachmann, R. (2008). *Anatomy of an ancient subduction channel in the depth range of its seismogenic coupling zone - insights from field studies in the Swiss Alps and Southern Chile*. Phd thesis, scientific technical report, FU Berlin and GFZ Potsdam. URL: `http://bib.gfz-potsdam.de/pub/str0801/0801.htm`.

Bancroft, J. C. (2007). *Practical Understanding of Pre- and Poststack Migrations*. Society of Exploration Geophysicists, SEG. URL: `http://tinyurl.com/yrgoy2`.

Barrientos, S. (1994). Large thrust earthquakes and volcanic eruptions. *Pure and Applied Geophysics 142*(1), 225–237. URL: `http://www.springerlink.com/index/U20811T19015QP2M.pdf`.

Barrientos, S. and S. Ward (1990). The 1960 Chile earthquake: inversion for slip distribution from surface deformation. *Geophys. J. Int. 103*, 589–598. URL: `http://tinyurl.com/4r28ml`.

Beaumont, E. A. and N. H. Foster (Eds.) (1989). *Geophysics I-IV*. AAPG Treatise of Petroleum Geology - Reprint Series No.13-15. Tulsa, OK, USA: American Association of Petroleum Geologists (AAPG). URL: `http://tinyurl.com/4gu7hq`.

Benz, H. M., B. . A. Chouet, P. B. Dawson, J. C. Lahr, R. A. Page, and J. A. Hole (1996, April). Three-dimensional P and S wave velocity structure of Redoubt Volcano, Alaska. *Journal of Geophysical Research 101*(B4), 8111–8128. URL: `http://www.agu.org/journals/jb/v101/iB04/95JB03046/`.

Bijwaard, H., W. Spakman, and R. E. Engdahl (1998, December). Closing the gap between regional and global travel time tomography. *J. Geophys. Res. 103*(B12), 30,055–30,078. URL: `http://www.agu.org/journals/jb/v103/iB12/98JB02467/`.

Bohm, M. (2004). *3-D Lokalbebentomographie der südlichen Anden zwischen 36° und 40° S*. Phd thesis, scientific technical report, FU Berlin and GFZ Potsdam. URL: `http://www.gfz-potsdam.de/bib/pub/str0415/0415.pdf`.

Bostock, M. G., R. D. Hyndman, S. Rondenay, and S. M. Peacock (2002, May). An inverted continental Moho and serpentinization of the forearc mantle. *Nature 417*, 536–538. URL: `http://www.nature.com/nature/journal/v417/n6888/abs/417536a.html`.

Brasse, H., G. Kapinos, Y. Li, L. Mütschard, W. Soyer, and D. Eydam (2008, submitted). Structural electrical anisotropy in the crust at the south central chilean continental margin as inferred from geomagnetic transfer functions. *Phys. Earth Planet. Inter.*.

Bräuer, B., T. Ryberg, and A. S. Lindeque (2007). Shallow seismic velocity structure of the Karoo Basin, South Africa. *South African Journal of Geology 110*(2-3), 439–448. URL: `http://sajg.geoscienceworld.org/cgi/content/abstract/110/2-3/439`.

Brocher, T. (2005). Empirical Relations between Elastic Wavespeeds and Density in the Earth's Crust. *Bulletin of the Seismological Society of America 95*(6), 2081–2092. URL: `http://bssa.geoscienceworld.org/cgi/content/abstract/95/6/2081`.

Bruhn, C. (2003). *Momententensoren hochfrequenter Ereignisse in Südchile*. Ph. D. thesis, University of Potsdam. URL: `http://tinyurl.com/3s7kpp`.

Burón Muñoz, P. J. (2003). Petrografía, Estructuras y Microtectónica del área de contacto entre las Series Metamórficas de Basemento Paleozoico entre los 38° 08' y 38° 21' S, Cordillera de Nahelbuta, Chile. Master's thesis, Universidad de Conceptión, Chile.

Calvert, A., M. Fisher, K. Ramachandran, and A. Tréhu (2003, December). Possible emplacement of crustal rocks into the forearc mantle of the Cascadia Subduction Zone. *Geophysical Research Letters 30*(23), 2196. URL: `http://www.agu.org/pubs/crossref/2003/2003GL018541.shtml`.

Cassidy, J. F. and R. M. Ellis (1993, March). S Wave Velocity Structure of the Northern Cascadia Subduction Zone. *Journal of Geophysical Research 98*(B3), 4407–4421. URL: `http://www.agu.org/pubs/crossref/1993/92JB02696.shtml`.

Castagna, J., M. Batzle, and R. Eastwood (1985). Relationships between compressional-wave and shear-wave velocities in clastic silicate rocks. *Geophysics 50*(4), 571–581. URL: `http://tinyurl.com/4d3rtw`.

Cembrano, J., F. Hérve, and A. Lavenu (1996). The Liquiñe Ofqui fault zone: a long-lived intra-arc fault system in southern Chile. *Tectonophysics 259*(1-3), 55–66. URL: `http://dx.doi.org/10.1016/0040-1951(95)00066-6`.

Červený, V., I. Molotkov, and I. Pšenčík (1977). *Ray method in seismology.* Univerzita Karlova, Prague. URL: `http://worldcat.org/wcpa/oclc/4208306`.

Christensen, N. I. and W. D. Mooney (1995, June). Seismic velocity structure and composition of the continental crust: A global view. *Journal of Geophysical Research 100*(B6), 9761–9788. URL: `http://www.agu.org/journals/jb/v100/iB06/95JB00259/`.

Cifuentes, I. L. (1989). The 1960 Chilean earthquake. *Journal of Geophysical Research 94(B1)*, 665–680. URL: `http://www.agu.org/pubs/crossref/1989/88JB03482.shtml`.

Cloos, M. and R. Shreve (1988a). Subduction-channel model of prism accretion, melange formation, sediment subduction, and subduction erosion at convergent plate margins: 1. Background and description. *Pure and Applied Geophysics 128*, 455–500. URL: `http://tinyurl.com/6bj8v9`.

Cloos, M. and R. Shreve (1988b). Subduction-channel model of prism accretion, melange formation, sediment subduction, and subduction erosion at convergent plate margins: 2. Implications and discussion. *Pure and Applied Geophysics 128*, 501–545. URL: `http://tinyurl.com/5k8sov`.

Daly, E., D. Keir, C. J. Ebinger, G. W. Stuart, I. D. Bastow, and A. Ayele (2008, March). Crustal tomographic imaging of a transitional continental rift: the Ethiopian rift. *Geophysical Journal International 172*(3), 1033–1048. URL: `http://tinyurl.com/66gfqf`.

Darwin, C. (1839). *Narrative of the surveying voyages of His Majesty's Ships Adventure and Beagle, between the years 1826 and 1836, describing their examination of the southern shores of South America, and the Beagle's circumnavigation of the globe. Volume 3.* URL: `http://www.gutenberg.org/etext/3704`.

Darwin, C. (2002). *Geological Observations on South America.* URL: `http://www.gutenberg.org/etext/3620`.

155

Dohr, G. P. (1985). Development of a procedure for the exploration of areas with poor reflections by the combined application different geophysical methods, taking the North-West German basin as an example. In R. De Bouw, E. Millich, J. Joulia, and D. Van Asselt (Eds.), *New Technologies for the Exploration and Exploitation of Oil and Gas Resources*, London, pp. 62–69. Graham and Trotman. URL: `http://tinyurl.com/4mguks`.

Engdahl, E. and A. Villaseñor (2002). 41. c Global Seismicity: 1900 - 1999. In W. Lee, H. Kanamori, P. Jennings, and C. Kisslinger (Eds.), *International handbook of earthquake & engineering seismology, part A*, Volume 81A, pp. 665–690. Academic Press. URL: `http://tinyurl.com/56x3nv`.

Farr, T. G., P. A. Rosen, E. Caro, R. Crippen, R. Duren, S. Hensley, M. Kobrick, M. Paller, E. Rodriguez, L. Roth, D. Seal, S. Shaffer, J. Shimada, J. Umland, M. Werner, M. Oskin, D. Burbank, and D. Alsdorf (2007, May). The Shuttle Radar Topography Mission. *Reviews of Geophysics 45*, RG2004. URL: `http://www.agu.org/pubs/crossref/2007/2005RG000183.shtml`.

Flück, P., R. D. Hyndman, and K. Wang (1997, September). Three-dimensional dislocation model for great earthquakes of the cascadia subduction zone. *Journal of Geophysical Research 102*(B9), 20,539–20,550. URL: `http://www.agu.org/pubs/crossref/1997/97JB01642.shtml`.

Forkmann, B. (1987). Geschwindigkeitsbestimmung, pp. 133–151, Apparativ-methodische Grundlagen, pp. 65–105. In H. Militzer and F. Weber (Eds.), *Angewandte Geophysik, Band 3, Seismik*. Springer-Verlag Wien/Akademie Verlag Berlin. URL: `http://adsabs.harvard.edu/abs/1987ange.book.....F`.

Gerya, T., J. Connolly, D. Yuen, W. Gorczyk, and A. Capel (2006). Seismic implications of mantle wedge plumes. *Physics of the Earth and Planetary Interiors 156*(1-2), 59–74. URL: `http://dx.doi.org/10.1016/j.pepi.2006.02.005`.

Glodny, J., H. Echtler, S. Collao, M. Ardiles, P. Burón, and O. Figueroa (2008, June). Differential Late Paleozoic active margin evolution in south central Chile (37° S - 40° S) - The Lanalhue Fault Zone. *Journal of South American Earth Sciences*. URL: `http://dx.doi.org/10.1016/j.jsames.2008.06.001`.

Glodny, J., H. P. Echtler, O. Figueroa, G. Franz, K. Gräfe, H. Kemnitz, W. Kramer, C. M. Krawczyk, J. Lohrmann, F. Lucassen, D. Melnick, M. Rosenau, and W. Seifert (2007, December). Long-Term Geological Evolution and Mass-Flow Balance of the south central Andes. In O. Oncken, G. Chong, G. Franz, P. Giese, H. Götze, V. Ramos, M. Strecker, and P. Wigger (Eds.), *The Andes - Active Subduction Orogeny*, Volume 1 of *Frontiers in Earth Sciences*, Chapter 19, pp. 401–428. Berlin: Springer Verlag. URL: `http://tinyurl.com/62va3w`.

Glodny, J., J. Lohrmann, H. Echtler, K. Gräfe, W. Seifert, S. Collao, and O. Figueroa (2005, February). Internal dynamics of a paleoaccretionary wedge: insights from combined isotope tectonochronology and sandbox modelling of the south central Chilean forearc. *Earth and Planetary Science Letters 231*(Issues 1-2), 23–39.

http://dx.doi.org/10.1016/j.epsl.2004.12.014.

Gray, S. H., J. Etgen, J. Dellinger, and D. Whitmore (2001, September). Seismic migration problems and solutions. *Geophysics 66*(5), 1622–1640. URL: `http://link.aip.org/link/?GPY/66/1622/1`.

Green, A., R. Clowes, C. Yorath, C. Spencer, E. Kanasewich, M. Brandon, and A. Sutherland Brown (1986). Seismic reflection imaging of the subducting Juan de Fuca plate. *Nature 319*, 210–213. URL: `http://www.nature.com/nature/journal/v319/n6050/abs/319210a0.html`.

Groß, K. (2008). *Deep seismic image of the Chilean subduction zone at 38° S - novel imaging techniques and geodynamic interpretation.* Ph. D. thesis, Free University Berlin. URL: `http://jorge.ub.fu-berlin.de/work/DissSearch`.

Groß, K., U. Micksch, and TIPTEQ Research Group (2008). The reflection seismic survey of project TIPTEQ – the inventory of the Chilean subduction zone at 38° S. *Geophysical Journal International 172*(2), 565–571. URL: `http://tinyurl.com/6ynwm4`.

Guo, J. and J. Young (2004). Complex structural velocity model building for depth imaging. *Journal of Geophysics and Engineering 1*(3), 216–220. URL: `http://stacks.iop.org/1742-2140/1/216`.

Haberland, C., A. Rietbrock, D. Lange, K. Bataille, and T. Dahm (2008, submitted). Structure of the seismogenic zone of the south central Chilean margin revealed by local earthquake travel-time tomography. *Journal of Geophysical Research*.

Haberland, C., A. Rietbrock, D. Lange, K. Bataille, and S. Hofmann (2006, December). Interaction between forearc and oceanic plate at the south central chilean margin as seen in local seismic data. *Geophysical Research Letters 33*, L23302. URL: `http://www.agu.org/pubs/crossref/2006/2006GL028189.shtml`.

Hensen, C., K. Wallmann, M. Schmidt, C. Ranero, and E. Suess (2004, March). Fluid expulsion related to mud extrusion off Costa Rica–A window to the subducting slab. *Geology 32*(3), 201–204. URL: `http://geology.geoscienceworld.org/cgi/content/abstract/32/3/201`.

Hérve, F. (1988). Late Paleozoic subduction and accretion in Southern Chile. *Episodes 11*, 183–188.

Hérve, F. (1994). The Southern Andes between 39 degrees and 44 degrees S latitude - the geological signature of a transpressive tectonic regime related to a magmatic arc. In K. Reutter, E. Scheuber, and P. Wigger (Eds.), *Andean Geodynamics. Frontiers in Earth Sciences*, pp. 243–248. Springer Verlag, Berlin. URL: `http://books.google.com/books?id=dLG6AAAACAAJ\&dq=3540552324`.

Hobro, J. W. D. (1999). *Three-dimensional tomographic inversion of combined reflection and refraction seismic travel-time data.* Ph. D. thesis, University of Cambridge, Department of Earth Sciences, Cambridge, UK. URL:
Thesis: `http://bullard.esc.cam.ac.uk/~hobro/thesis/index.html`
JIVE3D: `http://bullard.esc.cam.ac.uk/~hobro/Jive3D/index.html`.

REFERENCES

Hobro, J. W. D., S. C. Singh, and T. A. Minshull (2003, January). Three-dimensional tomographic inversion of combined reflection and refraction seismic traveltime data. *Geophysical Journal International 152*(1), 79–93. URL: `http://tinyurl.com/3e3jqu`.

Hoffmann-Rothe, A., N. Kukowski, G. Dresen, H. Echtler, O. Oncken, J. Klotz, E. Scheuber, and A. Kellner (2007, December). Oblique Convergence along the Chilean Margin: Partitioning, Margin-Parallel Faulting and Force Interaction at the Plate Interface. In O. Oncken, G. Chong, G. Franz, P. Giese, H. Götze, V. Ramos, M. Strecker, and P. Wigger (Eds.), *The Andes - Active Subduction Orogeny*, Volume 1 of *Frontiers in Earth Sciences*, Chapter 6, pp. 125–126. Berlin: Springer Verlag. URL: `http://tinyurl.com/62va3w`.

Hole, J. A., T. Ryberg, G. S. Fuis, F. Bleibinhaus, and A. K. Sharma (2006, April). Structure of the San Andreas fault zone at SAFOD from a seismic refraction survey. *Geophysical Research Letters 33*, L07312. URL: `http://www.agu.org/journals/gl/gl0607/2005GL025194/`.

Hole, J. A. and B. C. Zelt (1995, May). 3-D finite-difference reflection travel times. *Geophysical Journal International 121*(2), 427–434. URL: `http://tinyurl.com/yostu7`.

Holliger, K. (2003). *Lecture notes: Inversion von Meßdaten.* . URL: `http://tinyurl.com/2m6vl5`.

Humphreys, E. and R. W. Clayton (1988, February). Adaptation of back projection tomography to seismic travel time problems. *Journal of Geophysical Research 93*(B2), 1073–1085. URL: `http://www.agu.org/journals/jb/v093/iB02/JB093iB02p01073/`.

Hyndman, R. D. (1988, November). Dipping Seismic Reflectors, Electrically Conductive Zones, and Trapped Water in the Crust Over a Subducting Plate. *Journal of Geophysical Research 93*(B11), 13,391–13,405. URL: `http://www.agu.org/pubs/crossref/1988/JB093iB11p13391.shtml`.

Hyndman, R. D. and S. M. Peacock (2003, July). Serpentinization of the forearc mantle. *Earth and Planetary Science Letters 212*(Issues 3-4), 417–432. URL: `http://dx.doi.org/10.1016/S0012-821X(03)00263-2`.

Hyndman, R. D. and K. Wang (1993, February). Thermal Constraints on the Zone of Major Thrust Earthquake Failure: The Cascadia Subduction Zone. *Journal of Geophysical Research 98*(B2), 2039–2060. URL: `http://www.agu.org/pubs/crossref/1993.../92JB02279.shtml`.

IRIS (Incorporated Research Institutions for Seismology) (2008, January). (mini)seed data format. URL: `http://www.iris.edu/manuals/SEED_appG.htm`.

Jones, E. J. W. (1999). *Marine Geophysics.* John Wiley and Sons, Ltd. URL: `http://eu.wiley.com/WileyCDA/WileyTitle/productCd-0471986941.html`.

Kanamori, H. (1977). The energy release in great earthquakes. *Journal of Geophysical Research 82*(B20), 2981–2988. URL: `http://www.agu.org/pubs/crossref/1977/JB082i020p02981.shtml`.

Kapinos, G. (2008). *Amphibious magnetotelluric experiment at the south central Chilean continental margin.* Ph. D. thesis, Free University Berlin. URL: `http://jorge.ub.fu-berlin.de/work/DissSearch`.

Kendrick, E., M. Bevis, R. Smalley, B. Brooks, R. Vargas, E. Lauría, and L. Fortes (2003). The Nazca–South America Euler vector and its rate of change. *Journal of South American Earth Sciences 16*(2), 125–131. URL: `http://dx.doi.org/10.1016/S0895-9811(03)00028-2`.

Khazaradze, G. and J. Klotz (2003, June). Short- and long-term effects of GPS measured crustal deformation rates along the south central Andes. *Journal of Geophysical Research 108*(B6), 2289. URL: `http://www.agu.org/pubs/crossref/2003/2002JB001879.shtml`.

Krawczyk, C. M., J. Mechie, S. Lüth, Z. Tašárová, P. Wigger, M. Stiller, H. Brasse, H. P. Echtler, M. Araneda, and K. Bataille (2007, December). Geophysical Signatures and Active Tectonics at the south central Chilean Margin. In O. Oncken, G. Chong, G. Franz, P. Giese, H. Götze, V. Ramos, M. Strecker, and P. Wigger (Eds.), *The Andes - Active Subduction Orogeny*, Volume 1 of *Frontiers in Earth Sciences*, Chapter 8, pp. 171–192. Berlin: Springer Verlag. URL: `http://tinyurl.com/62va3w`.

Krawczyk, C. M., O. Oncken, and SPOC & IMTEQ Working Groups (2002). Subduction Processes Off Chile (SPOC) - Combined offshore-onshore experiments in Central Chile. *International Symposium on Andean Geodynamics. Inst. de Rech. Develop., Paris*, 355–358.

Krawczyk, C. M. and the SPOC Team (2003, August). Amphibious seismic survey images plate interface at 1960 Chile earthquake. *EOS Trans. Am. Geophys. Union 84*(32), 301,304–305. URL: `http://www.agu.org/pubs/eos/eo0332.shtml`.

Kurtz, R. D., J. M. DeLaurier, and J. C. Gupta (1986). A magnetotelluric sounding across Vancouver Island detects the subducting Juan de Fuca plate. *Nature 321*(6070), 596–599. URL: `http://dx.doi.org/10.1038/321596a0`.

Lohrmann, J. (2002). *Identification of parameters controlling the accretive and tectonically erosive mass-transfer mode at the South-Central and North Chilean Forearc using scaled 2D sandbox experiments.* Phd thesis, scientific technical report, FU Berlin and GFZ Potsdam. URL: `http://bib.gfz-potsdam.de/pub/str0210/0210.htm`.

Lohrmann, J., N. Kukowski, C. Krawczyk, O. Oncken, C. Sick, M. Sobiesiak, and A. Rietbrock (2007, December). Subduction channel evolution in brittle forearc wedges - a combined study with scaled sandbox experiments, seismological and reflection seismic data and geological field evidences. In O. Oncken, G. Chong, G. Franz, P. Giese, H. Götze, V. Ramos, M. Strecker, and P. Wigger (Eds.), *The Andes - Active Subduction Orogeny*, Volume 1 of *Frontiers in Earth Sciences*, Chapter 11, pp. 237–262. Berlin: Springer Verlag. URL: `http://tinyurl.com/62va3w`.

Luis, J. F. (2007). Mirone: A multi-purpose tool for exploring grid data. *Computers and Geosciences 33*(1), 31–41. URL:

http://dx.doi.org/10.1016/j.cageo.2006.05.005,
MIRONE: http://w3.ualg.pt/~jluis/mirone/.

Lüth, S., J. Mechie, P. Wigger, E. R. Flueh, C. M. Krawczyk, C. Reichert, M. Stiller, E. Vera, and S. R. Group (2003). Subduction Processes Off Chile (SPOC) - results from the amphibious wide-angle seismic experiment across the Chilean subduction zone. *Geophysical Research Abstracts 5*, 04129. URL: http://www.cosis.net/abstracts/EAE03/04129/EAE03-J-04129.pdf.

Lüth, S., P. Wigger, and ISSA Working Group (2003). A crustal model along 39° S from a seismic refraction profile - ISSA 2000. *Revista Geológica de Chile 30*(1), 83–101. URL: http://tinyurl.com/3kylql.

Malinowski, M., A. Zelazniewicz, M. Grad, A. Guterch, and T. Janik (2005, May). Seismic and geological structure of the crust in the transition from Baltica to Palaeozoic Europe in SE Poland–CELEBRATION 2000 experiment, profile CEL02. *Tectonophysics 401*(1-2), 55–77. URL: http://dx.doi.org/10.1016/j.tecto.2005.03.011.

Melnick, D. (2007). *Neogene seismotectonics of the south central Chile margin : subduction-related processes over various temporal and spatial scales*. Phd thesis, scientific technical report, University Potsdam, GFZ Potsdam. URL: http:///bib.gfz-potsdam.de/pub/str0701/0701.htm.

Melnick, D., B. Bookhagen, H. Echtler, and M. Strecker (2006). Coastal deformation and great subduction earthquakes, Isla Santa Maria, Chile (37° S). *Bulletin of the Geological Society of America 118*(11-12), 1463–1480. URL: http://bulletin.geoscienceworld.org/cgi/content/abstract/118/11-12/1463.

Melnick, D. and H. P. Echtler (2007, December). Morphotectonic and geologic digital map compilations of the south central Andes (36-43° S). In O. Oncken, G. Chong, G. Franz, P. Giese, H. Götze, V. Ramos, M. Strecker, and P. Wigger (Eds.), *The Andes - Active Subduction Orogeny*, Volume 1 of *Frontiers in Earth Sciences*, Chapter 30, pp. 565–568. Berlin: Springer Verlag. URL: http://tinyurl.com/62va3w.

Mpodozis, C. and V. Ramos (1989). The Andes of Chile and Argentina. In G. Ericksen, M. Pinochet, and J. Reinemund (Eds.), *Geology of the Andes and its relation to hydro-carbon and mineral resources*, Volume 11 of *Earth Sciences Series*, Houston, TX., pp. 59–90. Circumpacific Council for Energy and Mineral Resources. URL: http://www.osti.gov/energycitations/product.biblio.jsp?osti_id=6831968.

Nedimović, M. R., R. D. Hyndman, K. Ramachandran, and G. D. Spence (2003, July). Reflection signature of seismic and aseismic slip on the northern Cascadia subduction interface. *Nature 424*(6947), 416–420. URL: http://dx.doi.org/10.1038/nature01840.

Nicholson, T., J. Cassidy, and M. Bostock (2005, June). New constraints on subduction zone structure in northern Cascadia. *Geophysical Journal International 161*(3), 846–859. URL: http://tinyurl.com/4axmqm.

Nolet, G. (1987). Seismic wave propagation and seismic tomography. In G. Nolet (Ed.), *Seismic Tomography: With Applications in Global Seismology and Exploration Geophysics*,

Chapter 1, pp. 1–23. Dordrecht: D. Reidel Publishing Company. URL: `http://tinyurl.com/2gzrss`.

Oleskevich, D., R. Hyndman, and K. Wang (1999, July). The updip and downdip limits to great subduction earthquakes: Thermal and structural models of Cascadia, south Alaska, SW Japan, and Chile. *Journal of Geophysical Research 104*(B7), 14965–14991. URL: `http://www.agu.org/pubs/crossref/1999/1999JB900060.shtml`.

Oncken, O., G. Chong, G. Franz, P. Giese, H. Götze, V. Ramos, M. Strecker, and P. Wigger (Eds.) (2007, December). *The Andes - Active Subduction Orogeny*, Volume 1 of *Frontiers in Earth Sciences*. Berlin: Springer Verlag. URL: `http://tinyurl.com/62va3w`.

Paige, C. C. and M. A. Saunders (1982, March). LSQR: An algorithm for sparse linear equations and sparse least squares. *ACM Transactions on Mathematical Software (TOMS) 8*(1), 43–71. URL: `http://doi.acm.org/10.1145/355984.355989`.

Patzwahl, R., J. Mechie, A. Schulze, and P. Giese (1999, April). 2-D-velocity models of the Nazca plate subduction zone between 19.5° S and 25° S from wide-angle seismic measurements during the CINCA 95 project. *Journal of Geophysical Research 104*(B4), 7293–7317. URL: `http://www.agu.org/pubs/crossref/1999/1999JB900008.shtml`.

Peacock, S. and R. Hyndman (1999, August). Hydrous minerals in the mantle wedge and the maximum depth of subduction thrust earthquakes. *Geophysical Research Letters 26*(16), 2517–2520. URL: `http://www.agu.org/pubs/crossref/1999/1999GL900558.shtml`.

Phillips, W. S. and M. C. Fehler (1991, October). Traveltime tomography: A comparison of popular methods. *Geophysics 56*(10), 1639–1649. URL: `http://link.aip.org/link/?GPY/56/1639/1`.

ProMAX (2003). Help files and reference manuals.

Ramachandran, K., S. E. Dosso, G. D. Spence, R. D. Hyndman, and T. M. Brocher (2005, February). Forearc structure beneath southwestern British Columbia: A three-dimensional tomographic velocity model. *Journal of Geophysical Research 110*, B02303. URL: `http://www.agu.org/pubs/crossref/2005/2004JB003258.shtml`.

Rauch, K. (2005, April). Cyclicity of Peru-Chile trench sediments between 36° and 38° S: A footprint of paleoclimatic variations? *Geophysical Research Letters 32*, L08302. URL: `http://www.agu.org/pubs/crossref/2005/2004GL022196.shtml`.

Rehak, K., M. Strecker, and H. Echtler (2008). Morphotectonic segmentation of an active forearc, 37°-41° S, Chile. *Geomorphology 94*(1-2), 98–116. URL: `http://dx.doi.org/10.1016/j.geomorph.2007.05.002`.

Reichert, C. and B. Schreckenberger (2002). Cruise report SO-161 leg 2 & 3, SPOC (Subduction Processes Off Chile). Technical report, BGR Hannover. pp. 142.

Rietbrock, A., C. Haberland, K. Bataille, T. Dahm, and O. Oncken (2005, August). Studying the Seismogenic Coupling Zone with a Passive Seismic Array. *EOS Trans. Am. Geophys. Union 86*(32), 293, 297. URL: `http://www.agu.org/pubs/crossref/2005/2005EO320001.shtml`.

Robertsson, J. O. A., K. Holliger, A. G. Green, A. Pugin, and R. De Iaco (1996, March). Effects of near-surface waveguides on shallow high-resolution seismic refraction and reflection data. *Geophysical Research Letters 23*(5), 495–498. URL: `http://www.agu.org/pubs/crossref/1996/96GL00384.shtml`.

Rodriguez-Tablante, J. I., C. Juhlin, and B. Bergman (2006, May). First Arrival Seismic Tomography (FAST) vs. PStomo_eq applied to crooked line seismic data from the Siljan ring area. *Computers & Geosciences 32*(4), 497–511. URL: `http://dx.doi.org/10.1016/j.cageo.2005.08.005`.

Romanowicz, B. (2001, May). GLOBAL MANTLE TOMOGRAPHY: Progress Status in the Past 10 Years. *Annual Review of Earth and Planetary Sciences 31*(1), 303–328. URL: `http://tinyurl.com/67t29v`.

Rosenau, M., D. Melnick, and H. Echtler (2006, August). Kinematic constraints on intra-arc shear and strain partitioning in the Southern Andes between 38° S and 42° S latitude. *Tectonics 25*, TC4013. URL: `http://www.agu.org/pubs/crossref/2006/2005TC001943.shtml`.

Roth, M., K. Holliger, and A. G. Green (1998, April). Guided waves in near-surface seismic surveys. *Geophysical Research Letters 25*(7), 1071–1074. URL: `http://www.agu.org/pubs/crossref/1998/98GL00549.shtml`.

Ryberg, T., M. H. Weber, Z. Garfunkel, and Y. Bartov (2007, August). The shallow velocity structure across the Dead Sea Transform fault, Arava Valley, from seismic data. *Journal of Geophysical Research 112*, B08307. URL: `http://www.agu.org/journals/jb/jb0708/2006JB004563`.

Sato, H., N. Hirata, K. Koketsu, D. Okaya, S. Abe, R. Kobayashi, M. Matsubara, T. Iwasaki, T. Ito, T. Ikawa, T. Kawanaka, K. Kasahara, and S. Harder (2005, July). Earthquake Source Fault Beneath Tokyo. *Science 309*(5733), 462–464. URL: `http://www.sciencemag.org/cgi/content/abstract/309/5733/462`.

Scales, J. A., P. Docherty, and A. Gersztenkorn (1990, February). Regularisation of nonlinear inverse problems: imaging the near-surface weathering layer. *Inverse Problems 6*(1), 115–131. URL: `http://stacks.iop.org/0266-5611/6/115`.

Schlumberger (2008, January). Schlumberger oilfield glossary. URL: `http://www.glossary.oilfield.slb.com/Display.cfm?Term=ground%20roll`.

Schmöller, R. (1987). Bearbeitung reflexionsseismischer Daten. In H. Militzer and F. Weber (Eds.), *Angewandte Geophysik, Band 3, Seismik*, pp. 188–231. Springer-Verlag Wien/Akademie Verlag Berlin. URL: `http://adsabs.harvard.edu/abs/1987ange.book.....F`.

Schneider, W. A. (1978, February). Integral formulation for migration in two and three dimensions. *Geophysics 43*(1), 49–76. URL: `http://link.aip.org/link/?GPY/43/49/1`.

SEG (The Society of Exploration Geophysicists) (2008, January). Seg-y rev 1. URL: `http://seg.org/publications/tech-stand`.

Sengupta, M. K. and M. K. Toksöz (1976). Three Dimensional Model of Seismic Velocity Variation in the Earth's Mantle. *Geophysical Research Letters 3*(2), 84–86. URL: http://www.agu.org/journals/gl/v003/i002/GL003i002p00084/.

SERNAGEOMIN (2003). Mapa Geológico de Chile: version digital. No. 4 (CD-ROM, versión 1.0,2003). Servicio Nacional de Geología y Minería, Santiago de Chile. URL: http://www.sernageomin.cl/.

Tašárová, Z. (2004). *Gravity data analysis and interdisciplinary 3–D modeling of a convergent plate margin (Chile, 36° S - 42° S)*. Phd thesis, FU Berlin. URL: http://www.diss.fu-berlin.de/2005/19/.

Tašárová, Z. (2007, September). Towards understanding the lithospheric structure of the southern Chilean subduction zone (36° S - 42° S) and its role in the gravity field. *Geophysical Journal International 170*(3), 995–1014. URL: http://tinyurl.com/6rtagk.

The ANCORP Working Group (1999, January). Seismic reflection image revealing offset of Andean subduction-zone earthquake locations into oceanic mantle. *Nature 397*(6717), 341–344. URL: http://www.nature.com/nature/journal/v397/n6717/abs/397341a0.html.

Thybo, H., A. Sandrin, L. Nielsen, H. Lykke-Andersen, and G. Keller (2006, June). Seismic velocity structure of a large mafic intrusion in the crust of central Denmark from project ESTRID. *Tectonophysics 420*(Issues 1-2), 105–122. URL: http://dx.doi.org/10.1016/j.tecto.2006.01.029.

Tichelaar, B. W. and L. J. Ruff (1993, February). Depth of seismic coupling along subduction zones. *Journal of Geophysical Research 98*(B2), 2017–2037. URL: http://www.agu.org/pubs/crossref/1993.../92JB02045.shtml.

Tryggvason, A., S. d. T. Rognvaldsson, and O. G. Flovenz (2002, December). Three-dimensional imaging of the P- and S-wave velocity structure and earthquake locations beneath Southwest Iceland. *Geophysical Journal International 151*(3), 848–866. URL: http://tinyurl.com/355f2y
PStomo_eq: http://www.geofys.uu.se/at/Pstomo_eq/documentation.html.

Van Wagoner, T. M., R. S. Crosson, K. C. Creager, G. Medema, L. Preston, N. P. Symons, and T. M. Brocher (2002, December). Crustal structure and relocated earthquakes in the Puget Lowland, Washington, from high-resolution seismic tomography. *Journal of Geophysical Research 107*(B12), 2381. URL: http://www.agu.org/pubs/crossref/2002/2001JB000710.shtml.

Various (1963). Oceanographic, Geologic, and Engineering Studies of The Chilean earthquakes of May 1960. *Bulletin of the Seismological Society of America - Special Issue 53*(6), 1123–1124. URL: http://bssa.geoscienceworld.org/content/vol53/issue6/.

Vidale, J. E. (1988, December). Finite-difference calculation of travel times. *Bulletin of the Seismological Society of America 78*(6), 2062–2076. URL:

`http://www.bssaonline.org/cgi/content/abstract/78/6/2062`.

Vidale, J. E. (1990, May). Finite-difference calculation of traveltimes in three dimensions. *Geophysics 55*(5), 521–526. URL:
`http://link.aip.org/link/?GPY/55/521/1`.

Wessel, P. and W. H. F. Smith (1991). Free software helps map and display data. *EOS Trans. Am. Geophys. Union 72*(41), 441. URL: `http://gmt.soest.hawaii.edu/` – see website and documentation (DOCS - section).

Wikipedia (2008a, March). Least squares. URL:
`http://en.wikipedia.org/wiki/Least_squares`.

Wikipedia (2008b, May). Speed of sound. URL:
`http://en.wikipedia.org/wiki/Speed_of_sound`.

Willner, A., J. Glodny, T. Gerya, E. Godoy, and H. Massonne (2004). A counterclockwise PTt path of high-pressure/low-temperature rocks from the Coastal Cordillera accretionary complex of south central Chile: constraints for the earliest stage of subduction mass flow. *Lithos 75*(3-4), 283–310. URL:
`http://dx.doi.org/10.1016/j.lithos.2004.03.002`.

Yilmaz, Ö. (2001). *Seismic Data Analysis: Processing, Inversion and Interpretation of Seismic Data, Volume I + II*. Society of Exploration Geophysicists, SEG. URL:
`http://tinyurl.com/2gengx`.

Yuan, X., G. Asch, K. Bataille, G. Bock, M. Bohm, H. Echtler, R. Kind, O. Oncken, and I. Wölbern (2006). Deep Seismic Images of the Southern Andes. In S. Kay and V. Ramos (Eds.), *Evolution of an Andean margin: A tectonic and magmatic view from the Andes to the Neuquen Basin (36-39° S)*, Volume 407, pp. 61–72. Geological Society of America Special Paper. URL: `http://tinyurl.com/3gtjls`.

Zelt, C. A. (1998, December). Lateral velocity resolution from three-dimensional seismic refraction data. *Geophysical Journal International 135*(3), 1101–1112. URL:
`http://tinyurl.com/3de22l`.

Zelt, C. A. (1999, October). Modelling strategies and model assessment for wide-angle seismic traveltime data. *Geophysical Journal International 139*(1), 183–204. URL:
`http://tinyurl.com/2re3an`.

Zelt, C. A. and P. J. Barton (1998, April). Three-dimensional seismic refraction tomography: A comparison of two methods applied to data from the Faeroe Basin. *Journal of Geophysical Research 103*(B4), 7187–7210. URL:
`http://www.agu.org/journals/jb/v103/iB04/97JB03536/`
FAST: `http://terra.rice.edu/department/faculty/zelt/fast.html`.

Zhao, D., A. Hasegawa, and H. Kanamori (1994, November). Deep structure of Japan subduction zone as derived from local, regional, and teleseismic events. *J. Geophys. Res 99*(B11), 22,313–22,329. URL:
`http://www.agu.org/journals/jb/v099/iB11/94JB01149/`.

A. Appendix: The seismic experiment – tables

Shotpoint coordinates and related shot information

FFID	SP	type	nloc	ch1	long	lat	elev	depth	charge	holes	dd	mm	yyyy	hh	mm	ss +3 ms
1	97	n	-44	1	-72.3720623	-38.2856601	343.86	25	100	1	13	1	2005	10	0	2.841
2	52	n	181	1	-72.6294014	-38.2878726	271.35	20	75	1	13	1	2005	10	6	33.449
3	56	n	121	1	-72.5605351	-38.289343	268.93	20	75	1	13	1	2005	10	53	10.423
4	98	n	-134	1	-72.2686493	-38.2792953	402.48	20	150	2	13	1	2005	11	2	1.857
5	13	e	761	1	-73.2929803	-38.2916884	623.25	27	250	2	13	1	2005	11	11	1.362
6	60	n	61	1	-72.4919306	-38.2874521	290.44	20	75	1	13	1	2005	11	20	30.221
7	64	n	8	1	-72.4301897	-38.2711307	315.73	20	75	1	13	1	2005	11	50	29.919
8	99	n	-224	1	-72.1658412	-38.2766819	478.15	25	200	2	13	1	2005	12	0	8.574
9	53	n	166	46	-72.6119828	-38.2828735	272.15	20	75	1	14	1	2005	10	0	8.095
10	61	ns	46	46	-72.4749349	-38.2820722	299.22	20	75	1	14	1	2005	10	5	30.551
11	61	ns	46	46	-72.4749349	-38.2820722	299.22	20	75	1	14	1	2005	10	20	30.283
12	61	ns	46	46	-72.4749349	-38.2820722	299.22	20	75	1	14	1	2005	10	36	13.404
13	49	ns	226	46	-72.6797131	-38.2827598	234.03	20	75	1	14	1	2005	12	8	21.157
14	50	n	211	91	-72.6629099	-38.2780334	266.81	20	75	1	15	1	2005	10	0	8.708
15	58	n	91	91	-72.526475	-38.2963049	266.09	20	75	1	15	1	2005	10	5	30.041
16	57	n	106	91	-72.5436217	-38.2939098	275.46	20	75	1	15	1	2005	10	26	30.183
FFID	SP	type	nloc	ch1	long	lat	elev	depth	charge	holes	dd	mm	yyyy	hh	mm	ss +3 ms

FFID	SP	type	nloc	ch1	long	lat	elev	depth	charge	holes	dd	mm	yyyy	hh	mm	ss +3 ms
17	46	n	272	91	-72.7320849	-38.2627647	207.01	20	75	1	15	1	2005	10	32	8.542
18	54	n	151	91	-72.5947258	-38.2819644	271.16	20	75	1	15	1	2005	10	52	30.847
19	43	ns	318	136	-72.7862451	-38.2827185	408.44	20	75	1	16	1	2005	10	0	15.021
20	55	ns	136	136	-72.5773782	-38.2857936	277.04	20	75	1	16	1	2005	10	20	30.235
21	22	e	631	136	-73.1430902	-38.2701814	479.19	25	200	2	16	1	2005	10	26	0.965
22	55	ns	136	136	-72.5773782	-38.2857936	277.04	20	75	1	16	1	2005	10	35	30.141
23	47	n	256	136	-72.7144114	-38.2609867	241.77	20	75	1	16	1	2005	10	45	7.039
24	55	ns	136	136	-72.5773782	-38.2857936	277.04	20	75	1	16	1	2005	10	50	29.955
25	51	n	196	136	-72.6461117	-38.2840145	266.19	20	75	1	16	1	2005	11	35	30.329
26	40	n	361	181	-72.8350307	-38.2839542	383.39	20	75	1	17	1	2005	10	0	7.843
27	52	n	181	181	-72.6294014	-38.2878726	271.35	20	75	1	17	1	2005	10	5	30.523
28	13	e	761	181	-73.2932425	-38.2913672	622.08	25	200	2	17	1	2005	10	25	45.512
29	48	n	241	181	-72.6968291	-38.2609283	190.4	20	75	1	17	1	2005	10	35	30.049
30	44	n	301	181	-72.7658757	-38.2773584	436.4	20	75	1	17	1	2005	10	45	7.522
31	37	ns	401	226	-72.8861375	-38.2813223	156.21	20	75	1	18	1	2005	10	0	7.51
32	49	ns	226	226	-72.6797131	-38.2827598	234.03	20	75	1	18	1	2005	10	5	30.333
33	25	e	586	226	-73.0917059	-38.2697767	692.92	20	150	2	18	1	2005	10	10	59.765
34	49	ns	226	226	-72.6797131	-38.2827598	234.03	20	75	1	18	1	2005	10	20	31.609
35	41	n	346	226	-72.8178575	-38.2775362	416.05	20	75	1	18	1	2005	10	30	8.969
36	45	n	286	226	-72.7489907	-38.281325	414.85	20	75	1	18	1	2005	11	5	30.439
37	38	n	392	271	-72.8708583	-38.2803917	207.51	20	75	1	19	1	2005	10	0	6.773
38	42	n	331	271	-72.8004583	-38.2795814	389.62	20	75	1	19	1	2005	10	20	30.636
39	34	n	450	271	-72.9378326	-38.3029456	421.82	20	75	1	19	1	2005	10	31	36.7
40	46	n	272	271	-72.7320849	-38.2627647	207.01	20	75	1	19	1	2005	10	50	30.338
41	35	n	436	316	-72.92073	-38.2911839	190.24	20	75	1	20	1	2005	10	0	7.391
42	43	ns	318	316	-72.7862451	-38.2827185	408.44	20	75	1	20	1	2005	10	5	30.077
FFID	SP	type	nloc	ch1	long	lat	elev	depth	charge	holes	dd	mm	yyyy	hh	mm	ss +3 ms

FFID	SP	type	nloc	ch1	long	lat	elev	depth	charge	holes	dd	mm	yyyy	hh	mm	ss +3 ms
43	43	ns	318	316	-72.7862451	-38.2827185	408.44	20	75	1	20	1	2005	10	20	32.513
44	22	e	631	316	-73.1433547	-38.2703038	477.34	20	150	2	20	1	2005	10	26	15.403
45	31	nse	496	316	-72.9898617	-38.3037895	570.77	20	75	1	20	1	2005	10	30	7.093
46	39	n	376	316	-72.8520961	-38.2848054	299.47	20	75	1	20	1	2005	10	50	58.975
47	32	n	480	361	-72.9711387	-38.3000446	564.73	20	75	1	21	1	2005	10	0	8.433
48	40	n	361	361	-72.8350307	-38.2839542	383.39	20	75	1	21	1	2005	10	5	30.376
49	28	n	541	361	-73.040109	-38.273935	675.93	20	75	1	21	1	2005	10	30	7.571
50	36	n	421	361	-72.9036542	-38.2887608	152.21	20	75	1	21	1	2005	10	35	30.35
51	37	nse	406	406	-72.8861375	-38.2813223	156.21	20	75	1	22	1	2005	10	5	47.588
52	29	n	526	406	-73.0233658	-38.2860123	610.45	20	75	1	22	1	2005	10	15	8.363
53	37	nse	406	406	-72.8861375	-38.2813223	156.21	20	75	1	22	1	2005	10	20	29.851
54	25	nse	586	406	-73.0918127	-38.2693698	692.84	20	75	1	22	1	2005	10	45	8.21
55	33	n	465	406	-72.9548035	-38.2974103	535.03	20	75	1	22	1	2005	10	50	30.365
56	34	n	450	451	-72.9378326	-38.3029456	421.82	20	75	1	23	1	2005	10	5	30.376
57	26	n	571	451	-73.0742472	-38.2633801	687.2	20	75	1	23	1	2005	10	16	7.357
58	30	n	511	451	-73.0063397	-38.2972071	605.2	20	75	1	23	1	2005	10	35	33.427
59	22	n	631	451	-73.142747	-38.2700589	478.52	20	75	1	23	1	2005	10	45	7.74
60	43	e	318	451	-72.7865587	-38.2825261	413.04	20	150	2	23	1	2005	11	33	20.621
61	27	n	556	496	-73.0561127	-38.2573221	733.8	20	75	1	24	1	2005	10	11	30.055
62	49	e	226	496	-72.6792934	-38.2827137	236.63	25	200	2	24	1	2005	10	20	29.815
63	23	n	616	496	-73.1259063	-38.2713291	578.55	20	75	1	24	1	2005	10	30	7.307
64	31	nse	496	496	-72.9898617	-38.3037895	570.77	20	75	1	24	1	2005	10	56	0.238
65	19	ns	675	496	-73.1924173	-38.2634285	112.07	20	75	1	24	1	2005	11	0	8.424
66	31	nse	496	496	-72.9898617	-38.3037895	570.77	20	75	1	24	1	2005	11	11	18.957
67	16	n	721	541	-73.2460495	-38.2783913	462.61	20	75	1	25	1	2005	10	5	30.011
68	24	n	601	541	-73.1094293	-38.2733574	623.62	20	75	1	25	1	2005	10	10	26.033
FFID	SP	type	nloc	ch1	long	lat	elev	depth	charge	holes	dd	mm	yyyy	hh	mm	ss +3 ms

FFID	SP	type	nloc	ch1	long	lat	elev	depth	charge	holes	dd	mm	yyyy	hh	mm	ss +3 ms
69	28	n	541	541	-73.040109	-38.273935	675.93	20	75	1	25	1	2005	10	40	9.751
70	20	n	661	541	-73.1766965	-38.2603192	167.55	20	75	1	25	1	2005	10	50	30.027
71	55	e	136	541	-72.5769885	-38.2858535	275.13	25	200	2	25	1	2005	11	15	7.357
72	13	ns	766	586	-73.2983541	-38.2960659	615.24	20	75	1	26	1	2005	10	0	8.331
73	25	ns	586	586	-73.0918127	-38.2693698	692.84	20	75	1	26	1	2005	10	28	5.418
74	17	n	707	586	-73.2301885	-38.2746011	462	20	75	1	26	1	2005	10	31	7.251
75	61	e	42	586	-72.4692791	-38.2802128	299.36	27	250	2	26	1	2005	10	35	29.879
76	25	ns	586	586	-73.0918127	-38.2693698	692.84	20	75	1	26	1	2005	10	41	18.633
77	21	n	647	586	-73.160392	-38.2618294	310.8	20	75	1	26	1	2005	11	15	6.556
78	37	e	401	586	-72.8806117	-38.2808298	178.12	20	150	2	26	1	2005	11	41	1.625
79	10	n	811	631	-73.3491034	-38.2818692	471.53	20	75	1	27	1	2005	10	5	30.361
80	18	n	691	631	-73.2114389	-38.2624123	379.75	20	75	1	27	1	2005	10	30	6.459
81	14	n	750	631	-73.2809179	-38.3014061	685.45	20	75	1	27	1	2005	10	37	51.233
82	43	e	318	631	-72.7866201	-38.2821424	414.95	25	200	2	27	1	2005	10	41	9.586
83	22	n	631	631	-73.142747	-38.2700589	478.52	20	75	1	27	1	2005	11	3	43.187
84	7	n	856	676	-73.3996048	-38.2657812	415.09	20	75	1	28	1	2005	10	15	7.265
85	49	e	226	676	-72.680056	-38.2824957	235.02	25	200	2	28	1	2005	10	23	15.576
86	19	ns	675	676	-73.1924173	-38.2634285	112.07	20	75	1	28	1	2005	10	28	52.345
87	11	n	796	676	-73.3321275	-38.2884502	529.75	20	75	1	28	1	2005	10	45	6.571
88	19	ns	675	676	-73.1924173	-38.2634285	112.07	20	75	1	28	1	2005	11	26	21.107
89	15	n	735	676	-73.2624556	-38.283122	529.05	20	75	1	28	1	2005	12	16	7.352
90	4	n	902	721	-73.4528825	-38.256676	176.16	20	75	1	29	1	2005	10	5	27.477
91	12	n	780	721	-73.3147971	-38.293251	575.37	20	75	1	29	1	2005	10	11	0.959
92	55	e	136	721	-72.5765427	-38.2859479	276.99	27	250	2	29	1	2005	10	17	7.915
93	8	n	841	721	-73.3831201	-38.2738437	411.11	20	75	1	29	1	2005	10	35	30.193
94	16	n	721	721	-73.2460495	-38.2783913	462.61	20	75	1	29	1	2005	10	56	0.481
FFID	SP	type	nloc	ch1	long	lat	elev	depth	charge	holes	dd	mm	yyyy	hh	mm	ss +3 ms

FFID	SP	type	nloc	ch1	long	lat	elev	depth	charge	holes	dd	mm	yyyy	hh	mm	ss +3 ms
95	1	ns	946	766	-73.5028182	-38.2642335	56.51	20	75	1	30	1	2005	10	5	29.368
96	9	n	826	766	-73.3658936	-38.2733236	443.65	20	75	1	30	1	2005	10	11	50.811
97	61	e	46	766	-72.4696993	-38.2803738	299.99	30	300	2	30	1	2005	10	15	7.811
98	1	ns	946	766	-73.5028182	-38.2642335	56.51	20	75	1	30	1	2005	10	20	30.157
99	1	ns	946	766	-73.5028182	-38.2642335	56.51	20	75	1	30	1	2005	10	35	30.219
100	13	ns	766	766	-73.2983541	-38.2960659	615.24	20	75	1	30	1	2005	10	41	56.109
101	13	ns	766	766	-73.2983541	-38.2960659	615.24	20	75	1	30	1	2005	10	55	1.393
102	97	e	-44	766	-72.3716957	-38.2858377	344.61	30	300	2	30	1	2005	11	0	7.66
103	5	n	885	766	-73.4344609	-38.2679317	302.22	20	75	1	30	1	2005	11	20	10.023
104	0	n	953	776	-73.5106499	-38.2606397	94.67	20	75	1	30	1	2005	22	15	10.159
FFID	SP	type	nloc	ch1	long	lat	elev	depth	charge	holes	dd	mm	yyyy	hh	mm	ss +3 ms

Table A.1.: Shotpoint coordinates and related shot information. FFID and corresponding shotpoint number (SP) are listed first. The type of experiment configuration (NVR = n ; SH = s ; ESP = e), the nearest peg number to a shot (nloc), and the peg position of the first channel of the active spread is listed next. This is followed by the coordinates and elevations of the shots and information on the boreholes and blasting agent charges. The exact shot time is given at last, whereas to each measured time at the shooting boxes a value of 3 ms was added to account for the time delay of the shot caused by the burning of the blasting cord.

Table of receiver coordinates & used EDL

peg	long	lat	elev	EDL
1	-72.42261	-38.27150	322.65	3129
2	-72.42379	-38.27134	324.81	6017
3	-72.42487	-38.27140	324	3165
4	-72.42597	-38.27138	322.6	3102
5	-72.42715	-38.27136	319.06	3131
6	-72.42830	-38.27136	317.13	3028
7	-72.42945	-38.27131	316.86	3171
8	-72.43059	-38.27119	316.57	3074
9	-72.43172	-38.27116	306.93	6015
10	-72.43291	-38.27124	305.9	3027
11	-72.43402	-38.27122	306.87	3024
12	-72.43522	-38.27117	311.12	3090
13	-72.43630	-38.27116	311.7	3157
14	-72.43744	-38.27112	311.22	3072
15	-72.43858	-38.27110	310.56	3201
16	-72.43972	-38.27108	310.45	3101
17	-72.44086	-38.27105	311.82	3137
18	-72.44201	-38.27103	311.78	3104
19	-72.44315	-38.27100	310.88	3133
20	-72.44431	-38.27098	310.85	3172
21	-72.44543	-38.27094	311.08	3092
22	-72.44657	-38.27093	311.65	3148
23	-72.44771	-38.27096	309.65	6010
24	-72.44890	-38.27099	309.47	3093
25	-72.45001	-38.27102	309.41	3103
26	-72.45116	-38.27105	309.22	3091
27	-72.45232	-38.27108	308.89	6011
28	-72.45346	-38.27112	308.55	6019
29	-72.45460	-38.27115	309.19	3043
30	-72.45575	-38.27118	308.64	3029
31	-72.45691	-38.27121	308.28	3076
32	-72.45805	-38.27125	308.48	3123
33	-72.45924	-38.27203	310.42	3110
34	-72.46043	-38.27305	307.03	3170
peg	long	lat	elev	EDL

peg	long	lat	elev	EDL
35	-72.46162	-38.27407	305.14	3173
36	-72.46282	-38.27511	304.82	3087
37	-72.46403	-38.27613	303.49	3111
38	-72.46523	-38.27716	303.51	3108
39	-72.46641	-38.27815	306.04	6014
40	-72.46761	-38.27900	295.94	3086
41	-72.46881	-38.28002	297.3	6012
42	-72.46998	-38.28062	295.97	3956
43	-72.47114	-38.28093	299.7	3083
44	-72.47235	-38.28127	295.59	3049
45	-72.47346	-38.28156	295.27	6016
46	-72.47463	-38.28188	296.98	3082
47	-72.47577	-38.28219	297.07	3058
48	-72.47694	-38.28251	296.87	3112
49	-72.47809	-38.28282	298.49	3136
50	-72.47926	-38.28314	295.65	3105
51	-72.48041	-38.28345	298.07	3095
52	-72.48157	-38.28373	293.09	3106
53	-72.48271	-38.28405	292.3	3121
54	-72.48389	-38.28436	291.07	3959
55	-72.48504	-38.28467	288.24	3149
56	-72.48623	-38.28500	289.7	3113
57	-72.48738	-38.28547	293.21	3021
58	-72.48854	-38.28594	292.73	3957
59	-72.48970	-38.28642	292.46	3130
60	-72.49086	-38.28690	291.79	3061
61	-72.49204	-38.28739	286.14	3219
62	-72.49319	-38.28799	286.61	3025
63	-72.49436	-38.28849	299.67	3114
64	-72.49552	-38.28895	308.43	3055
65	-72.49669	-38.28926	291.05	3122
66	-72.49785	-38.28974	291.67	3119
67	-72.49902	-38.29023	286.31	3135
68	-72.50019	-38.29071	286.6	6013
69	-72.50134	-38.29116	287.93	3067
70	-72.50251	-38.29156	288.26	3089
71	-72.50369	-38.29231	285.26	3097
peg	long	lat	elev	EDL

peg	long	lat	elev	EDL	peg	long	lat	elev	EDL
72	-72.50486	-38.29323	276.92	3094	109	-72.54699	-38.28859	271.22	3051
73	-72.50604	-38.29352	272.34	3116	110	-72.54812	-38.28834	270.44	3160
74	-72.50717	-38.29384	269.45	3100	111	-72.54925	-38.28807	269.96	3208
75	-72.50834	-38.29415	271.33	3141	112	-72.55038	-38.28744	267.8	3181
76	-72.50948	-38.29435	272.09	3139	113	-72.55149	-38.28723	265.75	3167
77	-72.51065	-38.29453	268.33	3041	114	-72.55265	-38.28726	266.17	3197
78	-72.51180	-38.29474	267.28	3099	115	-72.55379	-38.28728	266.64	3186
79	-72.51298	-38.29509	270.85	3855	116	-72.55495	-38.28757	264.26	3176
80	-72.51407	-38.29535	265.72	3145	117	-72.55611	-38.28790	266.11	3214
81	-72.51526	-38.29565	268.37	3159	118	-72.55726	-38.28849	267.67	3203
82	-72.51643	-38.29577	270.61	3066	119	-72.55844	-38.28887	265.13	3221
83	-72.51755	-38.29588	266.8	3078	120	-72.55959	-38.28910	267.73	3053
84	-72.51870	-38.29592	266.96	3034	121	-72.56073	-38.28948	268.84	3185
85	-72.51987	-38.29588	265.23	3035	122	-72.56193	-38.29011	269.16	3023
86	-72.52102	-38.29596	266.8	3150	123	-72.56309	-38.29033	268.49	3210
87	-72.52215	-38.29610	269.12	3174	124	-72.56423	-38.29058	267.08	3212
88	-72.52329	-38.29628	266.76	3158	125	-72.56537	-38.29083	267.08	3216
89	-72.52444	-38.29643	265.75	3140	126	-72.56652	-38.29107	263.46	3030
90	-72.52561	-38.29648	266.24	3031	127	-72.56770	-38.29130	264.08	3169
91	-72.52671	-38.29624	266.87	3047	128	-72.56883	-38.29142	263.18	3163
92	-72.52786	-38.29610	265.33	3177	129	-72.56989	-38.28958	272.02	3054
93	-72.52900	-38.29606	265.67	3211	130	-72.57105	-38.28969	273.31	3195
94	-72.53016	-38.29632	267.92	3184	131	-72.57214	-38.28825	274.65	3218
95	-72.53131	-38.29638	269.01	3191	132	-72.57323	-38.28724	274.92	3217
96	-72.53243	-38.29620	269.11	3179	133	-72.57435	-38.28649	275.39	3224
97	-72.53359	-38.29612	270.31	3178	134	-72.57547	-38.28609	273.51	3190
98	-72.53471	-38.29585	271.96	3153	135	-72.57659	-38.28591	275.6	3192
99	-72.53586	-38.29562	273.84	3161	136	-72.57771	-38.28571	276.22	3951
100	-72.53698	-38.29540	274.1	3155	137	-72.57885	-38.28549	278.38	3154
101	-72.53811	-38.29518	273.9	3194	138	-72.57997	-38.28525	274.46	3182
102	-72.53925	-38.29496	272.53	3057	139	-72.58112	-38.28504	274.33	3199
103	-72.54039	-38.29474	271.92	3223	140	-72.58225	-38.28485	276	3205
104	-72.54153	-38.29451	272.56	3168	141	-72.58338	-38.28466	276.5	3206
105	-72.54265	-38.29423	275.06	3209	142	-72.58452	-38.28433	276.02	3222
106	-72.54378	-38.29387	278.05	3166	143	-72.58566	-38.28408	276.36	3215
107	-72.54492	-38.29365	275.82	3220	144	-72.58678	-38.28377	277.12	3070
108	-72.54604	-38.29342	276.2	3187	145	-72.58793	-38.28368	275.38	3955
peg	long	lat	elev	EDL	peg	long	lat	elev	EDL

peg	long	lat	elev	EDL	peg	long	lat	elev	EDL
146	-72.58907	-38.28362	274.66	3196	183	-72.63158	-38.28762	274.87	3102
147	-72.59020	-38.28330	274.55	3183	184	-72.63271	-38.28744	271.93	6017
148	-72.59135	-38.28297	274.63	3180	185	-72.63385	-38.28737	270.89	3129
149	-72.59246	-38.28266	272.94	3065	186	-72.63501	-38.28736	270.38	6015
150	-72.59361	-38.28234	272.42	3132	187	-72.63614	-38.28721	271.23	3074
151	-72.59469	-38.28203	271.36	3117	188	-72.63727	-38.28697	271.05	3171
152	-72.59582	-38.28174	272.57	3107	189	-72.63839	-38.28668	270.42	3028
153	-72.59699	-38.28139	272.12	3033	190	-72.63954	-38.28641	270.36	3104
154	-72.59813	-38.28107	272.32	3200	191	-72.64066	-38.28614	269.48	3101
155	-72.59964	-38.29004	271.41	3188	192	-72.64180	-38.28583	269.84	3137
156	-72.60078	-38.28936	271.4	3147	193	-72.64292	-38.28534	275.66	3201
157	-72.60189	-38.28858	271.79	3036	194	-72.64405	-38.28487	273.44	3157
158	-72.60300	-38.28787	272.35	3207	195	-72.64515	-38.28433	268.06	3090
159	-72.60413	-38.28719	272.65	3198	196	-72.64629	-38.28392	265.2	3072
160	-72.60524	-38.28657	272.79	3213	197	-72.64739	-38.28341	266.48	3027
161	-72.60635	-38.28596	272.4	3202	198	-72.64854	-38.28320	267.79	3024
162	-72.60747	-38.28533	271.68	3134	199	-72.64967	-38.28276	265.26	3133
163	-72.60860	-38.28470	271.86	3115	200	-72.65079	-38.28241	261.05	3093
164	-72.60971	-38.28413	273.13	3146	201	-72.65191	-38.28199	262.74	3148
165	-72.61079	-38.28350	273.84	3138	202	-72.65303	-38.28150	261.92	3092
166	-72.61192	-38.28289	272	3071	203	-72.65416	-38.28107	261.91	3172
167	-72.61305	-38.28229	272.72	3037	204	-72.65526	-38.28048	262.74	3103
168	-72.61416	-38.28169	271.12	6020	205	-72.65640	-38.28027	263.13	6011
169	-72.61524	-38.28113	268.79	3175	206	-72.65755	-38.28000	261.43	6010
170	-72.61638	-38.28053	271.24	3193	207	-72.65867	-38.27997	260.74	3091
171	-72.61747	-38.27993	268.16	3162	208	-72.65978	-38.27919	260.8	3123
172	-72.61861	-38.27933	267.06	3079	209	-72.66089	-38.27865	266.16	3076
173	-72.61971	-38.27865	274.47	3953	210	-72.66203	-38.27864	264.7	3087
174	-72.62082	-38.27780	267.62	3142	211	-72.66318	-38.27802	265.9	3029
175	-72.62192	-38.27700	267.75	3189	212	-72.66427	-38.27751	264.98	3173
176	-72.62305	-38.27653	268.01	3960	213	-72.66539	-38.27702	267.53	3043
177	-72.62415	-38.27604	267.4	3164	214	-72.66651	-38.27645	262.23	3170
178	-72.62527	-38.27550	267.29	3080	215	-72.66773	-38.27808	260.07	3110
179	-72.62639	-38.27495	269.23	3059	216	-72.66895	-38.27952	259.92	6019
180	-72.62750	-38.27439	268.43	3143	217	-72.67016	-38.28098	259.51	3049
181	-72.62930	-38.28786	270.32	3131	218	-72.67137	-38.28252	256.58	6012
182	-72.63043	-38.28782	273.11	3165	219	-72.67253	-38.28266	254.52	6016
peg	long	lat	elev	EDL	peg	long	lat	elev	EDL

peg	long	lat	elev	EDL	peg	long	lat	elev	EDL
220	-72.67366	-38.28252	260.26	6014	257	-72.71482	-38.26104	240.14	3041
221	-72.67478	-38.28198	264.34	3086	258	-72.71595	-38.26085	238.21	3145
222	-72.67588	-38.28115	259.56	3083	259	-72.71710	-38.26094	235.71	3159
223	-72.67698	-38.28029	257.64	3108	260	-72.71824	-38.26082	233.66	3066
224	-72.67809	-38.27953	258.79	3111	261	-72.71938	-38.26084	230.56	3035
225	-72.67921	-38.27891	262.45	3956	262	-72.72053	-38.26084	228.01	3150
226	-72.68032	-38.27838	261.78	3105	263	-72.72171	-38.26088	225.8	3958
227	-72.68145	-38.27788	258.42	3136	264	-72.72286	-38.26167	224.23	3078
228	-72.68255	-38.27736	257.65	3112	265	-72.72403	-38.26190	224.09	3034
229	-72.68368	-38.27694	253.83	3058	266	-72.72517	-38.26201	223.34	3099
230	-72.68480	-38.27646	252.73	3082	267	-72.72630	-38.26169	214.88	3174
231	-72.68593	-38.27597	252.2	3130	268	-72.72747	-38.26208	209.34	3031
232	-72.68704	-38.27524	255.73	3957	269	-72.72864	-38.26231	205.39	3140
233	-72.68813	-38.27454	251.11	3113	270	-72.72978	-38.26236	205.25	3158
234	-72.68922	-38.27344	248.78	3959	271	-72.73095	-38.26268	207.66	3211
235	-72.68977	-38.26266	188.58	3149	272	-72.73209	-38.26264	206.62	3047
236	-72.69093	-38.26292	203.34	3021	273	-72.73323	-38.26250	199.85	3191
237	-72.69206	-38.26265	200.46	3121	274	-72.73434	-38.26210	201.44	3177
238	-72.69316	-38.26198	198.5	3095	275	-72.73547	-38.26210	196.27	3184
239	-72.69425	-38.26124	198.62	3106	276	-72.73667	-38.26286	188.05	3179
240	-72.69536	-38.26055	189.66	3061	277	-72.73784	-38.26330	189.72	3178
241	-72.69649	-38.26059	188.69	3025	278	-72.73903	-38.26397	199.14	3153
242	-72.69769	-38.26113	193.63	3219	279	-72.74083	-38.27616	394.97	3161
243	-72.69886	-38.26171	194.71	6013	280	-72.74202	-38.27785	406.83	3155
244	-72.69999	-38.26175	199.9	3122	281	-72.74322	-38.27932	412.81	3057
245	-72.70113	-38.26158	207.58	3135	282	-72.74441	-38.27986	408.46	3194
246	-72.70212	-38.26161	223.96	3055	283	-72.74567	-38.28033	414.3	3223
247	-72.70341	-38.26152	236.01	3119	284	-72.74674	-38.28055	406.99	3166
248	-72.70453	-38.26116	240.16	3114	285	-72.74784	-38.28043	415.1	3220
249	-72.70566	-38.26085	244.52	3067	286	-72.74906	-38.28122	416.2	3209
250	-72.70680	-38.26072	249.1	3094	287	-72.75020	-38.28118	419.2	3168
251	-72.70792	-38.26028	256.77	3097	288	-72.75135	-38.28143	417.04	3160
252	-72.70905	-38.26009	264.98	3116	289	-72.75247	-38.28076	414.63	3051
253	-72.71018	-38.26022	262.36	3089	290	-72.75360	-38.28014	408.92	3208
254	-72.71136	-38.26067	255.74	3139	291	-72.75476	-38.27960	410.44	3187
255	-72.71251	-38.26083	250.77	3141	292	-72.75586	-38.27897	409.81	3176
256	-72.71367	-38.26083	244.8	3100	293	-72.75701	-38.27837	407.5	3053
peg	long	lat	elev	EDL	peg	long	lat	elev	EDL

peg	long	lat	elev	EDL	peg	long	lat	elev	EDL
294	-72.75804	-38.27792	413.24	3221	331	-72.80043	-38.27970	393.53	3207
295	-72.75921	-38.27830	419.33	3214	332	-72.80157	-38.27911	391.44	3198
296	-72.76029	-38.27860	419.41	3203	333	-72.80269	-38.27868	390.97	3036
297	-72.76151	-38.27875	423.15	3068	334	-72.80380	-38.27819	402.77	3147
298	-72.76261	-38.27766	434	3167	335	-72.80493	-38.27797	413.66	3200
299	-72.76367	-38.27712	431.58	3181	336	-72.80605	-38.27742	416.47	3117
300	-72.76485	-38.27701	433.75	3197	337	-72.80719	-38.27745	430.37	3033
301	-72.76602	-38.27741	438.03	3212	338	-72.80835	-38.27779	430.39	3107
302	-72.76715	-38.27748	440.28	3185	339	-72.80950	-38.27788	426.1	3188
303	-72.76830	-38.27743	448.47	3030	340	-72.81064	-38.27761	421.21	3134
304	-72.76944	-38.27739	451.64	3210	341	-72.81177	-38.27744	419.99	3115
305	-72.77060	-38.27743	448.62	3054	342	-72.81289	-38.27700	419.52	3202
306	-72.77176	-38.27696	450.47	3169	343	-72.81403	-38.27706	412.41	3146
307	-72.77283	-38.27656	439.6	3023	344	-72.81520	-38.27725	416.14	3213
308	-72.77397	-38.27643	432.38	3163	345	-72.81634	-38.27729	418.65	6020
309	-72.77508	-38.27640	432.77	3216	346	-72.81748	-38.27756	420.34	3193
310	-72.77645	-38.27959	425.99	3190	347	-72.81868	-38.27828	410.6	3175
311	-72.77760	-38.28047	425.31	3224	348	-72.81985	-38.27891	409.4	3079
312	-72.77879	-38.28126	432.03	3217	349	-72.82102	-38.27954	407.07	3162
313	-72.78001	-38.28234	417.13	3218	350	-72.82220	-38.28019	404.35	3138
314	-72.78121	-38.28402	406.13	3195	351	-72.82338	-38.28103	404.81	3037
315	-72.78233	-38.28388	406.35	3192	352	-72.82458	-38.28206	396.95	3953
316	-72.78348	-38.28355	415.16	3154	353	-72.82576	-38.28285	391.51	3071
317	-72.78460	-38.28325	414.68	3951	354	-72.82697	-38.28397	385.7	3080
318	-72.78571	-38.28312	408.22	3182	355	-72.82811	-38.28433	378.75	3960
319	-72.78686	-38.28236	412.39	3199	356	-72.82928	-38.28449	370.76	3059
320	-72.78794	-38.28182	413.87	3206	357	-72.83042	-38.28451	384.25	3143
321	-72.78907	-38.28127	413.33	3205	358	-72.83156	-38.28464	379.66	3164
322	-72.79022	-38.28072	415.78	3070	359	-72.83271	-38.28470	378.6	3142
323	-72.79136	-38.28015	420.88	3215	360	-72.83384	-38.28455	382.29	3189
324	-72.79245	-38.27980	425.69	3196	361	-72.83497	-38.28421	385.94	6015
325	-72.79359	-38.27981	425.45	3222	362	-72.83609	-38.28368	381.08	3171
326	-72.79473	-38.27977	418.4	3183	363	-72.83724	-38.28368	376.53	3129
327	-72.79587	-38.27962	405.34	3180	364	-72.83842	-38.28462	362.74	6017
328	-72.79700	-38.27966	400.3	3955	365	-72.83964	-38.28587	346.02	3074
329	-72.79817	-38.27983	396.95	3132	366	-72.84078	-38.28593	350.12	3165
330	-72.79932	-38.28015	398.67	3065	367	-72.84194	-38.28651	347.82	3131
peg	long	lat	elev	EDL	peg	long	lat	elev	EDL

peg	long	lat	elev	EDL	peg	long	lat	elev	EDL
368	-72.84311	-38.28692	341.91	3102	405	-72.88522	-38.28140	154.14	6016
369	-72.84426	-38.28710	344.25	3090	406	-72.88636	-38.28141	153.66	3136
370	-72.84540	-38.28688	344.69	3027	407	-72.88752	-38.28145	146.99	3112
371	-72.84654	-38.28708	338.75	3072	408	-72.88867	-38.28184	137.74	3957
372	-72.84769	-38.28684	333.95	3024	409	-72.88982	-38.28185	120.54	3105
373	-72.84883	-38.28665	329.16	3157	410	-72.89103	-38.28328	95.74	3130
374	-72.84994	-38.28649	316.64	3201	411	-72.89218	-38.28345	73.81	3113
375	-72.85106	-38.28563	301.07	3137	412	-72.89342	-38.28583	96.92	3082
376	-72.85215	-38.28437	295.29	3028	413	-72.89459	-38.28595	109.3	3058
377	-72.85322	-38.28275	267.09	3101	414	-72.89573	-38.28622	115.35	3959
378	-72.85428	-38.28084	249.31	3104	415	-72.89690	-38.28670	120.44	3021
379	-72.85536	-38.27931	241.11	3123	416	-72.89806	-38.28697	116.49	3106
380	-72.85650	-38.27890	238.92	3093	417	-72.89920	-38.28687	120.14	3061
381	-72.85760	-38.27864	233.43	6010	418	-72.90034	-38.28684	131	3121
382	-72.85875	-38.27845	225.6	3172	419	-72.90148	-38.28702	141.84	3095
383	-72.85988	-38.27803	225.81	3133	420	-72.90267	-38.28786	143.68	6013
384	-72.86099	-38.27773	227.56	6011	421	-72.90387	-38.28895	155.09	3144
385	-72.86215	-38.27785	217.95	3091	422	-72.90510	-38.29139	166.6	3219
386	-72.86332	-38.27809	215.86	3092	423	-72.90624	-38.29145	166.16	3119
387	-72.86448	-38.27873	217.51	3103	424	-72.90742	-38.29203	164.8	3094
388	-72.86566	-38.27939	217.65	3148	425	-72.90857	-38.29236	166.11	3097
389	-72.86683	-38.27994	215.86	3087	426	-72.90969	-38.29237	172.85	3055
390	-72.86801	-38.28063	215.37	3110	427	-72.91082	-38.29179	184.23	3135
391	-72.86915	-38.28076	212.8	3076	428	-72.91192	-38.29077	205.6	3122
392	-72.87030	-38.28064	205.33	3170	429	-72.91304	-38.29014	215.53	3114
393	-72.87142	-38.28045	212.11	3029	430	-72.91416	-38.28973	219.47	3067
394	-72.87256	-38.28028	217.69	6019	431	-72.91534	-38.29028	202.74	3089
395	-72.87371	-38.28042	219.06	3173	432	-72.91649	-38.29043	192.81	3025
396	-72.87487	-38.28075	209.83	3043	433	-72.91763	-38.29046	187.61	3116
397	-72.87606	-38.28097	206.13	6012	434	-72.91879	-38.29066	186.68	3041
398	-72.87716	-38.28064	200.66	3049	435	-72.91995	-38.29093	184.34	3100
399	-72.87833	-38.28100	191.03	3111	436	-72.92109	-38.29124	192.8	3139
400	-72.87946	-38.28087	185.63	3956	437	-72.92225	-38.29134	198.11	3141
401	-72.88062	-38.28092	178.99	3108	438	-72.92342	-38.29212	206	3145
402	-72.88173	-38.28077	180.28	3083	439	-72.92456	-38.29215	216	3159
403	-72.88290	-38.28095	177.45	3086	440	-72.92570	-38.29179	227.19	3035
404	-72.88405	-38.28111	167.87	6014	441	-72.92688	-38.29173	230.22	3066
peg	long	lat	elev	EDL	peg	long	lat	elev	EDL

peg	long	lat	elev	EDL	peg	long	lat	elev	EDL
442	-72.92799	-38.29181	222.54	3174	479	-72.97050	-38.29922	560.42	3023
443	-72.92909	-38.29121	229.63	3158	480	-72.97168	-38.29989	556.49	3054
444	-72.93022	-38.29081	234.28	3078	481	-72.97281	-38.29996	558.05	3169
445	-72.93136	-38.29105	252.58	3099	482	-72.97397	-38.29981	553.94	3163
446	-72.93259	-38.29287	258.28	3034	483	-72.97509	-38.29967	561.36	3030
447	-72.93380	-38.29500	293.35	3031	484	-72.97624	-38.29999	544.83	3210
448	-72.93497	-38.29558	311.62	3140	485	-72.97739	-38.30008	537.9	3197
449	-72.93613	-38.29609	323.15	3855	486	-72.97818	-38.30068	524.43	3185
450	-72.93748	-38.30244	419.52	3150	487	-72.97974	-38.30146	507.45	3212
451	-72.93865	-38.30295	424.13	3177	488	-72.98089	-38.30164	498.27	3181
452	-72.93978	-38.30295	434.29	3191	489	-72.98205	-38.30208	494.73	3192
453	-72.94094	-38.30307	438.65	3047	490	-72.98321	-38.30262	504.81	3195
454	-72.94208	-38.30298	448.39	3211	491	-72.98438	-38.30330	520.88	3218
455	-72.94321	-38.30276	457.4	3184	492	-72.98554	-38.30380	524.14	3217
456	-72.94435	-38.30259	460.45	3178	493	-72.98670	-38.30360	539.76	3224
457	-72.94548	-38.30222	460.88	3153	494	-72.98781	-38.30336	549.44	3190
458	-72.94662	-38.30222	467.17	3179	495	-72.98879	-38.30345	556.85	3216
459	-72.94778	-38.30268	481	3223	496	-72.99008	-38.30360	572.39	3182
460	-72.94891	-38.30234	481.24	3194	497	-72.99126	-38.30346	579.2	3951
461	-72.95001	-38.30128	481.62	3057	498	-72.99238	-38.30328	573.25	3205
462	-72.95113	-38.30062	496.39	3155	499	-72.99351	-38.30316	576.45	3199
463	-72.95223	-38.29961	511.39	3161	500	-72.99467	-38.30299	583.02	3154
464	-72.95333	-38.29829	522.86	3209	501	-72.99578	-38.30286	593.97	3070
465	-72.95444	-38.29778	531.85	3168	502	-72.99694	-38.30296	604.47	3206
466	-72.95556	-38.29713	540.95	3160	503	-72.99808	-38.30281	598.78	3215
467	-72.95668	-38.29660	550.42	3220	504	-72.99917	-38.30167	592.79	3198
468	-72.95773	-38.29556	560.77	3166	505	-73.00029	-38.30120	592.04	3036
469	-72.95894	-38.29533	560.36	3176	506	-73.00145	-38.30115	595.54	3065
470	-72.96006	-38.29502	572.78	3214	507	-73.00257	-38.30101	605.14	3207
471	-72.96120	-38.29487	581.56	3167	508	-73.00368	-38.30012	619.37	3132
472	-72.96231	-38.29468	587.31	3203	509	-73.00481	-38.29917	626.59	3183
473	-72.96347	-38.29483	576.55	3051	510	-73.00591	-38.29797	602.31	3955
474	-72.96467	-38.29624	555.23	3068	511	-73.00699	-38.29686	612.78	3180
475	-72.96584	-38.29690	538.89	3187	512	-73.00808	-38.29476	628.79	3196
476	-72.96702	-38.29805	539.71	3208	513	-73.00909	-38.29219	610.61	3222
477	-72.96819	-38.29845	547.07	3053	514	-73.01019	-38.29063	618.03	3146
478	-72.96935	-38.29903	546.28	3221	515	-73.01132	-38.29033	605.71	3202
peg	long	lat	elev	EDL	peg	long	lat	elev	EDL

peg	long	lat	elev	EDL	peg	long	lat	elev	EDL
516	-73.01240	-38.28872	590.39	3200	553	-73.05312	-38.25833	719.7	3027
517	-73.01354	-38.28808	590.62	3033	554	-73.05412	-38.25564	730.98	3157
518	-73.01460	-38.28745	583.43	3107	555	-73.05531	-38.25684	739.85	3090
519	-73.01572	-38.28716	584.99	3117	556	-73.05648	-38.25760	739.62	3102
520	-73.01689	-38.28699	599.07	3188	557	-73.05764	-38.25816	746.77	3123
521	-73.01803	-38.28705	604.78	3115	558	-73.05883	-38.25805	736.3	3101
522	-73.01919	-38.28703	607.48	3134	559	-73.05993	-38.25773	729.08	3104
523	-73.02030	-38.28688	608.46	3147	560	-73.06106	-38.25726	726.68	3172
524	-73.02145	-38.28675	600.97	3079	561	-73.06218	-38.25691	728.59	6010
525	-73.02258	-38.28655	612.13	3193	562	-73.06333	-38.25697	725.08	3093
526	-73.02371	-38.28595	613.27	6020	563	-73.06449	-38.25712	724.21	3103
527	-73.02482	-38.28554	612.74	3213	564	-73.06564	-38.25740	725.1	3091
528	-73.02596	-38.28513	614.91	3175	565	-73.06682	-38.25778	715.76	3110
529	-73.02706	-38.28440	621.1	3071	566	-73.06814	-38.26054	694.74	3087
530	-73.02822	-38.28355	628.25	3162	567	-73.06929	-38.26105	690.75	3148
531	-73.02931	-38.28333	630.47	3037	568	-73.07046	-38.26136	685.4	3092
532	-73.03043	-38.28319	642.42	3953	569	-73.07162	-38.26162	682.52	6011
533	-73.03158	-38.28310	644.05	3138	570	-73.07283	-38.26276	683.26	3133
534	-73.03268	-38.28255	646.62	3189	571	-73.07401	-38.26347	685.96	3111
535	-73.03381	-38.28220	651.61	3142	572	-73.07513	-38.26343	692.87	3049
536	-73.03492	-38.28171	651.27	3164	573	-73.07629	-38.26335	682.21	3173
537	-73.03598	-38.28009	644.33	3143	574	-73.07745	-38.26373	675.27	6012
538	-73.03708	-38.27869	651.37	3960	575	-73.07863	-38.26410	672.75	6019
539	-73.03816	-38.27765	661.34	3080	576	-73.07981	-38.26459	668.95	3043
540	-73.03915	-38.27468	676.7	3059	577	-73.08098	-38.26528	664.07	3029
541	-73.04027	-38.27382	674.02	3171	578	-73.08221	-38.26683	649.35	3170
542	-73.04135	-38.27282	673.93	6015	579	-73.08339	-38.26738	647.96	3076
543	-73.04224	-38.26805	671.33	6017	580	-73.08453	-38.26733	652.79	3083
544	-73.04336	-38.26760	677.48	3129	581	-73.08568	-38.26765	660.21	6014
545	-73.04449	-38.26731	678.97	3074	582	-73.08682	-38.26772	665.36	6016
546	-73.04562	-38.26704	684.09	3165	583	-73.08799	-38.26798	673.56	3956
547	-73.04675	-38.26678	684.49	3131	584	-73.08916	-38.26819	678.1	3086
548	-73.04785	-38.26604	679.16	3137	585	-73.09030	-38.26837	681.62	3108
549	-73.04889	-38.26416	674.14	3201	586	-73.09147	-38.26888	683.48	3113
550	-73.04995	-38.26252	694.5	3028	587	-73.09279	-38.27232	683.5	3130
551	-73.05090	-38.25947	708.97	3024	588	-73.09398	-38.27325	676.83	3105
552	-73.05200	-38.25890	710.83	3072	589	-73.09515	-38.27356	667.6	3957
peg	long	lat	elev	EDL	peg	long	lat	elev	EDL

peg	long	lat	elev	EDL	peg	long	lat	elev	EDL
590	-73.09629	-38.27362	660.59	3112	627	-73.13839	-38.26869	515.15	3031
591	-73.09743	-38.27367	660.68	3136	628	-73.13951	-38.26835	507.95	3140
592	-73.09858	-38.27358	660.68	6013	629	-73.14065	-38.26840	502.78	3099
593	-73.09972	-38.27361	662.85	3121	630	-73.14181	-38.26867	498.71	3034
594	-73.10087	-38.27335	662.08	3144	631	-73.14301	-38.26937	489.13	3178
595	-73.10196	-38.27279	660.9	3095	632	-73.14416	-38.26974	483.53	3184
596	-73.10312	-38.27275	661.2	3959	633	-73.14535	-38.27065	464.23	3191
597	-73.10425	-38.27281	665.59	3079	634	-73.14650	-38.27055	458.18	3211
598	-73.10540	-38.27268	659.96	3082	635	-73.14764	-38.27063	449.3	3047
599	-73.10655	-38.27273	651.81	3058	636	-73.14881	-38.27085	443.18	3177
600	-73.10771	-38.27286	642.68	3061	637	-73.14995	-38.27099	435.58	3155
601	-73.10885	-38.27301	632.01	3021	638	-73.15111	-38.27115	418.37	3223
602	-73.11001	-38.27330	624.9	3114	639	-73.15219	-38.26977	398.58	3057
603	-73.11113	-38.27287	627.85	3097	640	-73.15330	-38.26890	381.36	3179
604	-73.11226	-38.27276	634.27	3219	641	-73.15438	-38.26778	364.69	3194
605	-73.11342	-38.27319	621.34	3055	642	-73.15555	-38.26829	356.17	3153
606	-73.11461	-38.27369	617.63	3135	643	-73.15668	-38.26790	351.05	3167
607	-73.11575	-38.27368	617.85	3119	644	-73.15776	-38.26696	341	3160
608	-73.11689	-38.27366	610.98	3122	645	-73.15885	-38.26532	326.66	3209
609	-73.11804	-38.27346	602.49	3094	646	-73.15977	-38.26152	294.89	3214
610	-73.11915	-38.27289	601.36	3145	647	-73.16089	-38.26106	285.75	3161
611	-73.12027	-38.27255	599.05	3141	648	-73.16202	-38.26095	275.7	3176
612	-73.12140	-38.27237	594.57	3100	649	-73.16315	-38.26035	261.4	3166
613	-73.12252	-38.27196	589.97	3139	650	-73.16422	-38.25899	211.72	3168
614	-73.12365	-38.27161	586.15	3116	651	-73.16533	-38.25827	198.39	3220
615	-73.12479	-38.27135	582.55	3041	652	-73.16646	-38.25758	158.8	3051
616	-73.12594	-38.27142	581.07	3025	653	-73.16756	-38.25747	155.32	3203
617	-73.12707	-38.27167	568.31	3067	654	-73.16873	-38.25794	142.82	3068
618	-73.12826	-38.27187	559.84	3089	655	-73.16993	-38.25878	122.2	3030
619	-73.12938	-38.27158	559.39	3066	656	-73.17111	-38.25918	116.49	3169
620	-73.13052	-38.27149	559.28	3035	657	-73.17227	-38.25956	112.33	3053
621	-73.13164	-38.27116	556.2	3159	658	-73.17340	-38.25910	110.93	3208
622	-73.13277	-38.27067	546.42	3174	659	-73.17456	-38.25936	111.37	3023
623	-73.13389	-38.27024	539.95	3158	660	-73.17570	-38.25939	113.3	3221
624	-73.13500	-38.26970	534.11	3078	661	-73.17684	-38.25915	111.23	3163
625	-73.13613	-38.26934	523.96	3958	662	-73.17796	-38.25892	110.04	3054
626	-73.13724	-38.26868	518.92	3150	663	-73.17911	-38.25883	112.45	3187
peg	long	lat	elev	EDL	peg	long	lat	elev	EDL

peg	long	lat	elev	EDL	peg	long	lat	elev	EDL
664	-73.18026	-38.25919	109.96	3195	701	-73.22320	-38.27213	499.1	3107
665	-73.18141	-38.25918	106.8	3218	702	-73.22445	-38.27362	488.55	3147
666	-73.18247	-38.25948	105.45	3217	703	-73.22559	-38.27361	480.32	3188
667	-73.18374	-38.25996	102.52	3181	704	-73.22674	-38.27373	472.52	3117
668	-73.18491	-38.26023	105.99	3192	705	-73.22786	-38.27413	472.68	3134
669	-73.18606	-38.26038	106.93	3212	706	-73.22907	-38.27468	464.85	3037
670	-73.18720	-38.26045	109.89	3185	707	-73.23025	-38.27466	459.13	3138
671	-73.18838	-38.26078	111.63	3197	708	-73.23134	-38.27492	460.41	3071
672	-73.18951	-38.26077	107.94	3210	709	-73.23249	-38.27464	444.44	3162
673	-73.19064	-38.26070	103.9	3224	710	-73.23363	-38.27448	438.48	3175
674	-73.19182	-38.26100	110.22	3190	711	-73.23480	-38.27491	431.92	3213
675	-73.19296	-38.26150	107.01	3216	712	-73.23594	-38.27506	423.61	6020
676	-73.19415	-38.26136	108.93	3182	713	-73.23710	-38.27515	419.37	3953
677	-73.19530	-38.26193	108.82	3199	714	-73.23823	-38.27519	417.01	3059
678	-73.19648	-38.26273	101.68	3154	715	-73.23938	-38.27515	424.64	3960
679	-73.19747	-38.26019	123.46	3951	716	-73.24052	-38.27498	427.67	3080
680	-73.19871	-38.26187	151.09	3205	717	-73.24164	-38.27500	433.99	3164
681	-73.19986	-38.26222	183.35	3070	718	-73.24283	-38.27566	453.76	3143
682	-73.20097	-38.26165	231.1	3065	719	-73.24402	-38.27715	454.88	3142
683	-73.20198	-38.25952	250.12	3183	720	-73.24520	-38.27826	462.03	3189
684	-73.20314	-38.25980	271.38	3036	721	-73.24641	-38.27863	463.89	3165
685	-73.20432	-38.26045	285.42	3215	722	-73.24762	-38.27903	468.14	3129
686	-73.20547	-38.25979	291.62	3132	723	-73.24876	-38.27918	473.45	3137
687	-73.20657	-38.25990	305.3	3198	724	-73.24988	-38.27939	473	3074
688	-73.20771	-38.25991	319.01	3207	725	-73.25104	-38.27954	479.12	6017
689	-73.20889	-38.26066	335.24	3206	726	-73.25215	-38.27973	480.62	6015
690	-73.21003	-38.26079	345.57	3200	727	-73.25331	-38.27986	490.04	3131
691	-73.21131	-38.26214	373.56	3033	728	-73.25443	-38.28027	493.03	3171
692	-73.21245	-38.26326	385.27	3222	729	-73.25563	-38.28092	482.33	-999
693	-73.21353	-38.26248	412.33	3146	730	-73.25683	-38.28141	480.89	3201
694	-73.21463	-38.26173	427.05	3180	731	-73.25798	-38.28185	487.86	3072
695	-73.21586	-38.26264	441.51	3149	732	-73.25911	-38.28199	488.9	3157
696	-73.21704	-38.26364	458.12	3196	733	-73.26031	-38.28259	503.44	3024
697	-73.21823	-38.26463	477.3	3955	734	-73.26147	-38.28315	513.6	3028
698	-73.21937	-38.26466	490.5	3193	735	-73.26262	-38.28319	521.73	3101
699	-73.22056	-38.26546	506.26	3115	736	-73.26378	-38.28364	534.76	3090
700	-73.22182	-38.26770	501.03	6018	737	-73.26494	-38.28427	548.87	3027
peg	long	lat	elev	EDL	peg	long	lat	elev	EDL

peg	long	lat	elev	EDL	peg	long	lat	elev	EDL
738	-73.26616	-38.28531	567.39	3102	775	-73.30883	-38.29458	612.17	3021
739	-73.26732	-38.28648	591.84	3104	776	-73.30996	-38.29445	604.04	3079
740	-73.26856	-38.28745	604.43	3091	777	-73.31109	-38.29408	600.6	3095
741	-73.26969	-38.28900	615.21	3128	778	-73.31224	-38.29421	592.57	3114
742	-73.27090	-38.29068	644.29	3172	779	-73.31340	-38.29459	586.89	3959
743	-73.27213	-38.29244	665.64	3103	780	-73.31452	-38.29372	585.61	3058
744	-73.27337	-38.29488	686.75	6010	781	-73.31566	-38.29301	575.41	3097
745	-73.27451	-38.29545	696.65	3110	782	-73.31675	-38.29242	575.34	3082
746	-73.27569	-38.29598	695.55	3093	783	-73.31786	-38.29158	564.57	3061
747	-73.27687	-38.29655	696.48	3087	784	-73.31901	-38.29107	556.25	3219
748	-73.27803	-38.29698	694.95	3148	785	-73.32012	-38.29050	547.13	3135
749	-73.27918	-38.29739	694.9	6011	786	-73.32122	-38.29012	541.96	3119
750	-73.28043	-38.30123	689.51	3133	787	-73.32238	-38.29006	540.96	3055
751	-73.28162	-38.30205	689.8	3111	788	-73.32343	-38.28819	539.89	3041
752	-73.28280	-38.30291	682.75	3029	789	-73.32456	-38.28709	534.84	3139
753	-73.28393	-38.30195	675.73	3043	790	-73.32568	-38.28705	526.44	3145
754	-73.28488	-38.29642	656.68	6019	791	-73.32685	-38.28738	517.49	3100
755	-73.28596	-38.29516	629.09	6012	792	-73.32799	-38.28792	514.49	3122
756	-73.28709	-38.29420	623.29	3173	793	-73.32914	-38.28781	521.37	3116
757	-73.28818	-38.29360	627.24	3049	794	-73.33029	-38.28759	526.92	3141
758	-73.28939	-38.29373	632.49	3108	795	-73.33144	-38.28798	528.04	3094
759	-73.29048	-38.29367	634.73	3956	796	-73.33260	-38.28827	529.28	3025
760	-73.29162	-38.29374	627.7	6016	797	-73.33377	-38.28930	528.97	3067
761	-73.29275	-38.29390	633.09	3086	798	-73.33493	-38.28963	527.86	3089
762	-73.29396	-38.29421	638.51	6014	799	-73.33612	-38.28986	525.09	3150
763	-73.29512	-38.29508	627.62	3170	800	-73.33724	-38.28998	523.4	3958
764	-73.29626	-38.29590	615.27	3083	801	-73.33838	-38.29004	519.99	3158
765	-73.29744	-38.29609	610.1	3076	802	-73.33936	-38.28637	526.65	3035
766	-73.29858	-38.29613	614.79	3144	803	-73.34046	-38.28493	528.56	3174
767	-73.29974	-38.29619	613.25	3121	804	-73.34152	-38.28321	520.16	3159
768	-73.30087	-38.29598	609.82	3136	805	-73.34263	-38.28225	510.12	3034
769	-73.30201	-38.29574	621.22	6013	806	-73.34373	-38.28184	509.72	3066
770	-73.30315	-38.29574	630.67	3105	807	-73.34488	-38.28161	500.03	3031
771	-73.30429	-38.29566	642.34	3113	808	-73.34602	-38.28154	494.44	3140
772	-73.30539	-38.29538	639.67	3957	809	-73.34717	-38.28156	493.78	3099
773	-73.30655	-38.29503	634.75	3130	810	-73.34832	-38.28210	480.76	3078
774	-73.30769	-38.29486	622.81	3112	811	-73.34948	-38.28159	464.72	3191
peg	long	lat	elev	EDL	peg	long	lat	elev	EDL

peg	long	lat	elev	EDL	peg	long	lat	elev	EDL
812	-73.35056	-38.28052	464.08	3211	849	-73.39225	-38.26754	411.59	3224
813	-73.35165	-38.27925	472.27	3178	850	-73.39332	-38.26629	401.77	3216
814	-73.35277	-38.27897	469.16	3184	851	-73.39442	-38.26557	400.12	3210
815	-73.35390	-38.27850	464.24	3223	852	-73.39557	-38.26550	405.18	-999
816	-73.35501	-38.27803	469.1	3179	853	-73.39671	-38.26550	408.4	3197
817	-73.35614	-38.27755	471.95	3194	854	-73.39784	-38.26564	412.14	3185
818	-73.35723	-38.27654	471.91	3155	855	-73.39899	-38.26567	419.16	3212
819	-73.35830	-38.27514	475.72	3057	856	-73.40013	-38.26544	413.56	3070
820	-73.35941	-38.27451	473.13	3047	857	-73.40124	-38.26483	400	3065
821	-73.36053	-38.27411	470.68	3177	858	-73.40239	-38.26416	387.06	3205
822	-73.36166	-38.27381	464.67	3166	859	-73.40347	-38.26344	385.91	3154
823	-73.36281	-38.27368	463.26	3161	860	-73.40457	-38.26291	384.45	3951
824	-73.36397	-38.27364	455.28	3160	861	-73.40572	-38.26287	387.19	3182
825	-73.36515	-38.27364	453.2	3167	862	-73.40691	-38.26320	377.18	3199
826	-73.36623	-38.27341	446.94	3168	863	-73.40806	-38.26349	373.27	3206
827	-73.36739	-38.27357	443.67	3214	864	-73.40921	-38.26381	371.29	3132
828	-73.36853	-38.27356	439.34	3153	865	-73.41042	-38.26406	382.27	3198
829	-73.36972	-38.27424	433.18	3209	866	-73.41154	-38.26436	359.05	3183
830	-73.37087	-38.27460	435.34	3176	867	-73.41269	-38.26466	360.62	3200
831	-73.37203	-38.27477	433.38	3203	868	-73.41387	-38.26494	362.91	3036
832	-73.37318	-38.27486	429.71	3220	869	-73.41500	-38.26515	357.5	3033
833	-73.37433	-38.27523	426.84	3068	870	-73.41618	-38.26545	354.19	3215
834	-73.37550	-38.27595	424.23	3023	871	-73.41732	-38.26573	353.75	3207
835	-73.37667	-38.27586	419.88	3208	872	-73.41849	-38.26616	347.71	3222
836	-73.37779	-38.27546	408.18	3053	873	-73.41967	-38.26639	347.8	3180
837	-73.37890	-38.27504	403.71	3169	874	-73.42081	-38.26659	343.38	3146
838	-73.38003	-38.27494	413.65	3030	875	-73.42198	-38.26689	344.27	3196
839	-73.38119	-38.27465	408.69	-999	876	-73.42311	-38.26716	339.52	3955
840	-73.38234	-38.27437	408.95	3054	877	-73.42429	-38.26745	332.04	3149
841	-73.38340	-38.27400	415.17	3192	878	-73.42546	-38.26781	324.36	3193
842	-73.38452	-38.27357	423.94	3217	879	-73.42658	-38.26772	323.92	3115
843	-73.38566	-38.27320	431.22	3195	880	-73.42771	-38.26743	319.56	6018
844	-73.38679	-38.27254	437.72	3163	881	-73.42883	-38.26714	311.88	3107
845	-73.38787	-38.27170	439.92	3218	882	-73.42998	-38.26705	304.73	3147
846	-73.38898	-38.27084	434.45	3181	883	-73.43109	-38.26651	309.38	3037
847	-73.39009	-38.26997	422.88	3221	884	-73.43225	-38.26660	308.68	3138
848	-73.39117	-38.26877	420.93	3187	885	-73.43342	-38.26741	301.07	3117
peg	long	lat	elev	EDL	peg	long	lat	elev	EDL

peg	long	lat	elev	EDL
886	-73.43462	-38.26814	300	3134
887	-73.43578	-38.26832	298.8	3188
888	-73.43688	-38.26758	296.22	3071
889	-73.43796	-38.26632	280.83	3162
890	-73.43900	-38.26472	263.49	3175
891	-73.44015	-38.26432	258.43	3213
892	-73.44123	-38.26376	264.44	6020
893	-73.44235	-38.26315	263.73	3960
894	-73.44348	-38.26264	256.67	3953
895	-73.44449	-38.26024	245.4	3059
896	-73.44553	-38.25827	230.02	3164
897	-73.44667	-38.25816	225.41	3189
898	-73.44780	-38.25793	219.38	3080
899	-73.44891	-38.25752	218.8	3142
900	-73.45004	-38.25703	203.49	3143
901	-73.45112	-38.25638	195.49	6015
902	-73.45230	-38.25664	181.08	3137
903	-73.45346	-38.25679	173.96	6017
904	-73.45463	-38.25726	166.68	3074
905	-73.45575	-38.25676	154.93	3165
906	-73.45687	-38.25656	144.77	3129
907	-73.45799	-38.25645	141.38	3157
908	-73.45914	-38.25593	140.18	3028
909	-73.46031	-38.25552	134.1	3072
910	-73.46128	-38.25345	114.42	3024
911	-73.46240	-38.25305	120.98	3190
912	-73.46355	-38.25347	127.81	3131
913	-73.46474	-38.25408	122.14	3201
914	-73.46591	-38.25462	118.62	3171
915	-73.46706	-38.25445	124.09	3090
916	-73.46816	-38.25372	125.72	3102
917	-73.46927	-38.25372	128.67	3027
918	-73.47046	-38.25396	118.05	3091
919	-73.47160	-38.25402	119.55	3104
920	-73.47276	-38.25408	115.79	3101
921	-73.47391	-38.25414	115.23	3128
922	-73.47503	-38.25404	112.26	3172
peg	long	lat	elev	EDL

peg	long	lat	elev	EDL
923	-73.47620	-38.25433	110.39	3110
924	-73.47736	-38.25461	108.11	6011
925	-73.47852	-38.25485	110.19	3148
926	-73.47967	-38.25491	112.23	3133
927	-73.48073	-38.25328	86.28	6010
928	-73.48181	-38.25230	82.21	3087
929	-73.48293	-38.25201	73.16	3103
930	-73.48406	-38.25168	66.31	3093
931	-73.48522	-38.25135	63.45	3108
932	-73.48635	-38.25171	54.32	6012
933	-73.48751	-38.25150	55.21	3043
934	-73.48862	-38.25149	45.38	3049
935	-73.48981	-38.25223	32.18	6019
936	-73.49108	-38.25402	37.14	3029
937	-73.49224	-38.25414	45.75	3069
938	-73.49339	-38.25468	29.86	3111
939	-73.49461	-38.25583	36.62	3076
940	-73.49582	-38.25668	35.78	3083
941	-73.49699	-38.25746	33.56	3170
942	-73.49824	-38.25933	22.29	6014
943	-73.49948	-38.26097	22.44	3086
944	-73.50059	-38.26150	21.92	6016
945	-73.50182	-38.26194	38.26	3956
946	-73.50303	-38.26306	56.74	3144
947	-73.50417	-38.26304	72.16	3136
948	-73.50529	-38.26287	84.92	3121
949	-73.50646	-38.26336	89.62	3112
950	-73.50761	-38.26339	93.42	3130
951	-73.50870	-38.26118	107.19	3113
952	-73.50971	-38.26008	107.41	3957
953	-73.51090	-38.26056	97.87	3021
954	-73.51202	-38.26020	51.15	3105
955	-73.51254	-38.25997	28.85	6013
peg	long	lat	elev	EDL

Table A.2.: List of the peg coordinates along the TIPTEQ profile where the 955 receivers were deployed and corresponding EDL numbers.

B. Appendix: Preprocessing

B.1. HOW2SEGY.TXT

```
How to convert EDL data to SEGY data, a quick walktrough

--------------------------------------------------------

First, the EDL data files have to be converted in PDAS file format.
This is done with the program mseed_pdas. Program must be run under a
LINUX system (e.g. dss8)! PDAS data is written in ./PDAS.

The EDL data files are 30 minute files, for example. Some may be
corrupt, and can therefore not be converted correctly! This may be due
problems during start-up or shut-down processes at non-continuous
recordings, so first or last files of the data set for each EDL contain
errors. Broken files also occur in the middle of the total data set out
of no obvious reason.

If the edl2pdas.linux program finds an error in a file, the whole trace
is not converted!

So, the PDAS data must be checked visually with the pdis program, run
from the PDAS directory.

For three component data this can be done 'quite fast'. Display all
data of all EDLs of one day for example of one component and after
pressing DRAW note the number of traces at the lower left corner of the
window. It may be needed to click DRAW in fast intervals...

If all channels show the same number of traces and they are identical
with the expected number of traces (see below) you're fine. Is there a
discrepancy, display all three traces and only some EDL units at once.
In addition it is recommended to zoom very close to the beginning of
the trace. The three traces of each EDL show a 'characteristic
signature' meaning the same start point or gaps. If only a pair of
traces can be seen, the corrupt EDL and component can be noted.
```

```
    ----  ---------------------------
    ----  ---------------------------
    ----  ---------------------------
  ------------------------------
  ------------------------------
  ------------------------------
---  -----------------------------
---  -----------------------------  only two traces!
  ------------------------------
  ------------------------------
  ------------------------------
```

The PVIEW program (windows) may be used to find the corrupt files. Load the files and check them visually. Sometimes corrupt files can not be loaded and the user is notified of the filename. Otherwise, the beginning of data may differ between the components or a trace shows no data or strange things. Delete the corresponding EDL raw-data files !

Delete also the corresponding pdas files in the PDAS directory for this EDL component and day, since the files are not overwritten during the next conversion !

Check now the mseed_pdas_pfad script and change the corresponding day, EDL number, etc. Run the file and only the former missing component files are now converted.

Check again with pdis for the complete number of traces.

everything ok ?? --> create segy files with m_segy on an UNIX machine.

Here, the length of the trace and the forerun time T0 must be given. Afterwards, a formatted *gmt file for each channel is created using inputfiles (e.g. *17_src.asc) for the locations of the source and receivers as input for the pdas2segy7 program. The needed things can be found in the m_segy file in the awk section.

Later on, the single segy files can be merged to one segy file containing all the shots of one day for one component, for example, with segymerge.

Usage: segymerge output_file input_file_1 input_file_2 ...

How to find the expected number of traces:

180 EDLs -> 3*180 traces

Some folders contain only a little amount of kb due to bad batteries,
stolen disks, gaps, etc. There is a kind of threshold kb value beyond
which is no useable data in a directory. The script emptycheck searches
for a directory with less than a given kb value and writes these
directories in a file. 180 minus the number of directories gives the
expected number of traces for pdis.

----
scripts and programs can be found in /tipteq/SEGY

B.2. Airblast and offset
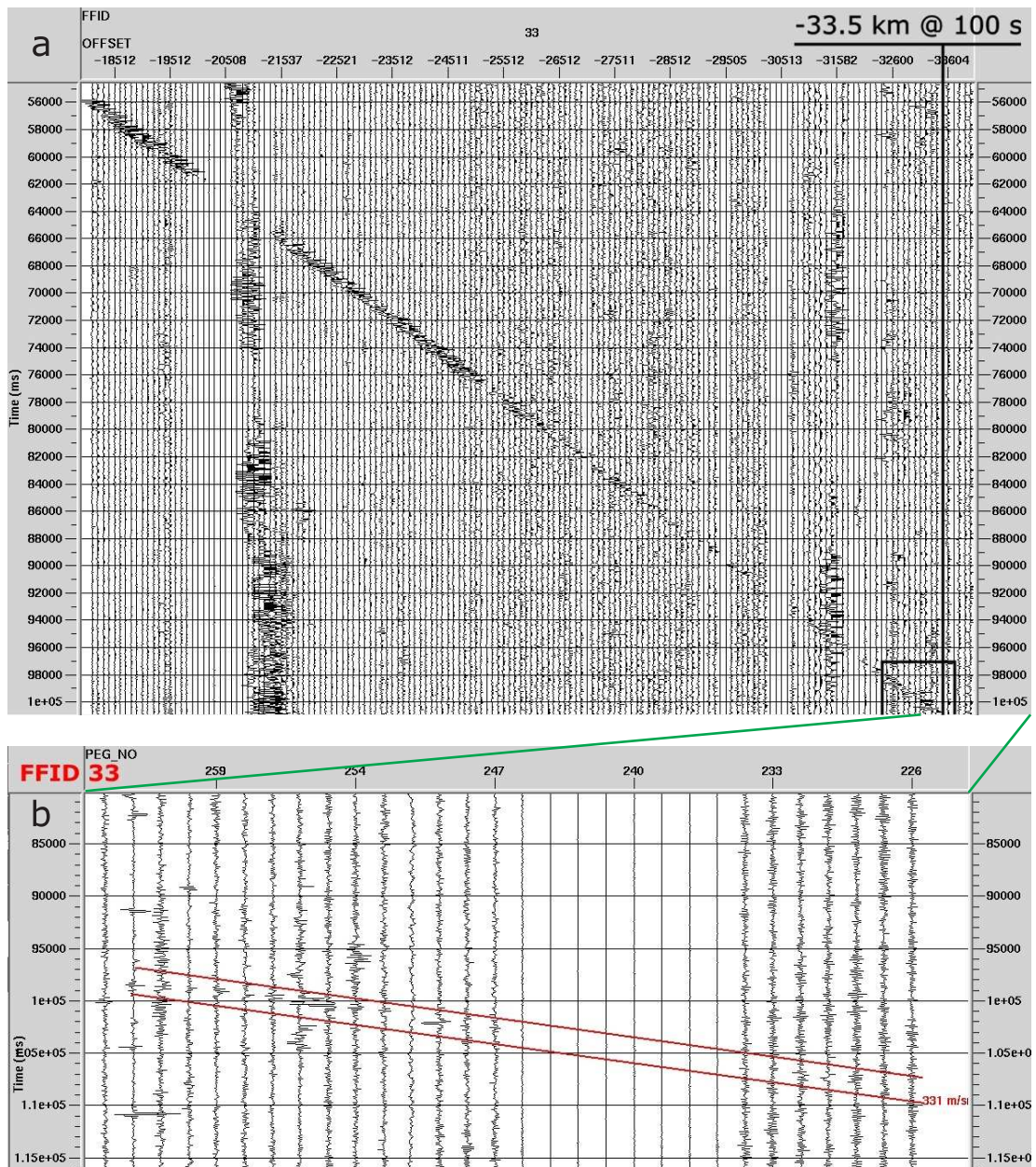
Figure B.1.: Airblast and offset in the shot gather of FFID 33 (shotpoint 25, not all 180 traces are shown). The total cutout length of 102 s (100 s after the shot) limits how far the airblast can be observed in the data (a), approximately 33.5 km should be the maximum. Panel b of the figure shows part of the same shot gather, but with longer traces than 102 s. Here, the airblast signal can be observed till an offset of $\approx$ 36 km in the last of the 180 traces. Not all ESP shots showed signals of the airblast in such far offsets. FFID 4 at shotpoint 98 in the Central Valley was another shot where the airblast signal was observed for $\approx$ 31 km.

B.3. How2pick-an-airblast.txt

How to pick an airblast mute with ProMAX and apply it to the data:

A good idea is to pick the airblast with the data reduced to 333 m/s
(LMO), because the airblast onset is then flattened and very easy to
pick. The times must be calculated then back to normal times and this
is offset dependent, so that the calculation must be carried out
outside ProMAX with AWK, and then read back into ProMAX. Another
problem is that the export from floats (offsets) from ProMAX is poorly
implemented. The offset is listed with only one decimal space, but
internally ProMAX keeps more decimal spaces. If you re-read the offsets
they do not fit the ProMAX trace offsets, just some by pure
coincidence. So, it can happen that you have 10 picks defining your
airblast, but if you re-read them into the non-LMO data, only two picks
or less picks are shown ... You will get a wrong interpolation and not
all of the airblast will be muted!

I would recommend to pick the airblast with following header values:
FFID, channelnumber. If you pick in this way, you need to pick every
trace, since otherwise there are wrong interpolations in the offset
domain. But this is easy, just pick the edges and kinks in the normal
way and choose then 'smooth picks' in the right mouse button flyout
menu, and set the smooth parameter in the smooth options to 3
beforehand! By this, you reduce broad shifting of your picks during
smoothing. Here, the only 'big' changes in your picks appear at the
start and end of the data set, where there are no traces for
interpolation, but the error is minor and will become less when the
data is reduced to 'normal' time.

The detailed procedure:

Use a flow similar to the following to pick your airblast surgical
mute:

Disk Data Input: input of raw shot data (ffid:channel:nvr)
 Trace DC Removal: correct for DC bias
 Trace Kill/Reverse: set disconnected geophones to zero
 Bandpass Filter: (optional) apply ormsby, low/high cut to reduce noise
 AGC: (optional) apply scaling to equalise traces (eg 3000)

  Trace Length: enlarge record length to avoid data loss during LMO (eg 150000ms)
  Linear Moveout Correction: align first-breaks (air blast speed 333 m/s)
  Trace Equalization: postLMO scaling with fixed time window (eg between 60-64s)
       --- test your picked mute ---
       Trace Muting: application of just picked surgical mute
       Linear Moveout Correction: inverse LMO for control
       Trace Equalization: (optional) scaling with general time window for control
       Trace Length: (optional) reduce record length (eg 20000)

  Trace Display (density mode, rev_sw_section2.rgb works fine)

Picking of the surgical mute within trace display: choose a filename
indicating LMO + your time shift (airblast_LMO_150s), choose channel as
secondary key, add second boundary of the surgical mute by right
clicking, pick your airblast, change smoothing parameter to 3, smooth
picks.

Go to the tables menu and export: FFID channel time1 time2, export a
list with all your offsets out of the database, get rid of unwanted
lines and paste (unix command: 'paste') these two files together to
create such a file :

FFID - channel - time1 - time2 - offset

Check e.g. with 'wc' the length of the three files for consistency.

To calculate real times (bulk shift here 125s):

awk '{printf("%4d %4d %10.1f %10.1f %10.1f\n", $1,
$2, $3-125000+sqrt($5*$5)/0.333, $4-125000+sqrt($5*$5)/0.333, $5)}'
u_mute_airblast_time-and-offset.asc >
u_mute_airblast_time-and-offset-4PROMAX.asc

Copy the old ProMAX airblast-table into an new one, since it seems not
possible to create a new surgical mute table with two picked times
(start+end time). Any ideas?. Import the just created ascii data.

et voila!

(An other idea is to create a new database entry of the offsets and
multiply that by 1000000000something to get rid of the floats, extract
this and use these values for calculation.)

C. Appendix: Processing

C.1. Processing sequence

Processing sequence
Disk data input <= all_data_with_geom_comp1
Trace length
Trace DC removal
Trace Kill/Reverse <= u_open_channels
Trace Muting <= u_airblast_read_in_NVR
Trace Muting <= u_car1-4
Hand statics
Header statics
Trace Muting <= u_top_mute
Bandpass filter
True amplitude recovery
Ensemble balance
Time-variant scaling
Automatic gain control
Trace equalization
Infill data
Trace equalization
F-X decon
Trace equalization
Blend
Dip scan stack
Normal moveout correction
Resample/Desample
Trace math transforms
CDP/Ensemble stack
Pad traces
Trace equalization
Kirchhoff depth migration and Trace display or disk data output

Table C.1.: Used ProMAX modules in the stacking and migration flow

D. Appendix: First-break tomography – Preparation, procedure and model setup
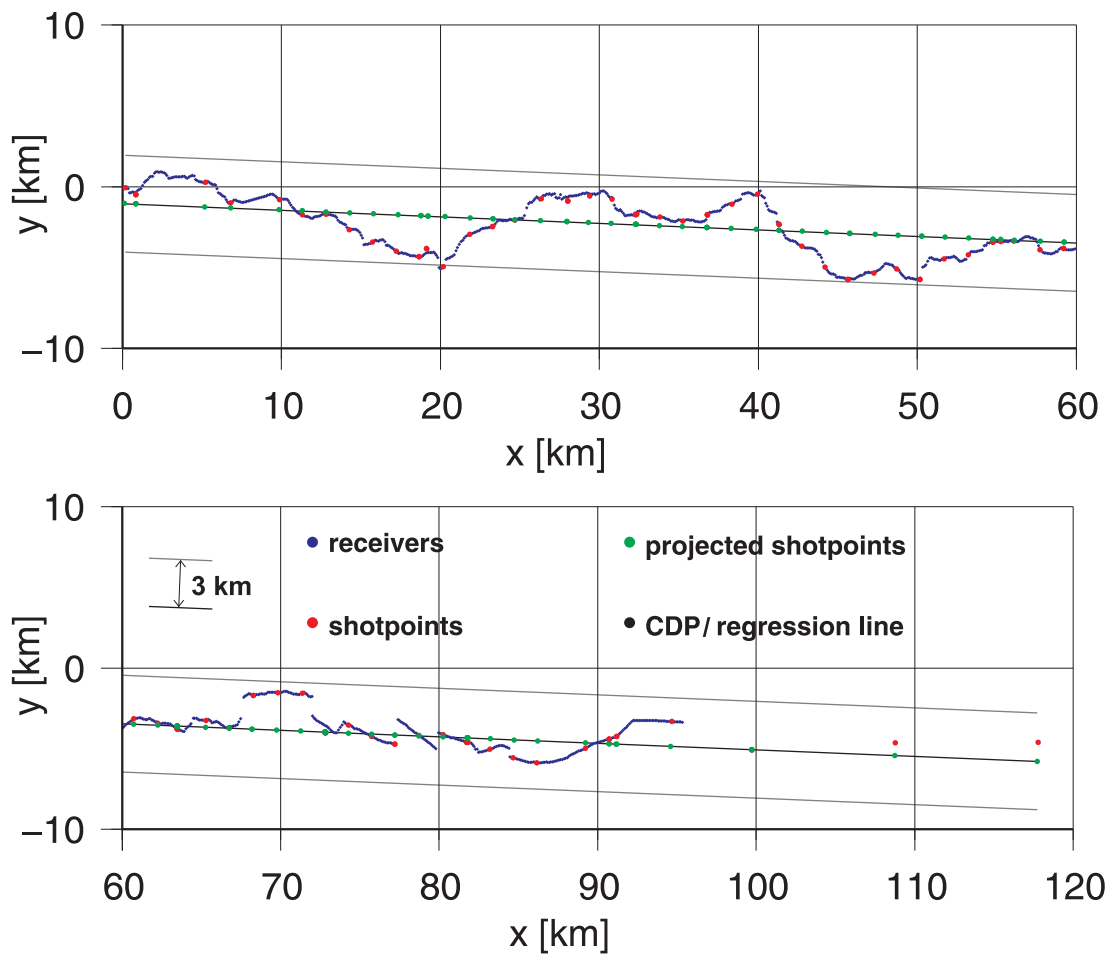
Figure D.1.: Receivers and shotpoints together with projected shotpoints and regression line.

E. Appendix: First-break tomography – first images and validation

E.1. Horizontal vs. vertical smoothness/flatness

Figures E.1 and E.2 show inversion results with varying s_z in 8 steps from 0 - 50. This parameter determines the relative importance of maintaining vertical versus horizontal model smoothness/flatness (cf. equation 6.2 on page 64). The term of the objective function which contains s_z ($\ldots + \lambda[m^T C_h^{-1} m + s_z m^T C_v^{-1} m]$) shows that a small s_z favors horizontal structures, whereas a large s_z leads to vertical structures (cf. relevant panels in figures E.1 and E.2). A s_z of 0.25 resulted in best fitting model with the smallest RMS value of 33.6 ms, thus favoring rather horizontal features.

E.2. Investigation of the damping factor (λ)

λ is the trade-off (damping) parameter between minimizing the residual between observed and calculated travel-times and the wish to produce a model of minimum structure (see equation term above). No damping is present if $\lambda = 0$, requesting that the model is over-determined. The larger the under-determined parts in the model the greater must be λ. If λ is too large, the model is damped to much, resulting in a very smooth/flat model with the effect that structural detail is lost, and the travel-time data is not fitted very well. Figures E.3 and E.4 (page 195) show 8 panels with λ values from 0 - 10000. The best starting value turned out to be 1000. The inversion with $\lambda = 0$ shows a chaotic, ringing result with a high RMS value of 70.4 ms, by using a λ of 10000 individual structures are lost, but the general velocity distribution is still imaged remarkably well.

E.3. One inversion cycle only

Figure E.5 (page 197) shows a compilation of results using only one inversion cycle and varying inversion cellsizes. As mentioned in section 6.4 on page 66, large cells result in a coarse velocity field, which does not justify the number of rays passing through the blocks. Small cells on the

other hand exhibit a smooth velocity field, but not necessarily of a better quality. In areas of little ray coverage the rays of one shot tend to focus in one 'single beam'. In all velocity images of figure E.5, the first few kilometers ($<$ 3 km) show similarities, regardless the cellsize. Below 3 km, the velocities change towards higher ones rather rapidly, especially good visible in the inversion results on the left side using coarser cellsizes. The degree of variance between the velocity models is also greater for the deeper part of the models. This variance might be related to the ray coverage in the deep parts of the models. Inversion results with a high number of inversion cells show that the deeper subsurface is only sampled by the rays of very few shots (lower right in figure E.5).
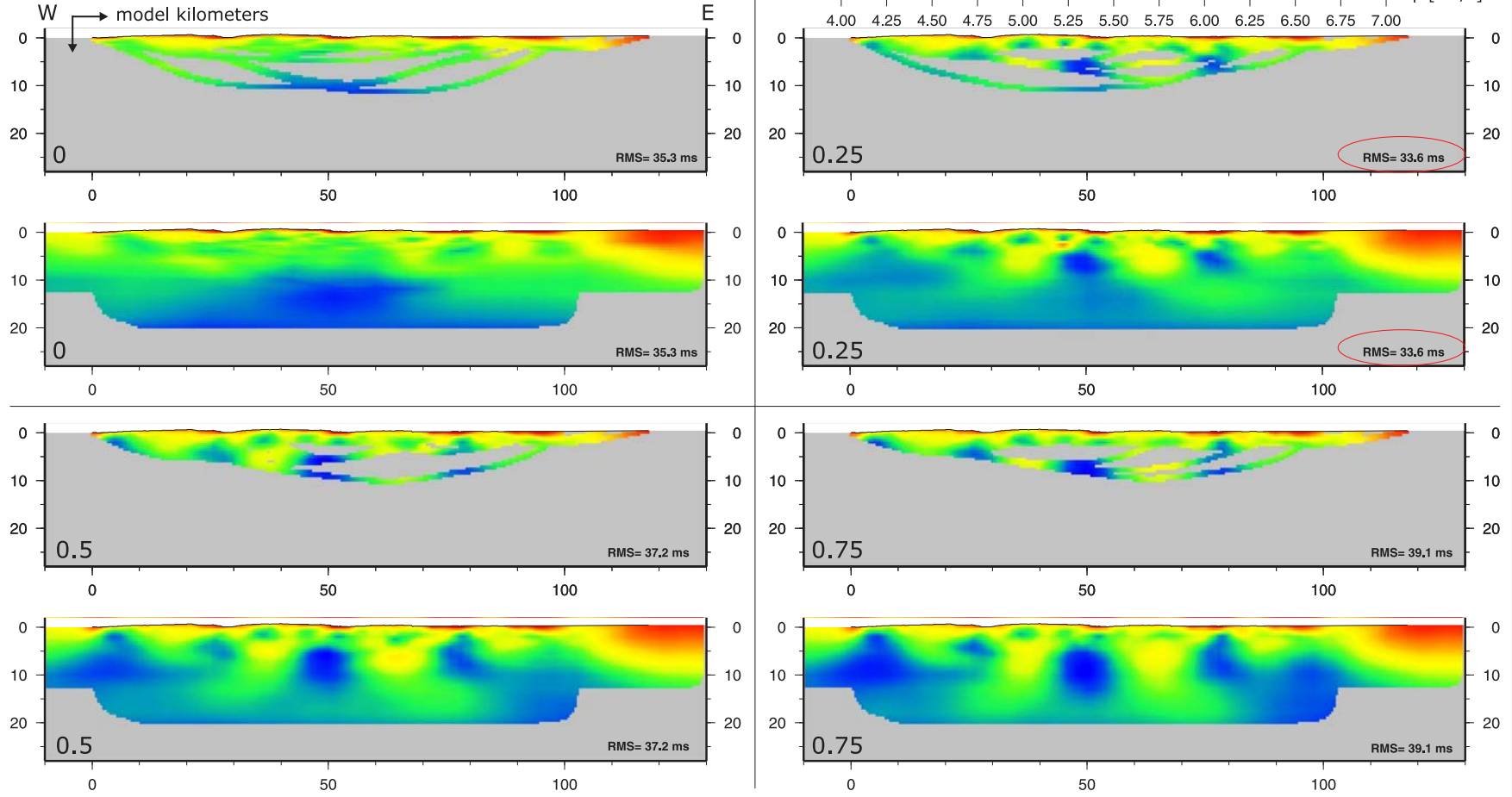
Figure E.1.: Horizontal vs. vertical smoothness/flatness investigation (ray and interpolated images) using s_z values of 0, 0.25, 0.5, and 0.75. The red ellipse marks the RMS value of the best fitting model. Shotpoint and receiver locations are not shown, the elevation along profile is represented by the thin black line.
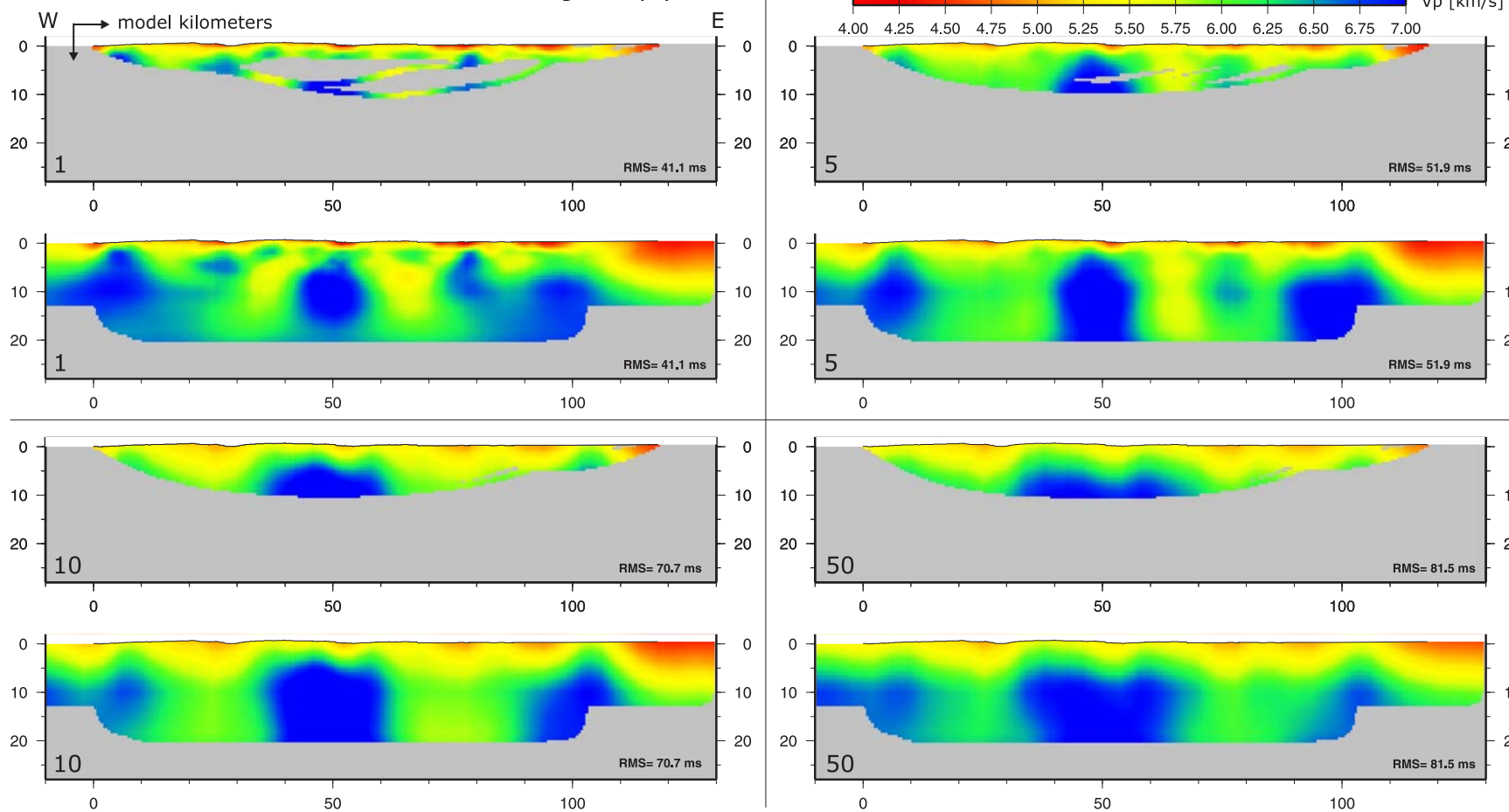
Figure E.2.: Horizontal vs. vertical smoothness/flatness investigation (ray and interpolated images) using s_z values of 1, 5, 10, and 50.
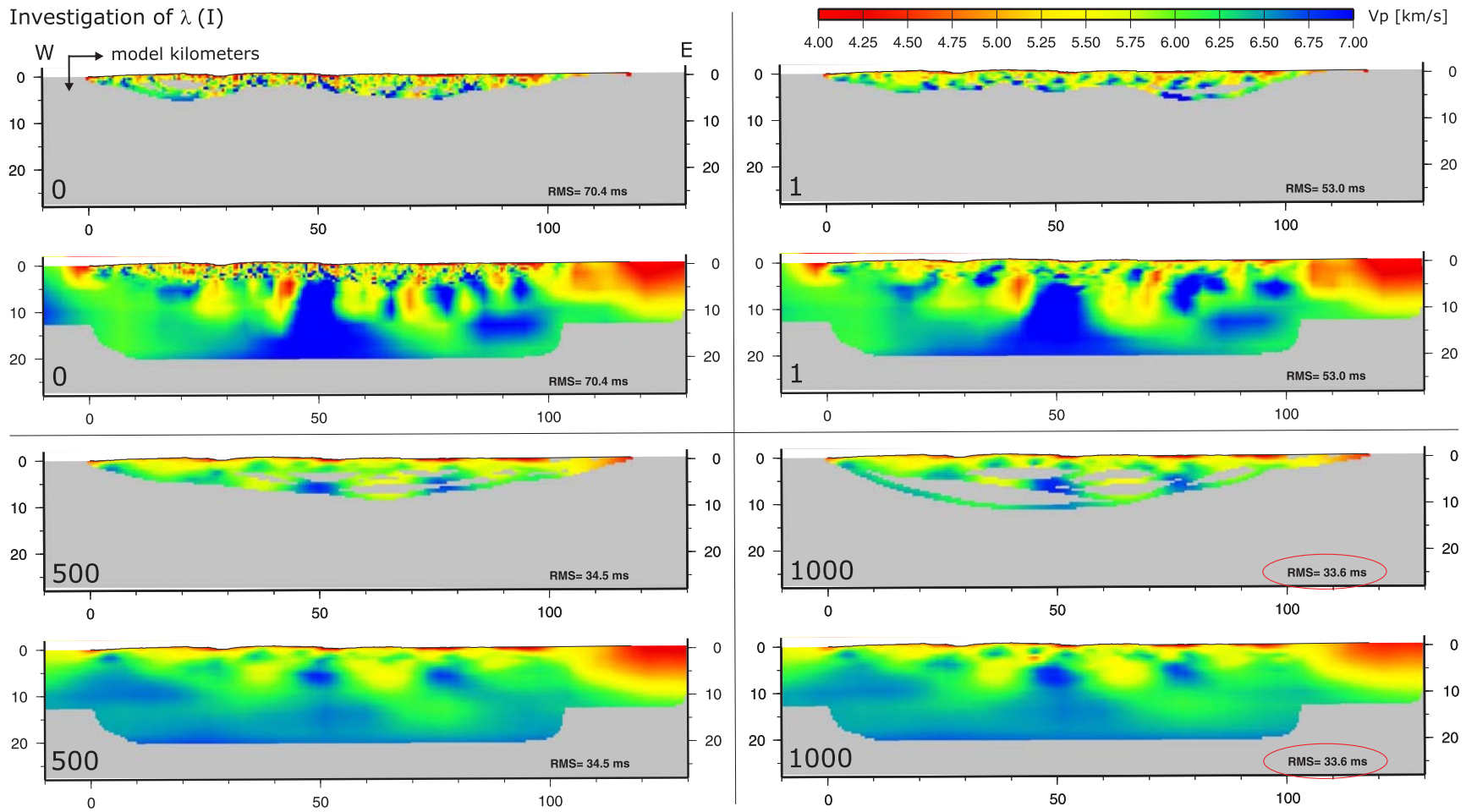
Figure E.3.: Investigation of λ using values of 0, 1, 500, and 1000, which turned out to be the best starting value for λ.
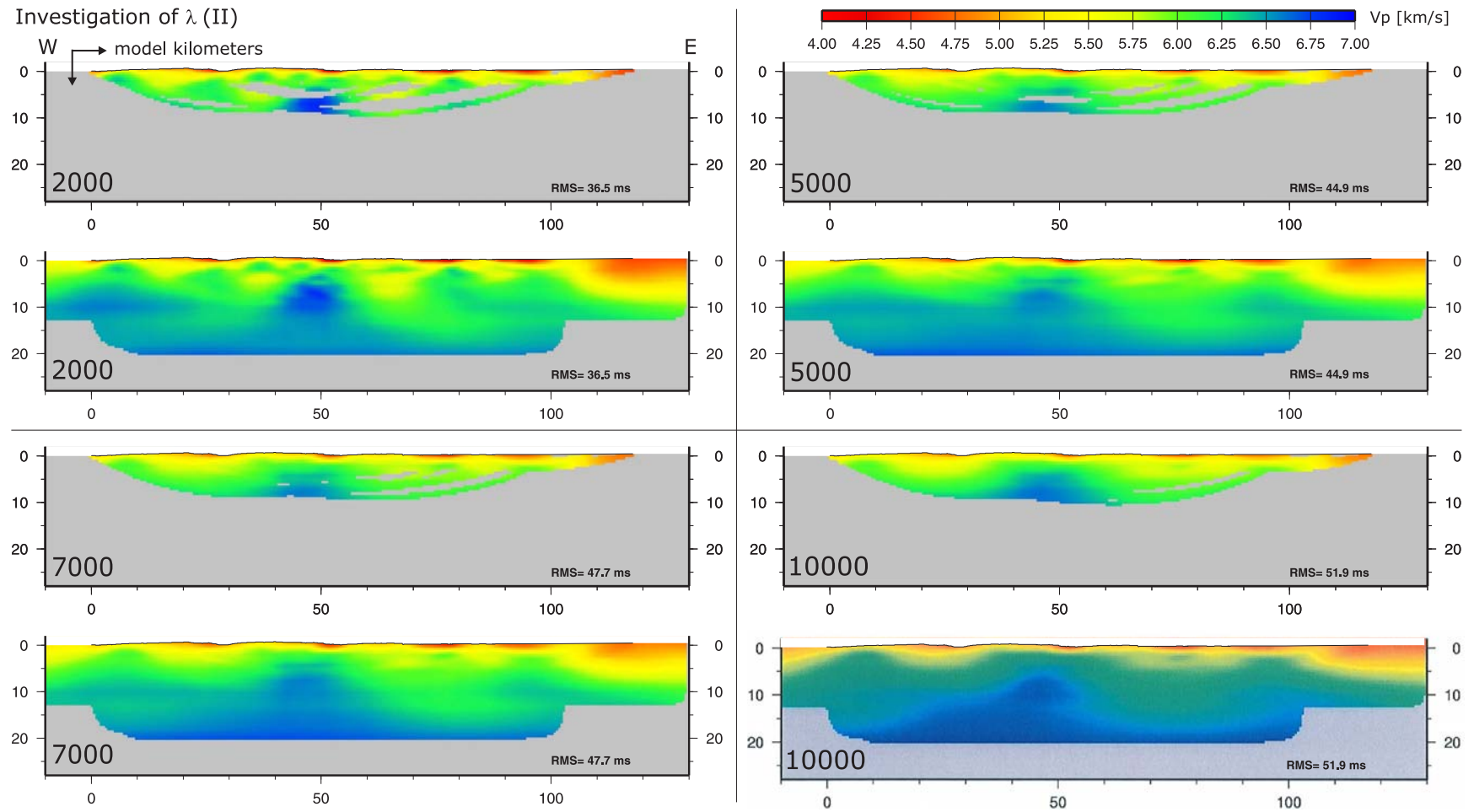
Figure E.4.: Investigation of λ using values of 2000, 5000, 7000, 10000. Large values of λ still image the basic velocity distribution quite well.
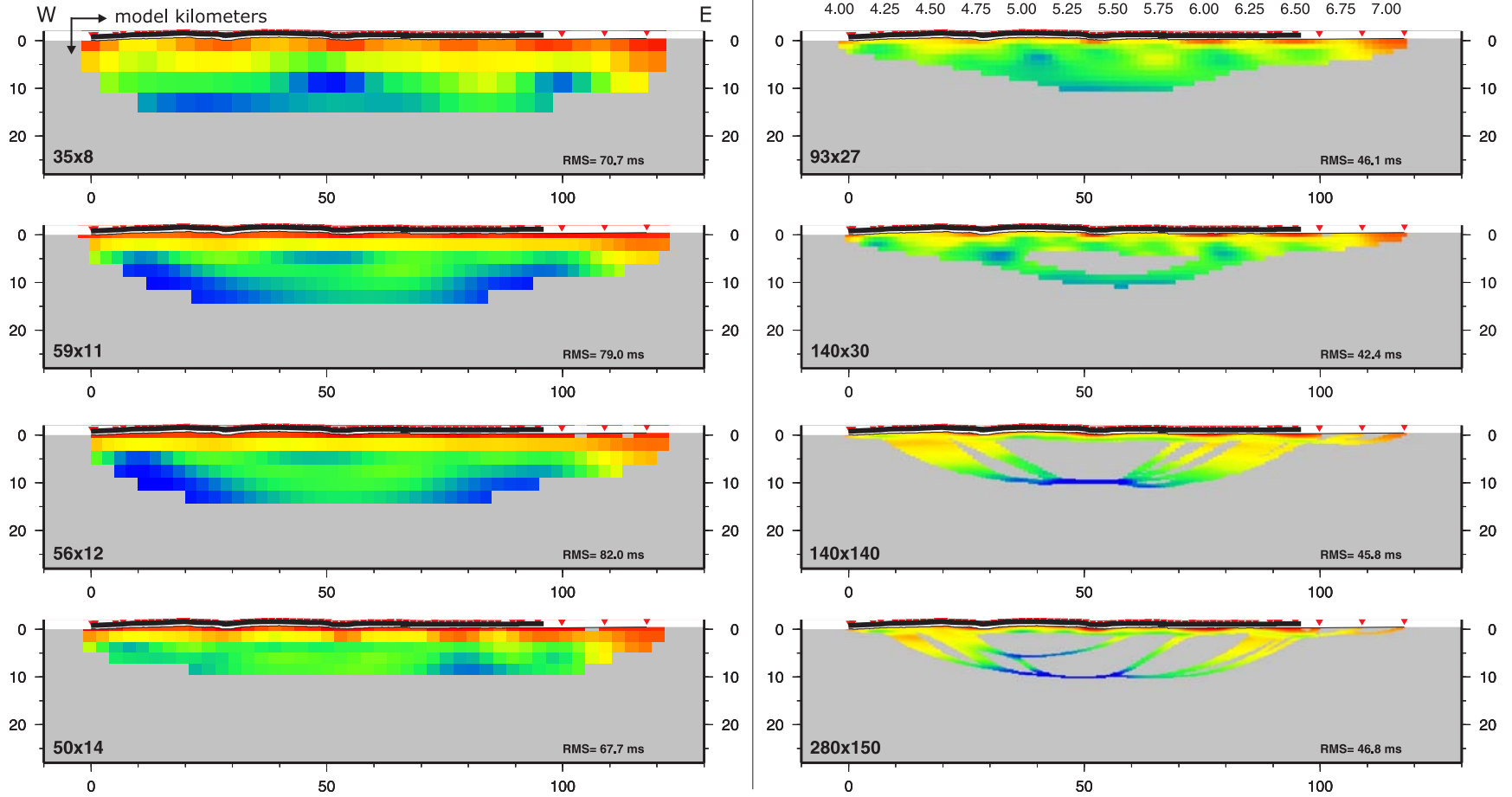
Figure E.5.: Results of one inversion cycle only with varying cellsizes. In shallow depths the results may be comparable to each other (< 3 km). Using only small cells, the rays of one shot tend to focus in one 'single beam' with unrealistic velocities (too smooth, too fast) along the travel path.

E.4. Features of the final velocity model of first tomographic result
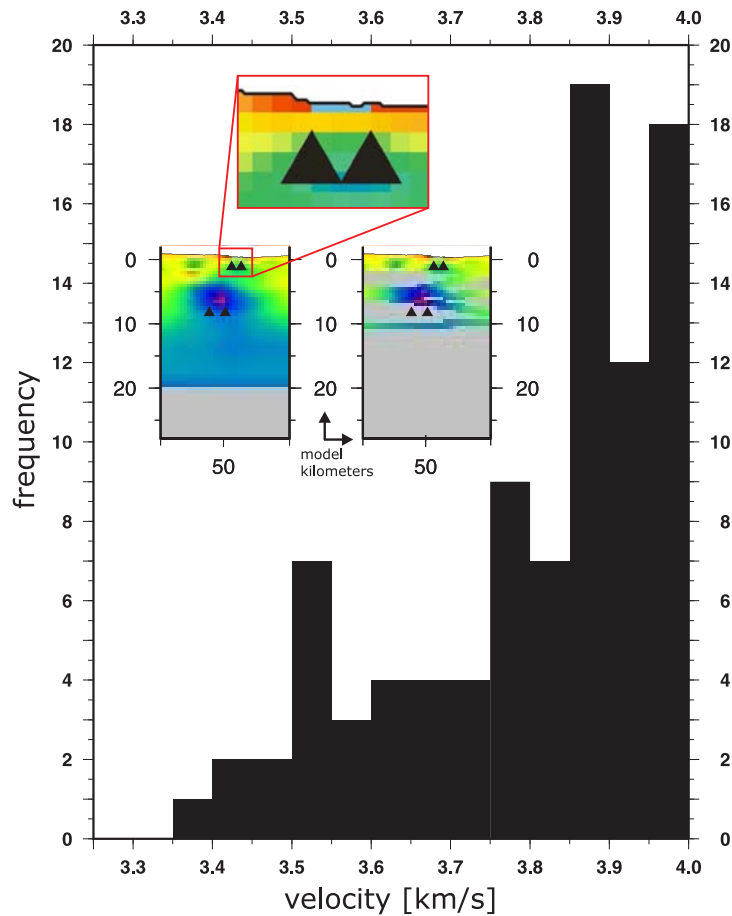
Figure E.6.: This figure shows a detail of a histogram of the final velocity grid of the first tomographic result (figure 7.2). The histogram shows ≈ 90 entries below 4 km/s, which are masked out by the topography mask. Two insets show part of the tomographic images. Black triangles point to the areas with the highest velocities ≥ 6.85 km/s (coded there in bright red, $v_{max} = 6.948$ km/s) and the lowest ones between 3.9 - 4.0 km/s (coded there in light blue). The blow-up shows a detail of the velocities below 4 km/s.

E.5. Tests with varying starting velocity models
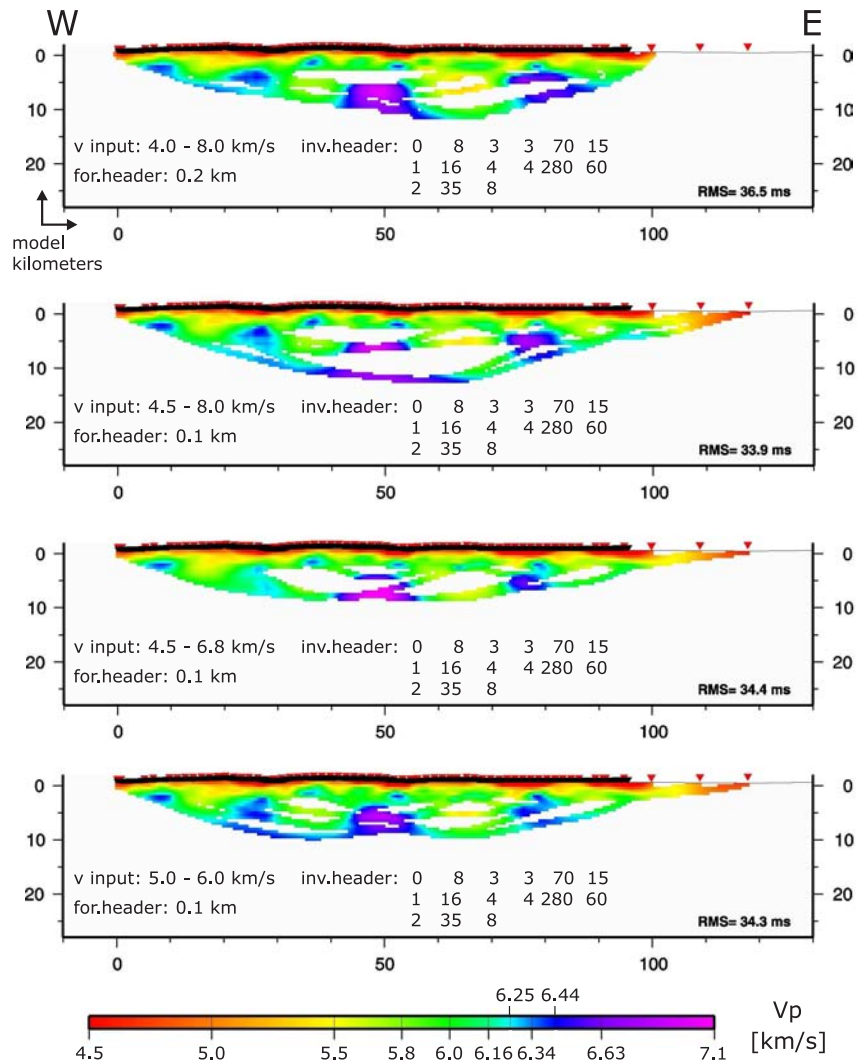
Figure E.7.: Results of inversion runs with varying starting velocities. All images show similar features, the changes in the velocity distribution create different ray paths for the ESP shots in depth (z > 3 km) and outline the main velocity structure similar to the interpolated images. All models show almost no variation in the first three kilometers. The changing cell size for the forward calculation from 0.2 to 0.1 km (0.2 km only in uppermost model) shows no visible effect.

E.6. Different minimum hitcounts per cell
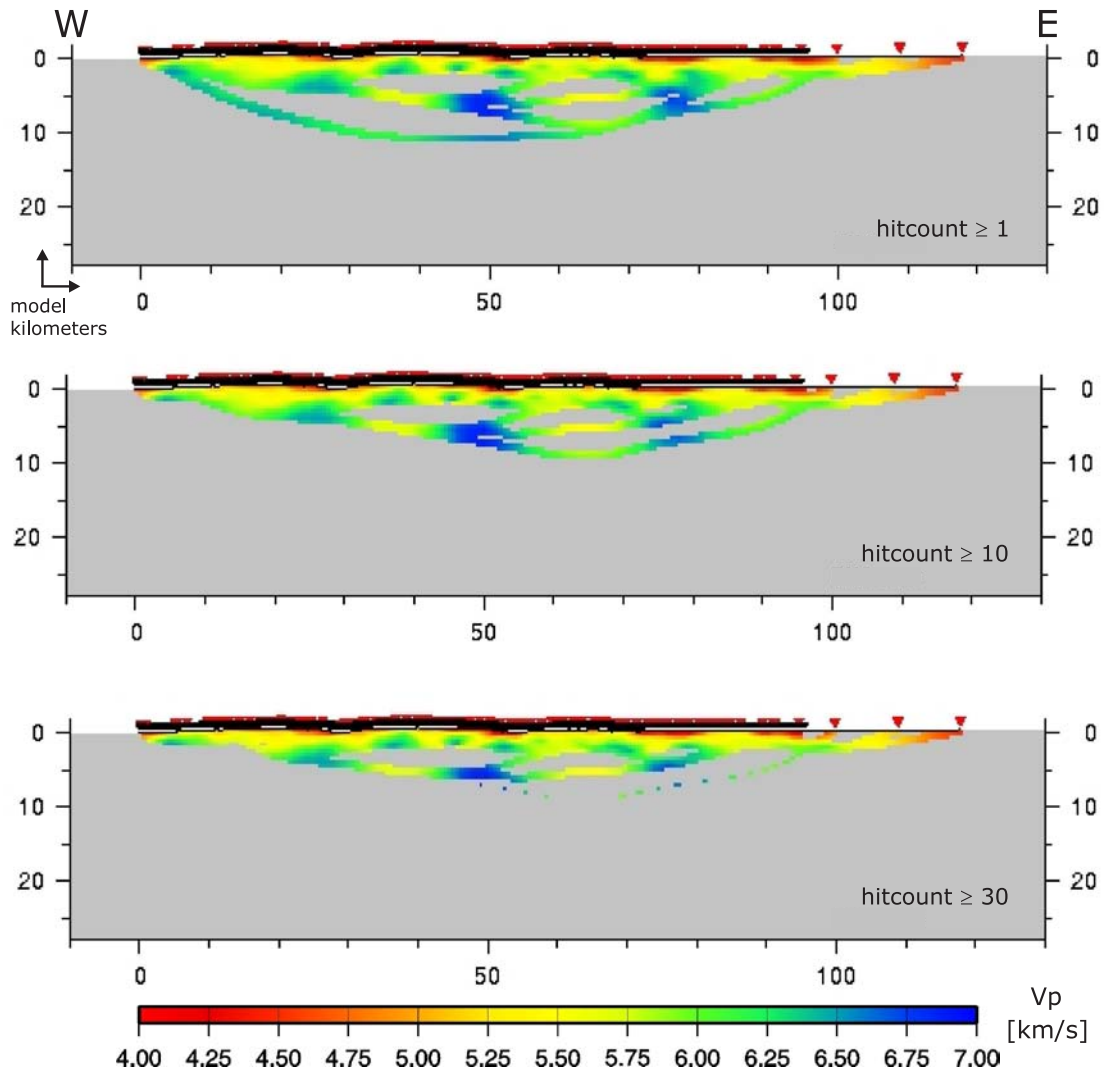
Figure E.8.: The effect of restricting the minimum hitcounts per cell to be plotted in the resulting velocity model is shown in this figure. The upper panel uses every cell at least one ray has passed through. The panel in the middle uses only cells with a hitcount of 10 and higher, the lower panel uses cells with hitcounts greater than 30.

E.7. Reducing the number of travel-times

104 shots times 180 receivers result in 18720 possible travel-times. 15471 travel-times (> 80 %) could be picked. This number was reduced successively by using every second, third, ... line of the travel-time file. Figure E.9 and E.10 show the results of these test runs.
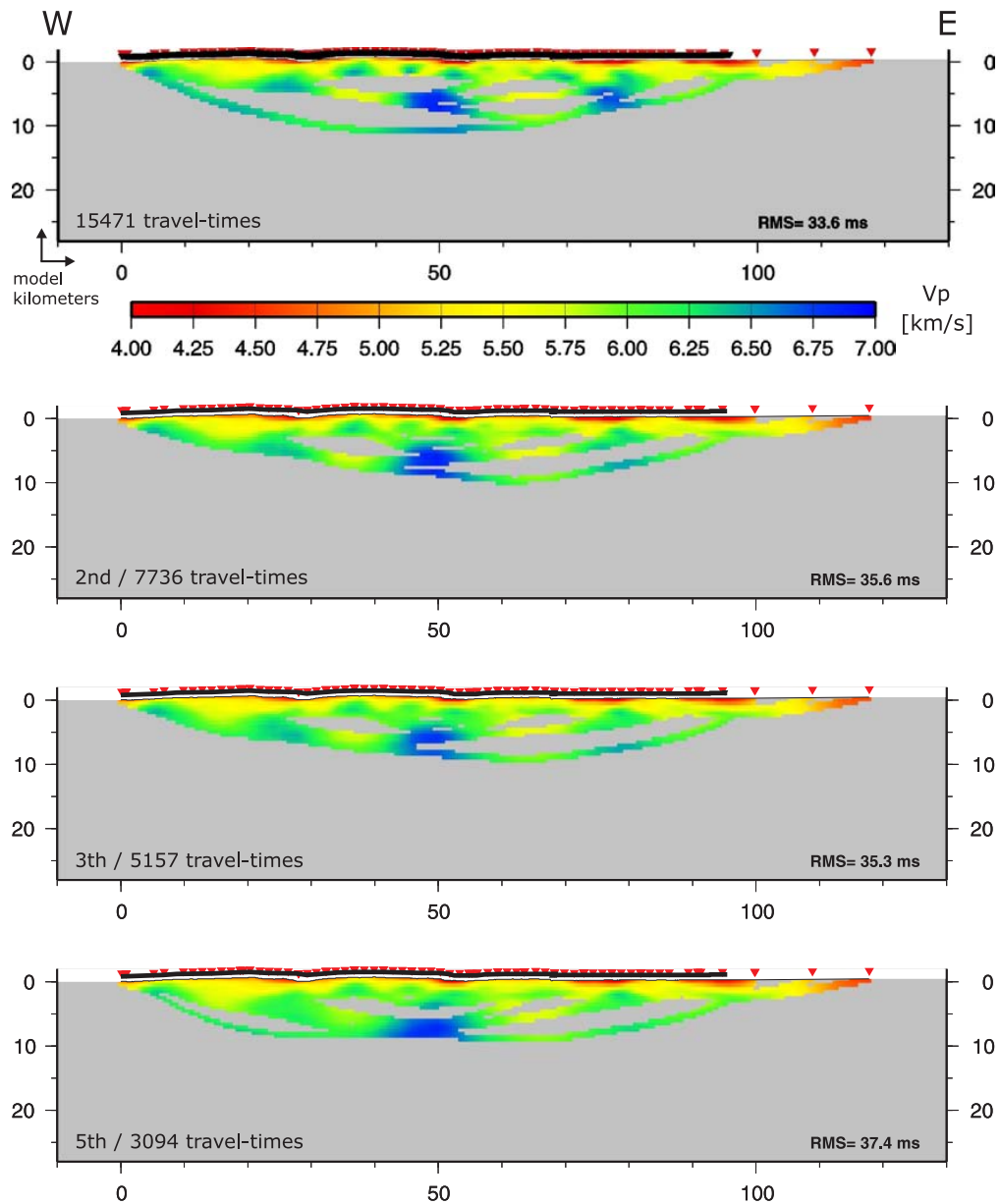
Figure E.9.: Inversions with a reduced number of travel-times using every second, third and fifth line of the travel-time file in comparison to all travel-times (upper panel).
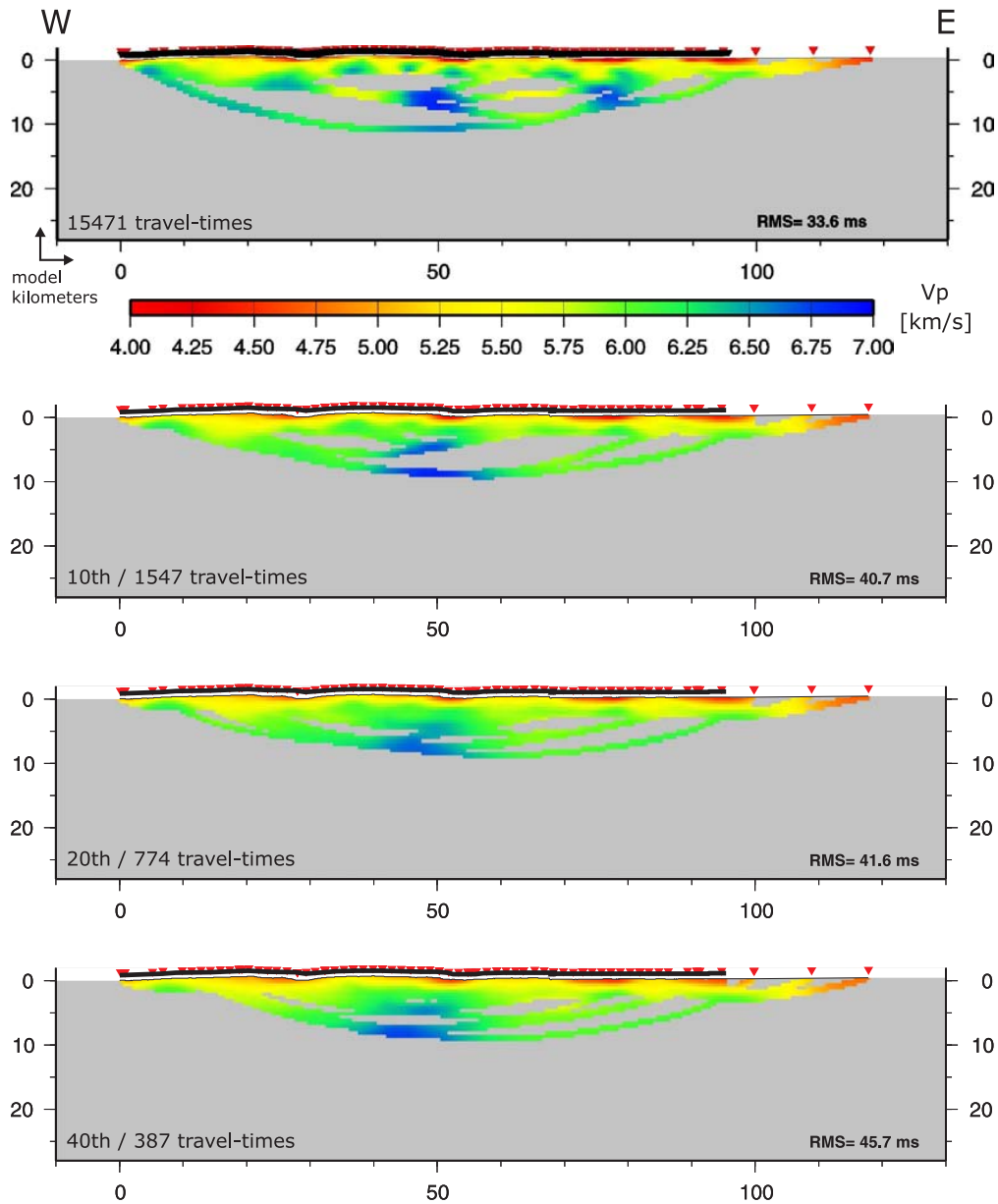
Figure E.10.: Inversions with a reduced number of travel-times using every tenth, twentieth and fortieth line of the travel-time file in comparison to all travel-times (upper panel).

The images with the reduced travel-times reproduce the general features of the inversion with all travel-times. Detail of the fine structures is lost for each travel-time reduction. The reduction acts like a low-pass filter, where the upper cut off frequency is reduced for each reduction of the travel-times. The RMS values increase 12 ms to 45.7 for only 387 traveltimes. This low number of travel-times reproduces the image using all available travel-times remarkably well.

E.8. Checkerboard tests with varying anomaly sizes

no.	1	2	3	4	5	6	7
length x width [km]	40 x 20	20 x 10	10 x 5	5 x 2.5	3 x 2	2 x 1	5 x 5

Table E.1.: Checkerboard anomaly sizes. The dimension of the checkerboards were set to favor horizontal structures, analog to the findings of the study of the s_z parameter (see appendix E.1).
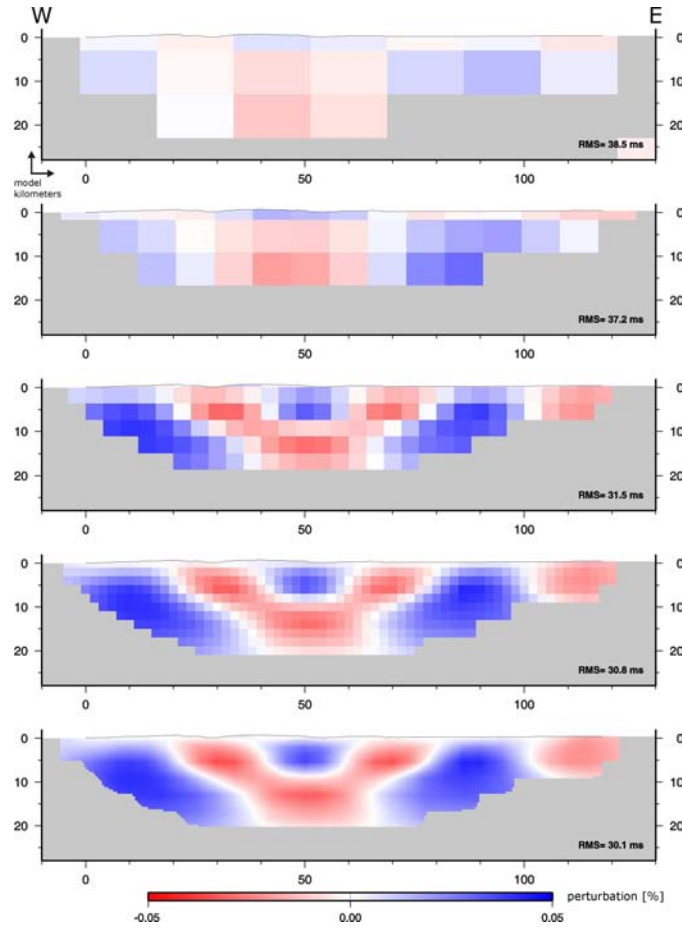
Figure E.11.: All five inversion cycles for a checker board calculation with a perturbation anomaly size of 20 x 10 km.

Figure E.12 shows the results of all conducted checkerboard tests after the fifth inversion cycle together with the corresponding perturbated models the synthetic travel-times were calculated with, and the used perturbation pattern. The velocity anomaly size increases from bottom to top. Besides the rectangular perturbations the uppermost panel shows a calculation using a quadratic anomaly pattern.
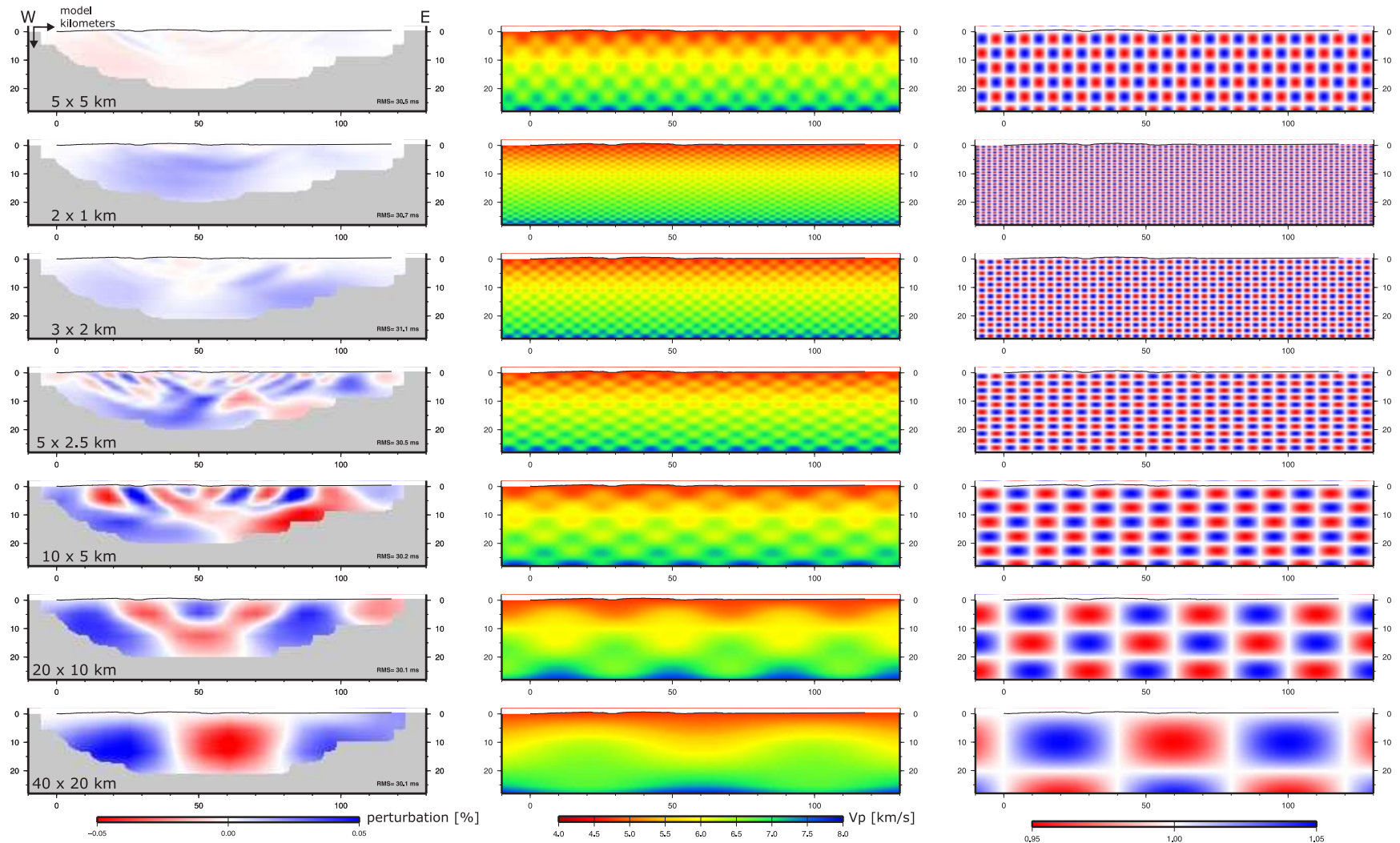
Figure E.12.: Results of all conducted checkerboard tests together with the corresponding perturbated models the synthetic travel-times were calculated with, and the used perturbation pattern.
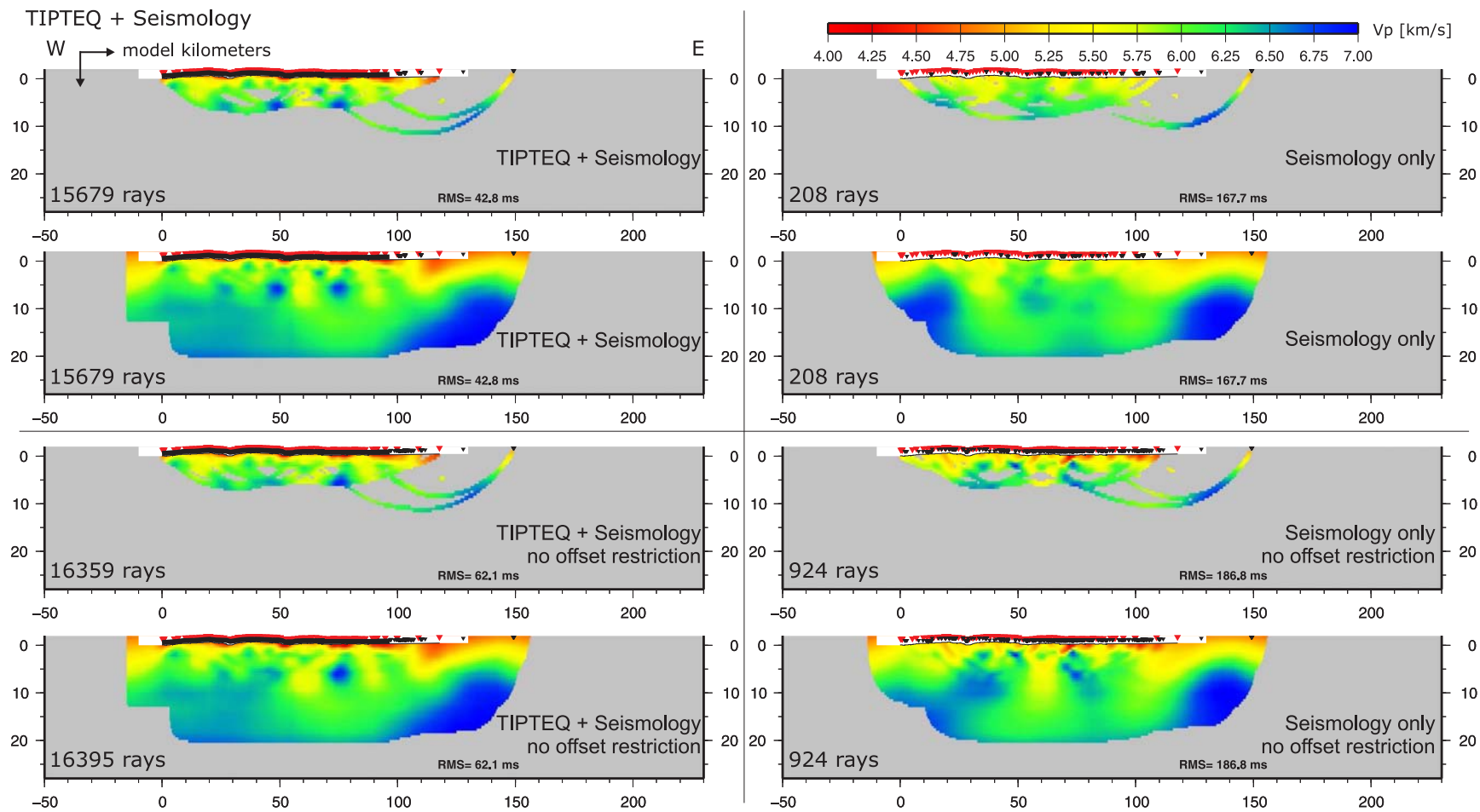
Figure E.13.: Two pairs of inversion results are presented. The left part shows results using 15471 plus 208 or 924 travel-times, depending if an offset restriction is applied. The right part of the figure shows the inversion results of the seismology picks alone.

E.10. Inversions with different pickerrors

A decreasing pickerror of 10 ms was used in each of the six inversions shown in figure E.14 (page 208), starting with a value of 60 ms. The first four inversions show that the calculations are stopped when the modeled travel-times are within the the given pickerror. Using a smaller pickerror than 30 ms does not improve the inversion result, since the best fitting models reach only a RMS value greater than 30 ms.

E.11. Picked and synthetic travel-times along profile

Figure E.15 (page 209) shows the picked first-breaks vs. profile kilometer in blue. The red lines are the calculated travel-times from the inversion result shown in figure 7.2 with added noise in the range of the pickerror of 30 ms. Close to the shotpoints (t = 0) the divergence between the calculated and picked travel-times seem to be admissible. Later than 2 s, the discrepancy increases rapidly up to ≈ 1.5 seconds for ESP shots (x = 0 - 5 km, t = 14 - 18 s), which can not be accepted.

E.12. RMS errors per shot along profile

The RMS error of the differences between all picked and synthetic travel-times for each shot is shown in figure E.16 (page 210). The values should cluster around the given pickerror, here 30 ms. Red dots indicate ESP shots. The scattered appearance does not argue for a good inversion result. The RMS values, also the ones in the following figures, belong to the inversion shown in figure 7.2.

E.13. RMS errors per receiver along profile

The RMS error of the differences between all picked and synthetic travel-times for each receiver is shown in figure E.17 (page 211). The points with values of ≈ 0.2 between x = 75 - 85 km belong to an ESP shot (FFID 5) which was fired 6 kilometer away from the coast, with the receivers in the central valley in the first spread (77 - 95 km away from the coast).

E.14. RMS errors per receiver vs. all offsets

Figure E.18 (page 211) shows again the differences between all picked and synthetic travel-times for each receiver, but this time plotted vs. all occurring offsets. The dashed line marks

the standard NVR offset of 18 kilometers, where we observe only little deviations. A general misfit of the data very close to each shotpoint (x = 0 km) is observed, also shown in the images in the following figure. Up to offsets of 50 kilometers, the deviations are minor.

E.15.   Reloaded synthetic picks into ProMAX

Figure E.19 (page 212) shows the picked (red) and smoother synthetic travel-times in blue together with shot data. Problems to fit the data occur close to the shotpoint for NVR shots, larger offsets than ≈ 5 kilometer are fitted in agreement with the pickerror of 30 ms. Omitting picks close to shotpoints resulted in no other inversion result than shown in figure 7.2, which is also observed by studies with a reduced number of picks (see figure E.9 and E.10). The suspicious structures in the images are created by the shots with large offsets. The near-surface structure is always very similar in each of the inverted images.
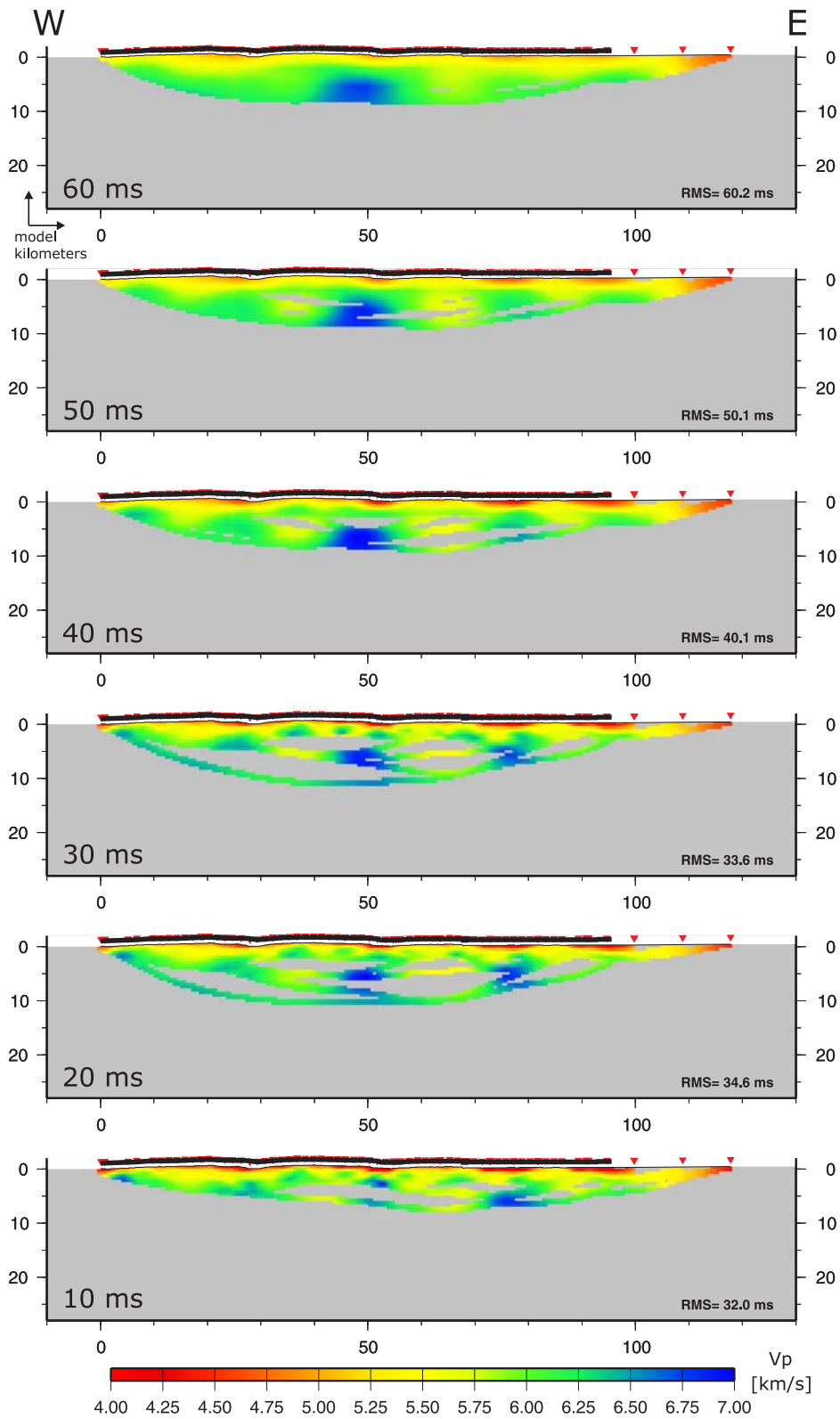
Figure E.14.: A decreasing pickerror of 10 ms was used in each of the six inversions. A pickerror below 30 ms does not lead to a better fitting model (see RMS values).
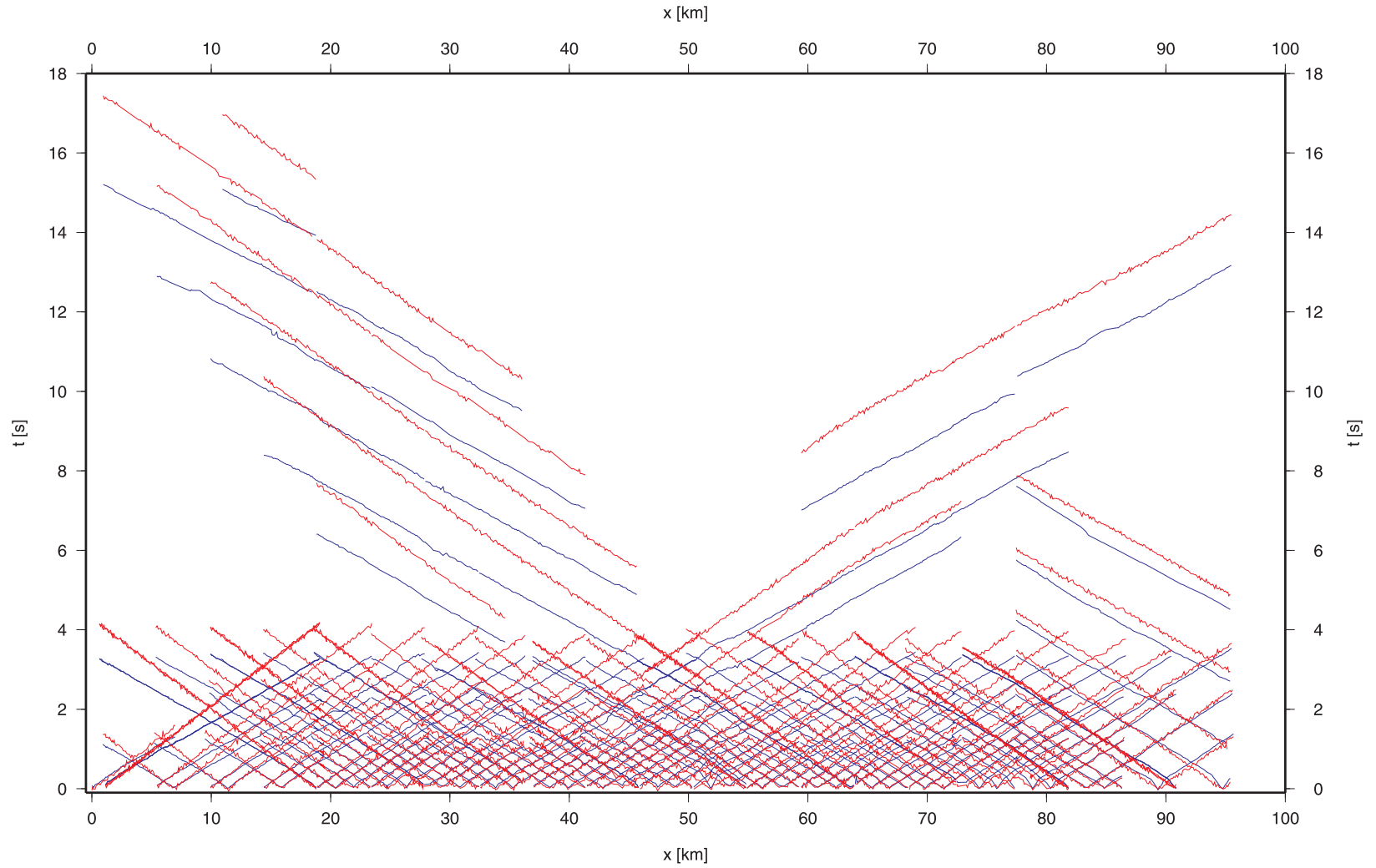
Figure E.15.: Picked (blue) and synthetic (red) travel-times along profile of all shots. Close to the shotpoints (t = 0) the divergence between the calculated and picked travel-times seem to be admissible. Later than 2 s, the discrepancy increases rapidly up to ≈ 1.5 seconds for ESP shots (x = 0 - 5 km, t = 14 - 18 s), which can not be accepted.
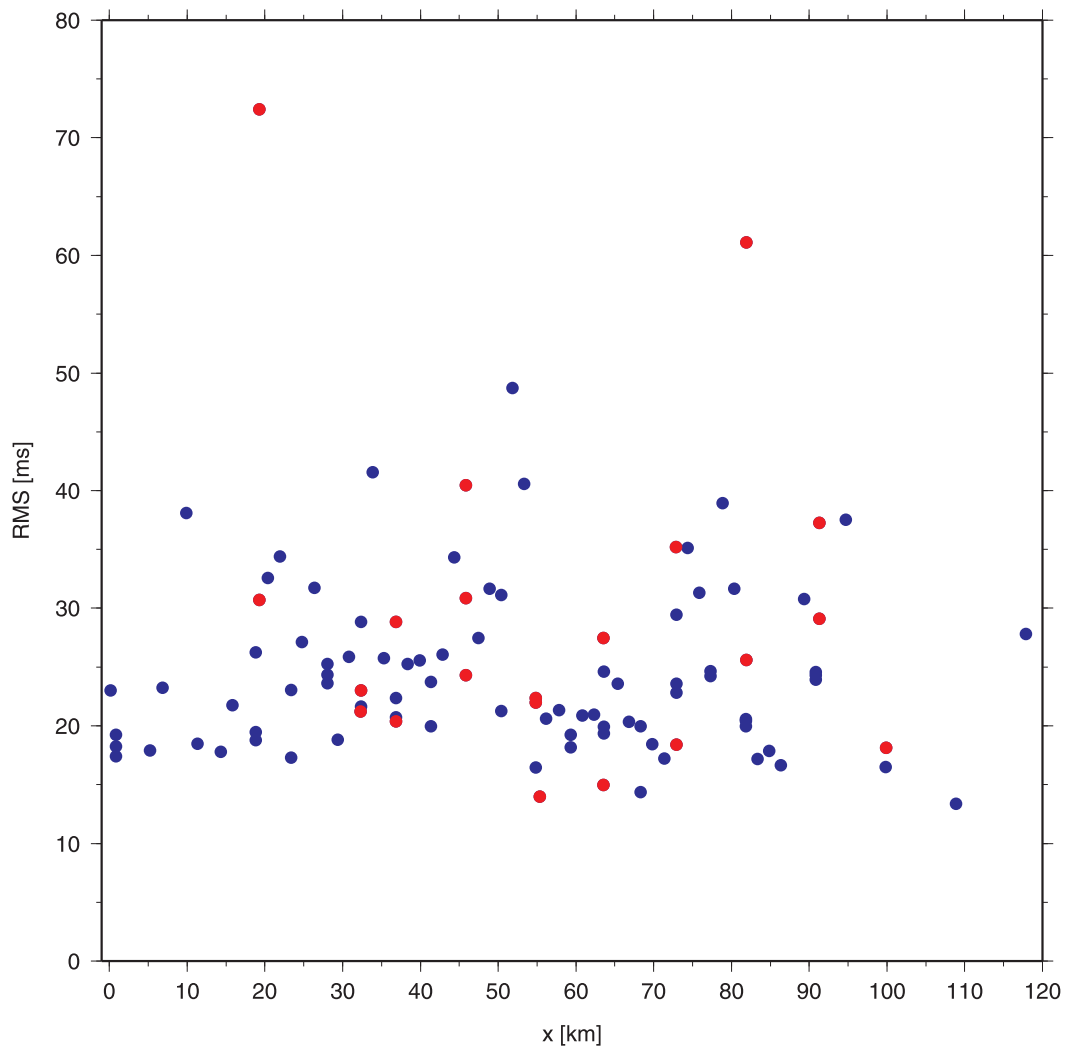
Figure E.16.: The RMS error of the differences between all picked and synthetic travel-times for each shot. Red dots indicate ESP shots.
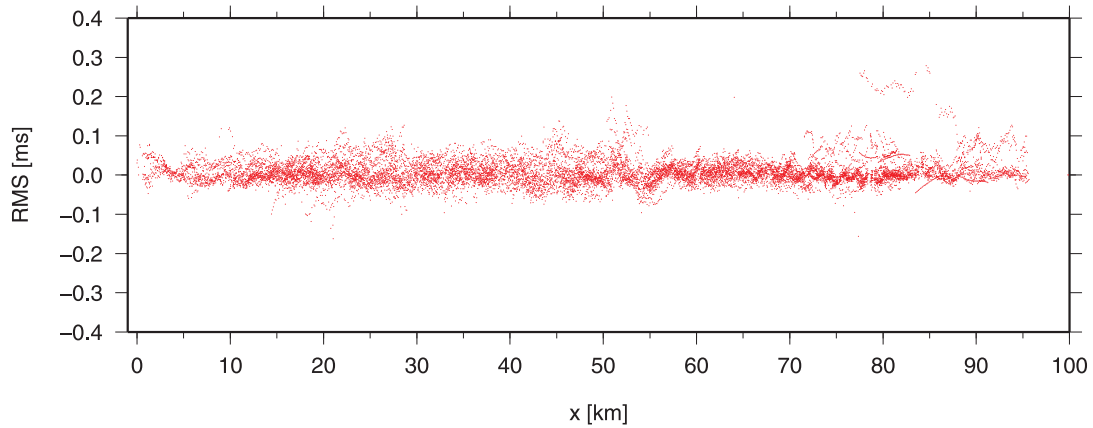
Figure E.17.: The RMS error of the differences between all picked and synthetic travel-times for each receiver.
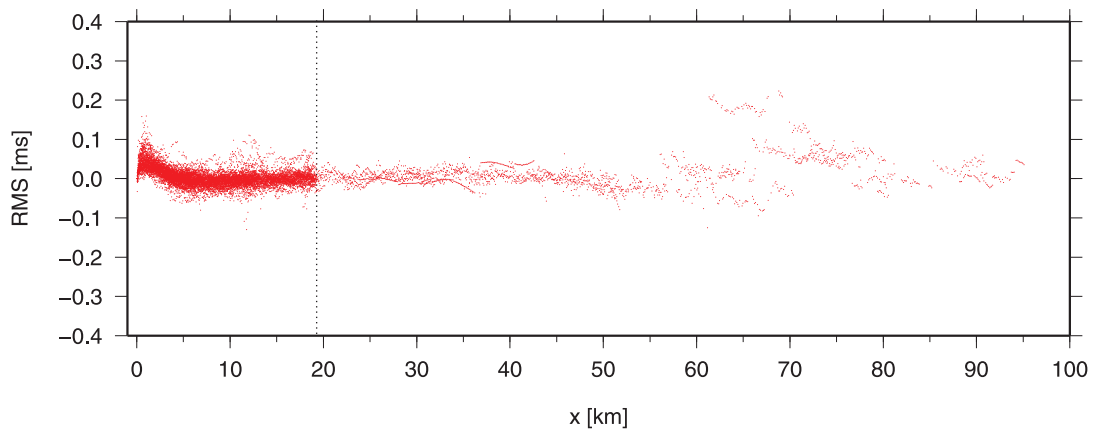
Figure E.18.: This figure shows again the differences between all picked and synthetic travel-times for each receiver, this time plotted vs. all occurring offsets. The dashed line points to the maximal offset of 18 km for the standard shot NVR configuration.
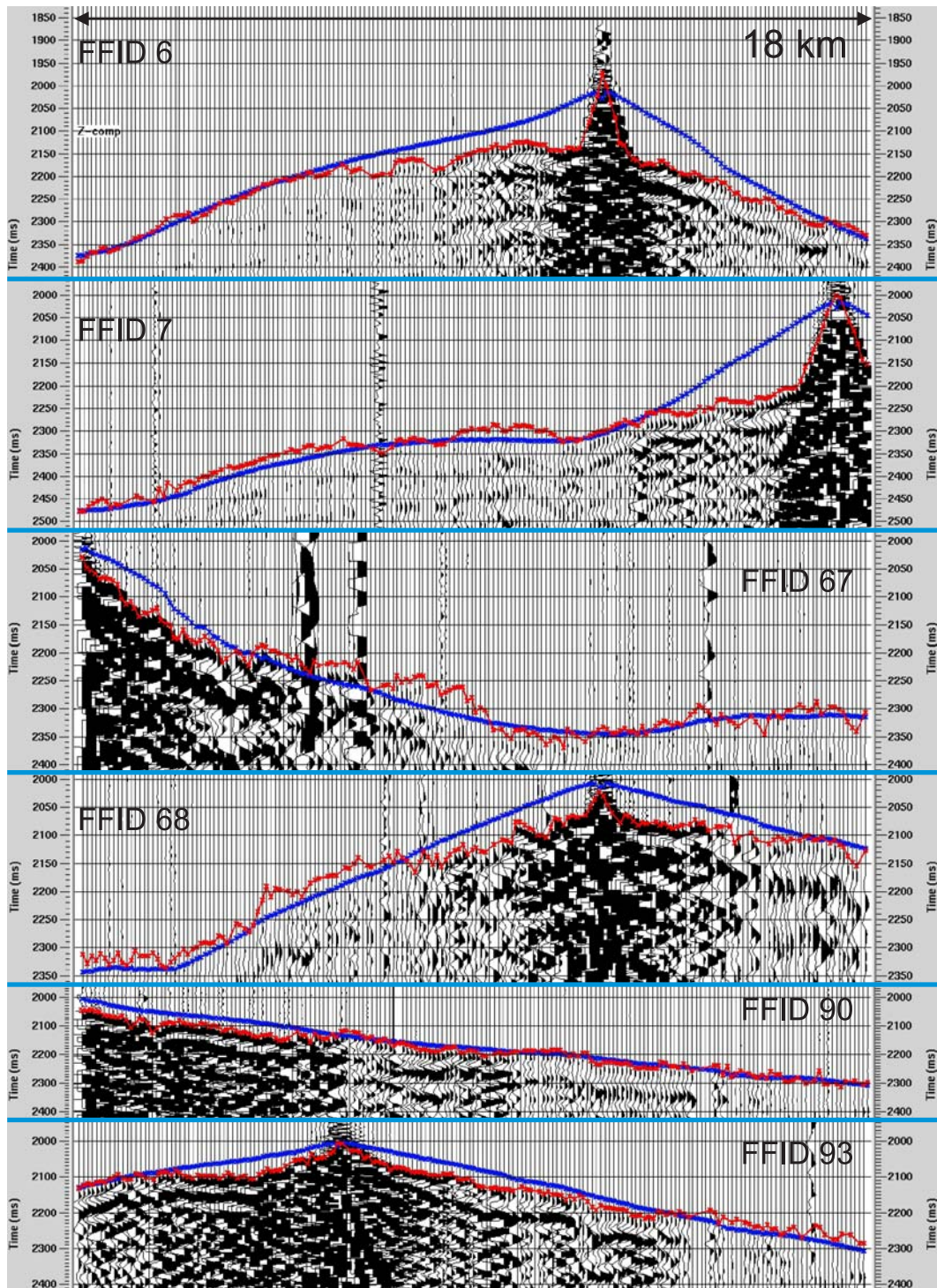
Figure E.19.: Synthetic (blue) and picked (red) travel-times are shown together with shot data of NVR shots.

F. Appendix: First-break tomography – NVR and SH shots only
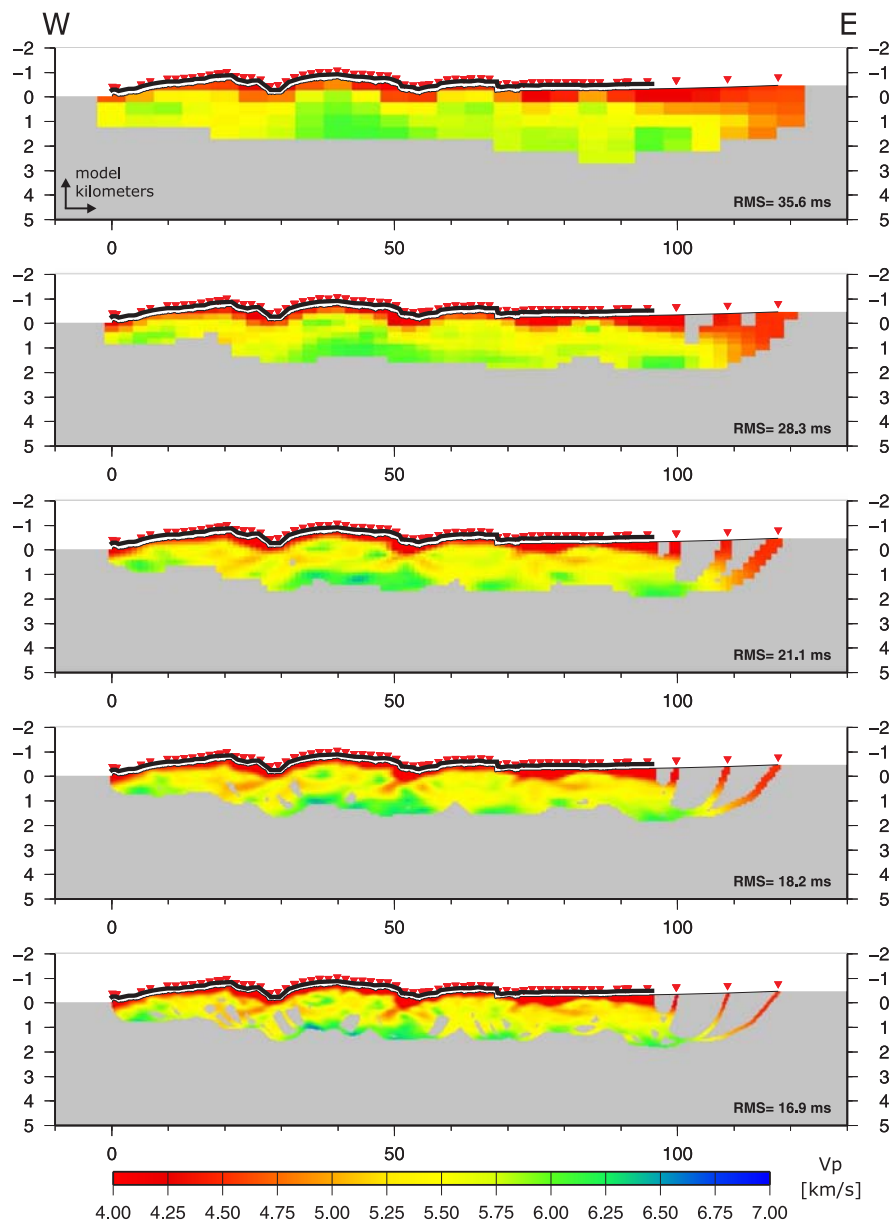
Figure F.1.: Example of all five inversion cycles for the NVR + SH shot configuration.
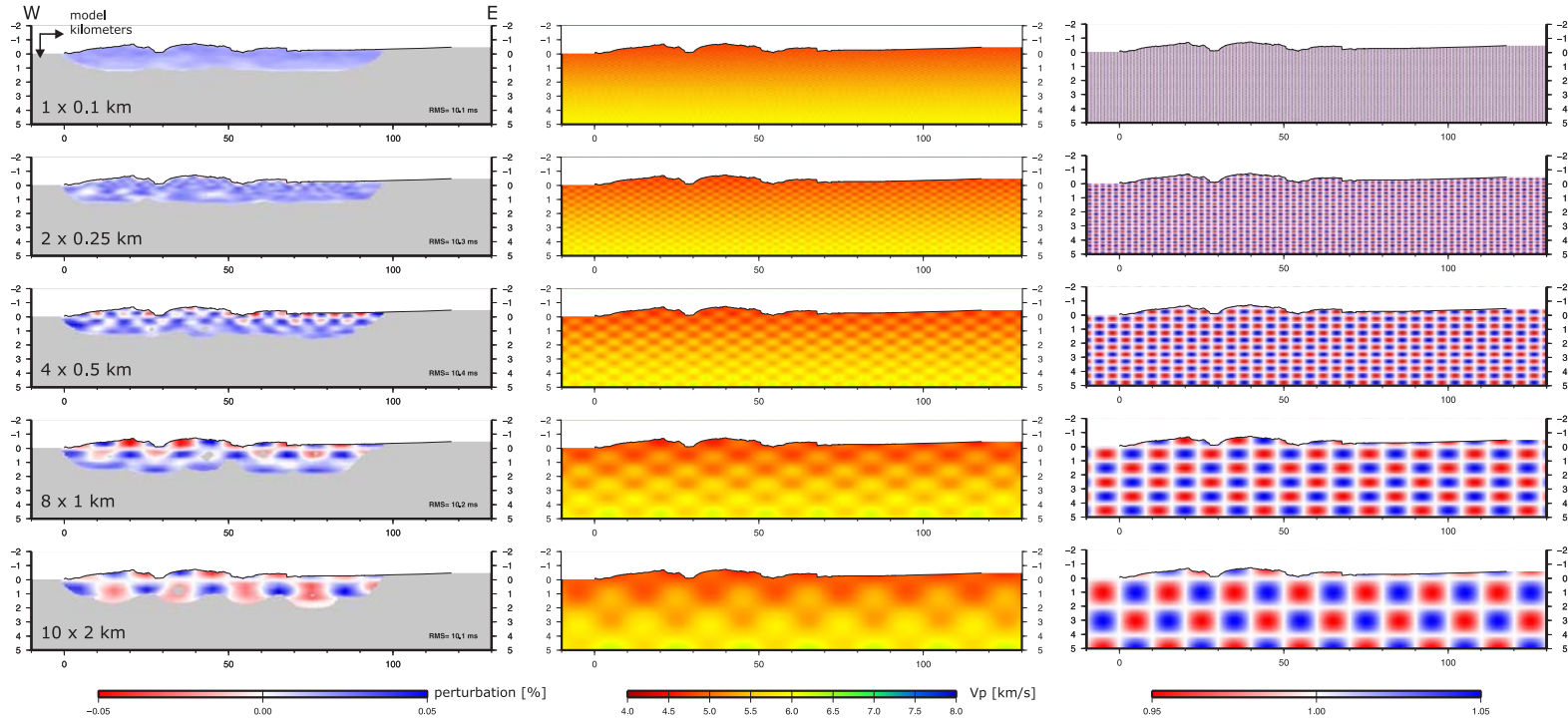
Figure F.2.: Results of all checkerboard calculations for the NVR + SH shot configuration shown together with the perturbated model and anomaly pattern.
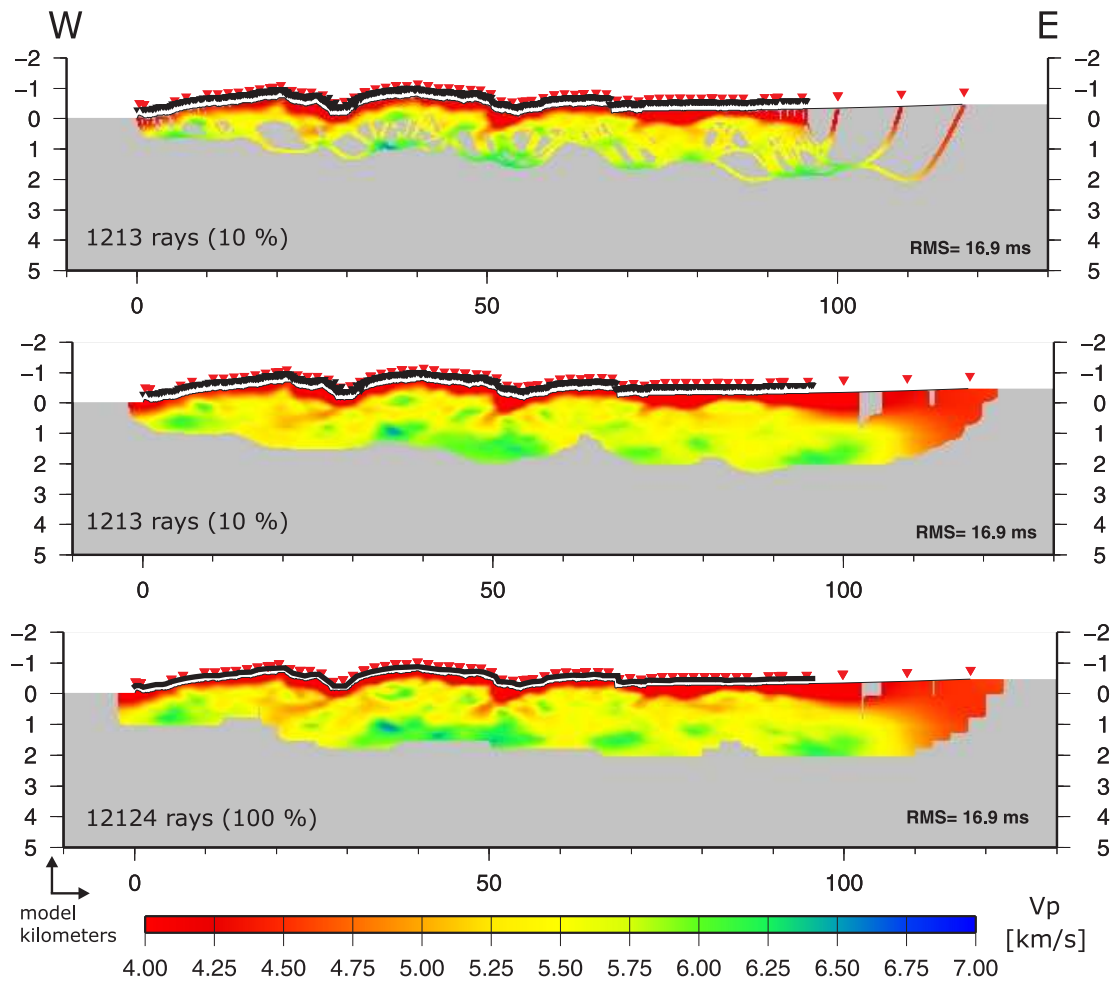
Figure F.3.: Reducing the number of travel-times (NVR + SH) down to 10 % just slightly alters the resultant image, even prominent small-scale structures are imaged with the reduced travel-times. The same RMS value for the two shown inversions points to a good, stable inversion.
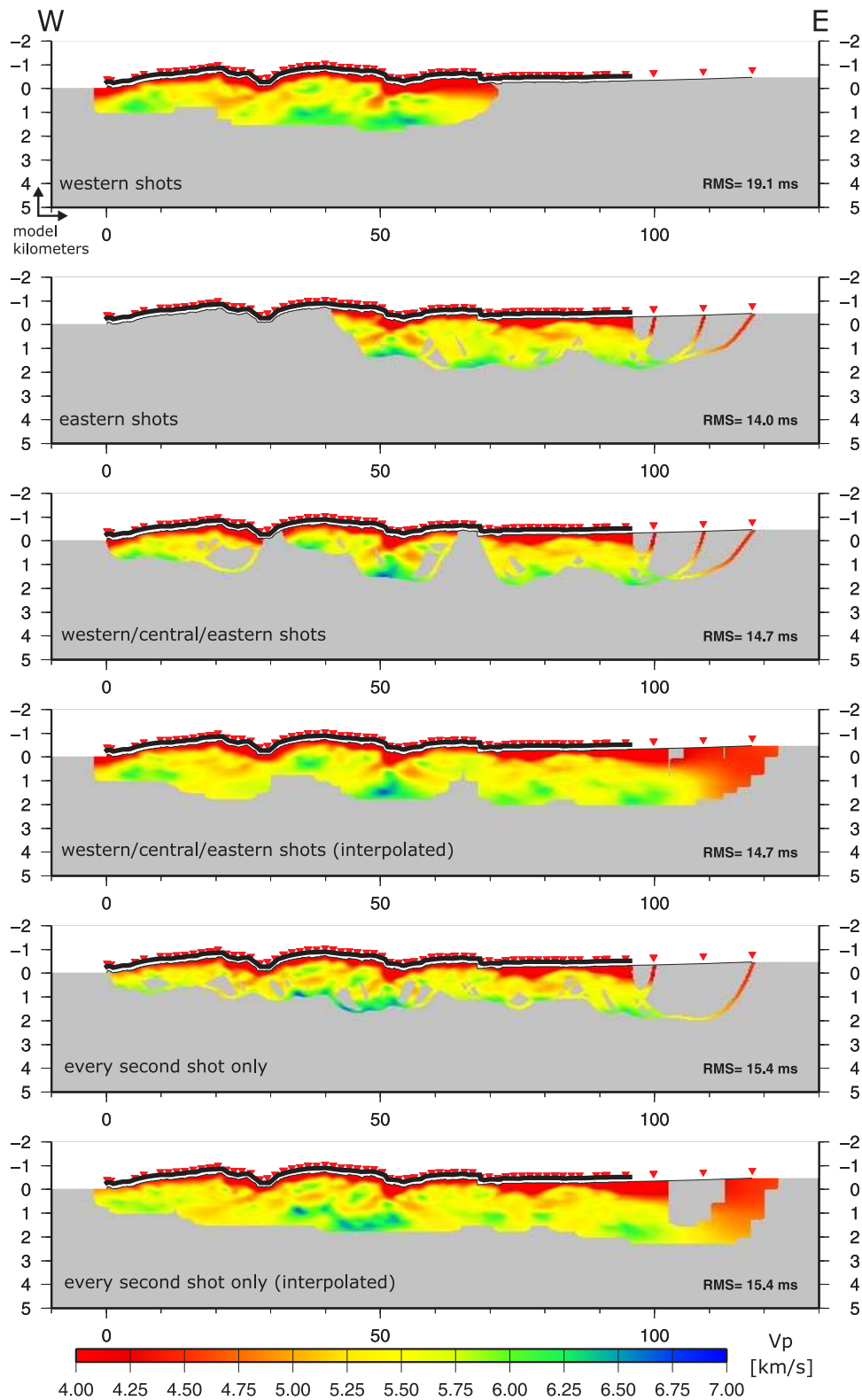
Figure F.4.: Variations in the number of NVR and SH shotpoints reproduce the observed structures and velocities using all NVR and SH shots. Notable differences occur in the central part of the profile (x = 40 - 50 km), where we observe very high velocities at the lower end of the profile.
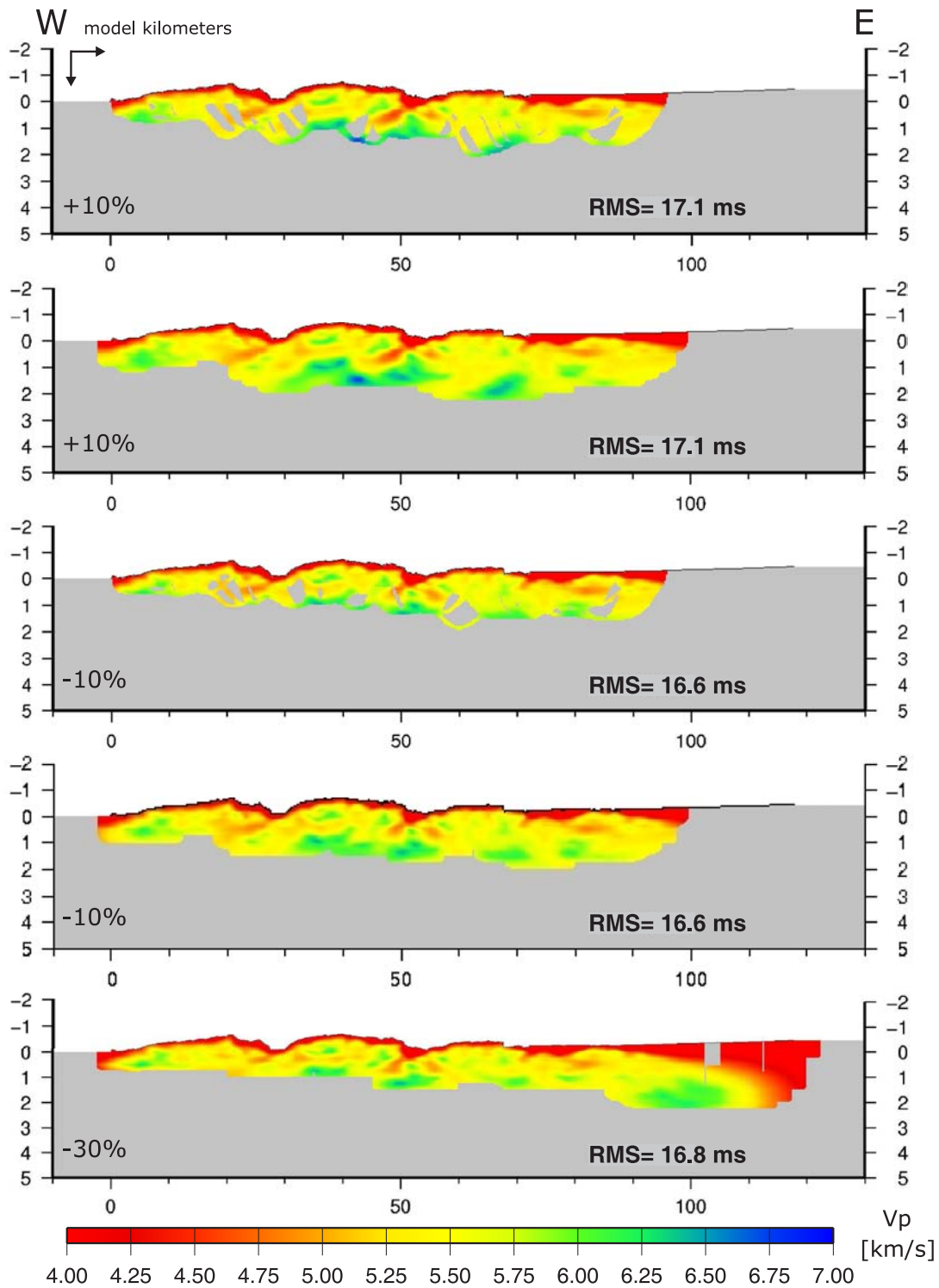
Figure F.5.: Variations in the starting velocity model produce only minor deviations. Reducing the velocities up to 30 % below the starting model still reproduces the observed structures. Differences occur again in the deeper, central part of the profile in the area of velocities greater than ≈ 6.4 km/s (blue colors)
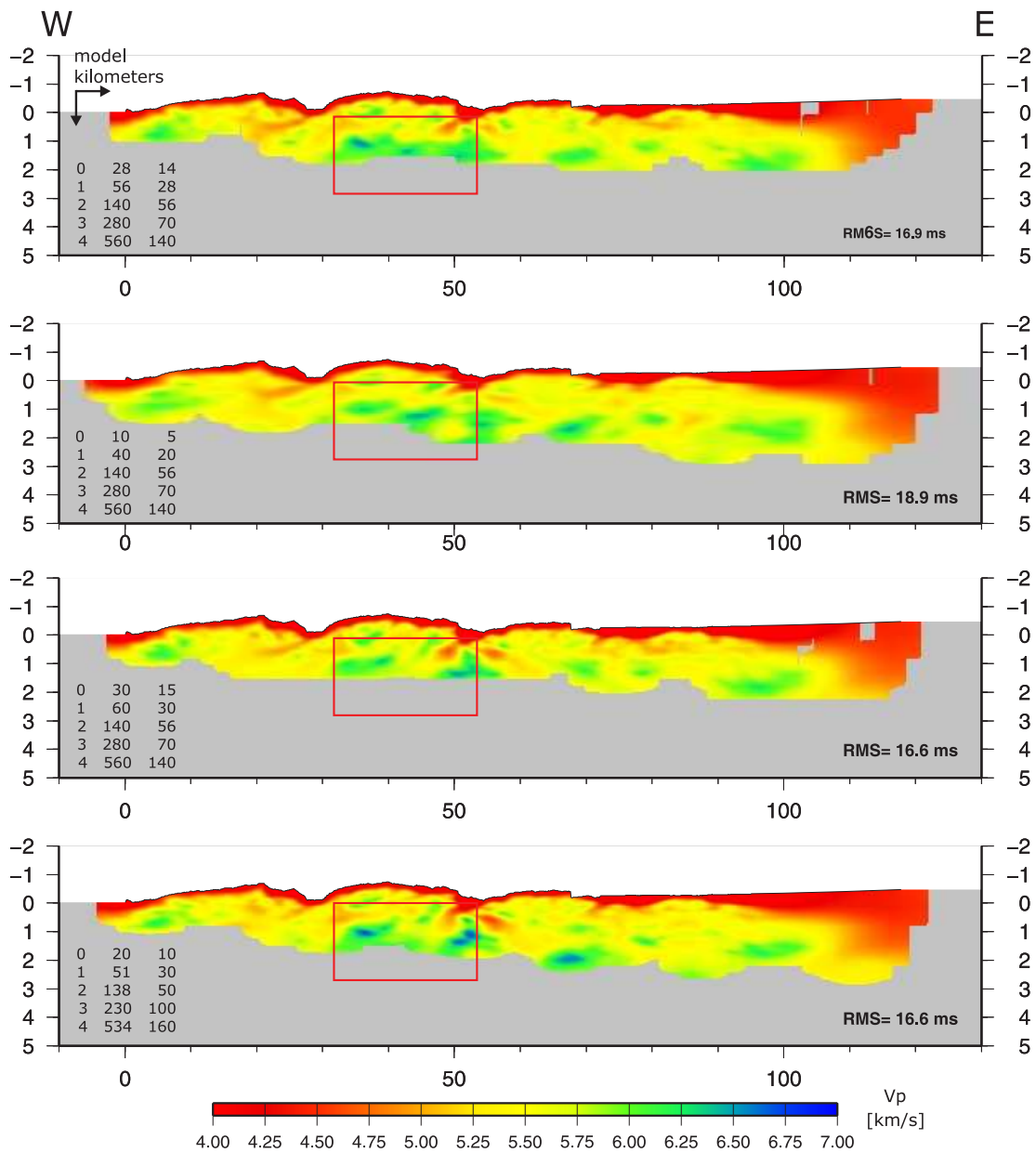
Figure F.6.: Effects produced by variations in the inversion cellsizes can also be observed in the inversion with the NVR + SH shots only, but of a lower magnitude. Major differences are marked by a red box in the central part of the profile.
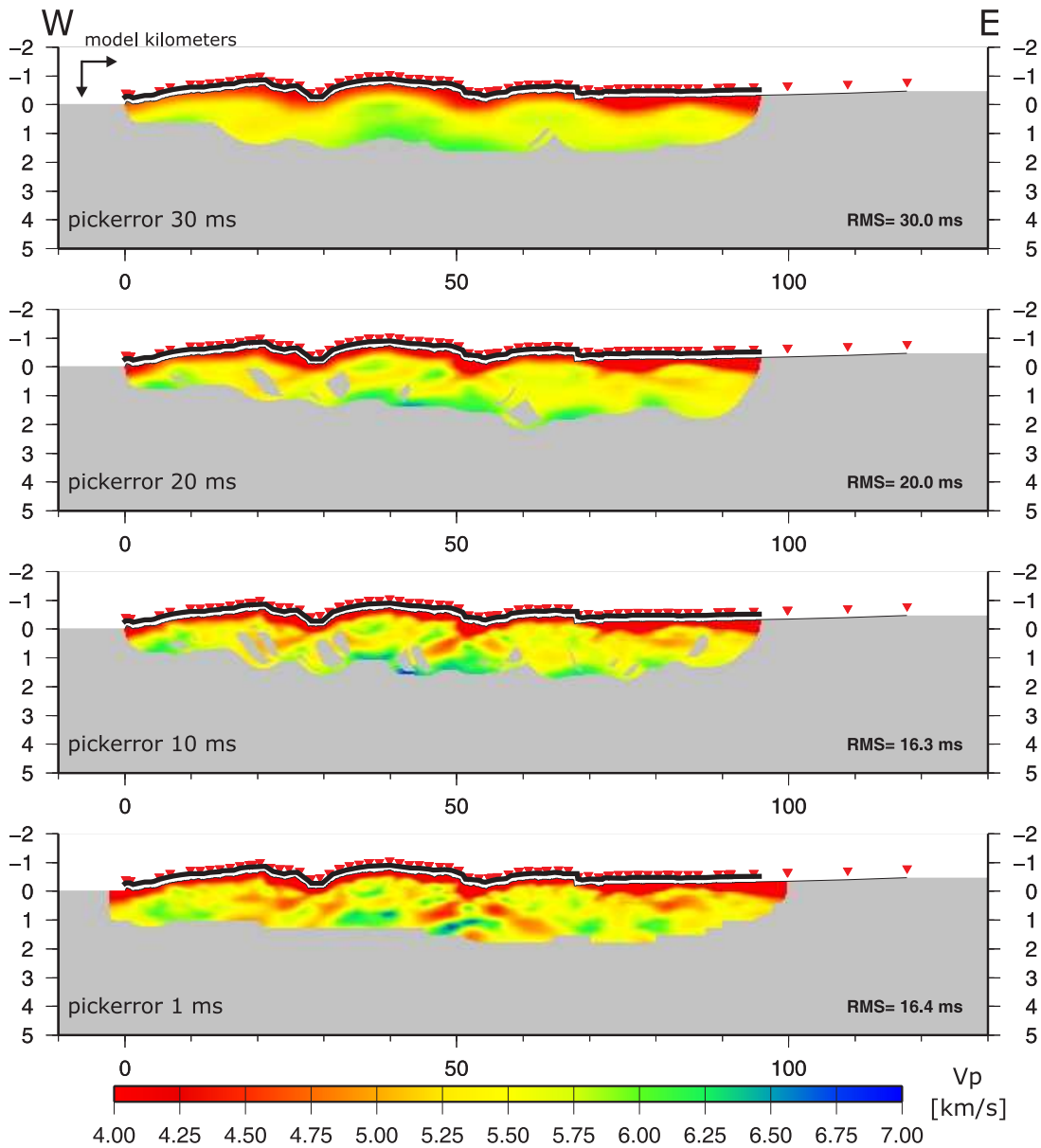
Figure F.7.: The smaller cells used in the inversion with only NVR and SH shots provide a better resolution of the subsurface, but only if a smaller pickerror is used. A pickerror of 0.03 and 0.02 seconds can be inverted for without problems (see RMS values). First finer structures can be observed with a pickerror of 20 ms. The inversion with a pickerror of 0.001 s points out that a better pickerror than 16.4 ms can not be reached, when the data is tried to be fitted perfectly. A realistic visual pickerror of 10 ms proved to be appropriate, resulting in a best RMS value of 16.3 ms. The deviation of 6.3 ms may be attributed to geometrical errors resulting from the projection of the crooked experiment geometry on a straight profile.
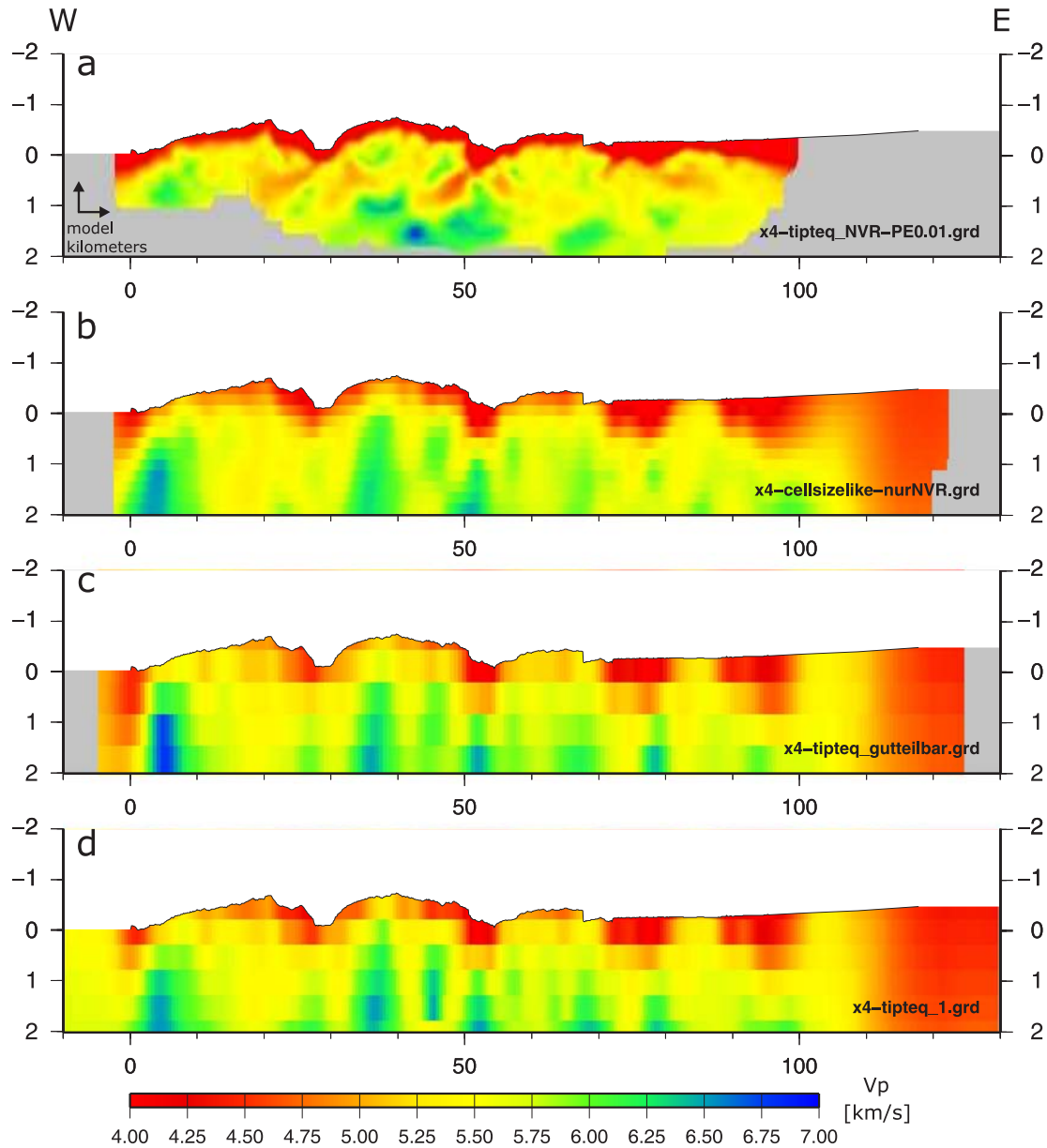
Figure F.8.: A comparison of the first kilometers of inversions using coarse and fine cells with different pickerrors. Results b - d belong to inversions including the ESP shots (z = -2 to 28 km), and use a pickerror of 0.03 s, whereas panel a uses 10 ms and lacks the ESP shots. The lower three images resemble each other remarkably well, and some features are even comparable with the fine-structured, low-pickerror inversion result shown in a.
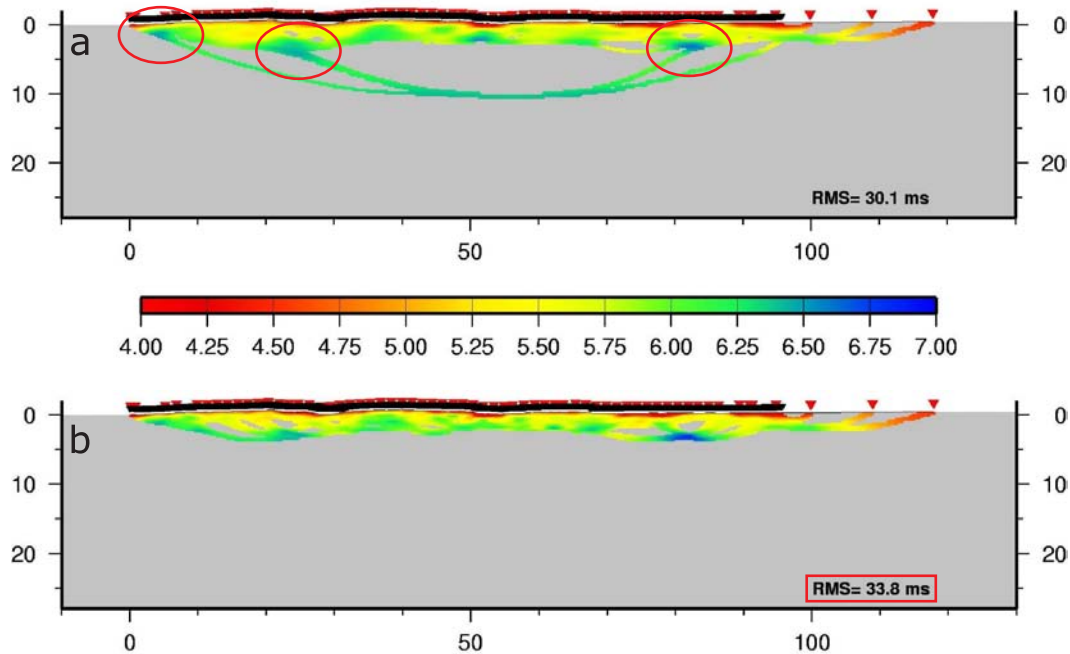
Figure F.9.: The inversion results are calculated using all available shots (including ESP shots), but using the same small cellsizes like the inversions without the ESP shots (see table 8.2). Two pickerrors were used for the calculations, 30 ms were used in the result shown in panel a, panel b shows a result using only 0.01 ms. The ESP ray paths are very narrow in a, because of the small inversion cells. At some intersections of the ESP rays with the area covered by NVR shots, high velocity zones appear, which are certainly artifacts (red circles). The result in panel b uses the same parameters like the inversions without ESP shots and shows also a shallow depth penetration. But the observed structures are not similar to the final inversion result shown in figure 8.7. The RMS error is also double the size than the RMS error of the final model, where the RMS error amounts to only 16.3 ms. These observations give further indicators which underline the importance to omit the ESP shots from the inversions and not only to limit the grid of the inversion with all shots to a depth of 3 - 5 kilometers.
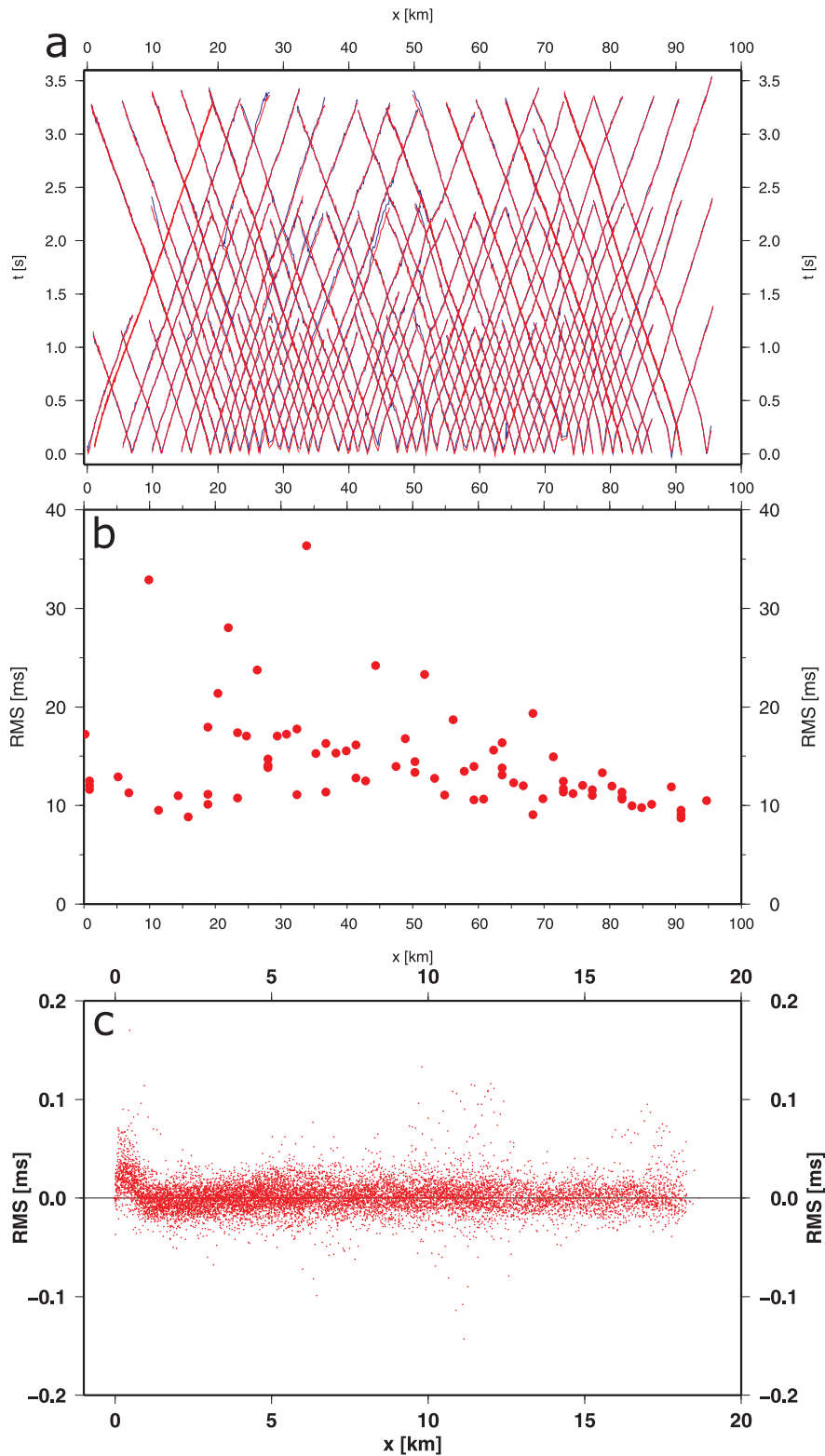
Figure F.10.: Figure F.10a shows the picked and calculated travel-times including a random pickerror of 10 ms. The two times match very closely. Part b shows the RMS error of each shot along profile which mainly lies between 10 and 20 ms. Panel c shows the RMS values of all receivers sorted after offset. A slight drop in point density can be observed for offsets greater than 12 kilometers, resulting from the shot/spread configuration (cf. figure 8.3).
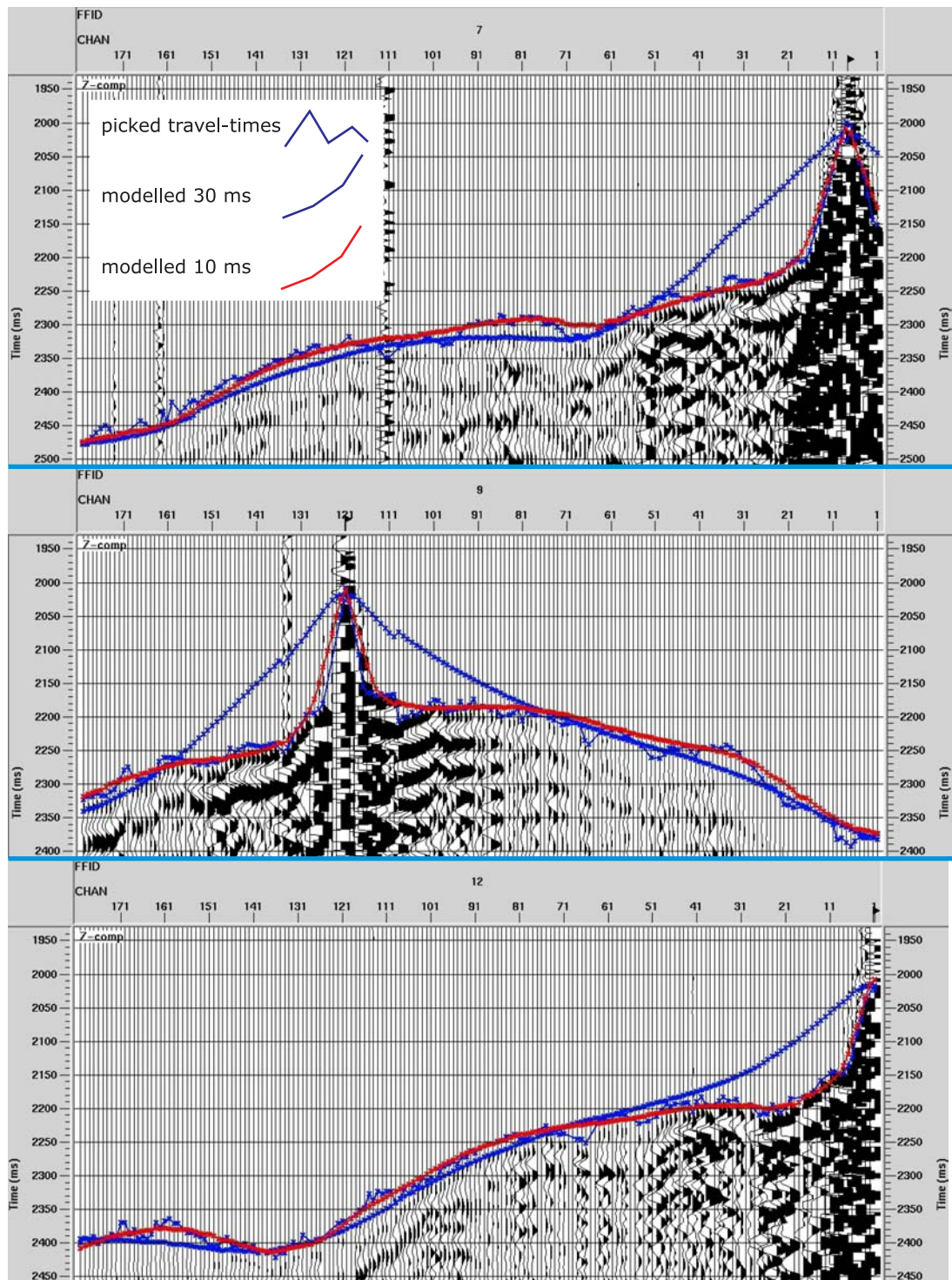
Figure F.11.: Synthetic and picked travel-times together with shot data. The jagged blue line belongs to the picked first-breaks, the smooth blue one to the synthetic calculated travel-times with a pickerror of 30 ms (including ESP shots). The red line shows the modeled travel-times, using a pickerror of only 10 ms (excluding ESP shots). The red line fits to the first-breaks much better, even close to the shots, where great deviations are observed in the synthetic travel-times calculated with a pickerror of 30 ms.
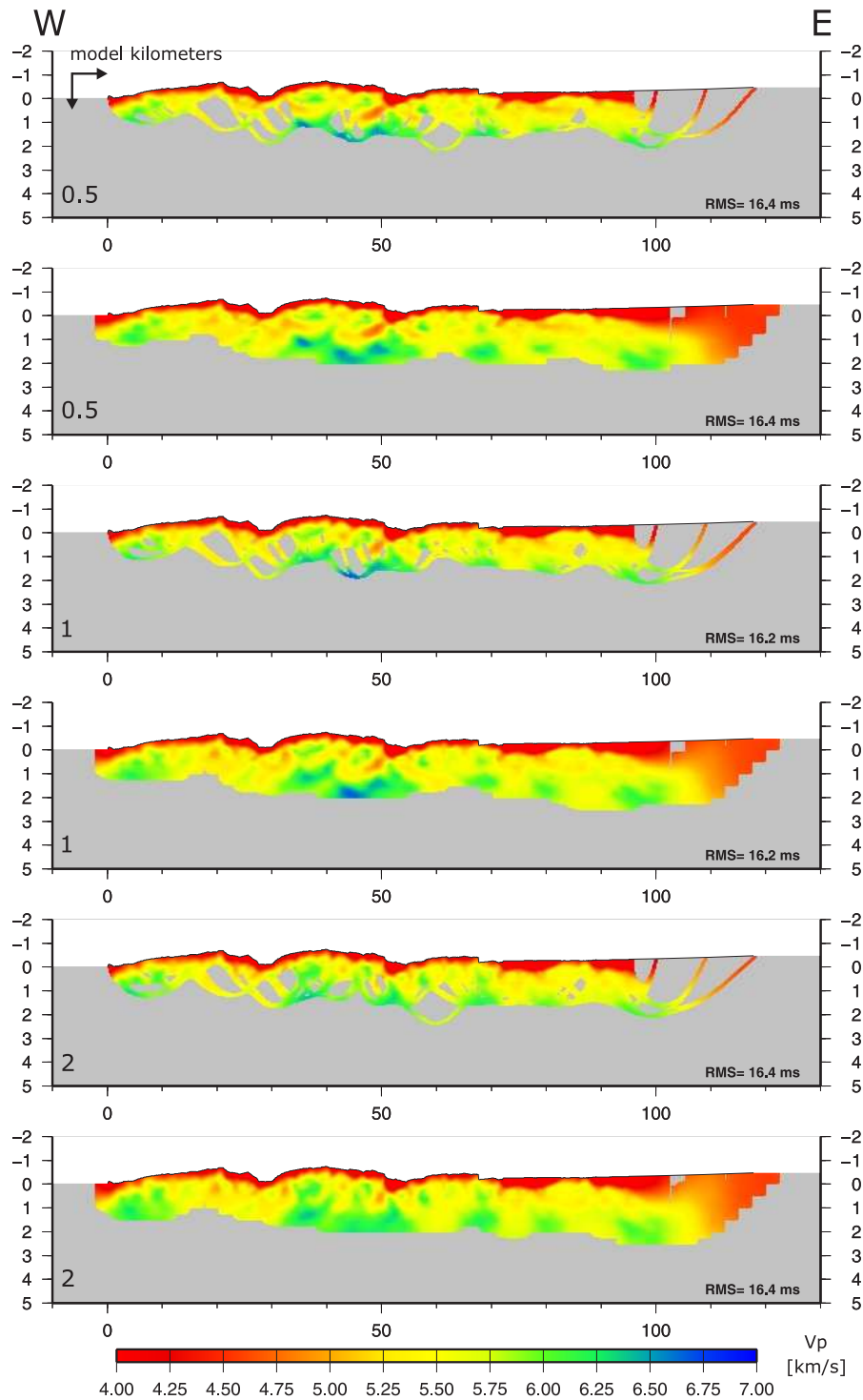
Figure F.12.: Horizontal vs. vertical smoothness/flatness investigation. A small s_z favors horizontal structures, whereas a large s_z leads to vertical structures. This trend is already visible in the small range of values for s_z used in the shown inversions. The RMS values lie between 16.2 to 16.4 ms. A value of 0.25 was used to obtain comparable results to the inversion with ESP shots, and provides a RMS value of 16.3 ms (cf. figure 8.2).
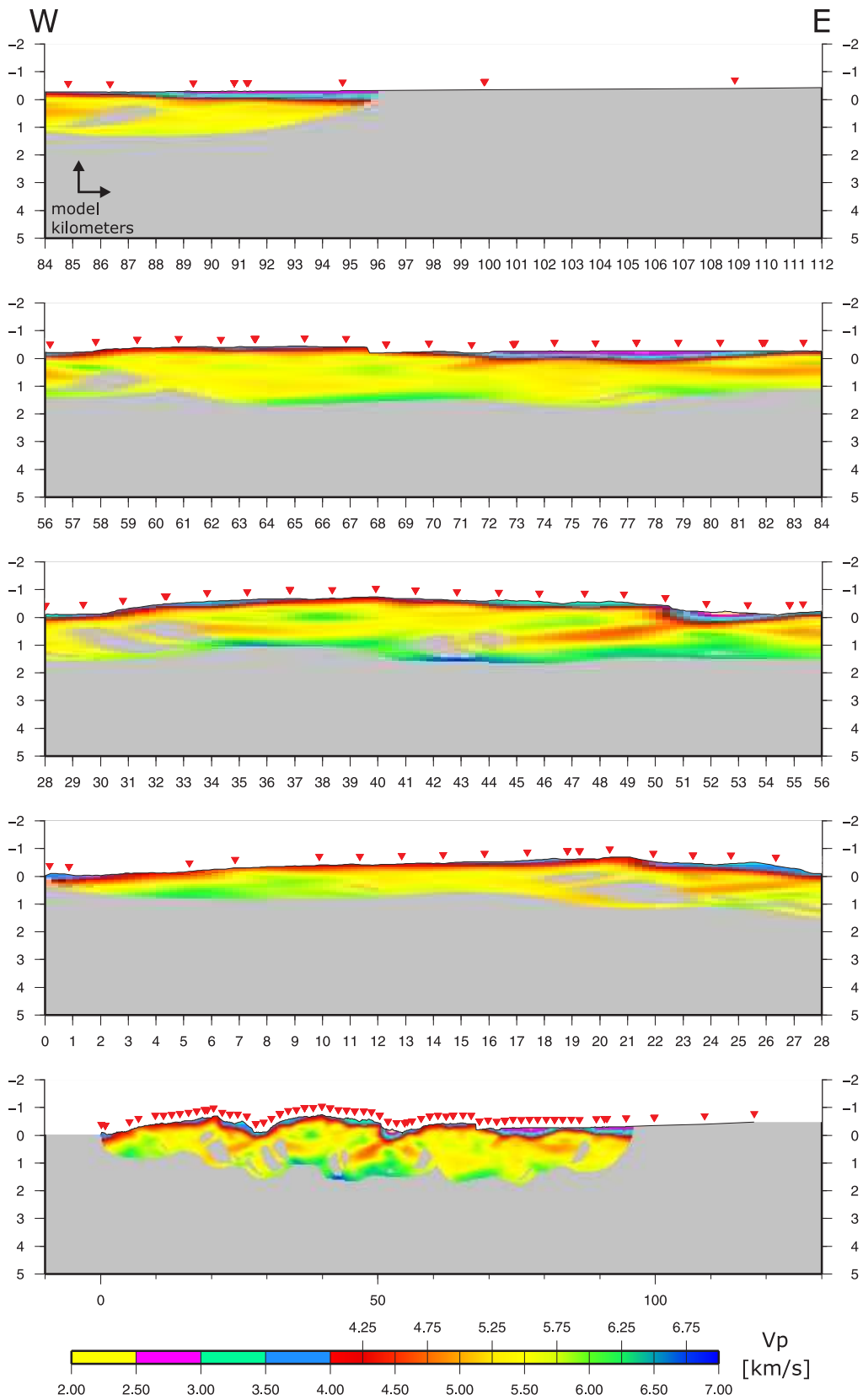
Figure F.13.: Final tomographic image without vertical exaggeration, lowermost panel shows total view.
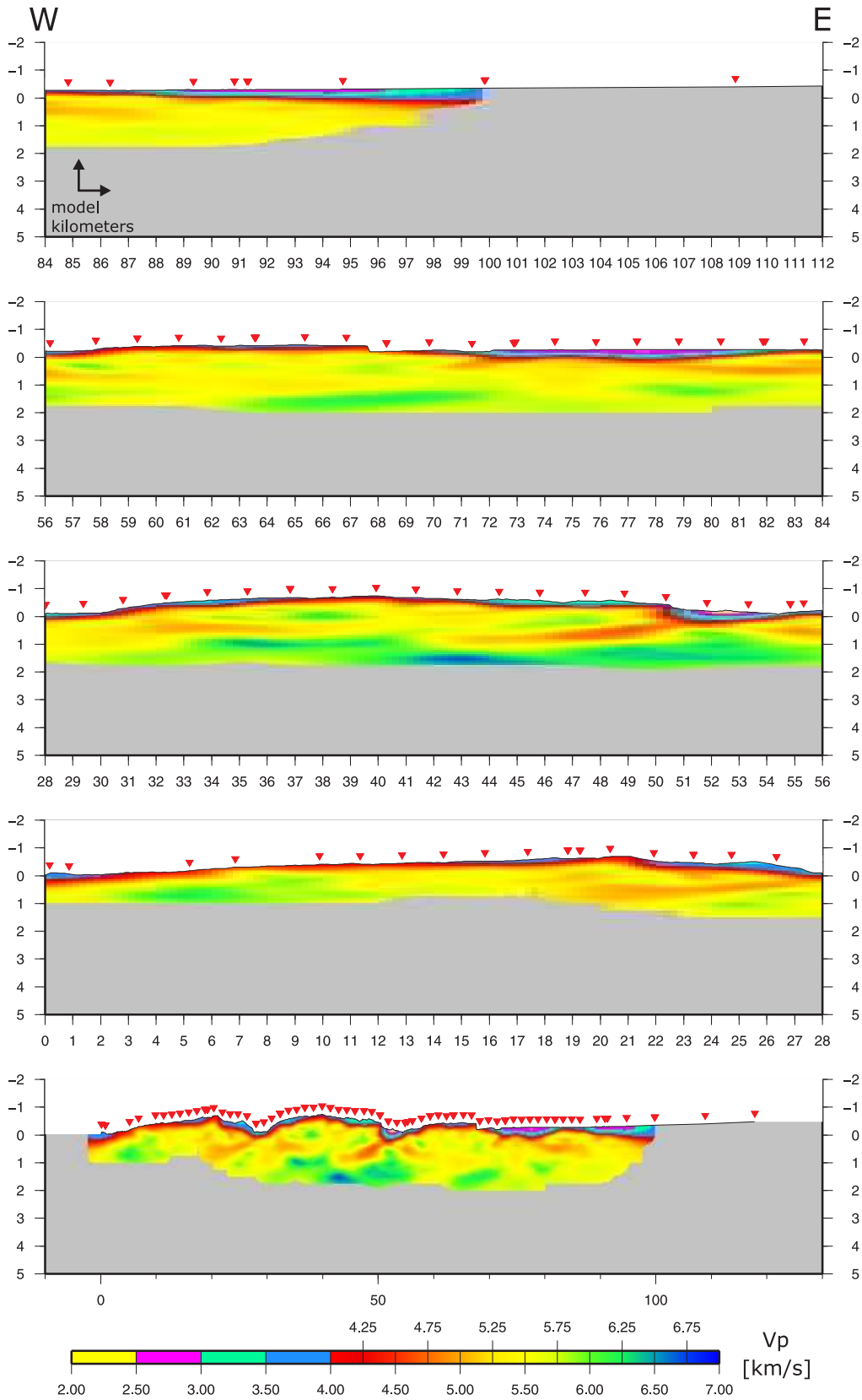
Figure F.14.: Final tomographic image without vertical exaggeration, lowermost panel shows total view, interpolated.
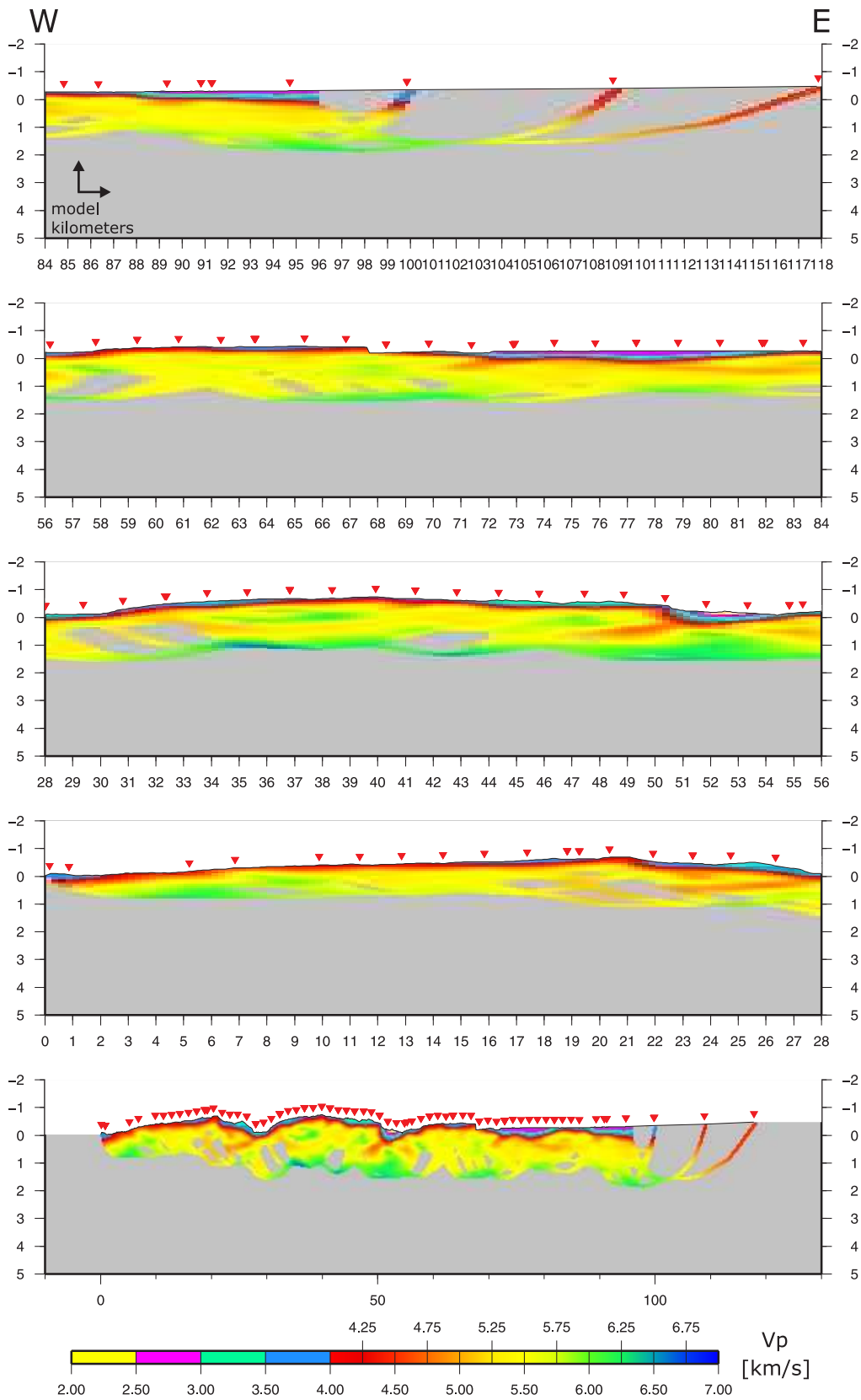
Figure F.15.: Final tomographic image without vertical exaggeration including shots off the line, lowermost panel shows total view.
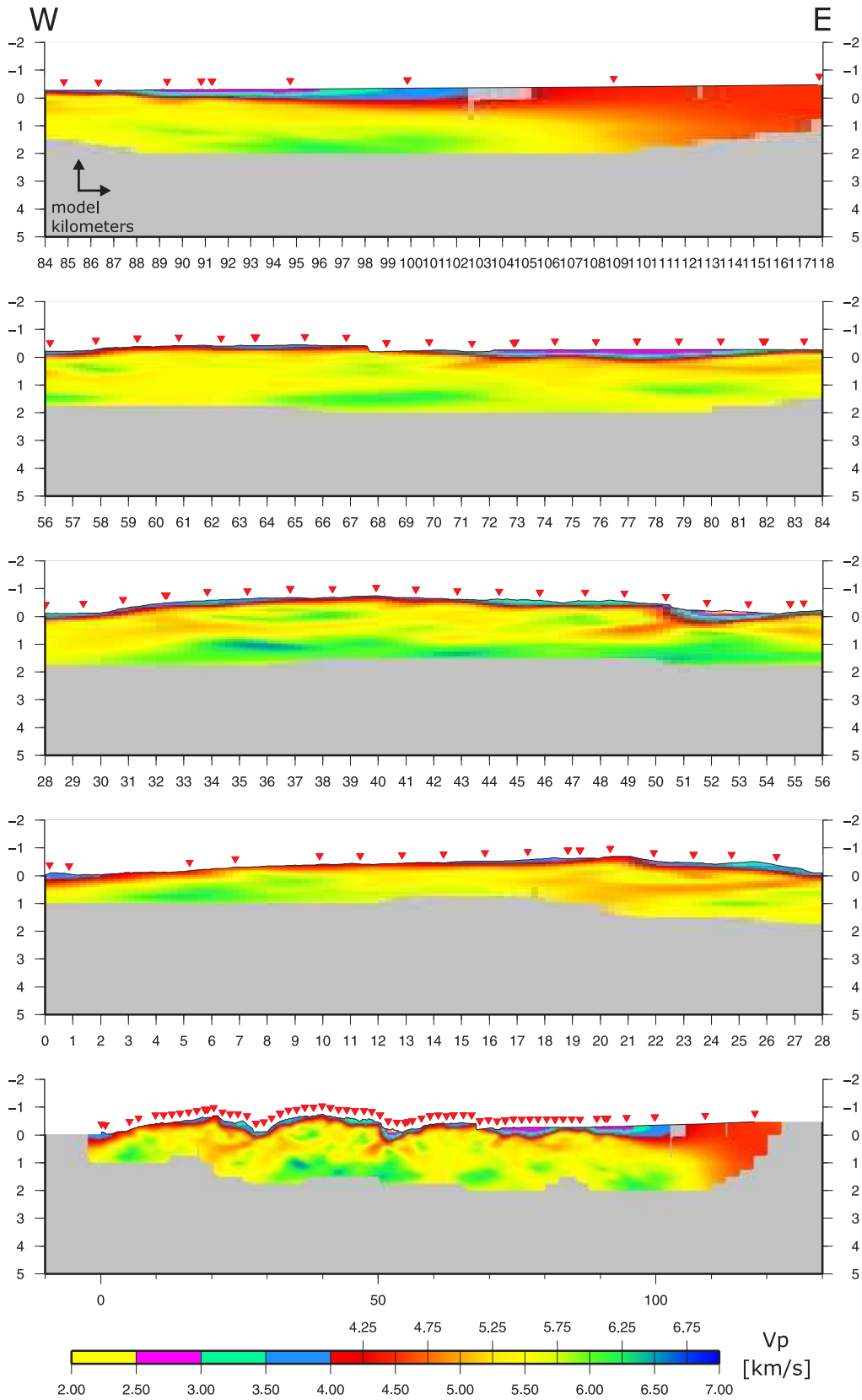
Figure F.16.: Final tomographic image without vertical exaggeration including shots off the line, lowermost panel shows total view, interpolated.

G. Appendix: Migration with different velocity models

G.1. Merging of velocity models wit MATLAB: modmerge.m

```
close all
clear all

%%%%%%%%%%%%%%%%%%%%%%%%%%%%%%%%%%%%%%%%%%%%%%%%%%%%%%%%%%%%%%%%
% Weitwinkel Modell einlesen und zurechtschneiden
%%%%%%%%%%%%%%%%%%%%%%%%%%%%%%%%%%%%%%%%%%%%%%%%%%%%%%%%%%%%%%%%

% Weitwinkel Modell einlesen und gesamt plotten

x_z_vp = dlmread('x-z-vp.asc','');
d1 =  x_z_vp(:,1);
d2 = -x_z_vp(:,2);
d3 =  x_z_vp(:,3);

x_all=reshape(d1,66,441);
z_all=reshape(d2,66,441);
v_all=reshape(d3,66,441);

figure(10);
p = pcolor(x_all,z_all,v_all);
   title('Weitwinkel gesamt')
   colorbar
   set(p,'linestyle','none');

% zurechtschnippeln

% hier den gewuenschten x/z Bereich angeben
km1 = 3;     % km1 immer kleiner km2 angeben tt=3-110 6-66
km2 = 130;   % km_min -200  / km_max 240
z1 =  6;     % Tiefe in km
```

```
z2 =   66;


x1 = 201+km1;
x2 = 201+km2;
x = x_all(z1:z2,x1:x2);
z = z_all(z1:z2,x1:x2);
v = v_all(z1:z2,x1:x2);


x = x-3;        % verschieben des Nullpunktes auf Tomo-Nullpunkt

figure(20);
p = pcolor(x,z,v);
    title('Weitwinkel im TIPTEQ Bereich')
    colorbar
    set(p,'linestyle','none');


%%%%%%%%%%
% Rausschreiben des Zwischenschritts um ihn mit GMT zu plotten
%%%%%%%%%%

rowscols0 = size(z);
laenge0 = rowscols0(:,1)*rowscols0(:,2);


x00 = reshape(x,laenge0,[]);
z00 = reshape(z,laenge0,[]);
v00 = reshape(v,laenge0,[]);


newfile = [x00 z00 v00];

filename=['Z:\umicksch\SPOC-tipteqbereich.asc'];
dlmwrite(filename,newfile,'delimiter','\t','precision','%.4f');

%%%%%%%%%%
% ENDE Rausschreiben des Zwischenschritts um ihn mit GMT zu plotten
%%%%%%%%%%

%%%%%%%%%%%%%%%%%%%%%%%%%%%%%%%%%%%%%%%%%%%%%%%%%%%%%%%%%%%%
% Tomografie einlesen und zurechtschneiden
%%%%%%%%%%%%%%%%%%%%%%%%%%%%%%%%%%%%%%%%%%%%%%%%%%%%%%%%%%%%

% Tomografie einlesen und gesamt plotten
```

```
x_z_vp_tomo = dlmread('tomo.grd.asc','');

c1 =  x_z_vp_tomo(:,1);
c2 = -x_z_vp_tomo(:,2);
c3 =  x_z_vp_tomo(:,3);

x_cll=reshape(c1,281,61);
z_cll=reshape(c2,281,61);
v_cll=reshape(c3,281,61);

x_cll_2=x_cll(1:2:end,:);
z_cll_2=z_cll(1:2:end,:);
v_cll_2=v_cll(1:2:end,:);

figure(30);
p = pcolor(x_cll_2,z_cll_2,v_cll_2);
    title('Tomografie gesamt')
    colorbar
    set(p,'linestyle','none');

% Zurechtschnippeln Tomographie

xa1 = 11;
xa2 = 130;
za1 = 1;
za2 = 57;

xa = x_cll_2(xa1:xa2,za1:za2);
za = z_cll_2(xa1:xa2,za1:za2);
va = v_cll_2(xa1:xa2,za1:za2);

figure(40);
p = pcolor(xa,za,va);
    title('Tomografie Tipteq area')
    colorbar
    set(p,'linestyle','none');

%%%%%%%%%%%%%%%%%%%%%%%%%%%%%%%%%%%%%%%%%%%%%%%%%%%%%%%%%%%%%%%%
% VERKNUEPFUNG DER MODELLE
%%%%%%%%%%%%%%%%%%%%%%%%%%%%%%%%%%%%%%%%%%%%%%%%%%%%%%%%%%%%%%%%

% interpolation der Gitter auf gleiches Gitter:
```

```
%1) erstellen eines leeren Gitters mit Gitterabstand dx
dx =.1;                         %interpolierter Gitterabstand, in km
[xi,zi] = meshgrid(-10:dx:130, -60:dx:0);    %leere Koordinaten

%2) Weitwinkel Modell interpoliert
[vWW]=griddata(x, z, v, xi, zi, 'nearest');  % 'nearest' 'linear'

%3) Tomo interpoliert
V2        = va;
V2(V2==0) = nan;               %tausche Nulls gegen NaNs
[vTomo]   = griddata(xa, za, V2, xi, zi, 'nearest');

%4)
mask = ~isnan(vTomo);

%5) output modell
vModell       = vWW;           %zuerst nur kopieren des alten WW Modells
vModell(mask) = vTomo(mask); %hier ersetzen durch Tomodaten, da wo Tomo Werte hat

%Plot:
figure(50)
p=pcolor(xi,zi,vModell);
 title('kombiniertes V modell')
 set(p,'linestyle','none');
 colormap((jet))
 caxis([3.5 8])
 colorbar

% zurechtschnippeln fuer output

% hier den gewuenschten x/z Bereich angeben
x1out = 101  ;    % in index Schritten
x2out = 1200 ;    %
z1out = 7    ;    % - 59 wegen interpolation am Ende
z2out = 601  ;    %

xout = xi(z1out:z2out,x1out:x2out);
zout = zi(z1out:z2out,x1out:x2out);
vout = vModell(z1out:z2out,x1out:x2out);

txt='Verschnittenes, geschnittenes Vp modell';
```

```
figure(60); clf  % clf = clear current figure
set(60,'name',txt,'NumberTitle','off');
p = pcolor(xout,zout,vout);
title(txt)
    colorbar
    colormap((jet))
    caxis([3.5 8])
    set(p,'linestyle','none');


%%%%%%%%%%%%%%%%%%%%%%%%%%%%%%%%%%%%%%%%%%%%%%%%%%%%%%%%%
% Ascii Export
%%%%%%%%%%%%%%%%%%%%%%%%%%%%%%%%%%%%%%%%%%%%%%%%%%%%%%%%

rowscols = size(zout);
laenge=rowscols(:,1)*rowscols(:,2);

xvmtww = reshape(xout,laenge,[]);
zvmtww = reshape(zout,laenge,[]);
vvmtww = reshape(vout,laenge,[]);

newfile = [xvmtww zvmtww vvmtww];
filename=['Z:\umicksch\vmtww.asc'];
dlmwrite(filename,newfile,'delimiter','\t','precision','%.4f');
```

G.2. Stacking velocities

The used stacking velocities were calculated from the imported x-z-v models within ProMAX with the module 'velocity manipulation'.
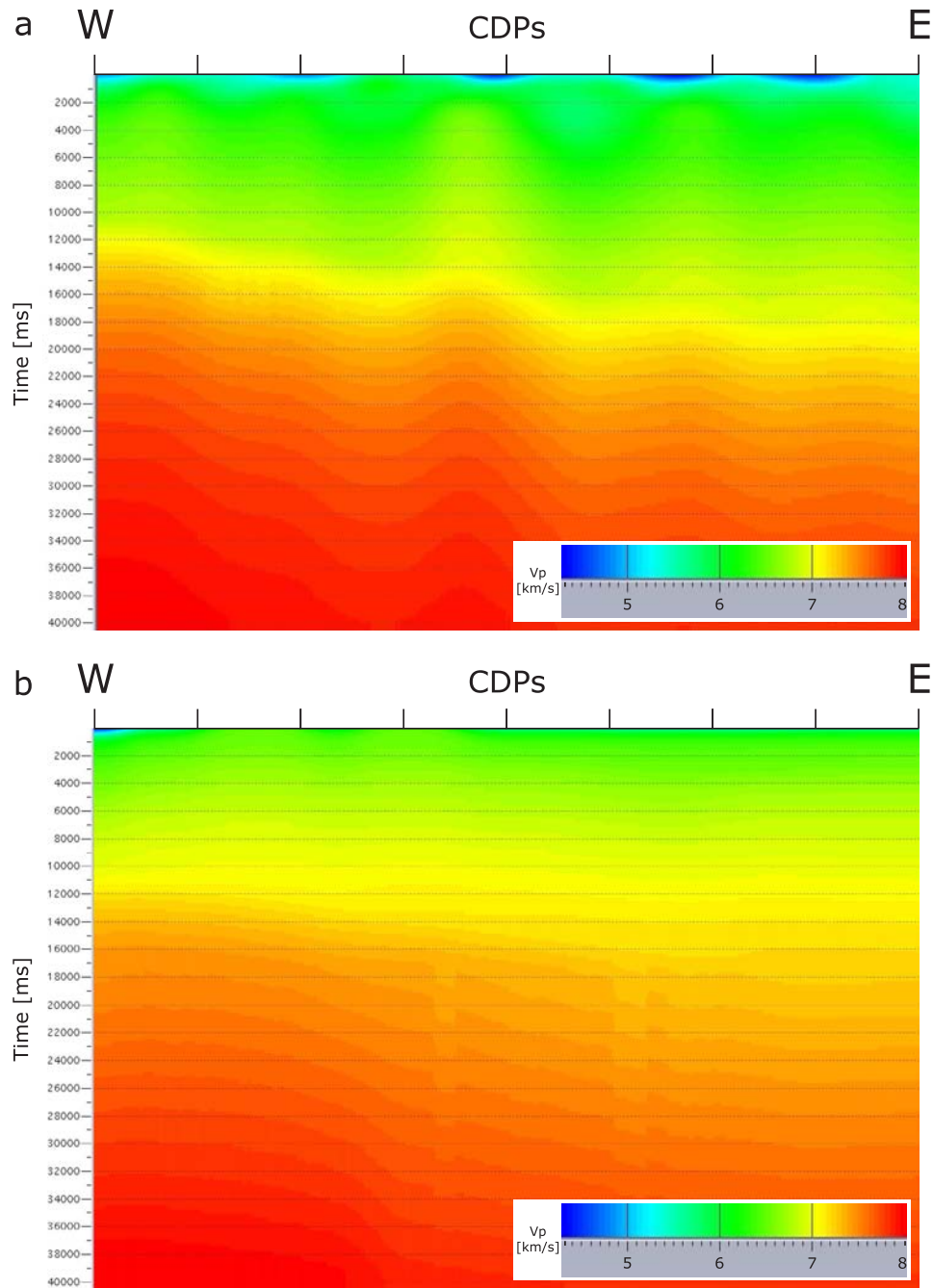
Figure G.1.: Panel a shows the stacking velocities of the merged velocity model (SPOC and tomography), part b of the figure shows the stacking velocities for the SPOC model for comparison.

G.3. Conversion of pixel-images to ASCII data: seismik2xyz*.m

```
close all
clear all

%%%%%%%%%%%%%%%%%%%%%%%%%%%%%%%%%%%%%%%%%%%%%%%%%%%%%%%%%%%%%%%%
% seismic image in PNG format 2 xyz to use with GMT (psxy) %
%%%%%%%%%%%%%%%%%%%%%%%%%%%%%%%%%%%%%%%%%%%%%%%%%%%%%%%%%%%%%

% PNG Bilder einlesen und darstellen mit Histogramm

imageBW=imread('Z:\umicksch\micksch-migration-only-CDP1110-4160-size-reduced.png','PNG');

%figure1 = figure ('Name','BW file');
%imagesc (imageBW);
%colormap(gray);
%figure2 = figure ('Name','BW file histogramm');
%imhist(imageBW);

% Pixelgroessen
rowscols = size(imageBW);
depth    = rowscols(:,1);                 % equals 70 km
length   = rowscols(:,2);                 % equals 152.5 km

laengeBW = rowscols(:,1)*rowscols(:,2);
bw = reshape(imageBW,laengeBW,[]);        % bw ist pixelbild in einer spalte

%Tiefe gleich Vektor 0-70 km in Inkrementschritten
dxt = 70000/depth;   % Tiefeninkrement pro pixel in m
x = 0;

tiefe = zeros (depth,1);

for i = 1:depth;
 tiefe(i,:) = x; x = x+dxt;
end

tiefenmatrix = repmat(tiefe,1,length);          % Werte an jeden Bildpunkt schreiben
tiefenvektor = reshape (tiefenmatrix,laengeBW,[]);  % Werte in eine Spalte schreiben

% xy Koordinaten / Winkel der Tipteqlinie ~ 2.291 (tan = -0.0400)
```

```
leftx  = 617475.81;
lefty  = 5763727.57;


rightx = 769896.62;  % zur Kontrolle ob die Berechnung der UTM-Werte etwa passt
                     % (letztes Element anschauen)
righty = 5757858.10; % ca 260 m


c = 152.5/length*1000;
dxx = cos((-2.291*pi)/180)*c;   % in m, length-mal auf left addieren
dxy = sin((-2.291*pi)/180)*c;


%x werte
utmx = zeros(1,length);


for j = 1:length;
 utmx(:,j) = leftx; leftx = leftx+dxx;
end


%y werte
utmy = zeros(1,length);


for k = 1:length;
 utmy(:,k) = lefty;
 lefty = lefty+dxy;
end


%% Bis hier laufen lassen dann das Untere einkommentieren und exportieren
%%
%% nun utmx' und utmy' zusammen rausschreiben (auf 7days) und
%% in der UNIX Welt mit Programm 'utm' in lo la umwandeln
%% wieder in matlab einladen und repmat+reshape anwenden
%% UNIX Befehle (script1-1110-4160.scr):
%%
%% awk '{print "utm", $1,$2, -18}' utmx-utmy4lola1110-4160.asc  > t1
%% chmod 777 t1
%% t1 > lalo4matlab.asc
%% \rm t1


%utmexport = [ utmx' utmy' ];
%filename = ['Z:\umicksch\utmx-utmy4lola110-4160.asc'];
%dlmwrite(filename,utmexport,'delimiter','\t','precision','%.4f');
```

```
%% Einelesen der umgeformten Datei und rausschreiben fuer GMT

% Einlesen der UTM Werte, umschreiben in komplette Matrix und aufteilen
% in Vektor

lola = dlmread('Z:\umicksch\lalo4matlab1110-4160.asc','');

lo = lola(:,1)';
la = lola(:,2)';

lomatrix = repmat(lo,depth,1);
lovektor = reshape(lomatrix,laengeBW,[]);
lamatrix = repmat(la,depth,1);
lavektor = reshape (lamatrix,laengeBW,[]);

clear c depth dxt dxx dxy i flilename i imageBW j k la laengeBW;
clear lamatrix leftx lefty length lo lola lomatrix rightx righty;
clear rowscols tiefe tiefenmatrix utmexport utmx utmy x;

lolazbw = [ lovektor lavektor tiefenvektor bw ];
filename=['Z:\umicksch\lolazbw-from-matlab1110-4160.asc'];
dlmwrite(filename,lolazbw,'delimiter','\t','precision','%.4f');

% lolazbw-from-matlab.asc file in UNIX mit script2-1110-4160.scr
% awk '{if ($4!=1.0000) print $1, $2, -$3}'
% lolazbw-from-matlab1110-4160.asc > seismic4psxyz1110-4160.asc
% verkleinern ('nur schwarze Punkte') und dann mit psxzy plotten
```

H. Appendix: Interpretation and discussion

H.1. Visualization with Google Earth

Two freeware programs can be used to visualize data in Google Earth very easily. GE-Path can be used to plot points, lines, and areas, as well as to calculate path lengths, perimeters, or areas. GE-Graph can visualize all sorts of diagrams, and export/import data from office suites. Both programs can be obtained at
`http://www.sgrillo.net/googleearth/index.htm`.

Image overlays or the visualization of 3–D structures can also be realized fast in Google Earth. Unfortunately, this interface can not display data below the surface, so it is of limited use for subsurface models and seismic data. See folder `/tipteq/GE` for TIPTEQ related data examples and figure H.1.

H.2. Visualization with Fledermaus and Mirone

Fledermaus by IVS3d can visualize all kinds of point data, 3–D models, or vertical or horizontal georeferenced pixel images. The software is also capable to record movies of the visualized 3–D model. More information: `http://www.ivs3d.com/products/`. A free viewer enables to fly through a 3–D model created of the TIPTEQ data such as seismic profiles or earthquake hypocenters. Find 3–D model and viewer in `/tipteq/fledermaus`). See figure H.2 for example view.

Mirone by Luis (2007) (freeware) can convert GMT gridfiles into a format usable for Fledermaus and many more useful things related to GMT and other plotting and GIS software. Visit website at `http://w3.ualg.pt/~jluis/mirone/` for more information.
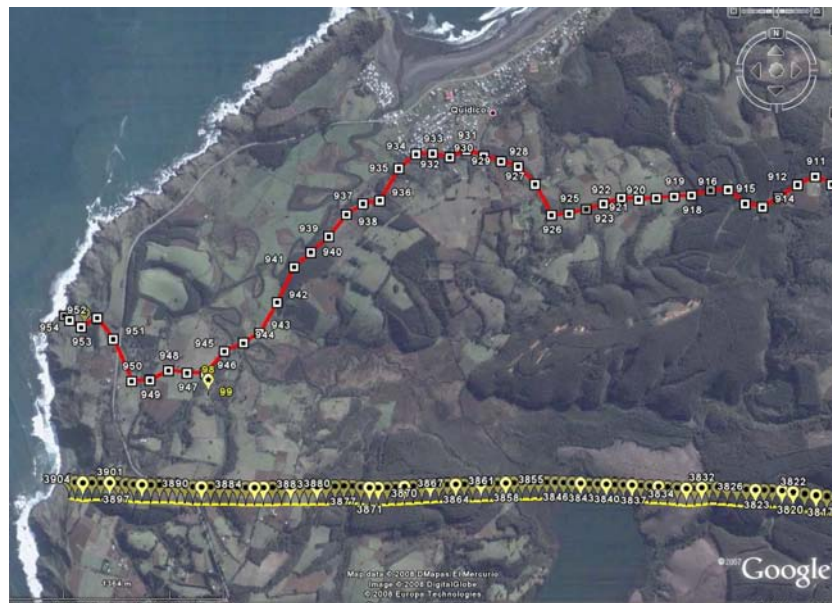
Figure H.1.: Two examples of the combination of TIPTEQ geometry data such as receiver stations and shotpoints (top) and CDP locations (bottom) in Google Earth. If the satellite pictures are of high quality in the survey area the fast visualization of Google Earth can be very helpful to relate experiment geometries, fault traces or point data like earthquake epicenters or sample positions.
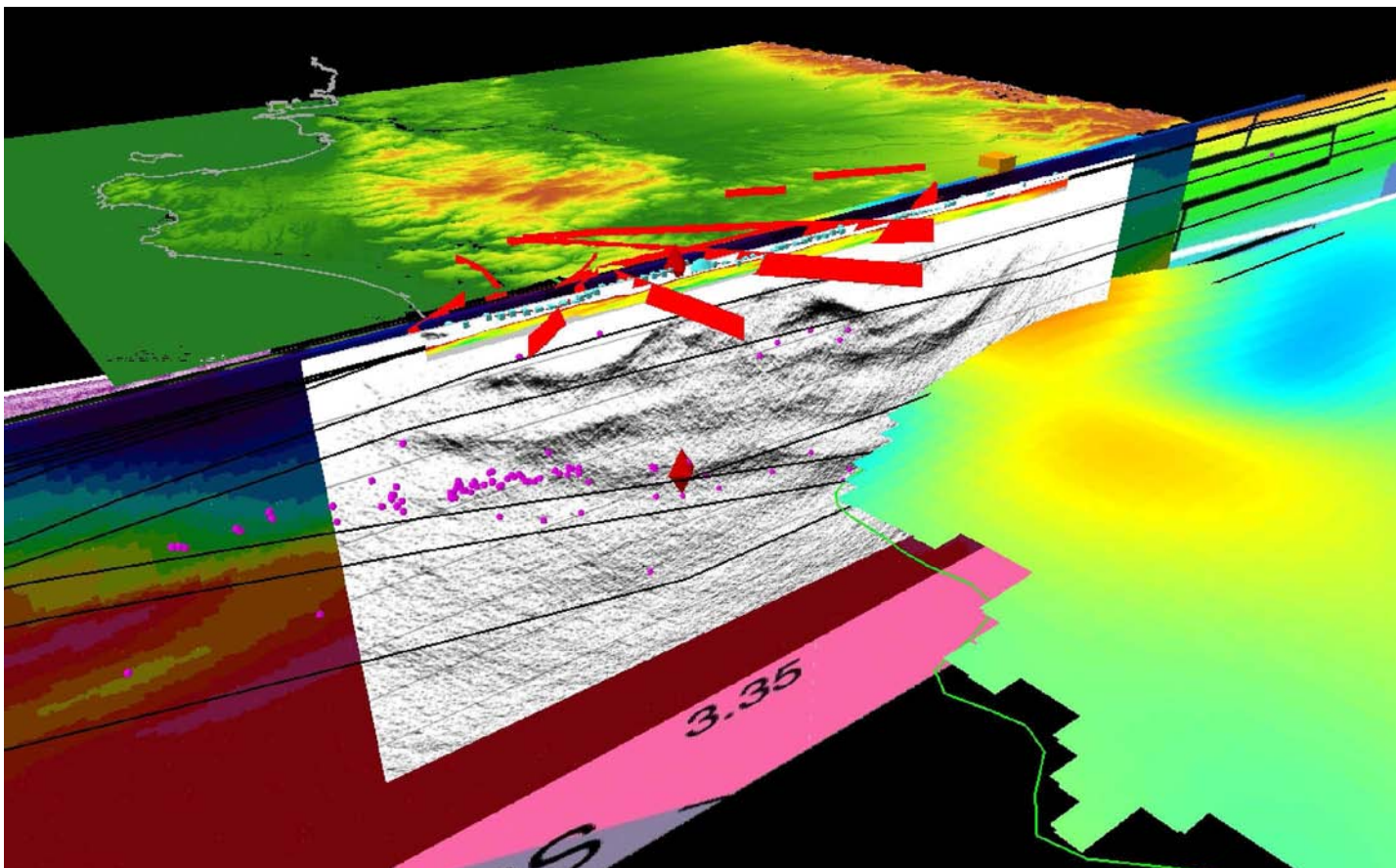
Figure H.2.: TIPTEQ related data visualized in Fledermaus. Besides the reflection seismic image in the center, tomographic velocity distributions, velocity and density interfaces, earthquake hypocenters, and digital elevations are shown.
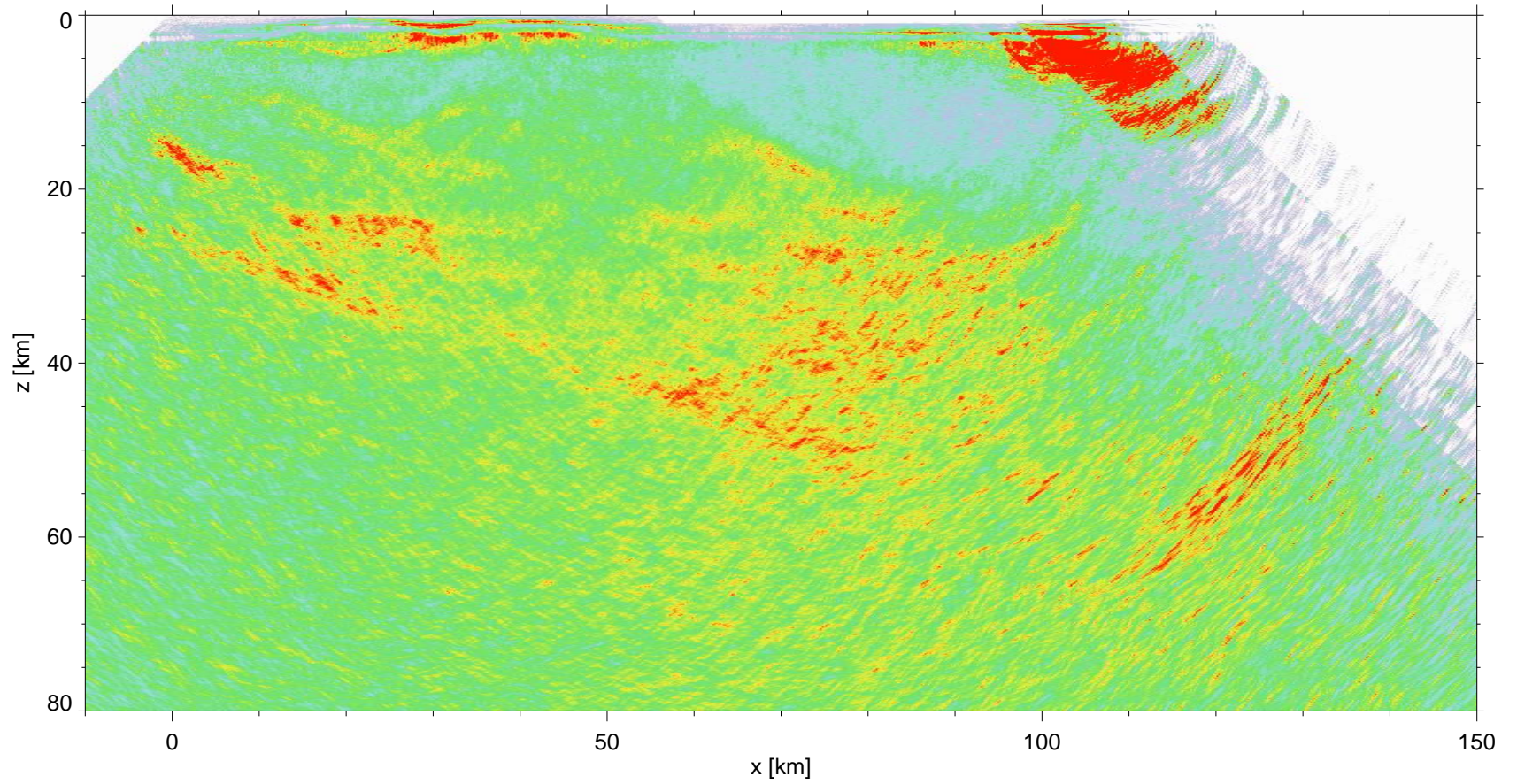
Figure H.3.: Kirchhoff Prestack Depth Migration of the TIPTEQ data (Groß, 2008), see subsection 10.2.1 for more details.
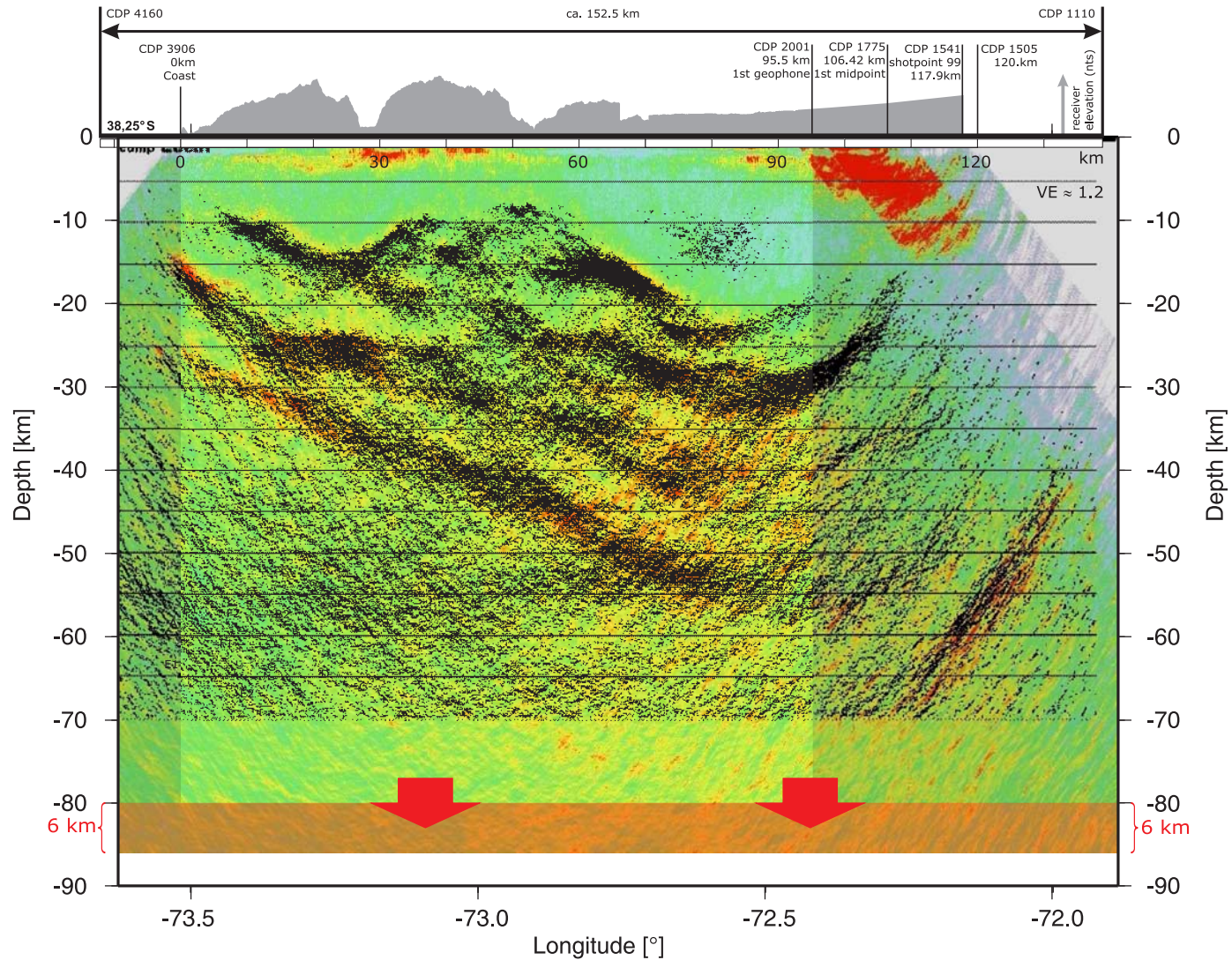
Figure H.4.: Illustration of the stretched KPSDM and poststack image. The lower end of the KPSDM image (z = 80 km) is stretched to z = 86 km depth, resulting in a stretch factor of 1.075. Of course, the poststack image can be bulged upwards the same amount to fit both sections.

H.5. Spatial errors in the tomographic images
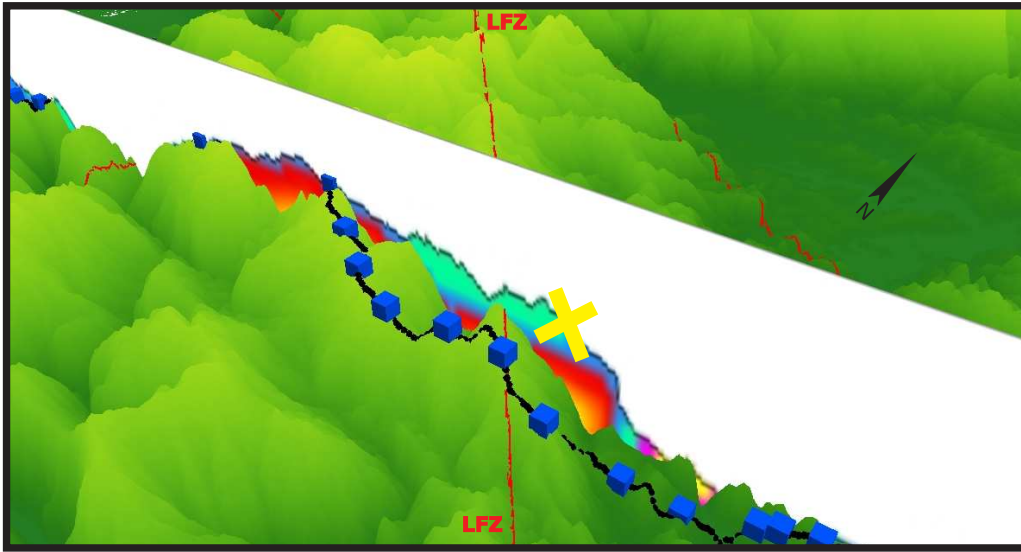
Figure H.5.: Figure H.5 shows an example of spatial errors occurring along the 2–D profile resulting from the crooked line geometry and oblique features such as mountain ranges or faults. The Lanalhue Fault Zone (LFZ, red line) meets the receiver line east of the point where it pierces the ideal 2–D line. The 'real' piercing point is marked by a yellow X'. The mountain range has no counterpart on the ideal profile which follows the CDP line of the reflection seismic section. This error is relatively small, but must be remembered when addressing oblique striking features. Shotpoints are shown in blue, receiver positions with black dots, elevation is coded in green shades. The view is from the southeast to the northwest (VE = 10).

Micksch/TIPTEQ peer-reviewed articles

Groß, K., U. Micksch, and TIPTEQ Research Group (2008). The reflection seismic survey of project TIPTEQ – the inventory of the Chilean subduction zone at 38° S. *Geophysical Journal International 172*(2), 565–571. URL: `http://tinyurl.com/6ynwm4`.

Micksch/TIPTEQ congress contributions

Groß, K., S. Buske, M. Araneda, K. Bataille, J. Bribach, C. M. Krawczyk, S. Lüth, J. Mechie, U. Micksch, A. Schulze, S. Shapiro, M. Stiller, P. Wigger, and T. Ziegenhagen (2005a). Numerical modelling of a 3-component reflection seismic survey at 38°S – comparison with first field data from project TIPTEQ. POSTER, LAK, GeoForschungsZentrum (GFZ) Potsdam. URL: `http://edoc.gfz-potsdam.de/gfz/6795`.

Groß, K., S. Buske, M. Araneda, K. Bataille, J. Bribach, C. M. Krawczyk, S. Lüth, J. Mechie, U. Micksch, A. Schulze, S. Shapiro, M. Stiller, P. Wigger, and T. Ziegenhagen (2005b). Numerical modelling of a 3-component reflection seismic survey at 38°S – comparison with first field data from project TIPTEQ. POSTER, Final Symposium SFB 267, GeoForschungsZentrum (GFZ) Potsdam. URL: `not_yet_in_GFZ-bib_database`.

Groß, K., S. Buske, P. Wigger, M. Araneda, K. Bataille, J. Bribach, C. M. Krawczyk, S. Lüth, J. Mechie, U. Micksch, A. Schulze, S. Shapiro, M. Stiller, and T. Ziegenhagen (2005). Numerical modelling of a 3-component reflection seismic survey at 38°S – comparison with first field data from project TIPTEQ. POSTER, Status Seminar 'Continental Margins', GeoForschungsZentrum (GFZ) Potsdam. URL: `http://edoc.gfz-potsdam.de/gfz/7505`.

Groß, K., S. Buske, P. Wigger, M. Araneda, K. Bataille, J. Bribach, C. M. Krawczyk, S. Lüth, J. Mechie, U. Micksch, A. Schulze, S. Shapiro, M. Stiller, T. Ziegenhagen, and TIPTEQ Research Group (2005). The Chilean subduction zone at 38°S: Results of the reflection seismic experiment within project TIPTEQ. POSTER, IASPEI, Santiago, Chile. URL: `http://edoc.gfz-potsdam.de/gfz/7901`.

Groß, K., S. Buske, P. Wigger, M. Araneda, K. Bataille, J. Bribach, C. M. Krawczyk, S. Lüth, J. Mechie, U. Micksch, A. Schulze, S. A. Shapiro, M. Stiller, T. Ziegenhagen, and TIPTEQ RESEARCH GROUP (2006). The onshore reflection seismic survey of project TIPTEQ: Imaging the Chilean subduction zone using prestack kirchhoff depth migration. POSTER, EGU, Vienna, Austria. URL: `http://edoc.gfz-potsdam.de/gfz/8629`.

Groß, K., S. Buske, P. Wigger, U. Micksch, C. M. Krawczyk, M. Stiller, M. Araneda, K. Bataille, J. Bribach, S. Lüth, J. Mechie, A. Schulze, S. Shapiro, T. Ziegenhagen, and TIPTEQ Research Group (2006). Imaging the Chilean subduction zone using kirchhoff prestack depth migration. TALK, TIPTEQ Workshop und Status Seminar, Kiel. URL: `not_yet_in_GFZ-bib_database`.

Groß, K., S. Buske, P. Wigger, U. Micksch, C. M. Krawczyk, M. Stiller, M. Araneda, K. Bataille, J. Bribach, S. Lüth, J. Mechie, A. Schulze, S. A. Shapiro, T. Ziegenhagen, and TIPTEQ RESEARCH GROUP (2005). Imaging the Chilean subduction zone at 38°S using prestack kirchhoff depth migration within project TIPTEQ. TALK, AGU, San Francisco, USA. URL: `http://edoc.gfz-potsdam.de/gfz/7983`.

Groß, K., S. Buske, P. Wigger, U. Micksch, C. M. Krawczyk, M. Stiller, M. Araneda, K. Bataille, J. Bribach, S. Lüth, J. Mechie, A. Schulze, S. A. Shapiro, T. Ziegenhagen, and TIPTEQ WORKING GROUP (2006). Structural image of the Chilean subduction zone at 38°S: The reflection seismic survey within project TIPTEQ. POSTER, DGG, Bremen. URL: `http://edoc.gfz-potsdam.de/gfz/8613`.

Groß, K., S. Buske, P. Wigger, M. Stiller, M. Araneda, K. Bataille, J. Bribach, C. M. Krawczyk, S. Lüth, J. Mechie, U. Micksch, A. Schulze, S. Shapiro, and T. Ziegenhagen (2005). A 3-component reflection seismic survey at 38°S illuminating the Chilean subduction zone with project TIPTEQ. POSTER, ISAG, Barcelona, Spain. URL: `http://edoc.gfz-potsdam.de/gfz/7904`.

Groß, K., U. Micksch, S. Buske, C. M. Krawczyk, P. Wigger, and TIPTEQ Research Group (2006). The reflection seismic survey of project TIPTEQ of central Chile (38°S). POSTER, XI Congreso Geologico Chileno, Antofagasta, Chile. URL: `not_yet_in_GFZ-bib_database`.

Krawczyk, C. M., M. Araneda, G. Asch, K. Bataille, H. Brasse, J. Bribach, S. Buske, T. Dahm, R. Galas, H.-J. Götze, K. Groß, V. Haak, C. Haberland, R. Hackney, W. Hanka, S. Hofmann, G. Kapinos, R. Kind, D. Lange, S. Lüth, J. Mechie, U. Meyer, U. Micksch, A. Rietbrock, O. Ritter, F. Scherbaum, A. Schulze, S. Shapiro, M. Stiller, and P. Wigger (2005). Geophysical images of plate interface properties at the southern Central Chilean margin – the onshore geophysical components of project TIPTEQ. TALK+POSTER, Status Seminar 'Continental Margins', GeoForschungsZentrum (GFZ) Potsdam. URL: `http://edoc.gfz-potsdam.de/gfz/6875`.

Krawczyk, C. M., M. Araneda, K. Bataille, J. Bribach, S. Buske, K. Groß, S. Lüth, J. Mechie, U. Micksch, A. Schulze, S. Shapiro, M. Stiller, P. Wigger, and T. Ziegenhagen (2005). A 3-component reflection seismic survey across the Chilean subduction zone – structural seismic imaging of the seismogenic coupling zone within the project TIPTEQ. TALK, LAK, GeoForschungsZentrum (GFZ) Potsdam. URL: `http://edoc.gfz-potsdam.de/gfz/6793`.

Krawczyk, C. M., U. Micksch, H. Echtler, H. Brasse, C. Haberland, P. Alasonati, K. Bataille, and TIPTEQ Research Group (2007). Crustal architecture and depth-graded properties of the seismogenic coupling zone in southern Central Chile (38°S) from geophysical observations. POSTER, Montpellier, France. URL: `http://edoc.gfz-potsdam.de/gfz/display.epl?mode=doc&id=10845`.

Krawczyk, C. M., U. Micksch, K. Groß, S. Buske, M. Stiller, P. Wigger, M. Araneda, K. Bataille, J. Bribach, S. Lüth, J. Mechie, A. Schulze, S. A. Shapiro, T. Ziegenhagen, and TIPTEQ RESEARCH GROUP (2005). Imaging the seismogenic coupling zone in

Chile: The 3-component reflection seismic survey of project TIPTEQ. TALK, AGU, San Francisco, USA. URL: `http://edoc.gfz-potsdam.de/gfz/7984`.

Micksch, U., K. Groß, C. M. Krawczyk, M. Stiller, M. Araneda, K. Bataille, J. Bribach, S. Buske, S. Lüth, J. Mechie, A. Schulze, S. Shapiro, P. Wigger, T. Ziegenhagen, and TIPTEQ Research Group (2006). Structural image and petrophysical interpretation of the Chilean subduction zone. TALK, TIPTEQ Workshop und Status Seminar, Kiel. URL: `not_yet_in_GFZ-bib_database`.

Micksch, U., G. K., S. Buske, C. M. Krawczyk, M. Stiller, P. Wigger, M. Araneda, K. Bataille, J. Bribach, S. Lüth, J. Mechie, A. Schulze, S. A. Shapiro, T. Ziegenhagen, and TIPTEQ RESEARCH GROUP (2005). 3-component reflection seismic survey across the seismogenic coupling zone in Chile (project TIPTEQ). POSTER, AGU, San Francisco, USA. URL: `http://edoc.gfz-potsdam.de/gfz/7985`.

Micksch, U., C. M. Krawczyk, M. Araneda, K. Bataille, J. Bribach, S. Buske, K. Groß, S. Lüth, J. Mechie, A. Schulze, S. Shapiro, M. Stiller, P. Wigger, and T. Ziegenhagen (2005a). High-resolution, three-component reflection seismic survey in the southern Central Chilean Andes at 38°S: First data from project TIPTEQ. POSTER, LAK, Geo-ForschungsZentrum (GFZ) Potsdam. URL: `http://edoc.gfz-potsdam.de/gfz/6794`.

Micksch, U., C. M. Krawczyk, M. Araneda, K. Bataille, J. Bribach, S. Buske, K. Groß, S. Lüth, J. Mechie, A. Schulze, S. Shapiro, M. Stiller, P. Wigger, and T. Ziegenhagen (2005b). High-resolution, three-component reflection seismic survey in the southern Central Chilean Andes at 38°S: First data from project TIPTEQ. POSTER, Final Symposium SFB 267, GeoForschungsZentrum (GFZ) Potsdam. URL: `http://edoc.gfz-potsdam.de/gfz/11043`.

Micksch, U., C. M. Krawczyk, M. Araneda, K. Bataille, J. Bribach, S. Buske, K. Groß, S. Lüth, J. Mechie, A. Schulze, S. Shapiro, M. Stiller, P. Wigger, T. Ziegenhagen, and TIPTEQ Research Group (2005). High-resolution, three-component reflection seismic survey in the southern Central Chilean Andes at 38°S. TALK, IASPEI, Santiago, Chile. URL: `http://edoc.gfz-potsdam.de/gfz/7902`.

Micksch, U., C. M. Krawczyk, T. Ryberg, K. Groß, S. Buske, M. Stiller, P. Wigger, and TIPTEQ Research Roup (2006). The seismogenic coupling zone in southern Central Chile, 38°S: Structure and state of the convergent margin between surface and down-dip end. TALK, AGU, San Francisco, USA. URL: `http://edoc.gfz-potsdam.de/gfz/9406`.

Micksch, U., C. M. Krawczyk, T. Ryberg, M. Stiller, and TIPTEQ Research Group (2007a). The crustal architecture and the seismogenic coupling zone in southern Central Chile (38°S) derived from reflection seismic imaging within project TIPTEQ. POSTER, EGU, Vienna, Austria. URL: `http://edoc.gfz-potsdam.de/gfz/display.epl?mode=doc&id=10846`.

Micksch, U., C. M. Krawczyk, T. Ryberg, M. Stiller, and TIPTEQ Research Group (2007b). The seismogenic coupling zone in southern Central Chile, 38°S: A reflection seismic

image of the subduction zone (Project TIPTEQ). POSTER, DGG, Aachen. URL: `http://edoc.gfz-potsdam.de/gfz/11427`.

Micksch, U., C. M. Krawczyk, M. Stiller, M. Araneda, K. Bataille, J. Bribach, S. Buske, K. Groß, S. Lüth, J. Mechie, A. Schulze, S. Shapiro, P. Wigger, and T. Ziegenhagen (2005). High-resolution, three-component reflection seismic survey in the southern Central Chilean Andes at 38°S. first data from Poject TIPTEQ. POSTER, Status Seminar 'Continental Margins', GeoForschungsZentrum (GFZ) Potsdam. URL: `http://edoc.gfz-potsdam.de/gfz/6876`.

Micksch, U., C. M. Krawczyk, M. Stiller, M. Araneda, K. Bataille, J. Bribach, S. Buske, K. Groß, S. Lüth, J. Mechie, A. Schulze, S. A. Shapiro, P. Wigger, T. Ziegenhagen, and TIPTEQ RESEARCH GROUP (2006). The onshore reflection seismic survey of project TIPTEQ: Structural image and petrophysical interpretation of the Chilean subduction zone. POSTER, EGU, Vienna, Austria. URL: `http://edoc.gfz-potsdam.de/gfz/8630`.

Micksch, U., C. M. Krawczyk, M. Stiller, K. Groß, S. Buske, P. Wigger, M. Araneda, K. Bataille, J. Bribach, S. Lüth, J. Mechie, A. Schulze, S. A. Shapiro, T. Ziegenhagen, and TIPTEQ RESEARCH GROUP (2006). High-resolution, three-component reflection seismic survey in the southern Central Chilean Andes, project TIPTEQ. TALK, DGG, Bremen. URL: `http://edoc.gfz-potsdam.de/gfz/8617`.

Micksch, U., C. M. Krawczyk, M. Stiller, and TIPTEQ Research Group, Seismics Team (2006). Reflection seismic survey across the seismogenic coupling zone in southern Central Chile at 38°S(Project TIPTEQ). POSTER, Shonan Village Center, Hayama, Japan. URL: `http://edoc.gfz-potsdam.de/gfz/11044`.

Micksch, U., C. M. Krawczyk, and TIPTEQ Research Group (2005). High-resolution, three-component reflection seismic survey in the southern Central Chilean Andes at 38°S: First data from project TIPTEQ. POSTER, EGU, Vienna, Austria. URL: `http://edoc.gfz-potsdam.de/gfz/6800`.

Micksch, U., C. M. Krawczyk, and TIPTEQ Research Group (2008a). The Chilean subduction zone at 38°S: Implications for the seismogenic coupling zone and the subduction channel from seismic reflection data of project TIPTEQ). POSTER, GEO2008, Aachen. URL: `not_yet_in_GFZ-bib_database`.

Micksch, U., C. M. Krawczyk, and TIPTEQ Research Group (2008b). The Chilean subduction zone at 38°S: Implications for the seismogenic coupling zone and the subduction channel from seismic reflection data of project TIPTEQ). POSTER, AGU, San Francisco, USA. URL: `not_yet_in_GFZ-bib_database`.

Schulze, A., U. Micksch, C. M. Krawczyk, T. Ryberg, M. Stiller, and Research Group TIPTEQ (2006). The seismogenic coupling zone in southern Central Chile, 38°S: A reflection seismic image of the subduction zone (project TIPTEQ). POSTER, AGU, San Francisco, USA. URL: `http://edoc.gfz-potsdam.de/gfz/9410`.

Acknowledgments

First, I would like to thank Prof. Dr. Charlotte Krawczyk for the support and advise throughout this PhD thesis. The support did not end after her transfer to the TU Berlin and the GGA Institute in Hannover. Additional thanks for the coordination of the entire TIPTEQ project! Many thanks to Prof. Dr. Onno Oncken for the possibility to conduct this thesis at department 3.1 of the German Research Center for Geosciences GFZ in Potsdam. I am grateful that he enabled me to touch a holy grail of geophysics on a field trip into the Alps: The Moho! Furthermore I would also like to thank the committee members of this dissertation (Prof. Dr. R. Kind, Prof. Dr. M. R. Handy, Dr. P. Wigger).

Thanks to the whole department 3.1 at GFZ, especially Helmut Echtler and Johannes Glodny for the helpful discussions on Geology that improved this thesis. Thanks to Petra Paschke for the help in administrative issues. I would also like to thank department 2.2 at GFZ, especially Ali Schulze and Klaus Bauer. Special thanks to Trond Ryberg for the help with and discussions about the first-break tomography! Thanks to my colleagues from the geophysical group at the FU Berlin and many thanks to Kolja Groß for the close collaboration and the very nice times we spent in Chile.

Thanks to Stefan Lüth, he provided the SPOC wide-angle velocity data and to Christian Haberland, who provided travel-times from recordings of the explosive shots on the regional seismology network of TIPTEQ. The integrated interpretation benefited from discussions with and data provided by Kolja Groß, Gerhard Kapinos, Christian Haberland, Andreas Rietbrock, Paolo Alasonati, Charlotte Krawczyk. Thanks to the TIPTEQ field team for their self-sacrificing work in the hot Chilean sun. Thanks also to the drilling contractor Detroman (Concepción) as well as Prof. Klaus Bataille (Universidad de Concepción), Manuel Araneda (SEGMI), and the Chilean inhabitants for having made this survey possible. The seismic stations were provided by the FU Berlin and the Geophysical Instrument Pool Potsdam (GIPP).

I also want to thank Prof. Dr. Peter Bormann, who convinced me to study geophysics during two internships at GFZ Potsdam before university.

Almost all figures were generated or constructed with the Generic Mapping Tools, GMT, by Wessel and Smith and the CorelDRAW Graphics Suite. A great tool to display and manipulate a large number of grid/image types is Mirone by Joaquim F. Luis, check it out! The text was produced with LaTeX 2_ε using MiKTeX and WinEdt.

This thesis is financially supported by the R&D-Program GEOTECHNOLOGIEN funded by the German Ministry of Education and Research (BMBF) (Grant 03G0594) and the German

> In the morning sun, I couldn't tell you
> I couldn't tell you so many things
> About how much I really love you
> About how much you really mean
>
> So far away but it's so easy to see you
> When I'm away I want to put my arms around you
> And I want to know - do you feel the same way?
> 'Cause if you do I want to stay forever
> With you
>
> **Stay forever - WEEN**

Curriculum Vitae

Uli Micksch

born 06.07.1977 in Kaiserslautern (Germany)

email: uli@ulimicksch.de

Education

07.2004 - **09.2008** **PhD in Geophysics** at GFZ Potsdam and Free University Berlin, Germany. Title of the thesis:
The Chilean subduction zone at 38.2° S: New geophysical images derived from seismic reflection data of project TIPTEQ - Implications for the subduction channel and the seismogenic coupling zone -.

10.1997 - **04.2004** **Diplom (Master's Degree) in Geophysics**, University of Karlsruhe, Germany. Title of the thesis: Sedimentary structure, subsidence history and roughness analysis of Nansen and Amundsen Basin, Arctic Ocean.

09.1987 - 05.1996 Abitur, Burggymnasium Kaiserslautern.

08.1983 - 07.1987 Primary school in Rodenbach.

Positions

07.2004 - 09.2008 Scientist at GeoForschungsZentrum Potsdam during PhD studies.

11.2002 - 07.2004 Research assistant at Alfred Wegener Institute for Polar and Marine Research (AWI) during diploma studies.

10.1997 - 11.2002 Research assistant, donie-geoconsult and ICP consulting engineers.

10.1997 - 11.2002 Research assistant, Geophysical Institute, University of Karlsruhe.

08.1996 - 08.1997 Zivildienst / alternative civilian service

Projects

01.2005 - 02.2005   Deployment of EDL reflection seismic and seismological stations in south central Chile within project TIPTEQ, GeoForschungsZentrum Potsdam.

08.2003 - 10.2003   RV Polarstern cruise 19/4 - EUROMARGINS, Alfred Wegener Institute for Polar and Marine Research (AWI). Deployment of OBS/OBH stations in the east Greenland Sea, the shelf and coastal regions as well as onshore RefTek stations, handling the air-gun and streamer equipment for reflection seismic surveys, magnetic survey flights, supervision of gravity and Parasound equipment and data processing on board Icebreaker Polarstern during EUROMARGINS (ARK19/4) expedition to east Greenland.

07.2001 - 10.2001   RV Polarstern cruise 17/2 - AMORE, Alfred Wegener Institute for Polar and Marine Research (AWI). Deployment of ice-borne RefTek refraction seismic and seismological stations, handling the air-gun and streamer equipment for reflection seismic surveys, magnetic survey flights, supervision of gravity and Parasound equipment, extracting sediment cores from the gravity corer and data processing on board Icebreaker Polarstern during AMORE (ARK17/2) expedition to Gakkel Ridge and adjacent Nansen and Amundsen Basin and North Pole.

04.2000 - 05.2000   RV Meteor cruise 47/2 - GERSHWIN, GEOMAR, Kiel. Deployment of OBS/OBH stations and data pre-processing on board RV METEOR during GERSHWIN expedition to the Mid-Atlantic-Ridge at 5° S.

07.1999 - 08.1999   CDRoM, University of Karlsruhe. Continental Dynamics - ROcky Mountain Project - Deployment of refraction seismic stations in the Rocky Mountains (Co, USA).

09.1998 - 09.1998   Transalp, LMU Munich. Deployment of RefTek and Pdas refraction seismic stations during TransAlp experiment, Central Alps.

07.1998 - 07.1998   Mining geophysics, University Freiberg. Mining geophysics in the teaching mine of the University of Freiberg.

02.1998 - 05.1998   SHIPS, USGS, Menlo Park, Ca, USA. Seismic Hazards Investigations in Puget Sound - Deployment of RefTek refraction seismic stations in the Seattle region (WA, USA).

05-06.97 and 09.1997   2 internships at GeoForschungsZentrum Potsdam before university.

STR08/14

Uli Micksch, The Chilean subduction zone at 38.2° S